CHARACTERIZING AND CONTROLLING OPTICAL PROPERTIES OF NANOMATERIALS FOR APPLICATIONS IN OPTICAL SUPER-RESOLUTION MICROSCOPY, CANCER THERANOSTICS, AND ARTS AND ARCHITECTURE

A Dissertation

Presented to the Faculty of the Graduate School

of Cornell University

In Partial Fulfillment of the Requirements for the Degree of

Doctor of Philosophy

by

Ferdinand Friedrich Erich Kohle

August 2018

CHARACTERIZING AND CONTROLLING OPTICAL PROPERTIES OF NANOMATERIALS FOR APPLICATIONS IN OPTICAL SUPER-RESOLUTION MICROSCOPY, CANCER THERANOSTICS, AND ARTS AND ARCHITECTURE

Ferdinand Friedrich Erich Kohle, Ph.D.

Cornell University 2018

Optical properties of nano-sized materials (optical nanomaterials) can either be the result of interactions of light with periodic material structures, *e.g.* in colloidal or block copolymer based photonic crystals, or stem from the incorporation of photoactive molecules into nano-sized, optically inactive materials, *e.g.* fluorescent dyes in organic-inorganic hybrid silica nanoparticles. This dissertation introduces representatives of both material classes.

The first case described here are ultrasmall (sub-10 nm) amorphous silica nanoparticles (SNPs) covalently encapsulating photoactive organic moieties. Such particles, referred to as Cornell prime dots (C' dots), have already shown tremendous success in the safe diagnosis of cancer in human clinical trials with melanoma patients. However, their full potential in the lab and clinical setting, as diagnostic as well as therapeutic probes, has not yet been fully explored. Furthermore, comprehensive understanding of particle structure-property correlations, *i.e.* core and surface properties, remains limited. In the first part of this dissertation, a new approach for characterizing the particles is introduced using a combination of fluorescence correlation spectroscopy (FCS), single particle bleaching, and high-performance liquid chromatography (HPLC). It is shown that the net charge of organic dyes introduced in the synthesis is a main

contributor to chemical surface heterogeneities of the particles. In the second part of this thesis a new class of ultrasmall theranostic silica nanoparticles for the application in photodynamic therapy is described. It is demonstrated that high effective singlet oxygen quantum yields can be achieved, while keeping particle size below the threshold for renal clearance (sub-10 nm). Next, the concept of particle molecular photo-engineering (PMPE) is introduced as a means to tailor photophysical properties of organic dye encapsulating SNPs. By precisely engineering the chemical composition of the amorphous silica particle core network around encapsulated organic dyes using specific functional groups, *i.e.* mercaptopropyl or iodopropyl groups, dye transient dark states can be controlled which in turn enables super-resolution microscopy and substantially enhanced singlet oxygen quantum yields, respectively.

The second class of optical nanomaterials in this dissertation is a self-assembled poly(styrene-block-tert-butyl methacrylate) (StB) diblock copolymer with a photonically active lamellar structure. Bottom-up self-assembly processes provide highly desired and cost-effective methods for the fabrication of large scale/area photonic coatings, making such materials interesting candidates for applications in architecture and design. In part three of this thesis the synthesis of ultralarge molar mass StB block copolymers and their application as iridescent and transparent thin film coatings is described. Development of a casting-lamination process to apply such coatings to window panels allowed the first architectural use of block copolymers as an iridescent façade in the form of the art installation *A needle woman: Galaxy Was a Memory, Earth is a Souvenir* by artist Kimsooja. Quantitative characterization of structural as well as optical properties of these coatings establishes that the block copolymer films behave as volume-phase gratings with grating periodicities close to 300 nm.

BIOGRAPHICAL SKETCH

Ferdinand Friedrich Erich Kohle grew up in Tübingen, Germany, where he attended the Geschwister-Scholl-Schule. He studied chemistry and physics at Karlsruhe Institute of Technology and Ruprecht-Karls-Universitity Heidelberg, graduating with a Bachelors of Science in Theoretical Chemistry under Prof. Horst Köppel and a Masters of Science in Physical Chemistry under Prof. Dirk-Peter Herten. In 2018 he received his Ph. D. in Materials Chemistry from Cornell University, working with Prof. Ulrich B. Wiesner on optical nanomaterials for biomedical and architectural and design applications.

Dedicated to patients whose hope lies in scientific research.

ACKNOWLEDGMENTS

I would like to thank a number of individuals and institutions that directly or indirectly contributed to this dissertation.

First, I would like to express my deep gratitude to my advisor Prof. Dr. Ulrich B. Wiesner for many insightful discussions and valuable academic and professional advice throughout the entire length of my Ph.D. I would also like to thank the members of my committee Prof. Dr. Lara Estroff and Prof. Dr. Barbara Baird for their support, for discussions, and for advice. Furthermore, I'd like to thank Prof. Dr. Warren Zipfel for valuable discussion and for his experimental support with numerous optical instruments and measurements.

I am grateful for the presence of all my fellow Ph.D. students and postdocs for countless scientific discussions, for experimental support and their friendship. In particular, I would like to thank, Joshua A. Hinckley, Thomas Gardinier, Peter Beaucage, Ethan Susca, Jacob Erstling, Melik Turker, Dr. Teresa Kao, Dr. Kasia Oleske, Dr. Kai Ma, Dr. Hiroaki Sai, Dr. Yusuke Hibi, Dr. Tangi Aubert, and Dr. Nirmalya Bag. I also express my gratitude for the commitment and motivation of a number of Masters and Undergraduate students that worked with me on various projects. In particular, I want to acknowledge, Songying Li, Nikhil Dhawan, and Naedum DomNwachukwu. In addition, I wish to thank various collaborators, as indicated in individual chapters, for their contribution.

Special thanks are extended to the staff of the Cornell Center for Materials Research (CCMR) and Nanobiotechnology Center (NBTC), particularly, John L. Grazul, Philip Carubia, Don Werder, and Teresa Porri for instrumental training and answering of countless questions. I also would like to express my gratitude to the administration of the department of Chemistry and Chemical Biology and the department of Materials Science and Engineering at Cornell University. Special thanks go to Pat Hine, and Dolores Dewbury, who were able to help me with various administrative challenges.

Beyond the scope of scientific research, I want to acknowledge Prof. Dr. Juan Hinestroza, Prof. Bill Gaskins, and Prof. Jenny Sabin, all of which have supported my interest in photography, design and architecture throughout my Ph. D., and have enabled me to educate myself in these fields either through classes or through private conversations. I also want to thank Stephanie Owens, Kimsooja, and Jaeho Chong for the opportunity to collaborate in the 2014 Cornell Council for the Arts (CCA) Biennial, "Intimate Cosmologies: The Aesthetics of Scale in an Age of Nanotechnology".

I express my outmost gratitude to my parents who have always unconditionally supported me in all stages of my education, and taught me tolerance and self-discipline that have enriched my life many times. I also want to apologize for countless times that I was absent minded in their presence thinking about research related problems and for family gatherings that I had to miss. This gratitude extends to my family at large and to all the friends that I have made along the way. I want to thank Dennis Dzendzo, Seraphine Meya and Meya family, Julien Lauto, Dr. Alexander Kurz, Thorsten Sauer, Dr. Nicolas Tessore, Gergely Jancsovics, Dr. Lukas Brückner, Tobias Kimpel, Dr.

Yunji Kim, Mickey Singer, Taro Naoi, Dr. Emily Sun, Thomas Swisher, So Yoon Ryu, and many others. All these individuals have supported me in one way or another and have majorly contributed to make this journey a rich experience. I also want to express my utmost gratitude to my grandfather, who has always supported and fostered my interest in science.

I would also like to thank the radio network SWR2 and its editorial staff whose excellent podcasts helped me to bear countless late and lonely hours in the lab.

Last but not least, I wish to acknowledge all funding sources that have supported my education. Here, in particular, I would like to thank the Markelstiftung (*i.e.* Marion Oertel-Nau), that has financially supported me for many years and enabled me to pursue academic research, the Cornell-Heidelberg Exchange Fellowship (*i.e.* Elisabeth Trnka-Hammel), that has assisted me during the transfer to Cornell University, the German Academic Exchange Service (DAAD) for research funding, and the Department of Energy (DOE) that have financially supported my research.

TABLE OF CONTENTS

LIST OF FIGURES

LIST OF TABLES

LIST OF ABBREVIATIONS

^{1}H NMR	proton nuclear magnetic resonance
3D	three-dimensional
ACF	autocorrelation function
AF647	Alexa Fluor 647, cyanine dye, absorption/emission at 650/665 nm
APD	avalanche photodiode detector
APTES	(3-aminopropyl)triethoxysilane
APTMS	(3-aminopropyl)trimethoxysilane
ASB	aluminum-tri-sec-butoxide
ATTO 647N	organic carborhodamine dye, absorption/emission at 646/664 nm
ATTO 680	organic dye, absorption/emission at 681/698 nm
BCP	block copolymer
BODIPY	boron-dipyrromethene, class of organic dyes.
BxPC3	cell line from human pancreas
C dots	Cornell dots, core-shell organic-inorganic hybrid silica nanoparticles. Synthesized using a modified Stöber process.
C' dots	Cornell prime dots, sub-10 nm organic-inorganic hybrid PEGylated silica nanoparticles. Synthesized in water.
c(RGDyC)	cyclic $\alpha_v\beta_3$ integrin–targeting peptide arginine–glycine–aspartic acid-tyrosine-cysteine
CCA	Cornell Council for the Arts
CP/MAS	cross polarization magic angle spinning
n-BuLi	n-butyllithium
cryoTEM	cryogenic Transmission Electron Microscopy
Cy3	cyanine dye, absorption/emission at 554/568 nm
Cy5	cyanine dye, absorption/emission at 660/670 nm
Cy5.5	cyanine dye, absorption/emission at 675/694 nm
DI water	deionized water
DLS	Dynamic Light Scattering
DM	dichroic mirror
DMSO	dimethylsulfoxide
DNA	deoxyribonucleic acid
DPBF	1,3-diphenylisobenzofuran
DPE	1,1-diphenylethylene
DSS	4,4-dimethyl-4-silapentane-1-sulfonic acid

EDS	Energy-Dispersive X-ray Spectroscopy
EMCCD	electron-multiplying charge-coupled device
ET	energy transfer
FBS	fetal bovine serum
FCS	Fluorescence Correlation Spectroscopy
FDA	US Food and Drug Administration
FP	fluorescent protein
FWHM	full width at half maximum
GAFF	general AMBER force field
GFP	green fluorescent protein
GMBS	N-γ-maleimidobutyryl-oxysuccinimide ester
GPC	Gel Permeation Chromatography
GSDM	Ground State Depletion Microscopy
HD	hydrodynamic diameter
HPLC	high-performance liquid chromatography
IND	investigational new drug
IPTMS	(3-iodopropyl)trimethoxysilane
IQR	inner quartile range
IRF	instrument response function
ISC	intersystem crossing
LAOS	large amplitude oscillatory shear
LC-MS	liquid chromatography coupled mass spectrometry
LED	light-emitting diode
LPF	long pass filter
MB	methylene blue
MB2	methylene blue derivate
MD	molecular dynamics
MeOH	methanol
MPTMS	(3-mercaptopropyl) trimethoxysilane
MWCO	molecular weight cut-off
NA	numerical aperture
NIR	near-infrared wavelength range (650-900nm)
NP	nanoparticle
OB	microscope objective
OD	optical density
PBS	phosphate-buffered saline
PDT	Photodynamic Therapy
PEG	poly(ethylene glycol)
PET	polyethylene terephthalate or positron emission tomography

PH	pinhole
pH	logarithmic scale for the description of acidity or basicity of an aqueous solution
PK	pharmacokinetics
PMMA	poly(methyl methacrylate)
PMPE	particle molecular photo-engineering
PPSMI	post-PEGylation surface modification by insertion
PS	polystyrene or photosensitizer
PS-*b*-PtBMA or StB	poly(styrene-*block*-tert-butyl methacrylate)
PSF	point spread function
PtBMA	poly-tert-butyl methacrylate
QD	quantum dot, semiconductor nanocrystal
R.E.S.P.	restrained electrostatic potential
ROI	region of interest
SEM	Scanning Electron Microscopy
SNP	silica nanoparticles
SPASER	surface plasmon amplified stimulated emission of radiation
SR	super-resolution
ssNMR	solid-state Nuclear Magnetic Resonance
StB or PS-*b*-PtBMA	poly(styrene-*block*-tert-butyl methacrylate)
STEDM	Stimulated Emission Depletion Microscopy
STORM	Stochastic Optical Reconstruction Microscopy
tBMA	tert-butyl methacrylate
TEM	Transmission Electron Microscopy
TEOS	tetraethoxysilane or tetraethyl orthosilicate
THF	tetrahydrofuran
TIRFM	Total Internal Reflection Fluorescence Microscopy
TMOS	tetramthoxysilane or tetramethyl orthosilicate
TMR	tetramethylrhodamine, organic dye, absorption/emission at 541/567 nm
TPPM	two-pulse phase-modulated
USAXS	Ultra-Small-Angle X-ray Scattering
UV	ultraviolet
βME	β-mercaptoethanol

CHAPTER 1

INTRODUCTION

In this Chapter, the chemistry of amorphous silica nanoparticles (SNPs) is introduced, and the content of this dissertation is contextualized within the historical background of ultrasmall (<10 nm) fluorescent organic-inorganic hybrid SNPs.

Since the pioneering report by Stöber et al. (*1*) on the fabrication of narrowly dispersed spherical silica particles in solution in 1968, these colloids have found numerous industrial applications, *e.g.* as catalyst supports, abrasive/anticaking agents in cosmetics, and fillers for rubber to name a few (*2*). The synthesis of Stöber particles is described by two reactions. First, an alkoxysilane (precursor), *e.g.* tetraethylorthosilicate (TEOS), is hydrolyzed to silicic acid ($Si(OH)_4$) under basic conditions in an alcohol-water mixture, and then condensed to silicondioxide (SiO_2, silica). The reactions can be expressed as

hydrolysis $$Si(OC_2H_5)_4 + 4\,H_2O \longrightarrow Si(OH)_4 + 4\,C_2H_5OH$$

condensation $$Si(OH)_4 \longrightarrow SiO_2 + 2\,H_2O$$

The resulting particle properties, *i.e.* size and dispersity, are sensitive to alkoxysilane reactant structure and details of the synthesis conditions. For example, at constant TEOS and water concentrations particle size increases with increasingly basic solution pH (*1*).

Typical sizes for narrowly dispersed particles range from ~50 nm to ~2000 nm. Generally, the use of smaller alcohols as solvent and precursors with smaller alkoxy groups yields faster reactions and smaller particles (*3, 4*). The rate of hydrolysis has a minimum at pH 7, and the rate of condensation has a maximum at pH ~8 and a minimum at pH ~2 (*4*).

In 1992 van Blaaderen and Vrij extended Stöber's work by covalently incorporating organic fluorophores into the silica matrix via silane-organic dye conjugates (*5*). However, particle diameters were in the hundreds of nanometers and therefore of no practical use for applications in bioimaging. In 2005, Ow et al. recognized that the size of narrowly distributed and fluorescently labeled SNPs could be decreased to ~20 to 30 nm in a Stöber-type synthesis by introducing a core-shell approach (*6*). These particles, termed Cornell dots or short C dots, contained a silica core that covalently embedded the fluorescent dyes, and a silica shell that was subsequently grown onto the fluorescent cores via careful dosing of TEOS precursor into the particle solution to suppress secondary particle nucleation. It was further found that the encapsulation of organic dyes within the silica network did not only allow co-localization of multiple dyes within one particle, increasing brightness, but also enhanced dye photostability by providing steric shielding from dissolved oxygen. Most importantly, covalent dye encapsulation substantially increased per dye fluorescent quantum yield, by suppressing non-radiative energy dissipation pathways, and enhancing radiative rates (*7*). In 2006, Burns et al. demonstrated that the core-shell architecture could be utilized to design ratiometric pH particle sensors. To that end, a reference dye with pH-independent emissive properties, here TRITC dye, was

encapsulated into the particle core and a pH sensor dye, here FITC dye, into the outer shell (*8*). In a review article of the same year, the versatility of silica chemistry for building functional nanoparticles was recognized and the concept of a *lab-on-a-particle* introduced. In analogy to the *lab-on-a-chip* idea, where chemistry reaction volumina are miniaturized, this concept predicted the formation of multifunctional particle entities that could perform sequences of chemical functions on a single particle (*9*). In 2009, Noginov et al. took the concept of fluorescent SNPs further by replacing the silica core with a 14 nm gold core with a surrounding 15 nm silica shell that contained the fluorescent dye Oregon Green 488. This architecture allowed the resonant energy transfer from excited dyes to surface plasmons and enabled surface plasmon amplified stimulated emission of radiation (the "SPASER" concept) thereby breaking the diffraction limit associated with lasing and creating the smallest nanolaser reported at the time (*10*).

At about the same time, C dots were investigated as a new platform for nanotechnology based medicines (nanomedicine). The strategic advantage of nanoparticles in medicine is the possibility of combining multiple functionalities within one entity. This may include increased potency of targeting moieties and drugs through multivalency effects (*11, 12*), personalized medicine, or combined diagnostics and therapeutics (theranostics) (*13, 14*). In 2009, it was demonstrated for the first time that C dots covalently encapsulating a range of near-infrared (NIR) emitting dyes could reach sizes below 10 nm (*15*). In the same year, such ultrasmall (hydrodynamic diameter, HD < 10 nm) NIR Cy5 dye encapsulating C dots, functionalized with a poly(ethylene glycol) (PEG) corona, exhibited high biostability, biocompatibility and efficient renal

clearance profiles in mice (*16*). Two years later, it was shown that these particles could further be surface-functionalized with the cyclic $\alpha_v\beta_3$ integrin–targeting peptide arginine–glycine–aspartic acid-tyrosine-cysteine (c(RGDyC)), which simultaneously allowed for radiolabeling with positron emission tomography (PET) active ^{124}I of the tyrosine moiety as well as conjugation to PEG-silanes via thiol-ene click chemistry using the cysteine residue. Effective targeting of melanoma cells was demonstrated with these particles (*17*). The combination of bulk renal clearance, favorable targeting- and pharmacokinetics (PK), improved dye properties, multimodal imaging capabilities (PET and optical), as well as biocompatibility demonstrated in pre-clincal studies (*17*) lead to a successful investigational new drug (IND) application to the US food and drug administration (FDA), and a subsequent first-in-human clinical trial of ultrasmall C dots in melanoma patients. Results suggested the safe use of C dots for cancer diagnostics (*18*).

These studies underlined the importance of particle sizes below 10 nm to avoid off-target toxicity via rapid renal clearance. Even the modified Stöber process described above was not ideal, however, for the fabrication of such ultrasmall fluorescent SNPs. While particle size distributions above ~20 nm could be well controlled via the core-shell approach (*vide supra*), the synthetic control below 10 nm was pushing the limits of both, particle size distribution control as well as particle stabilization, in particular in solutions with high salt concentrations around 0.1 M typically encountered e.g. in blood serum. In addition to small particle sizes, it is essential for medical applications to move from a state of charge-stabilization in water via deprotonated silica surface silanol (-Si-OH) groups to a state of steric stabilization, *e.g.* via particle surface functionalization

with PEG chains, to avoid particle aggregation under physiological conditions (*16*). During SNP surface functionalization, particles transiently move through a state where the remaining surface charges are insufficient to provide full charge stabilization, while the surface PEG coating is not yet sufficient to assure full steric stabilization (*19*). This "valley-of-death" either leads to wider size distributions or complete particle destabilization, aggregation, and ultimately particle precipitation. Ultrasmall SNPs are especially vulnerable during this transition due to their high surface energy. Consequently, fast PEGylation kinetics are desired. However, even small amounts of alcohol (*e.g.* ethanol >20% v/v) in water/alcohol mixtures used in the Stöber process prevent rapid PEG adsorption on SNP surfaces, likely due to the suppression of hydrogen bonding between the ether oxygen in PEG chains and surface silanol groups, thereby slowing down covalent bond formation between the particle surface and PEG-silanes (*19*). These arguments suggested the need for an improved synthesis approach to ultrasmall fluorescent and surface-functionalized SNPs. In 2015, Ma et al. introduced a new synthetic method for the synthesis of ultrasmall SNPs with size control down to 5 nm HD and single atomic silica layer precision (*20*). Figure 1.1 illustrates this new synthesis in comparison to the previously used Stöber-type approach to C dots.

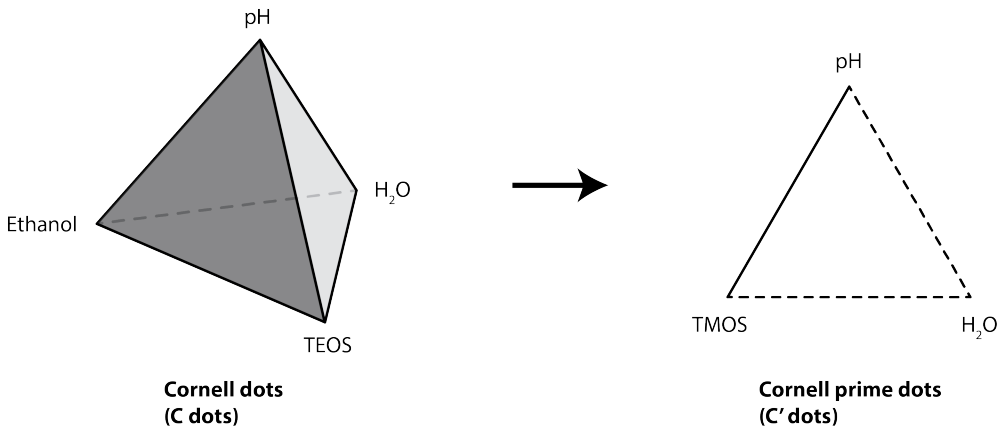

Figure 1.1. Comparison of reaction parameter space for Cornell dot (C dot) and Cornell prime dot (C' dot) syntheses at room temperature (see text for details).

The old C dot synthesis approach is governed by a four-dimensional reaction parameter space (left side), indicated by the four corners of a tetrahedron labeled as TEOS, pH, H_2O, and ethanol, respectively. The relative concentrations of these reactants are responsible for the final particle size and size distribution and ultimately play a role in particle PEGylation. In the new method, ethanol is removed from the parameter space and water simultaneously acts as reactant and solvent. This change collapses the four-dimensional parameter space into a pseudo two-dimensional parameter space, where water is available in excess (indicated by the dashed sides of the right triangle). Now, particle formation solely depends on the type and concentration of precursor and the solution pH. Importantly, in the new method water-insoluble TEOS is replaced with water-soluble TMOS, thereby substantially increasing the rate of hydrolysis, leading to simultaneous SNP seed formation (i.e. substantially reduced secondary nucleation), and resulting in narrowly-dispersed ultrasmall SNPs. These water-based SNPs were named

Cornell prime dots or simply C' dots (Figure 1.2), and marked a breakthrough for the synthetic control of ultrasmall SNPs.

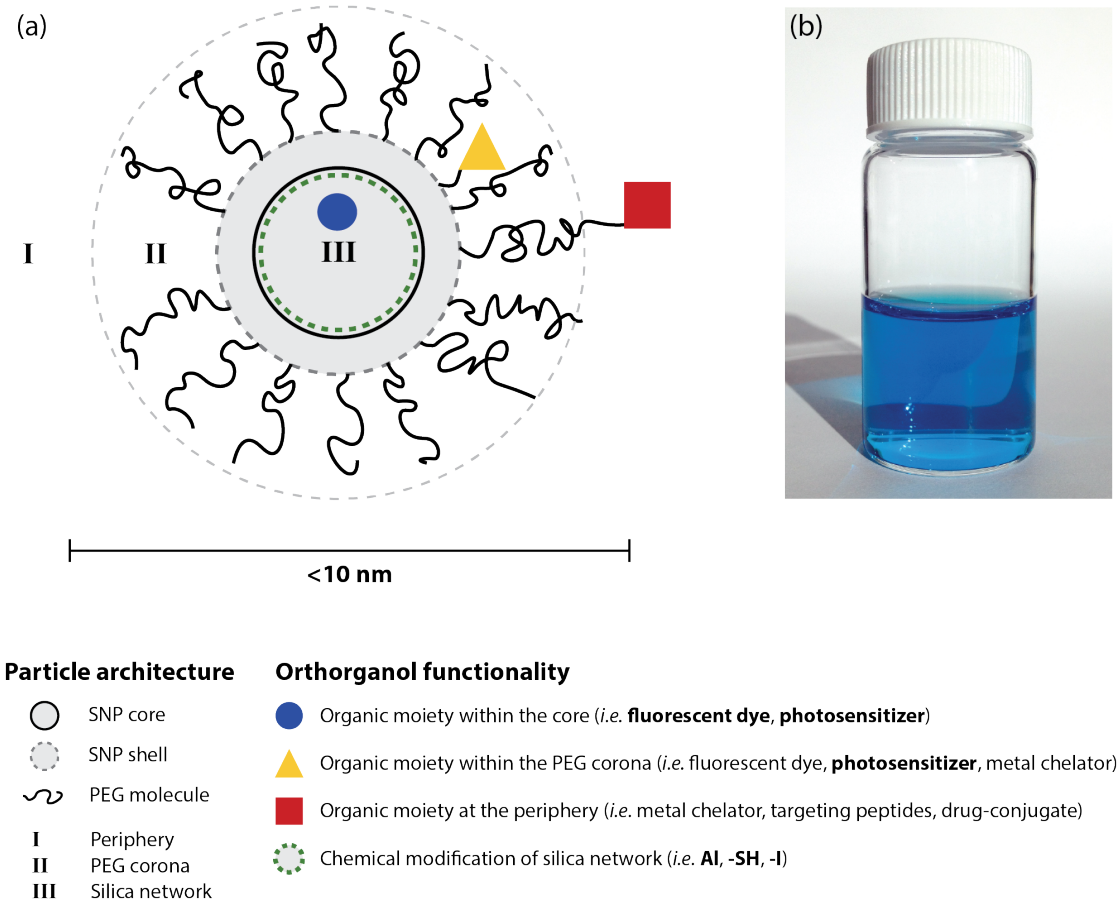

Figure 1.2. (a) Summary of C' dot architecture and orthogonal functionalities that were reported in the literature and in this thesis. Functionalities discussed in this thesis are bolded. (b) Photograph of PEGylated Cy5 encapsulating C' dots in aqueous solution.

For example, in addition to rapid particle nucleation the use of water as a solvent also allowed the development of robust PEGylation protocols and gave room for growth-quenching approaches. Similar to "living" ionic polymerization approaches, where macromolecular size distributions are kept narrow by allowing all chains to

simultaneously grow for the exact same amount of time, SNP nucleation and growth initiated by TMOS addition can be finely controlled before the full particle size is reached by quenching the reaction via addition of PEG chains to the growth solution leading to rapid association with SNP surfaces and preventing further monomer addition to the growing surface (*20*). Due to this favorable PEGylation kinetics in water, the door to a wide range of surface functionalization was pushed open. For example, in the same paper it was demonstrated that heterobifunctional PEGs functionalized on one end with a peptide, e.g. (cRGDyC), have an even higher affinity to silica surfaces as the parent PEG-silanes. This in turn facilitates very high surface functionalization yields with PEG-peptide conjugates lowering production costs (*20*).

First steps towards therapeutic particles were taken in 2015, when ultrasmall fluorescent C' dots were covalently labeled with a PEG-drug-conjugate that could be released through enzymatic hydrolysis (*21*). Furthermore, while investigating the effects of higher C' dot concentrations typical in therapeutic applications on cells, in 2016 it was discovered that C' dots can induce ferroptosis in nutrient- (i.e. amino-acide-) deprived cancer cells and cancer-bearing mice likely due to chelating of iron(III) cations by surface silanol groups in micropores of the particles, which is then carried into cells via endocytosis (*22*). Contrary to earlier assumptions that the amorphous silica mainly serves as a rigidifying matrix enhancing dye brightness, this study drew attention to the silica network as an active contributor to therapeutic particle properties. More recently, the earlier PET radiotracer ^{124}I was replaced by the radiometal ^{89}Zr to study the biodistribution of targeted c(RGDyC) bearing C' dots in mice. It was shown that such C' dots either targeted the tumor or cleared from the body, thereby encouraging future

applications as a radiotherapeutic with chelated lutetium-177 or actinium-225 (*23*). Finally, sub-7 nm theranostic C' dots with a record of five functionalities, including optical detection and pH sensing, specific cell targeting, radioisotope chelation, and drug delivery, were demonstrated in 2017 together with a spectroscopic method to quantitatively assess the number of each individual functional group (*24*)**.**

This dissertation describes the continuation of research on ultrasmall inorganic-organic SNPs obtained from water-based synthesis protocols. The emphasis of this work lies on the precise control of optical particle properties via the introduction of specific organic moieties into the silica dye environment. One additional chapter is dedicated to bottom-up derived photonic materials in the form of self-assembled block copolymer films that are used as iridescent materials for the arts and architecture. The spectrum of work presented here can roughly be divided into three parts.

Part one (Chapter 2 and Chapter 3) discusses methods for the in-depth characterization of ultrasmall SNPs containing fluorescent organic dyes. Chapter 2 introduces fluorescence correlation spectroscopy (FCS) and its potential to study fast photophysical processes of dye-encapsulating ultrasmall SNPs to learn about the correlation between particle silica core composition/architecture and dye photophysical properties. Chapter 3 investigates heterogeneities of surface chemical properties of dye encapsulating C' dots. To that end, findings from Chapter 2 and single particle step-wise bleaching experiments are applied in combination with high-performance liquid chromatography (HPLC) experiments to assess the origin of these heterogeneities.

Part two (Chapter 4 and Chapter 5) describe the synthesis and characterization of two new classes of optically active C' dots. Chapter 4 discusses C' dots with the capability to generate singlet oxygen upon near infrared (NIR) excitation, adding a new therapeutic modality to the family of C' dots, *i.e.* for use in photodynamic therapy. Chapter 5 introduces the concept of particle molecular photo-engineering, or simply PMPE, to control the photophysical properties of utrasmall SNPs. It is shown that the silica matrix itself can be utilized to create local environments with unique chemical properties to precisely influence the optical properties of encapsulated organic dyes. It is demonstrated that PMPE opens the door for ultrasmall SNPs to be used in optical super-resolution microscopy.

Part three (Chapter 6) documents the development of an iridescent polystyrene-*b*-poly(tert-butyl methacrylate) diblock copolymer façade coating for the ~14 m tall installation *A needle woman: Galaxy Was a Memory, Earth is a Souvenir* by artist Kimsooja. A separate introduction to block copolymers and structural color can be found in the first part of Chapter 6.

REFERENCES

(*1*) Stöber, W., Fink, A., Bohn, E. Controlled growth of monodisperse silica spheres in the micron size range. *J. Colloid Interface Sci.*, **26,** 62–69 (1968).

(*2*) Giesche, H. Medical and technological application of monodispersed colloidal silica particles. In Medical Applications of Colloids; Matijević, E., Ed.; Springer: New York, pp 42– 66 (2008).

(*3*) Sadasivan, S., Dubey, A. K., Li, Y., Rasmussen, D. H. Alcoholic Solvent Effect on Silica Synthesis-NMR and DLS Investigation. *J. Sol-Gel Sci. Technol.*, **12,** 5–14 (1998).

(*4*) Iler, R. K. The chemistry of silica: solubility, polymerization, colloid and surface propertoes, and biochemitsry. Wiley-Interscience (1979).

(*5*) Van Blaaderen, A., Vrij, A. Synthesis and characterization of colloidal dispersions of fluorescent, monodisperse silica spheres. *Langmuir*, **8,** 2921–2931 (1992).

(*6*) Ow, H., Larson, D. R., Srivastava, M., Baird, B. A., Webb, W. W., Wiesner, U. Bright and Stable Core−Shell Fluorescent Silica Nanoparticles. *Nano Lett.*, **5,** 113–117 (2005).

(*7*) Larson, D. R., Ow, H., Vishwasrao, H. D., Heikal, A. A., Wiesner, U., Webb, W. W. Silica Nanoparticle Architecture Determines Radiative Properties of Encapsulated Fluorophores. *Chem. Mater.*, **20,** 2677–2684 (2008).

(*8*) Burns, A., Sengupta, P., Zedayko, T., Baird, B., & Wiesner, U. Core/Shell Fluorescent Silica Nanoparticles for Chemical Sensing: Towards Single-Particle Laboratories. *Small*, **2,** 723–726 (2006).

(*9*) Burns, A., Ow, H., Wiesner, U. Fluorescent core–shell silica nanoparticles: towards “Lab on a Particle” architectures for nanobiotechnology. *Chem. Soc. Rev.*, 35, 1028–1042 (2006).

(*10*) Noginov, M. A., Zhu, G., Belgrave, A. M., Bakker, R., Shalaev, V. M., Narimanov, E. E., Stout, S., Herz, E., Suteewong, T, Wiesner, U. Demonstration of a spaser-based nanolaser. *Nature*, **460,** 1110–1112 (2009).

(*11*) Mammen, M., Choi, S.-K., Whitesides, G. M. Polyvalent Interactions in Biological Systems: Implications for Design and Use of Multivalent Ligands and Inhibitors. *Angew. Chem. Int. Ed.*, **37,** 2754–2794 (1998).

(*12*) Angioletti-Uberti, S. Theory, simulations and the design of functionalized nanoparticles for biomedical applications: A Soft Matter Perspective. *Npj Computational Materials*, **3,** (2017).

(*13*) Ferrari, M. Cancer nanotechnology: opportunities and challenges. *Nat. Rev. Cancer*, **5,** 161–171 (2005).

(*14*) Wagner, V., Dullaart, A., Bock, A.-K., Zweck, A. The emerging nanomedicine landscape. *Nat. Biotechnol.*, **24,** 1211–1217 (2006).

(*15*) Herz, E., Ow, H., Bonner, D., Burns, A., Wiesner, U. Dye Structure – Optical Property Correlations in Near-Infrared Fluorescent Core-Shell Silica Nanoparticles, *J. Mater. Chem.*, **19,** 6341-6347 (2009).

(*16*) Burns, A. A., Vider, J., Ow, H., Herz, E., Penate-Medina, O., Baumgart, Larson, S. M., Wiesner, U., Bradbury, M. Fluorescent Silica Nanoparticles with Efficient Urinary Excretion for Nanomedicine. *Nano Lett.*, **9,** 442–448 (2009).

(*17*) Benezra, M., Penate-Medina, O., Zanzonico, P. B., Schaer, D., Ow, H., Burns, A., DeStanchina, E., Longo, V., Herz, E., Iyer, S.,Wolchok, J., Larson, S. M., Wiesner, U., Bradbury, M. S. Multimodal silica nanoparticles are effective cancer-targeted probes in a model of human melanoma. *J. Clin. Investig.*, **121,** 2768–2780 (2011).

(*18*) Phillips, E., Penate-Medina, O., Zanzonico, P. B., Carvajal, R. D., Mohan, P., Ye, Y., Humm, J., Gonen, M., Kalaigian, H., Schoder, H., Strauss, H. W., Larson, S. M., Wiesner, U., Bradbury, M. S. Clinical translation of an ultrasmall inorganic optical-PET imaging nanoparticle probe. *Sci Transl Med.*, **6,** 260ra149-260ra149 (2014).

(*19*) Ma, K., Zhang, D., Cong, Y., Wiesner, U. Elucidating the Mechanism of Silica Nanoparticle PEGylation Processes Using Fluorescence Correlation Spectroscopies. *Chem. Mater.*, **28,** 1537–1545 (2016).

(*20*) Ma, K., Mendoza, C., Hanson, M., Werner-Zwanziger, U., Zwanziger, J., & Wiesner, U. Control of Ultrasmall Sub-10 nm Ligand-Functionalized Fluorescent Core–Shell Silica Nanoparticle Growth in Water. *Chem. Mater.*, **27,** 4119–4133 (2015).

(*21*) Yoo, B., Ma, K., Zhang, L., Burns, A., Sequeira, S., Mellinghoff, I., Brennan, C., Wiesner, U., Bradbury, M. S. Ultrasmall dual-modality silica nanoparticle drug conjugates: Design, synthesis, and characterization. *Bioorganic Med. Chem.*, **23,** 7119–7130 (2015).

(*22*) Kim, S. E., Zhang, L., Ma, K., Riegman, M., Chen, F., Ingold, I., Conrad, M., Turker, M. Z., Gao, M., Jiang, X., Monette, S., Pauliah, M., Gonen, M, Zanzonico, P., Quinn, T., Wiesner, U., Bradbury, M. S., Overholtzer, M. Ultrasmall nanoparticles induce ferroptosis in nutrient-deprived cancer cells and suppress tumour growth. *Nat. Nanotechnol.*, **11,** 977–985 (2016).

(*23*) Chen, F., Ma, K., Zhang, L., Madajewski, B., Zanzonico, P., Sequeira, S., Gonen, M., Wiesner, U., Bradbury, M. S. Target-or-Clear Zirconium-89 Labeled Silica Nanoparticles for Enhanced Cancer-Directed Uptake in Melanoma: A Comparison of Radiolabeling Strategies. *Chem. Mater.*, **29,** 8269–8281 (2017).

(*24*) Ma, K., Wiesner, U. Modular and Orthogonal Post-PEGylation Surface Modifications by Insertion Enabling Penta-Functional Ultrasmall Organic-Silica Hybrid Nanoparticles. *Chem. Mater.*, **29,** 6840–6855 (2017).

CHAPTER 2

PROBING DYE ENCAPSULATION IN FLUORESCENT CORE-SHELL SILICA NANOPARTICLES BY FLUORESCENCE CORRELATION SPECTROSCOPY*

Abstract

Synthetic advances in the formation of ultrasmall (<10 nm) fluorescent poly(ethylene glycol)-coated (PEGylated) core-shell silica nanoparticles (SNPs), enabling improved particle size and surface chemical property control have led to successful clinical translation of SNPs as diagnostic probes in oncology. Despite the success of such probes, details of the dye incorporation and resulting silica architecture are still poorly understood. Here, we employ fluorescence correlation spectroscopy (FCS) to monitor fast fluorescence fluctuations (lag times $<10^{-5}$ s) of the negatively charged cyanine dye Cy5 as a probe to study such details for dye encapsulation in 5 nm silica cores of PEGylated core-shell SNPs. Upon deposition of additional silica shells over the silica core we find that the amplitude of photo-induced cis-trans isomerization decreases, suggesting that the Cy5 dyes are located near or on the surface of the original SNP cores. In combination with time correlated fluorescence decay measurements we deduce radiative and non-radiative rates of the Cy5 dye in these particles. Results demonstrate that FCS is a well-suited tool to investigate aspects of the photophysics of

* Ferdinand F. E. Kohle, Joshua A. Hinckley, Ulrich B. Wiesner. Probing Dye Encapsulation in Fluorescent Core-Shell Silica Nanoparticles by Fluorescence Correlation Spectroscopy. Manuscript in preparation.

fluorescent nanoparticles, and that conformational changes of cyanine dyes like Cy5 are excellent indicators for the local dye environment within ultrasmall SNPs.

Introduction

The ability to control the size of fluorescent organic-inorganic hybrid silica nanoparticles (SNPs) down to a few nanometers, along with well controlled particle surface chemistry, has proven to be a synthetic milestone for the translation of SNPs as diagnostic probes into the clinical setting (*1, 2*).

With the translation of ultrasmall poly(ethylene glycol)-coated (PEGylated) fluorescent SNPs into the clinic comes further need to understand such nanomaterials in more detail. Sub-10 nm SNPs are often functionalized with expensive fluorophores or targeting moieties. While providing pivotal advantages for biomedical applications, this presents challenges for traditional in-depth SNP characterization techniques including dynamic light scattering (DLS), transmission electron microscopy (TEM), or zeta-potential measurements. Studies of size, nanoparticle-morphology, chemical composition, or degree of functionalization is often accompanied by low signal-to-noise (*i.e.* in TEM), material incompatibility due to fluorescence (*i.e.* in DLS), the need for large sample amounts (*i.e.* in zeta-potential measurements or solid-state nuclear magnetic resonance (ssNMR) spectroscopy), or expensive and slow experimental procedures (*i.e.* in cryo-TEM). In addition, the development of novel classes of SNP materials typically requires many iterations of particle synthesis followed by characterization of each batch, an often tedious, time-consuming, and cost-intensive task.

In order to accelerate the development of ultrasmall functionalized SNPs, fast, inexpensive, sensitive, and versatile characterization techniques are desirable. With the molar mass of such SNPs falling into the regime of macromolecules (~100k Da),

methods typically used for biomolecular research, *i.e.* chromatography and fluorescence based microscopy and spectroscopy, can present a complimentary path for nanomaterials characterization. Fluorescence correlation spectroscopy (FCS) stands out among such characterizations techniques for its high information density obtained in a single measurement conducted at nanomolar sample concentrations. FCS accesses information by detecting fluorescence fluctuations around the thermodynamic equilibrium rather than average fluorescence signals (*3*-*6*). Key to this technique is a very small detection volume, typically a femto to sub-femto liter (10^{-15} L), a thousand times smaller than an eukaryotic cell. Due to the small detection volume and low sample concentrations, no individual molecule or particle is constantly inside the detection volume, allowing to resolve fluorescence fluctuations with high time resolution. To interpret fluorescence fluctuations and extract relaxation times of physical processes, the recorded fluorescence traces are tested for self-similarity by an auto-correlation function.

Due to its versatility and minimally invasive nature, FCS has become a well-established technique with a wide spectrum of applications, reaching from the study of photophysical processes, *i.e.* triplet state dynamics (*3*), photo-induced conformational changes (*7*), to chemical reaction kinetics (*8*), and the study of protein folding (*9*) and living cells (*10*). In principle, every physical process that involves transient non-fluorescent (or weakly fluorescent) states can be studied by FCS. In practice, the accessible relaxation times on a simple confocal setup range from nanoseconds to several hundred milliseconds. Slower processes are typically limited by the emitters' photostability.

The versatility of FCS has led to an increased adoption of FCS in materials science over the last 20 years. Here, FCS is often used employing lag times $>10^{-5}$ s for studies of polymer melts, gels and solutions (*11, 12*), colloidal and/or photophysical properties of NPs (*1, 13, 14-16*), or to study physical adsorption processes to NP surfaces (*17, 18*). However, approaches to extend the temporal resolution to fast fluorescence fluctuations (lag times $<10^{-5}$ s) to study NP properties, *e.g.* rotational diffusion and polarization, remain limited (*19, 20*).

In this study, we use fast fluorescence fluctuations of the cyanine dye Cy5, caused by photo-induced cis-trans isomerization around its polymethic chain (Figure 2.1A), to interrogate the local dye environment in organic-inorganic hybrid core-shell SNPs with different silica shell architectures.

The photo-physics of cyanine dyes have been studied in detail (*21*). At low excitation intensities (< 10 kW cm^{-2}), the photophysical relaxation pathways of Cy5 are mostly limited to conformational changes, while the population of triplet states is negligible. The rates of inter-system crossing and triplet state decay are further reduced upon steric shielding of Cy5 from dissolved oxygen (*7*). In general, large side groups, high viscosity, and low temperatures can retard the conformational reorganizations and reduce the rates for photo-induced isomerization and back-isomerization of cyanine dyes (*7*), making them suitable fluorescence sensors for probing the steric properties of local environments (*22, 23*).

Here, we synthesized a series of sub-10 nm PEGylated core-shell SNPs containing covalently bound Cy5 in the silica core and progressively increasing silica shell thickness before PEGylation. Using FCS, we show that during the formation

process of the silica core a fraction of Cy5 molecules is located near or on the silica core particle surface which in turn is suitable to subsequently probe the deposition of additional silica layers onto the core. In combination with fluorescence lifetime measurements we deduce radiative and non-radiative rates of the Cy5 dye in these particles. We finally conclude that the study of fast dye relaxation kinetics as revealed by FCS is a useful approach to gain detailed insights into the architecture of ultrasmall fluorescent and PEGylated core-shell SNP for applications in biology, nanomedicine, and beyond.

Materials and Methods

Materials

Ammonia solution (2.0 M in ethanol), dimethyl sulfoxide (DMSO), (3-mercaptopropyl) trimethoxysilane (MPTMS), tetramethyl orthosilicate (TMOS), and tetraethyl orthosilicate (TEOS, ≥99%), were purchased from Sigma−Aldrich. Methoxy-terminated poly(ethylene glycol) (PEG-silane, molar mass of ~0.5 kg/mol) was purchased from Gelest. Cy5-meleimide florescent dye and Cy3-meleimide florescent dye were purchased from GE Healthcare. All chemicals were used as received. Deionized (DI) water (18.2 MΩ·cm) was generated using a Millipore Milli-Q system.

Synthesis of fluorescent and PEGylated core-shell silica nanoparticles

Fluorescent core-shell silica nanoparticles were synthesized according to a modified previously published synthesis protocol (*1*). *Core particle synthesis:* For the core particle synthesis 0.367 μmol Cy5-maleimide are conjugated to MPTMS via sulfhydryl-maleimide click chemistry under nitrogen atmosphere in the dark overnight (molar ratio dye: MPTMS = 1:25). Then, for a 10 mL batch synthesis 0.43 mmol (68 uL) of TMOS are added to 10 mL basic DI water (pH 8.5) in a 25 mL round bottom flask under vigorous stirring, immediately followed by the addition of all previously prepared Cy5-silane. The precursors are left to react at room temperature under vigorous stirring in the dark for 12 hours. The particle dispersion is then transferred to a 100 mL round bottom flask and diluted with 40 mL DI water (1:4). Before the growth of a silica shell, an aliquot of 10 mL is separated for PEGylation (“core particle”). *PEGylation:*

During PEGylation SNPs need to transition from a state of charge stabilization to a state of steric stabilization. In the transition from one state to the other, SNPs are exceptionally vulnerable to aggregation ("valley of death") (*17*). Therefore, it is important that PEGylation kinetics are fast and sufficient PEG molecules are provided to fully cover a SNP. It has been shown that small polyethylene glycol molecules (molar mass of ~500 g/mol) non-covalently adsorb to the surface of SNPs with high adsorption rates by establishing multiple hydrogen bonds between ethoxy units and silica silanol groups in aqueous solutions (*17*). To account for this mechanism, 0.115 mmol of PEG-silane (MW 500 g/mol) are rapidly added to the 10 mL aliquot followed by dropwise addition of another 0.115 mmol of PEG-silane. The purpose of a two-step PEG-addition is to avoid PEG self-aggregation which would reduce the concentration of free PEG monomers in solution. After PEG-addition, the reaction is left stirring at room temperature in the dark for 12 hours. To promote further covalent bond formation, a subsequent 8 hours 80 °C heating step is followed. *Silica shell growth:* The pH of the 40 mL left-over particle dispersion is adjusted to pH 9 by a diluted aqueous ammonia solution. To reduce hydrolysis kinetics and increase the control of monomer addition to existing core particles, a TEOS:DMSO dilution (1:10) is dosed into the solution with an auto-dispenser (EDOS 5222, Eppendorf) at a rate of 10 uL per 15 min for 50 times. After the last addition, the reaction is left for another 30 min before an aliquot of 10 mL is separated ("1 shell particle"). The next 3 shells were added in the same way. After each TEOS addition, an aliquot of 10 mL was taken (with the exception of the last aliquot). The respective rates were: 75 x (10 uL/15 min) ("2-shell particle"), 70 x (15 uL/15 min) ("3-shell particle"), 140 x (15 uL/15 min) ("4-shell particle"). The increased

TEOS amounts account for the cubic scaling of particle volume with particle radius. All particles were PEGylated according to the core particle protocol (*vide supra*).

Particle dialysis

After PEGylation, the particle dispersions were cooled down to room temperature and dialyzed to remove small unreacted precursors. Each sample was transferred to a dialysis membrane tube (Pierce, 10k MWCO) and placed in 2 L of slowly stirring DI water in the dark for at least 6 hours. Water was exchanged for a minimum of three times before further steps were taken.

Gel permeation chromatography

Gel permeation chromatography (GPC) served as a preparative and analytical tool to monitor the dispersity of a particle reaction. Based on different elution times of different species in the reaction mixture, the core-shell silica nanoparticles can be separated from unreacted precursors or self-condensed PEG molecules. A BioLogic LP system equipped with a 275 nm UV detector was used. The stationary phase was a Superdex 200 resin (GE Healthcare) in a 2 cm x 20 cm glass column operated at a flow rate of 2 mL/min. The mobile phase was a 5% (w/v) sodium chloride aqueous solution. Particle concentrations were increased with a spin-filter (GE healthcare Vivaspin, 30k MWCO) before sample loading. Typical injection volumes were 500 to 600 μL. Fractions at different elution times were collected by a BioFrac fraction collector. For long time storage, all particles were transferred to DI water using a spin-filter by exchanging solvent at least five times.

Steady state absorption and emission spectroscopy

Absorbance spectra were recorded in DI water on a Varian Cary 5000 spectrophotometer in a 3 mL quartz cuvette against a reference quartz cuvette with DI water. The absorption of particles and dyes were adjusted to the same optical density before emission spectra were recorded. Optical density values were kept between 0.01 and 0.06 for all samples. Emission spectra of the same samples were recorded on a Photon Technologies International Quantamaster spectrofluorometer. Samples containing Cy5 were excited at 645 nm and recorded from 655 nm to 800 nm. All emission spectra were corrected for wavelength dependent detector quantum efficiency differences.

Fluorescence correlation spectroscopy

FCS setup: A 635 nm (Cy5) continuous wave solid state laser (LDCU5/8283, Power Technology, Inc.) was reflected by a dichroic mirror and focused onto the object plane of a water immersion microscope objective, see Figure 2.2B (Zeiss Plan-Neofluar 63x NA 1.2). The laser power was controlled by inserting neutral OD filters with varying attenuation into the beam path. The laser power was measured by a power meter before the objective. The fluorescence was collected by the same objective and spatially filtered by a 50 μm pinhole located at the image plane. The fluorescence was then split into two paths with a beam splitter, spectrally filtered by two separate 665 nm long pass filters (ET665lp, Chroma), and detected by two avalanche photodiode detectors (SPCM-AQR-14, PerkinElmer). To avoid effects of dead time and afterpulsing, the two

fluorescence time traces were cross-correlated by a hardware correlator card (Flex03LQ, Correlator.com). This allowed for time resolution of 15 ns.

Data fitting: Autocorrelation functions (ACFs) were fitted using a Levenberg–Marquardt non-linear least squares algorithm (*24*). ACFs, $G(\tau)$, of core-shell SNPs were fitted with a model accounting for translational diffusion, photo-induced cis-trans isomerization, and rotational diffusion:

$$G(\tau) = 1 + \frac{1}{N_m}\left(\frac{1}{1+\tau/\tau_D}\right)\left(\frac{1}{1+\tau/(\tau_D\kappa^2)}\right)^{1/2} (1 + \alpha' \exp(\tau/\tau_P)) (1 + \alpha_{Rot}\, exp\, (\tau/\tau_{Rot})) \quad (1)$$

N_m denotes the average dye or particle number within the observation volume, τ_D is the characteristic diffusion time through the ellipsoidal observation volume defined by the structure factor $\kappa = \omega_z/\omega_{xy}$ with axial (ω_z) and radial (ω_{xy}) radii (see Figure 2.2). The third line of equation 1 describes fast relaxation processes caused by photo-induced cis-trans isomerization. Fluctuations in fluorescence arise from transitioning between a fluorescence trans conformation and a non-fluorescent cis-conformation. α' is the pre-exponential amplitude of Cy5 cis-trans isomerization. The transition between the two states is characterized by the relaxation time τ_P. The last line in equation 1 describes a second fast process assigned to particle rotation that can be expressed in a first approximation as a single exponential (*25-28*). α_{Rot} is the pre-exponential amplitude of particle rotation, and τ_{Rot} the characteristic rotational diffusion time. This is assuming

a linear dipole emission of a spherical particle. ACFs of free dyes were fitted without the contribution of rotational diffusion. ACFs were normalized for the mean number of particles, N_m, diffusing through the observation volume:

$$G(\tau) = (G(\tau) - 1)\, N_m \qquad (2)$$

Calibration of observation volume: Before each measurement, the effective FCS observation volume, V_{eff}, was calibrated with a standard dye with known diffusion coefficient. A dye stock solution in DMSO was diluted with DI water to nanomolar concentrations. AlexaFluor 647 (diffusion coefficient 3.3 10^{-6} cm^2s^{-1}) (*29*) was used as calibration dye for the above mentioned excitation-emission combination at room temperature (20 ± 1 °C). Typical diffusion times through the observation volume were 200 ± 5 µs (AlexaFluor 647). Calibration and measurements were recorded at low excitation intensities of 5 kW cm^{-2} (Cy5) to avoid singlet-triplet transitions.

Sample Preparation and measurement: FCS samples were prepared by diluting a stock solution of particles (~15 µM) with DI water. Before the FCS measurements an absorption spectrum of the diluted sample was recorded. The same sample was further diluted to nanomolar concentrations. 200 uL of this dilution were placed into a 35 mm glass bottom dish (MatTek Corporation, No. 1.5 coverslip, 10 mm glass diameter) to be placed onto the objective. Each sample was measured five times in five individual runs, each run was 30 s long.

Determination of diffusion constant and particle diameter: The typical diffusion time, τ_D, as obtained from the fit was used to determine the diffusion constant, *D*, while the

Stokes-Einstein relation was applied to determine the particle hydrodynamic diameter, *d*:

$$D = \frac{{\omega_{xy}}^2}{4\tau_D} \tag{3}$$

$$d = 2\frac{k_B T}{6\pi\eta D} \tag{4}$$

where k_B stands for the Boltzmann's constant, T is the absolute temperature, and η is the dynamic viscosity. A first order approximation of the rotational diffusion constant is (*26*):

$$D_{Rot} = \frac{1}{6\tau_{Rot}} \tag{5}$$

where all higher order contributions of the angular momentum (l > 1) are ignored. Particle hydrodynamic diameters were determined with the Stokes-Einstein relation for rotational diffusion:

$$d = 2\left(\frac{k_B T}{8\pi\eta D_{Rot}}\right)^{1/3} \tag{6}$$

Characterization of cis-trans isomerization: Because each dye undergoes independent isomerization, despite possible co-diffusion on one particle, the measured amplitude of isomerization, α', is linearly dependent on the average number of dyes per particle, n_m (*7, 30*). The amplitude of isomerization for a single dye, α_P, is related by $\alpha' = \alpha_P / n_m$ and the fraction of cyanine dyes being in their cis conformation, P, by $P = \alpha_P/(1 + \alpha_P)$.

To determine n_m, the measured optical density of each sample was compared to the mean particle concentration as obtained by FCS:

$$n_m = \frac{C_{Abs}}{\langle C \rangle_{FCS}} \tag{7}$$

with

$$\langle C \rangle_{FCS} = \frac{N_m}{V_{eff}} \tag{8}$$

and

$$V_{eff} = \pi^{3/2} {\omega_{xy}}^2 \omega_z \tag{9}$$

Transmission electron microscopy and image analysis

Transmission electron microscopy **(**TEM) images were taken on a FEI Tecnai T12 Spirit electron microscope operated at an acceleration voltage of 120 kV. Sample grids were prepared by dropping 10 µL of a 50:50 particle and ethanol dispersion onto a TEM grid (EMS, carbon film 300 mesh on copper grids). Sample grids were allowed to dry for at least two hours before they were imaged.

Nanoparticle size distributions were calculated by measuring the area of 200 to 300 nanoparticles per sample, then converting to diameter. Outliers were eliminated if the data point was lower than the 1st quartile – inner quartile range (IQR) * 1.5 or higher than 3rd quartile + IQR * 1.5 then plotted as a 0.1 nm binned histogram.

Fluorescence lifetime measurements

Fluorescence lifetimes were taken on an Edinburgh Instruments FLS1000 spectrometer at sample concentrations of 0.5 µM to 1 µM in deionized water and in a 3

mL 10 mm pathlength quartz cuvette at 90 degrees. Particle samples were excited using a 405 nm pulsed excitation (Edinburgh Instruments EPL-405 pulsed diode laser with ~500 ps pulsewidth, 5 mW) operated at a 500 ns pulse period. Fluorescence was collected with a photon counting photomultiplier tube and decay curves were fitted in the Edinburgh Instruments software using

$$I(t) = \int_{-\infty}^{t} IRF(t') \sum_{i=1}^{n} \alpha_i \exp\left(\frac{-t-t'}{\tau_i}\right) dt \qquad (10)$$

where I(t) is the fluorescence decay function, $IRF(t')$ the instrument response function, α_i is the amplitude of the i-th lifetime, τ_i, and n is the number of fitting components. The IRF was determined using 40 nm SNPs. The fit quality was evaluated based on χ^2 values.

All decay curves were fitted to a bi-exponential decay model (n=2).

Determination of relative fluorescence quantum yields

The relative fluorescence quantum yield, Φ_F, for SNPs was determined using a comparative method against free Cy5 dye (Φ_F = 0.20) as a standard (*31, 32*).

$$\Phi_{F,i} = \Phi_{F,ref} \frac{\mathrm{A}_{ref}}{\mathrm{A}_i} \frac{\int \mathrm{I}_i(\lambda)\, \mathrm{d}\lambda}{\int \mathrm{I}_{ref}(\lambda)\, \mathrm{d}\lambda} \qquad (11)$$

where $\int \mathrm{I}_i\,(\lambda)\mathrm{d}\lambda$ is the integrated mean fluorescence intensity from of a sample, *i*, or a reference, *ref*. Data were recorded in deionized water and at room temperature using absorption values between 0.01 and 0.09. Samples were excited at 620 nm and

fluorescence recorded and integrated from 630 nm to 800 nm. Relative fluorescence quantum yields by FCS, $\boldsymbol{\varphi_F}$, were determined via the mean photon counts of the APDs normalized for the mean number of dyes or particles, n_m, in the observation volume.

Determination of rate constants

Radiative and non-radiative rates were determined from their relations to measured fluorescence quantum yield and fluorescence lifetime:

$$k_r = \frac{\Phi_F}{\tau_F} \tag{12}$$

$$k_{nr} = \frac{(1 - \Phi_F)}{\tau_F} \tag{13}$$

Results and Discussion

A series of ultrasmall and PEGylated core-shell SNPs with precisely controlled silica shell thickness was first synthesized according to a previously reported method (*1*). This method is derived from the principle of living polymerization, that is used for the synthesis of organic polymers with low molar mass/size dispersity (*33*): In order to obtain narrow size distributions, all species have to start to grow at the same time, and have to be terminated at the same time. To that end, first the silane precursor TMOS was added into basic aqueous solution, immediately followed by Cy5-silane addition. The exposure to water causes fast hydrolysis and fast condensation of TMOS leading to rapid seed particle nucleation, followed by particle growth via monomer addition. Then, either further particle growth was suppressed/terminated by the rapid addition of PEG-silane leading to sterically stabilized PEGylated particles which will be referred to as "core particles" in the following, or further silane precursor was added in small doses to slowly deposit one or more silica shells around the existing particle cores before final PEGylation. Figure 2.1B depicts the principle of the core particle synthesis and shell addition using the silane precursors TMOS and TEOS, respectively. Key for the shell addition is keeping silane precursor concentrations below the threshold for secondary particle nucleation at any time. TEOS in comparison to TMOS hydrolyzes slower. This allows the precursor to spread throughout the solution before hydrolysis, keeping the local concentrations low enough to suppress secondary particle formation, and leading to steady primary particle growth upon TEOS dose addition. After the desired amount of TEOS was added, an aliquot of the particle solution was removed and sterically stabilized by PEG-silane addition. In this way five different particles with increasing

shell thicknesses were synthesized originating from the same core synthesis (See Materials and Methods): the core-particles and particles with one, two, three, or four additional silica shells, respectively (Figure 2.1B).

Insufficient charge stabilization during synthesis and non-optimized PEGylation protocols can lead to a highly uncontrolled particle dispersity (*17*). Gel permeation chromatography (GPC) is an excellent analytical tool to study particle size distributions and heterogeneities, as well as a preparative tool to separate any unreacted precursors, fluorophores, aggregates, secondary particles, or PEG-silane from the native solution (*1*). GPC separates analytes based on hydrodynamic radii, by eluting analytes together with a mobile phase through a porous stationary phase. Smaller analytes remain longer in the stationary phase and elute at later times. To clean the different core-shell SNPs from all possible side-products, we submitted every sample to two GPC runs. The GPC elugram of the first run (Figure 2.1C) consisted of mainly three peaks for every sample, consistent with earlier observations (*1*). The first peak at around 9 min was a sharp peak that did not change for different samples, and likely stems from PEG aggregates and/or undyed particle aggregates (Figure S2.1, Appendix A). Across the particle series, the second peak displayed a clear shift towards shorter elution times with additional silica shells (from 15 min to 12 min). It is therefore assigned to the main core-shell SNP peak. Some of the core-shell SNP peaks, i.e. for the 2-shell and 3-shell particles, showed a minor right shoulder. We suspect this shoulder to be a result of particle PEGylation of aliquots before GPC (*e.g.* PEG-silane adducts), since the 4-shell particle does not display any such shoulder. It is likely due to an excess of unreacted precursor that was still present in the reaction at the time of PEGylation. Finally, the third peak was a broad

low-intensity band positioned between 17 min and 25 min (indicated by a black arrow) and was present in all samples. This band is originating from monomeric and low molar mass precursors (Figure S2.1, Appendix A).

Shifts of the main GPC particle peak towards shorter elution times were expected due to particle growth through silica shell additions. In order to eliminate the shoulder in the particle size distributions and optimize sample quality, a two-sigma fraction from each main particle peak was collected (grey area under curves in Figure 2.1C) and submitted to another GPC run (Figure 2.1D). These elugrams now all showed symmetric shapes. As a cross-check, from these second GPC runs further two-sigma fractions were taken and again submitted to subsequent GPC runs. Within the variance of these measurements, the main particle peak positions remained unchanged, indicating successful steric stabilization of the various core-shell SNPs via the PEGylation process.

After sample preparation, fluorescence correlation spectroscopy (FCS) was used to characterize the five core-shell SNPs in detail. FCS derives information on dynamic processes from spontaneous fluctuations of fluorescence over time (*4-6*). The observation of fluctuations in intensity is realized by restricting the detection of fluorescence to a very small observation volume. Figure 2.2A illustrates the effective observation volume, V_{eff}, that is created by focusing a laser beam with a confocal lens. V_{eff} is defined as $V_{eff} = \pi^{3/2}{\omega_{xy}}^2\omega_z$, with ω_{xy} and ω_z being the radial and axial $1/e^2$ radii from the center of a Gaussian-shaped focused laser beam. Only when a particle diffuses through V_{eff} fluorescence is emitted. This yields high signal-to-noise fluorescence signals and allows detection of fluctuations from single particles. The information about physical processes is subsequently extracted from the self-similarity

of the fluorescence time trace after a lag time, τ, by analyzing the fluctuations with the normalized autocorrelation function, $G(\tau)$:

$$G(\tau) = \frac{\langle I(t)I(t+\tau)\rangle}{\langle I(t)\rangle^2} = \frac{\langle[\langle I(t)\rangle + \delta I(t)][\langle I(t)\rangle + \delta I(t+\tau)]\rangle}{\langle I(t)\rangle^2} = 1 + \frac{\langle \delta I(t)\delta I(t+\tau)\rangle}{\langle I(t)\rangle^2} \quad (14)$$

Here $I(t)$ is the detected fluorescence intensity at time t, $\langle I(t)\rangle$ is the mean fluorescence intensity over time, and $\delta I(t)$ is the fluctuation of $I(t)$ around its mean. Figure 2.2B shows a typical confocal FCS setup. A continuous wave laser is reflected by a dichroic mirror (DM) and then focused by the microscope objective (OB) down to the diffraction limit. The same objective that previously focused the laser, now collects the fluorescence. The Stokes-shifted fluorescence passes the same DM, is then spatially filtered from scattered photons by a pinhole (PH) in the image plane, and spectrally filtered from excitation photons by an emission long pass filter (LPF). A fluorescence time trace is detected by an avalanche photodiode detector (APD), and auto-correlated by a correlator card (Figure 2.2C). Figure 2.2D shows the respective autocorrelation curve (ACF).

When a photon reaches the sensitive APD, a photo current is created, that often cause a second follow-up electrical pulse (afterpulsing). During that time, the detector can't detect more photons (dead time). These effects occur with a periodicity of 10 ns to 100 ns, and in this time window lead to a large background in the ACF (curve (i) in Figure 2.2D). To accurately measure fast transient states (τ < 0.5 μs), effects by detector afterpulsing therefore need to be avoided. This can be achieved by splitting the

fluorescence signal into two paths and detecting each path with a separate detector (*34*). The two fluorescence time traces (Figure 2.2C) are then cross-correlated, uncovering the underlying photophysical phenomena in the ACF (curve (ii) in Figure 2.2D). For a nanoparticle that is diffusing in three dimensions through a sample observation volume, and carrying a fluorescent dye molecule with the ability to undergo photo-induced conformational changes, the contributions in the ACF can be roughly divided into three regions on the lag time axis (Figure 2.2D): Region I is reflecting the translational diffusion of particles (τ > 10 μs), region II corresponds to photo-isomerization processes (10 μs > τ > 0.1 μs), and region III detects effects from particle rotation (τ < 0.1 μs). The normalized diffusion autocorrelation function can then be described as:

$$G(\tau) = G(0)G_D(\tau)G_P(\tau)G_{Rot}(\tau) + 1 \tag{15}$$

with

$$G(0) = {N_m}^{-1} = {V_{eff}}^{-1}\langle C\rangle^{-1} \tag{16}$$

$$G_D(\tau) = (1 + \tau/\tau_D)^{-1}(1 + \tau/(\tau_D\kappa^2))^{-1/2} \tag{17}$$

$$G_P(\tau) = (1 + \alpha' \, exp\,(\tau/\tau_P)) \tag{18}$$

$$G_{Rot}(\tau) = (1 + \alpha_{Rot} \exp\,(\tau/\tau_{Rot})) \tag{19}$$

where N_m is the mean number of emitters in the effective observation volume, V_{eff}, at the mean sample concentration $\langle C\rangle$, τ_D is the average particle diffusion time through the observation volume, $\kappa = \omega_z/\omega_{xy}$ is the structure factor defined by the observation volume dimensions, α' is pre-exponential amplitude associated with ci-trans photoisomerization, τ_P is the relaxation time of a single cyanine dye molecule

undergoing photo-isomerization, α_{Rot} is the pre-exponential amplitude of particle rotation, and τ_{Rot} is the characteristic particle rotation time.

In the following, for our set of ultrasmall fluorescent and PEGylated core-shell SNPs FCS was used to characterize particle hydrodynamic diameter, d_{FCS}, particle concentrations, cis-trans isomerization, and particle rotation. Figure 2.3 summarizes the information obtained from the FCS measurements on these SNPs with embedded Cy5 molecules. Figure 2.3A compares the ACFs for free Cy5 dye, the core particle, and the four core-shell particles, with corresponding fits according to equation 15 superimposed over the data. The relative shift of the SNPs to longer lag times relative to free Cy5 indicates increasingly slower diffusion (enlarged in inset (i) of Figure 2.3A). The average translational diffusion constants were determined from the characteristic diffusion times and translated into particle hydrodynamic diameters using the Stokes-Einstein relation. Average hydrodynamic diameters ranged from 5.0 ± 0.1 nm (core particle), 5.6 ± 0.1 nm (1-shell particle), 6.3 ± 0.1 nm (2-shell particle), 7.4 ± 0.1 nm (3-shell particle), to 9.5 ± 0.2 nm (4-shell particle) (Figure 2.3B). The average shell thicknesses for each core-shell particle were calculated from the incremental particle growth. These were 0.3 nm, 0.7 nm, 1.2 nm, and 2.3 nm for the 1-, 2-, 3-, and 4-shell core-shell SNPs, respectively, suggesting a synthesis precision down to the deposition of a single atomic SiO_2 layer between particles (~0.4 nm) (*1*).

For comparison, particle diameters, of core, 2-shell, and 4-shell particles were determined using transmission electron microscopy (TEM) as 3.4 ± 0.4 nm, 3.9 ± 0.5 nm, and 8.0 ± 1.1 nm, respectively (Figure S2.2A to S2.2D). These TEM based diameters, d_{TEM}, are expected to be smaller than those determined by FCS as they only

account for the inner silica part of the particles, but not for the PEG layer nor for the water shell dragged with the particles and detected in hydrodynamic diameter measurement techniques such as FCS. As the particle diameters increase the ratio between particle-surface and particle-volume decrease. Consequently, the contributions from surface PEGylation and solvation layer to d_{FCS} reduce and d_{FCS} and d_{TEM} converge.

At fluorescence fluctuations below τ < 100 ns the embedded Cy5 dye cannot be assumed to be a rotationally isotropic emitter anymore, since the change in the orientation of the Cy5 dipole moment is linked to the rotation of the entire particle, whose mobility is significantly slowed down compared to a free Cy5 dye. The afterpulse-corrected ACF (region (iii) in Figure 2.3A) reveals the time scale and population of rotational diffusion of the entire particles. With increasing particle diameter the relaxtion time of this rotational diffusion process (τ_{Rot}) is noticeably shifting towards larger lag times and manifests itself by slightly increasing amplitude, α_{Rot} (Table S2.1). The molecular rotation motion of free Cy5 dye lies beyond the accessible time resolution of our setup and therefore does not display any contribution to the measured ACFs.

We also used τ_{Rot} to determine the particle sizes and shell thicknesses with the assumption of a linear dipole emission and a negligible contribution of higher order angular momentum l (l > 1) (*25-28*). Figure 2.3B illustrates a comparative graph of particle diameters plotted against shell thickness, as obtained from translational and rotational diffusion, respectively. Three observations were made: First, the average particle diameters as calculated from particle rotation are systematically larger than those from translational diffusion. Second, the errors associated with the diameters

determined from rotational diffusion decrease with increasing particle sizes. Lastly, the determined average shell thickness almost perfectly matches the ones determined by translational diffusion. The larger errors for smaller particles are expected due to fitting of only the onsets of the rotational diffusion relaxation (see Figure 2.3A). The systematic deviations of particle diameters as determined by translational versus rotational diffusion can be explained by the presence of more than one emitter per particle. The transition dipole moments of multiple Cy5 dye molecules in one particle are likely not aligned, leading to enhanced fluorescence signal despite a rotating particle. This additional fluorescence signal is reflected in an apparently larger particle diameter than determined by translational diffusion.

Unlike free Cy5 dye, where dye molecules are expected to diffuse independently of each other, SNPs can carry multiple Cy5 molecules. The average number of Cy5 dyes per SNP (n_m) can be calculated by dividing the concentration of fluorophores as obtained from steady-state absorption spectroscopy measurements by the mean concentration of SNPs as determined by FCS measurements for the same sample. This analysis revealed about 1.7 ± 0.1 dyes per SNP for all particles (Figure 2.3C).

The rotational diffusion amplitude, α_{Rot}, should be independent from the number of dyes per particle. However, we find that the amplitude slightly increases with progressive silica deposition. Yin *et al.* found a dye number dependence of rotational diffusion amplitudes for a TMR labeled DNA Holliday junction, and concluded that the amplitude of rotational relaxation is dye number dependent only if vibrational motion and wobbling are faster or on the order of rotational motion (*30*). With this assumption and the same number of dyes for all core-shell SNPs, we infer that the increasing

amplitude, α_{Rot}, suggests a correlation between the shell thickness and a decrease in dye mobility within the particles, both by the suppression of isomerization, as well as by the restriction of vibrational movement and wobbling.

The brightness of the core particle is a factor 3 higher than that of the free dye and asymptotically increases to nearly a factor of 4 for the largest silica shell thickness (Figure 2.3D). By calculating the brightness per dye, one can see that the average dye brightness increases with increasing shell thickness (Figure 2.3E). This behavior asymptotically approaches an upper threshold at a factor of around 2.6 times the brightness of free Cy5, or in other words, the deposition of more silica beyond this upper threshold is not expected to influence the brightness of Cy5 much further. The increase of fluorescence brightness (brightness enhancement) of organic dyes upon covalent encapsulation in silica has been described before and is dependent on the silica architecture and the chemical structure of the dye (*1, 13, 35*). From the fact that the brightness per dye changes upon further silica deposition we conclude that some Cy5 molecules are originally located on the surface of the core particle or are only partially embedded within the silica network of the core particle. Two arguments support this hypothesis. First, during the synthesis (pH 8.5), SNPs are stabilized through Coulomb repulsion of negative surface charges while Cy5 dye itself also has a net charge of minus one. It is expected that the associated charge repulsion hinders the full covalent dye incorporation of Cy5-silane into the particle core. This is supported by the low dye incorporation of Cy5 found by GPC analysis of the synthesis solution shown in Figure S2.1B. Second, the core particle has a radius of only about 2.5 nm, while the measured size of Cy5 along the long molecular axis is about 1.2 nm. With an average number of

approximately two Cy5 molecules per particle it appears that the likelihood of all fluorophores being fully surrounded by silica is low.

This conclusion of near surface dye molecules was further supported by behavior of the FCS curves in region II of Figure 2.3A (see also inset (ii) in this figure). The fluorescence fluctuations in that region are due to photo-induced conformational changes of the Cy5 dye. Since multiple embedded fluorophores can co-diffuse with one particle but undergo isomerization independently from each other, the measured amplitude of isomerization, α', scales with $1/n_m$. By determining the number of dyes per particle on can calculate the fraction of Cy5 dyes being in their cis state, *P* (see methods) (*30*). With increasing shell thickness, we can observe a clear reduction in the second amplitude of the ACF (see arrow in inset (ii) of Figure 2.3A). Figure 2.3G shows the comparative results of the cis-conformers fraction, P. Starting from nearly 50% for Cy5 dye in solution, the fraction P asymptotically decreased to reach a value of about 27% for the 4-shell particle. This behavior can explain the previously described changes in fluorescence brightness. Cis-conformers are only weakly fluorescent and therefore don't contribute significantly to the overall particle brightness (*7*). With increasing silica shell thickness the likelihood of a rigid silica dye environment increases, prohibiting the spatially demanding conformational changes of Cy5. Interestingly, despite being encapsulated in a particle with a thick shell (2.3 nm) and seemingly reaching a limit of brightness increase, the fraction of cis conformer, P, is still at 27%. This finding suggests that some Cy5 molecules can still undergo isomerization despite being fully encapsulated. Silica is an amorphous and microporous material when synthesized in water (*36*). It therefore does not surprise that there remain large enough cavities for

some dyes to undergo conformational changes. In addition, it is likely that the slow deposition of further silica onto existing SNPs (as compared to the faster core reaction) is disturbed by the presence of near-surface dyes. These molecules therefore likely maintain a larger cavity in the silica shell network than dyes encapsulated in the silica core network.

At the excitation intensity employed (5 kW/cm^2), the quantum yield of triplet formation is assumed to be low and triplet kinetics are further reduced due to steric shielding of Cy5 from dissolved oxygen by the silica network. Consequently, the energy relaxation pathway in region II can solely be attributed to photo-induced cis-trans isomerization (*7*). Transitions between singlet ground, S_0, and singlet excited, S_1, states of both dye conformations take place on the nanosecond time scale and cannot be resolved by our FCS setup (temporal resolution 15 ns). The corresponding rates of these processes can be expected to be much faster than the rates of the transition process between the fluorescent trans-state and the non-fluorescent cis-state. Therefore, there is no need for differentiation of singlet state transitions in a kinetic model. The transition between the different conformations can be described in terms of a simple two-state model, Trans ⇌ Cis, with an effective rate for isomerization k_{iso} and an effective rate for back-isomerization k_{biso} (Figure 2.1A). With the determined fractions, P, and the relaxation times, τ_P, from FCS one can calculate the effective isomerization rates and the equilibrium constant, K:

$$\tau_P = \frac{1}{k_{iso} + k_{biso}} \tag{20}$$

$$\mathrm{P} = \frac{k_{iso}}{k_{iso} + k_{biso}} = \frac{1}{1 + K} \tag{21}$$

All results from this analysis are summarized in Table 2.1. Both, the rate of isomerization and the rate of back-isomerization are retarded by a factor of 2 to 3 upon Cy5 encapsulation into the core particle and further reduced with silica shell deposition. In comparison, k_{iso} is slightly smaller than k_{biso} and reduces slightly more with dye encapsulation. The equilibrium of photo-induced cis-trans isomerization shifts towards the trans conformation with progressive silica deposition.

In previous studies the increased fluorescence brightness of dye encapsulating SNPs has been explained by an increase in radiative rate, k_r, and/or a decrease in non-radiative rate, k_{nr} , of embedded tetramethyl-rhodamine dye molecules (*35*). Combinations of fluorescence quantum yield, φ_F, and fluorescence lifetime, τ_F, were used to determine these rates based on: $k_r = \varphi_F/\tau_F$ and $k_{nr} = (1 - \varphi_F)/\tau_F$. The fluorescence quantum yield was estimated from the brightness enhancement per dye that was obtained by FCS measurements. Since excitation intensities are low, and saturation effects can be expected to be low as well, this should be a reasonable estimation.

Figure S2.3A compares time resolved fluorescence decay curves for the five different SNPs of this study. All curves were fitted with a bi-exponential decay model. The corresponding fluorescence lifetime values are plotted against the shell thickness in Figure 2.4A. The fluorescence lifetime increases with silica shell thickness. The

increase is most pronounced between free dye and core particle, but continues with silica shell thickness.

Table 2.2 summarizes the corresponding radiative and non-radiative rates as obtained from FCS and time resolved fluorescence decay measurements. Most noticeable is a strong decrease of non-radiative rates that correlates with increasing shell thickness. The largest decrease (about a factor of 2.5) is observed upon Cy5 encapsulation into the core particle. However, upon further silica addition, these values decreased by another factor of ~1.5, reflecting the restricted conformational mobility of Cy5 dye and supporting the previous hypothesized near-surface location of Cy5 dye molecules in the core particles.

In contrast, radiative rates do not significantly increase. This behavior is very different compared to rhodamine dyes. For example, a 2.3-fold increase of radiative rates was measured for different silica nanoparticle architectures embedding TRITC dye (*35*) and a 2.1-fold increase for calcium phosphate nanoparticles embedding Cy3 dye (*37*). The values obtained in our study (~1.0 to 1.2-fold increase) lie far below these literature values. k_r can be estimated by applying an expression derived by Strickler and Berg (*38*), which describes the relationship between k_r, the excitation spectrum, the emission spectrum, and the square of the refractive index of the surrounding medium (equation 22 in (*38*)). Here, we compared free Cy5 dye in water, $n_1 = 1.33$, and Cy5 dye encapsulated in silica, $n_2 = 1.46$. Our calculated values of normalized values for k_r were ~1.20 for all particles, and agreed best with our experimentally determined value for the 4-shell particle, and slightly overestimated the values for the other particles (see Table 2.2). Since excitation and emission profiles do not significantly change upon silica

encapsulation, the difference of radiative rates is mostly due to changes of refractive index (*39*). As mention above, silica is a porous material that can be penetrated by water, especially when the silica thickness is on the order of a few atomic layers. Therefore, the effective refractive index for the core-shell particles probably lies between 1.33 and 1.46, and approaches 1.46 with increasing shell thickness (*40*).

For comparison, we determined the same radiative rates and non-radiative rates using steady-state absorption and emission spectroscopy. Figure 2.4B shows the intensity matched steady-state absorption and corresponding emission spectra of Cy5 and Cy5 particles in water. Upon embedding Cy5 into the silica matrix a minor solvatochromic red-shift (~5 nm) relative to Cy5 in water was observed. This was the case for all particles and did not noticeably change with thicker shell. The emission spectra showed a relative brightness enhancement in comparison to free Cy5 dye, that was more pronounced with increasing shell thickness. The relative fluorescent quantum yields, Φ_F, for the SNP were deduced by using the comparative method by Williams *et al.* (*31*), which is based on the integration of corresponding emission spectra for different sample absorbances (Figure S2.3B). In this case Cy5 was used as the standard with $\Phi_F = 0.20$. All results are summarized in Table 2.3. We find that both, FCS and steady-state spectroscopy, yield similar results. We conclude that the observed brightness enhancement for the core-shell SNP series is mostly the result of a decrease of non-radiative rates, and only weakly dependent on a minor increase of radiative rates. The relative decrease of non-radiative rates is strongly coupled to the relative decrease of the effective isomerization rates, and therefore to the increased rigidity of the silica dye environment. This in turn is consistent with earlier findings for TRITC dye

encapsulation in silica (*35*). It is likely that for Cy5 the reduced capability for conformational changes within the silica matrix is the biggest contributor to the reduction of non-radiative relaxation pathways at the given excitation intensity.

Conclusion

In this study, we synthesized and characterized a series of ultrasmall and PEGylated fluorescent core-shell silica nanoparticles (SNPs) with covalently encapsulated cyanine Cy5 dye and increasing silica shell thickness using a combination of gel permeation chromatography, GPC, fluorescence correlation spectroscopy, FCS, time-resolved fluorescence decay measurements, and steady state absorption and emission spectroscopy. We learned that a significant fraction of Cy5 dye molecules are located near the surface or on the surface of the 5 nm silica core used for the synthesis of all these particles.

The photo-induced cis-trans isomerization of Cy5 as monitored by FCS at lag times $<10^{-5}$ s allowed to probe the effects of silica deposition at the single atomic layer level onto the core SNP. A silica shell of 2.3 nm, about double the length of Cy5, is sufficient to cover these dyed SNPs with silica. This leads to a maximum brightness enhancement of 2.6 as compared to free Cy5 dye in aqueous solution. In these maximum brightness particles still about 27% of the Cy5 population are able to undergo photo-isomerization, likely in free volume cavities within the NP silica matrix, giving room for further improvements in brightness utilizing alternative synthesis methods.

Results demonstrated that FCS is a powerful tool for the characterization of fluorescent SNPs. Fast measurements, low sample concentrations, relatively low cost and high information density, make FCS compatible with high throughput synthetic approaches for development of ultra-small nanoparticles, *i.e.* many batch iterations, or instrumental coupling with microfluidic devices for nanoparticle syntheses. In combination with other sensitive techniques, such as high resolution chromatography

and single particle methods, new insights into the structure and optical properties of ultra-small SNP can be achieved.

Figures

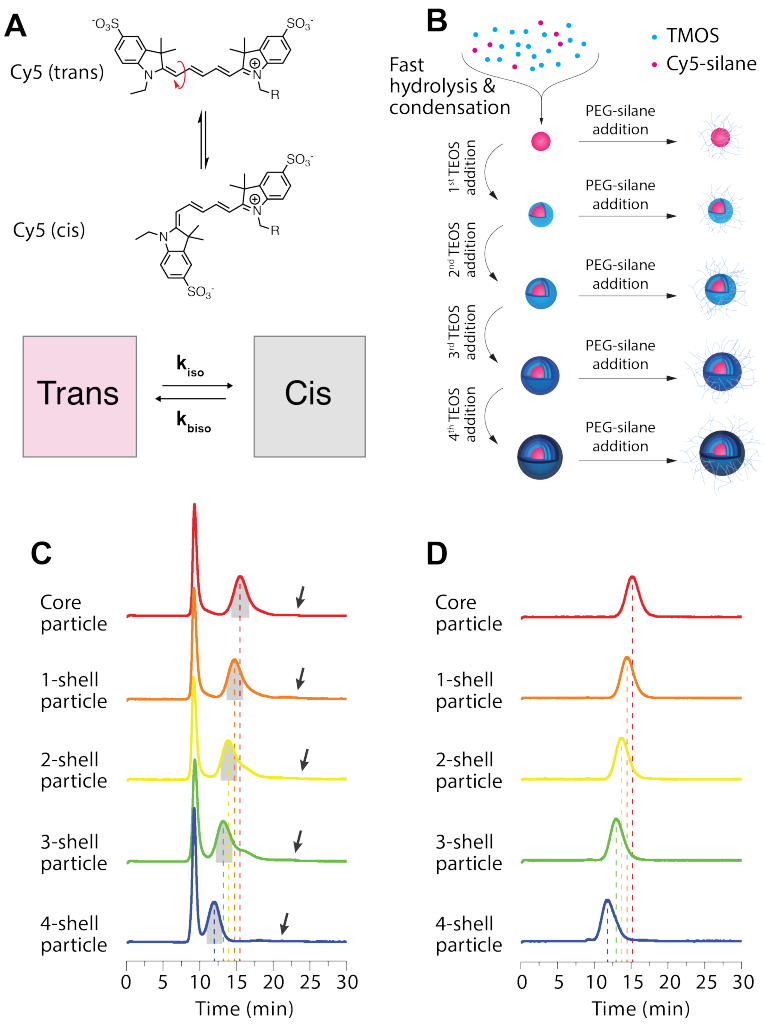

Figure 2.1. ***Dye details, particle synthesis, and particle characterization.*** (A) Cy5 photo-induced cis-trans isomerization around the polymethinic chain, and corresponding kinetic model. (B) Schematic representation of step-wise synthesis of dye-encapsulating fluorescent core−shell SNPs. (C, D) GPC elugrams of as synthesized (C) and GPC purified (D) dye-encapsulating core−shell SNPs.

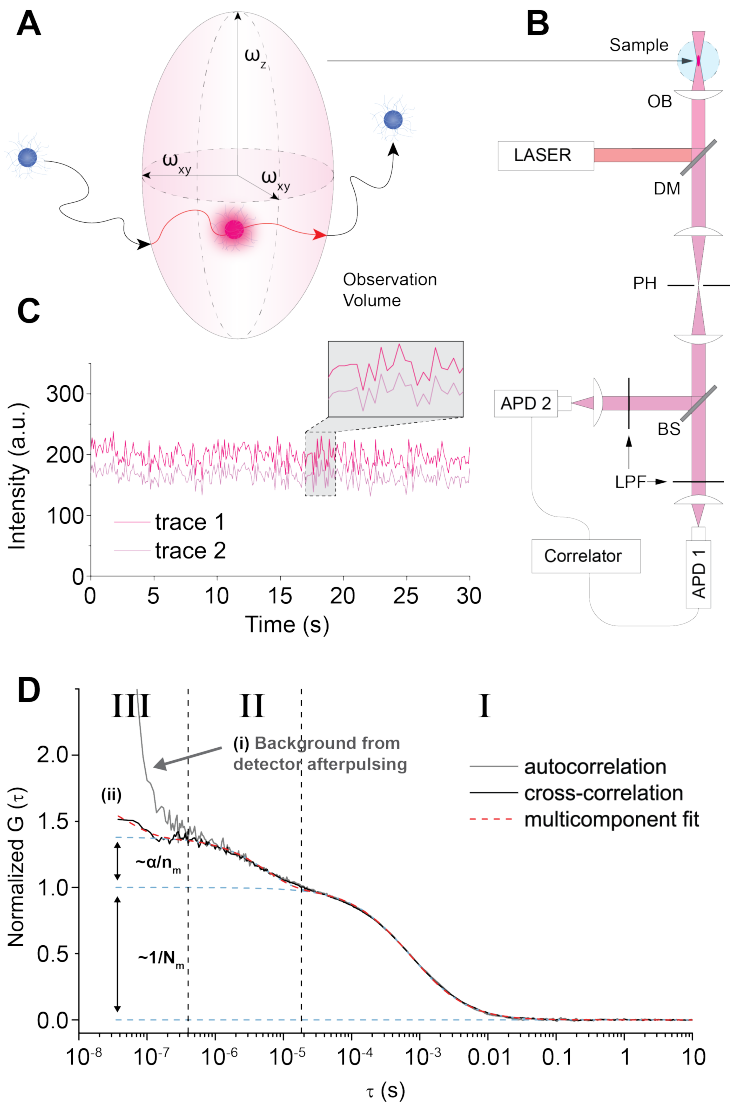

Figure 2.2. ***FSC schematic with effects of detector afterpulsing***. (A) Sample observation volume element of FCS laser beam with axial dimension, w_z, radial dimensions, w_{xy}, and showing a fluorescent particle diffusing through. (B) Schematic of confocal FCS setup to remove effects of afterpulsing, depicting laser beam focal volume position, objective (OB), laser, dichroic mirror (DM), pinhole (PH), beam splitter (BS), long-pass filter (LPF), two avalanche photodiode detectors (APD 1 & 2), and correlator. (C) Fluorescence traces as recorded by APD 1 and APD 2 from FCS measurement. Inset shows enlarged time window. (D) Characteristic FCS ACFs of fluorescent silica nanoparticles in this study: (i) with effects of afterpulsing (grey); with afterpulsing effects removed (black), and corresponding fit (red). Region I: translational diffusion; region II: photo-isomerization of cyanine dyes; and region III: high background from detector afterpulsing (i) or particle rotational diffusion (ii).

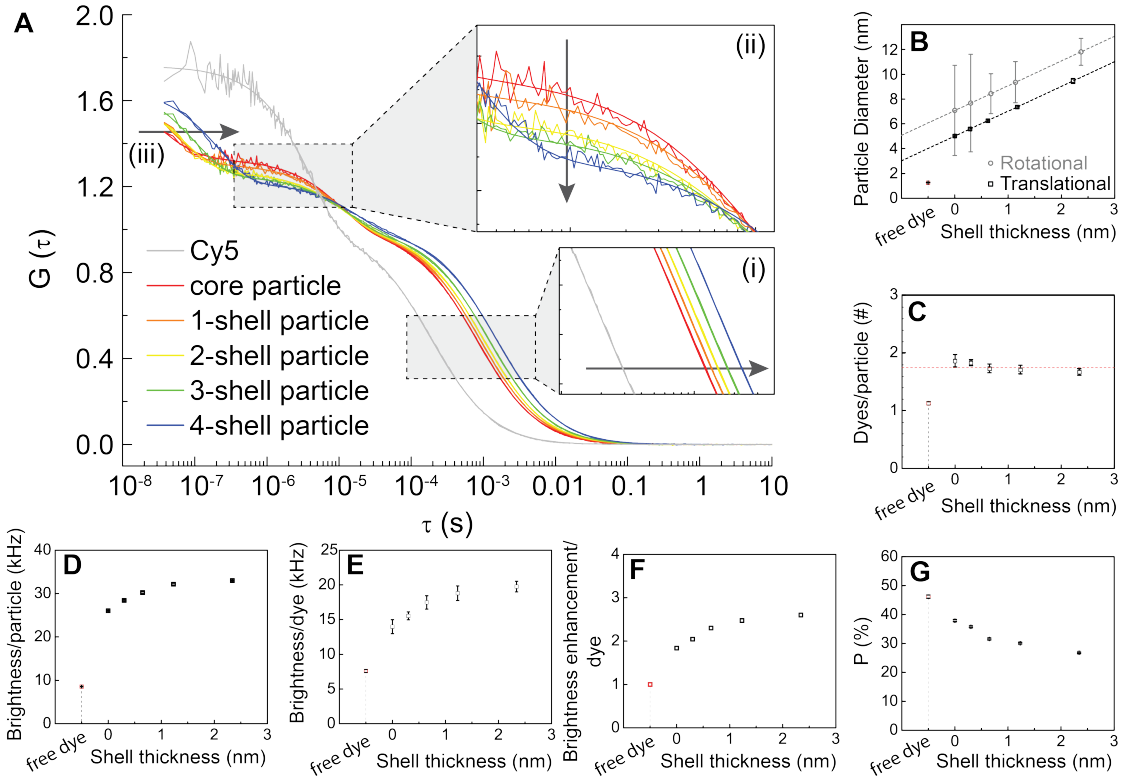

Figure 2.3. ***FCS measurements and associated analyses.*** (A) Comparison of FCS results (with afterpulsing effects removed) for pure Cy5 (grey) and Cy5-encapsulating core-shell SNPs (colored) together with associated fits. (B) Particle diameter as a function of silica shell thickness as determined by translational diffusion (black) versus rotational diffusion (grey). (C) Dyes per particle as determined by a combination of FCS and absorption spectroscopy. (D) Brightness per particle as a function of silica shell thickness. (E) Brightness per encapsulated dye as a function of silica shell thickness. (F) Brightness enhancement per dye as a function of silica shell thickness. (G) Percentage of photoisomerizing dyes as determined by FCS as a function of silica shell thickness.

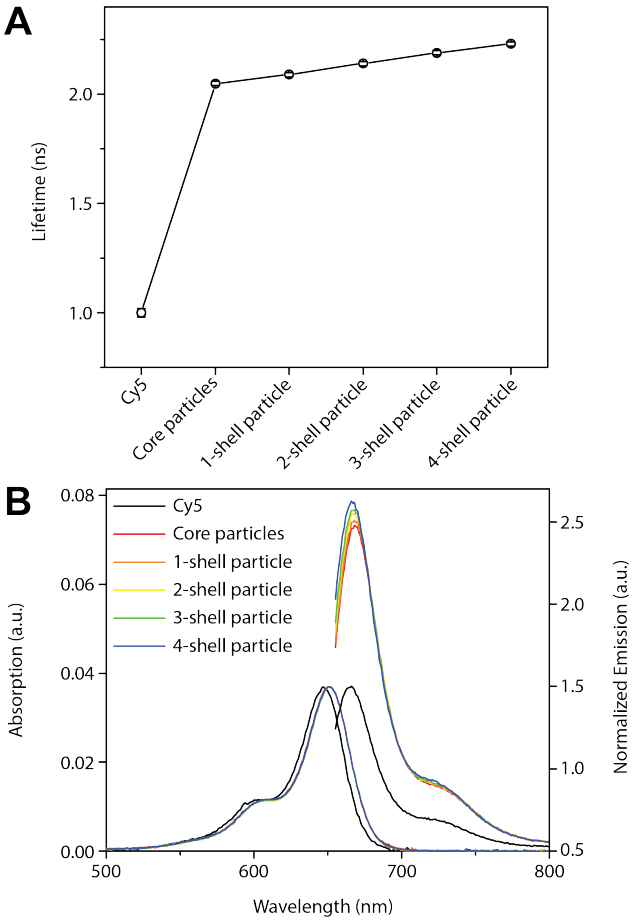

Figure 2.4. ***Fluorescence lifetimes*** **and** ***steady-state absorption and emission.*** (A) Comparison of fluorescence lifetimes of Cy5-encapsulating core-shell SNPs versus free Cy5 dye. (B) Intensity-matched absorption spectra of free Cy5 dye and Cy5-encapsulating fluorescent core−shell SNPs together with corresponding emission spectra. Emission spectra are normalized with respect to Cy5 in water.

Tables

Shell thickness	P [%]	τ_P [us]	k_{iso} [us^{-1}]	k_{iso} (normalized)	k_{biso} [us^{-1}]	k_{biso} (normalized)	K
Cy5	46.2 ± 0.6	3.9 ± 0.1	0.118 ± 0.003	1.00 ± 0.03	0.137 ± 0.006	1.00 ± 0.06	1.16 ± 0.06
0 nm	37.9 ± 0.3	10.6 ± 0.5	0.036 ± 0.002	0.30 ± 0.02	0.058 ± 0.005	0.43 ± 0.04	1.64 ± 0.15
0.3 nm	35.8 ± 0.3	11.2 ± 0.1	0.032 ± 0.001	0.27 ± 0.01	0.057 ± 0.001	0.42 ± 0.02	1.80 ± 0.04
0.7 nm	31.6 ± 0.3	12.0 ± 0.8	0.026 ± 0.002	0.22 ± 0.02	0.057 ± 0.006	0.42 ± 0.05	2.17 ± 0.27
1.2 nm	30.1 ± 0.3	13.1 ± 0.6	0.023 ± 0.001	0.20 ± 0.01	0.054 ± 0.003	0.39 ± 0.03	2.32 ± 0.18
2.3 nm	26.8 ± 0.2	17.7 ± 0.7	0.015 ± 0.001	0.13 ± 0.01	0.041 ± 0.002	0.30 ± 0.02	2.73 ± 0.18

Table 2.1. Fraction of Cy5 molecules being in the non-fluorescent cis conformation, P, relaxation time of Cy5 cis-trans isomerization, τ_P, effective rate of isomerization from trans to cis, k_{iso}, effective rate of back-isomerization form cis to trans, k_{biso}, equilibrium constant of back-isomerization, *K*. Normalized values are with respect to Cy5 in water at 20 °C.

Shell thickness	φ_F [%] (FCS)	τ_F [ns]	k_r [ns^{-1}] (FCS)	k_r (normalized) (FCS)	k_{nr} [ns^{-1}] (FCS)	k_{nr} (normalized) (FCS)
Cy5	0.20[a]	1.00	0.20	1.00	0.80	1.00
0 nm	0.37	2.05	0.18	0.90	0.31	0.39
0.3 nm	0.41	2.09	0.20	0.98	0.28	0.35
0.7 nm	0.46	2.14	0.21	1.07	0.25	0.31
1.2 nm	0.49	2.19	0.23	1.13	0.23	0.29
2.3 nm	0.52	2.23	0.23	1.16	0.22	0.27

Table 2.2. Quantum yield as determined by FCS, φ_F, fluorescence lifetime, τ_F, radiative rate, k_r, and non-radiative rate, k_{nr}. Normalized values are with respect to Cy5 in water. [a]Quantum yield from reference (*41*).

Shell thickness	Φ_F [%]	k_r [ns^{-1}]	k_r (normalized)	k_{nr} [ns^{-1}]	k_{nr} (normalized)
Cy5	0.20[a]	0.20	1.00	0.80	1.00
0 nm	0.48	0.23	1.17	0.25	0.32
0.3 nm	0.49	0.24	1.18	0.24	0.30
0.7 nm	0.50	0.23	1.17	0.23	0.29
1.2 nm	0.51	0.23	1.17	0.22	0.28
2.3 nm	0.54	0.24	1.20	0.21	0.26

Table 2.3. Quantum yield as determined by steady-state absorption and emission spectroscopy, Φ_F, fluorescence lifetime, τ_F, radiative rate, k_r, and non-radiative rate, k_{nr}. Normalized values are with respect to Cy5 in water.[a] Quantum yield from reference (*41*).

Acknowledgements

This study was funded by the U.S. Department of Energy, Office of Science, Basic Energy Sciences under Award No. DE-SC0010560 and National Institutes of Health (NIH) under Award No. U54CA199081. This work made use of the Cornell Center for Materials Research shared facilities which are supported through the NSF MRSEC program (DMR-1719875) at Cornell. The authors gratefully acknowledge Dr. W. Zipfel and Dr. L. Estroff (Cornell University) for helpful discussion and kind experimental assistance, as well as Dr. Nirmalya Bag for insightful discussions.

F. F. E. Kohle and U. B. Wiesner developed the experimental design. F. F. E. Kohle synthesized nanoparticles, conducted and analyzed steady-state absorption and emission spectroscopy, FCS, quantum yield measurements, and lifetime measurements. J. A. Hinckley, carried out TEM measurements and image analysis.

REFERENCES

(*1*) Ma, K., Mendoza, C., Hanson, M., Werner-Zwanziger, U., Zwanziger, J., Wiesner, U. Control of Ultrasmall Sub-10 nm Ligand-Functionalized Fluorescent Core–Shell Silica Nanoparticle Growth in Water. *Chem. Mater.*, **27,** 4119–4133 (2015).

(*2*) Phillips, E., Penate-Medina, O., Zanzonico, P. B., Carvajal, R. D., Mohan, P., Ye, Y., Humm, J., Gonen, M., Kalaigian, H., Schoder, H., Strauss, H. W., Larson, S. M., Wiesner, U., Bradbury, M. S. Clinical translation of an ultrasmall inorganic optical-PET imaging nanoparticle probe. *Sci Transl Med.*, **6,** 260ra149-260ra149 (2014).

(*3*) Widengren, J., Mets, U., Rigler, R. Fluorescence correlation spectroscopy of triplet states in solution: a theoretical and experimental study. *J. Phys. Chem.*, **99,** 13368–13379 (1995).

(*4*) Elson, E. L., Magde, D. Fluorescence correlation spectroscopy. I. Conceptual basis and theory. *Biopolymers*, **13,** 1–27 (1974).

(*5*) Magde, D., Elson, E. L., Webb, W. W. Fluorescence correlation spectroscopy. II. An experimental realization. *Biopolymers*, **13,** 29–61 (1974).

(*6*) Magde, D., Elson, E., Webb, W. W. Thermodynamic Fluctuations in a Reacting System—Measurement by Fluorescence Correlation Spectroscopy. *Phys. Rev. Lett*, **29,** 705–708 (1972).

(*7*) Widengren, J., Schwille, P. Characterization of Photoinduced Isomerization and Back-Isomerization of the Cyanine Dye Cy5 by Fluorescence Correlation Spectroscopy. *J. Phys. Chem. A*, **104,** 6416–6428 (2000).

(*8*) Hom, E. F. Y., Verkman, A. S. Analysis of Coupled Bimolecular Reaction Kinetics and Diffusion byTwo-Color Fluorescence Correlation Spectroscopy: Enhanced Resolution of Kinetics by Resonance Energy Transfer. *Biophys. J*, **83,** 533–546 (2002).

(*9*) Michalet, X., Weiss, S., Jäger, M. Single-Molecule Fluorescence Studies of Protein Folding and Conformational Dynamics. *Chem. Rev*, **106,** 1785–1813 (2006).

(*10*) Schwille, P. Fluorescence Correlation Spectroscopy and Its Potential for Intracellular Applications. *Cell Biochem. Biophys.*, **34,** 383–408 (2001).

(*11*) Wöll, D. Fluorescence correlation spectroscopy in polymer science. *RSC Adv.*, **4,** 2447–2465(2014).

(*12*) Nath, P., Mangal, R., Kohle, F., Choudhury, S., Narayanan, S., Wiesner, U., Archer, L. A. Dynamics of Nanoparticles in Entangled Polymer Solutions. *Langmuir*, **34,** 241–249 (2017).

(*13*) Ow, H., Larson, D. R., Srivastava, M., Baird, B. A., Webb, W. W., Wiesner, U. Bright and Stable Core−Shell Fluorescent Silica Nanoparticles. *Nano Lett.*, **5,** 113–117 (2005).

(*14*) Doose, S., Tsay, J. M., Pinaud, F., Weiss, S. Comparison of Photophysical and Colloidal Properties of Biocompatible Semiconductor Nanocrystals Using Fluorescence Correlation Spectroscopy. *Anal. Chem.*, **77,** 2235–2242 (2005).

(*15*) Zhang, B., Lan, T., Huang, X., Dong, C., Ren, J. Sensitive Single Particle Method for Characterizing Rapid Rotational and Translational Diffusion and Aspect Ratio of Anisotropic Nanoparticles and Its Application in Immunoassays. *Anal. Chem.*, **85,** 9433–9438 (2013).

(*16*) Kuyper, C. L., Fujimoto, B. S., Zhao, Y., Schiro, P. G., Chiu, D. T. Accurate Sizing of Nanoparticles Using Confocal Correlation Spectroscopy. *J. Phys. Chem. B*, **110,** 24433–24441 (2006).

(*17*) Ma, K., Zhang, D., Cong, Y., Wiesner, U. Elucidating the Mechanism of Silica Nanoparticle PEGylation Processes Using Fluorescence Correlation Spectroscopies. *Chem. Mater.*, **28,** 1537–1545 (2016).

(*18*) Röcker, C., Pötzl, M., Zhang, F., Parak, W. J., Nienhaus, G. U. A quantitative fluorescence study of protein monolayer formation on colloidal nanoparticles. *Nat. Nanotechnol*, **4,** 577–580 (2009).

(*19*) Tsay, J. M., Doose, S., Weiss, S. Rotational and Translational Diffusion of Peptide-Coated CdSe/CdS/ZnS Nanorods Studied by Fluorescence Correlation Spectroscopy. *J. Am. Chem. Soc*, **128,** 1639–1647 (2006).

(*20*) Fortunati, I., Weber, V., Giorgetti, E., Ferrante, C. Two-Photon Fluorescence Correlation Spectroscopy of Gold Nanoparticles under Stationary and Flow Conditions. *J. Phys. Chem. C*, **118,** 24081–24090 (2014).

(*21*) Levitus, M., Ranjit, S. Cyanine dyes in biophysical research: the photophysics of polymethine fluorescent dyes in biomolecular environments. *Q. Rev. Biophys.*, **44,** 123–151 (2010).

(*22*) Chmyrov, V., Spielmann, T., Hevekerl, H., Widengren, J. Trans–Cis Isomerization of Lipophilic Dyes Probing Membrane Microviscosity in Biological Membranes and in Live Cells. *Anal. Chem.*, **87,** 5690–5697 (2015).

(*23*) Yeh, H.-C., Puleo, C. M., Ho, Y.-P., Bailey, V. J., Lim, T. C., Liu, K., Wang, T.-H. Tunable Blinking Kinetics of Cy5 for Precise DNA Quantification and Single-Nucleotide Difference Detection. *Biophys. J.*, **95,** 729–737 (2008).

(*24*) Marquardt, D. W. An Algorithm for Least-Squares Estimation of Nonlinear Parameters. *SIAM J Appl Math*, **11,** 431–441 (1963).

(*25*) Ehrenberg, M., Rigler, R. Rotational brownian motion and fluorescence intensify fluctuations. *Chemical Physics*, **4,** 390–401 (1974).

(*26*) Aragón, S. R., Pecora, R. Fluorescence correlation spectroscopy and Brownian rotational diffusion. *Biopolymers*, **14,** 119–137 (1975).

(*27*) Kask, P., Piksarv, P., Pooga, M., Mets, Ü., Lippmaa, E. Separation of the rotational contribution in fluorescence correlation experiments. *Biophys. J*, **55,** 213–220 (1989).

(*28*) Widengren, J., Mets, Ü., Rigler, R. Photodynamic properties of green fluorescent proteins investigated by fluorescence correlation spectroscopy. *Chemical Physics*, **250,** 171–186 (1999).

(*29*) Kapusta, P. Absolute Diffusion Coefficients: Compilation of Reference Data for FCS Calibration. Application Note, PicoQuant GmbH (2010).

(*30*) Yin, Y., Yuan, R., & Zhao, X. S. Amplitude of Relaxations in Fluorescence Correlation Spectroscopy for Fluorophores That Diffuse Together. *J Phys Chem Lett.*, **4,** 304–309 (2013).

(*31*) Williams, A. T. R., Winfield, S. A., Miller, J. N. Relative fluorescence quantum yields using a computer-controlled luminescence spectrometer. *The Analyst*, **108,** 1067 (1983).

(*32*) Allen, W. A. Measurement of Fluorescence Quantum Yields. Technical Note: 52019, Thermo Fisher Scientific, (2010).

(*33*) Introduction to polymers Young, Robert Joseph. and Lovell, P. A. Boca Raton [etc.]: CRC Press (2011).

(*34*) Zhao, M., Jin, L., Chen, B., Ding, Y., Ma, H., Chen, D. Afterpulsing and its correction in fluorescence correlation spectroscopy experiments. *Appl. Opt.*, **42,** 4031 (2003).

(*35*) Larson, D. R., Ow, H., Vishwasrao, H. D., Heikal, A. A., Wiesner, U., Webb, W. W. Silica Nanoparticle Architecture Determines Radiative Properties of Encapsulated Fluorophores. *Chem. Mater.*, **20,** 2677–2684 (2008).

(*36*) Iler, R. K. The Chemistry of Silica: Solubility, Polymerizaion, Colloid and Surface Properties, and Biochemistry; Wiley: New York (1979).

(*37*) Muddana, H. S., Morgan, T. T., Adair, J. H., Butler, P. J. Photophysics of Cy3-Encapsulated Calcium Phosphate Nanoparticles. *Nano Lett.*, **9,** 1559–1566 (2009).

(*38*) Strickler, S. J., Berg, R. A. Relationship between Absorption Intensity and Fluorescence Lifetime of Molecules. *J. Chem. Phys*, **37,** 814–822 (1962).

(*39*) Hirayama, S., Phillips, D. Correction for refractive index in the comparison of radiative lifetimes in vapour and solution phases. *J Photochemistry*, **12,** 139–145 (1980).

(*40*) Van Helden, A. ., Vrij, A. Contrast variation in light scattering: Silica spheres dispersed in apolar solvent mixtures. *J. Colloid Interface Sci*, **76,** 418–433 (1980).

(*41*) Mujumdar, R. B., Ernst, L. A., Mujumdar, S. R., Lewis, C. J., Waggoner, A. S. Cyanine dye labeling reagents: Sulfoindocyanine succinimidyl esters. *Bioconjugate Chem.*, **4,** 105–111 (1993).

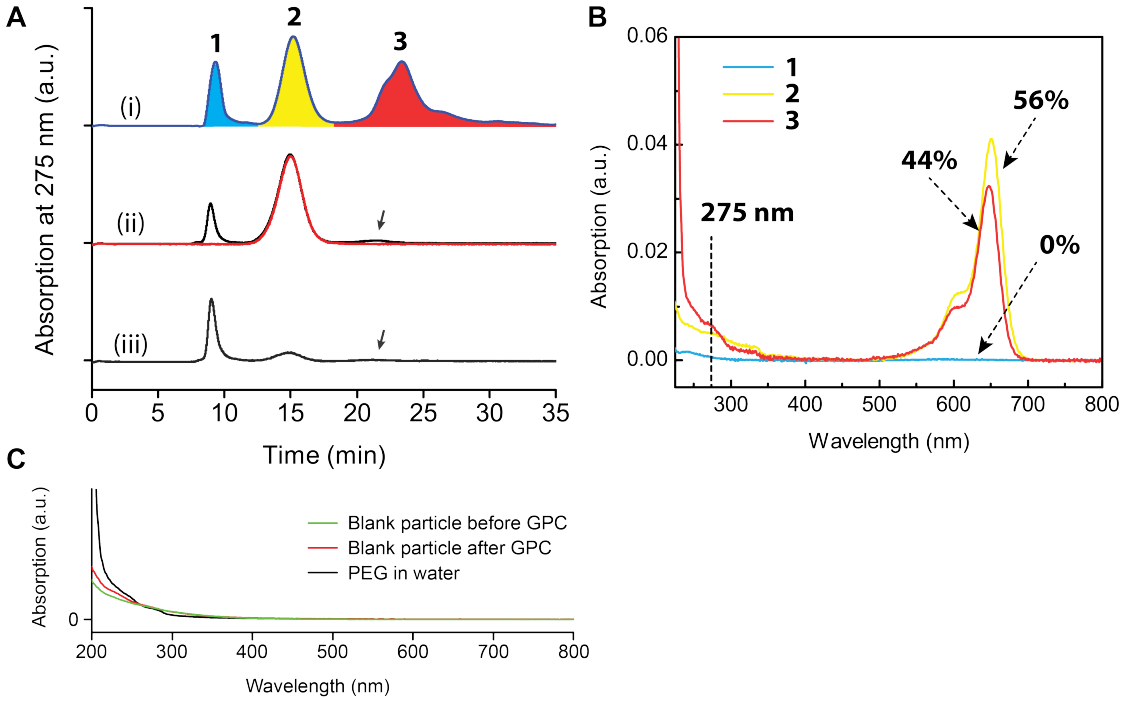

Figure S2.1. ***Gel permeation chromatography (GPC) and optical spectra of Cy5 core particles.*** (A) i: GPC elugram of native solution immediately after nanoparticle synthesis (without dialysis), and (B) corresponding absorption spectra of the collected fractions **1** (blue), **2** (yellow), and **3** (red). The percentages indicate relative amounts of Cy5. About 56% of the Cy5 dye used in the synthesis is associated with the particles. 44% of Cy5 dye is washed away by dialysis or GPC. No Cy5 dye is associated with peak 1; ii: GPC elugrams of first GPC run (black line) and second GPC run (red line); iii: GPC elugram of undyed silica nanoparticles. Black arrows indicate elution times of small molar mass compounds. The differences of relative peak heights between Figure S2.1A and Figure 2.1C stems from different particle concentrations. (C) Absorption spectra of blank particles before and after GPC, as well as of PEG (0.5 kDa) in water.

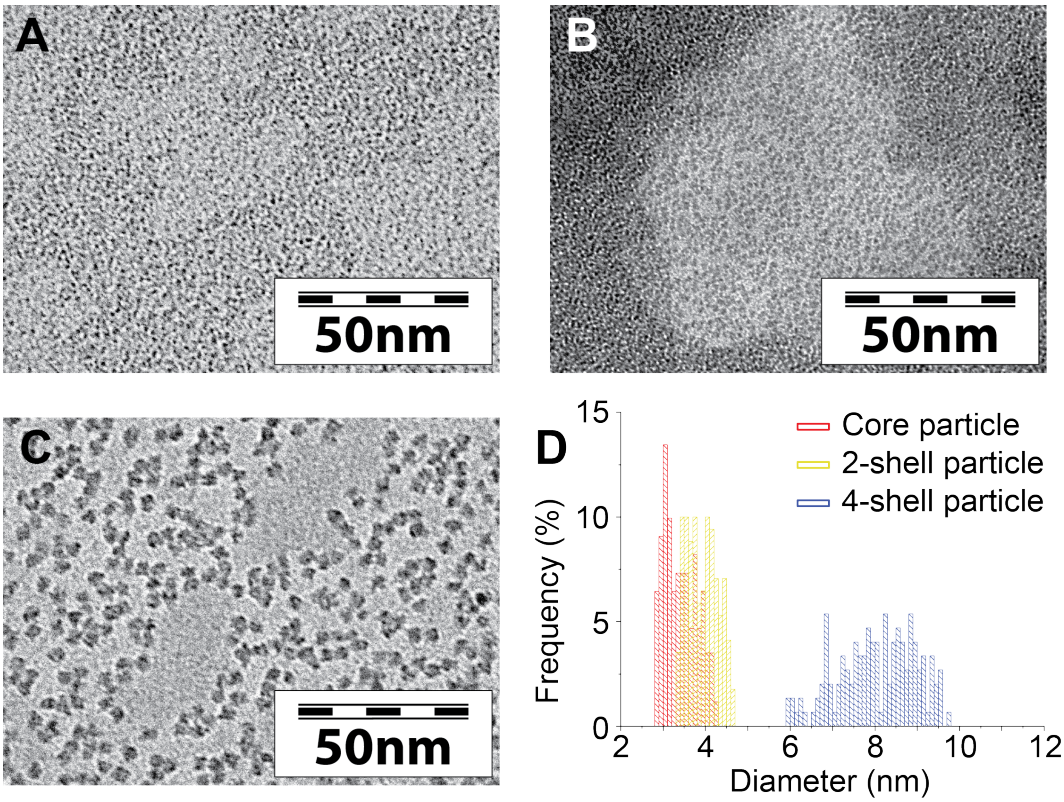

Figure S2.2. ***Transmission electron microscopy (TEM) and resulting particle size distributions.*** TEM images, of (A) core particles, (B) 2-shell particles, and (C) 4-shell particles with corresponding size analysis (D).

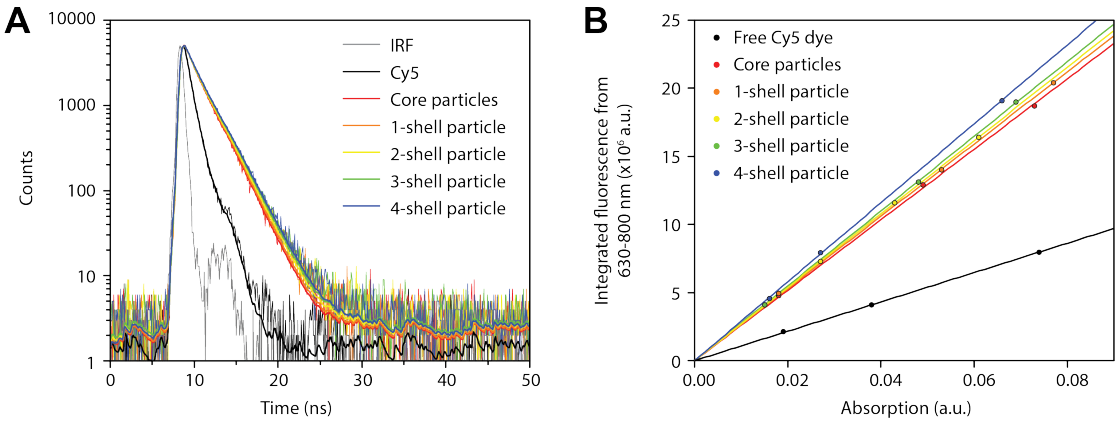

Figure S2.3. ***Fluorescence lifetimes and quantum yields.*** (A) Comparison of time resolved fluorescence decay curves of Cy5 and Cy5-encapsulating core-shell SNPs. (B) Comparison of fluorescence quantum yield measurements of free Cy5 dye and Cy5-encapsulating core-shell SNPs.

	Translational Diffusion			Rotational Diffusion		
Shell thickness	τ_D **[ms]**	D_T **[μs^2 s^{-1}]**	**Shell thickness**	τ_{Rot} **[ns]**	α_{Rot}	D_{Rot} **[μs^{-1}]**
Cy5	0.188 ± 0.003	357.00 ± 5.64	-	-	-	-
0 nm	0.786 ± 0.010	85.57 ± 1.06	**0 nm**	4.59 ± 2.36	0.30 ± 0.15	3.63 ± 1.87
0.3 nm	0.875 ± 0.012	76.81 ± 1.04	**0.3 nm**	5.85 ± 2.99	0.32 ± 0.10	2.85 ± 1.46
0.7 nm	0.979 ± 0.013	68.70 ± 0.93	**0.7 nm**	7.75 ± 1.47	0.30 ± 0.03	2.15 ± 0.41
1.2 nm	1.152 ± 0.013	58.37 ± 0.66	**1.1 nm**	10.60 ± 1.88	0.34 ± 0.05	1.57 ± 0.28
2.3 nm	1.482 ± 0.033	45.37 ± 1.00	**2.4 nm**	21.33 ± 1.95	0.36 ± 0.02	0.78 ± 0.07

Table S2.1. Characteristic particle translational diffusion time, τ_D, particle translational diffusion constant, D_T, characteristic particle rotational diffusion time, τ_{Rot}, pre-exponential amplitude of particle rotation, α_{Rot}, particle rotational diffusion constant, D_{Rot}. Values obtained from FCS fits.

Sample	τ_1 **[ns]**	α_1 **[%]**	τ_2 **[ns]**	α_2 **[%]**	χ^2
Cy5	0.35 ± 0.02	37.75	1.00 ± 0.02	62.25	1.09
Core particle	0.35 ± 0.03	9.86	2.05 ± 0.01	90.14	1.41
1-shell particle	0.33 ± 0.03	9.04	2.09 ± 0.01	90.96	1.28
2-shell particle	0.32 ± 0.03	9.38	2.14 ± 0.01	90.62	1.26
3-shell particle	0.29 ± 0.03	8.54	2.19 ± 0.01	91.46	1.25
4-shell particle	0.41 ± 0.05	8.25	2.23 ± 0.01	91.75	1.11

Table S2.2. Fitting parameters of fluorescence lifetime measurements. Fluorescence lifetimes, τ_1 and τ_2, and amplitudes, α_1 and α_2. All fluorescence lifetime measurements did show a minor short lifetime between 0.35 and 0.40 ns (τ_1), that is likely due to scattering artefacts from the instrument. This is further supported by the τ_2 of Cy5 which agrees with the literature value for Cy5 in aqueous solution (*7*). We therefore used τ_2 for further calculation.

CHAPTER 3

HETEROGENEITIES IN SURFACE CHEMICAL PROPERTIES OF ULTRASMALL FLUORESCENT SILICA NANOPARTICLES[*]

Abstract

In contrast to small molar mass compounds, detailed structural investigations of nanoparticles remain challenging. Assessment of batch reaction induced heterogeneities of surface chemical properties and their correlation with particle size has been a particularly long-standing issue. Applying a combination of high-performance liquid chromatography (HPLC) and gel permeation chromatography (GPC) to ultrasmall (< 10 nm) poly(ethylene glycol) coated (PEGylated) fluorescent core-shell silica nanoparticles, here we elucidate previously unknown surface heterogeneities resulting from varying dye conjugation to nanoparticle silica cores and surfaces. Heterogeneities are predominantly governed by dye charge as corroborated by molecular dynamics simulations. Since surface chemical properties are key to all nanoparticle interactions, we expect these methods and fundamental insights to become relevant to a number of systems for applications including bioimaging and nanomedicine.

[*] T. Gardinier[†], F. F. E. Kohle[†], J. Peerless, K. Ma, M. Turker, Y. G. Yingling, U. B. Wiesner. Heterogeneities in Surface Chemical Properties of Ultrasmall Fluorescent Silica Nanoparticles. Manuscript in preparation. [†] Indicates equal contribution.

Introduction

The study of ultrasmall (< 10 nm diameter) nanoparticles (NPs) is an area of rapidly growing academic and technological interest as a result of size dependent properties and applications ranging from catalysis to nanomedicine (*1–3*). While in the past decade the library of ultrasmall NPs has expanded substantially, detailed characterization of heterogeneities in surface-chemical composition has remained challenging. Biological nanomaterials such as proteins, antibodies, and their fragments have the advantage of consistent molar mass, and are now routinely analyzed by techniques such as high-performance liquid chromatography (HPLC) and liquid chromatography coupled mass spectrometry (LC-MS) (*4–6*). In contrast, single-batch ultrasmall synthetic NPs often composed of inorganic and organic components typically display a distribution of sizes, masses, and surface chemistries that is not well characterized (*7, 8*), despite being of paramount importance, e.g. for the therapeutic and diagnostic application of nanomaterials (*9–11*).

Here we turn to a combination of HPLC and gel permeation chromatography (GPC) for ultrasmall NP assessment. While the use in particular of HPLC for the characterization of organic compounds and macromolecules is ubiquitous (*12*), its application to organic-inorganic hybrid NPs is scarce (*8*). We show that the extreme sensitivity of HPLC to small changes in chemistry applied to ultrasmall inorganic NPs stabilized with organic ligands provides hitherto unknown insights into surface-chemical heterogeneity and its control. In combination with other techniques, including single molecule photo-bleaching experiments, fluorescence correlation spectroscopy (FCS), and molecular dynamics (MD) simulations, we elucidate the molecular origin of

these heterogeneities and correlate them to particle size via coupled GPC-HPLC runs. We expect that our approach will be applicable to other ultrasmall hybrid NPs systems and will enable synthesis of better defined materials for applications, e.g. in bioimaging and nanomedicine.

Materials and Methods

Materials

UHPLC grade acetonitrile was purchased from BDH. Superdex 200 resin was purchased from GE Healthcare Life Sciences. Vivaspin 30k MWCO spin filters were purchased from GE Healthcare Life Sciences. 5 M NaCl in water solution was purchased from Santa Cruz Biotechnology. Dimethyl sulfoxide (DMSO), Tetramethyl orthosilicate (TMOS), (3-Mercaptopropyl)trimethoxysilane (MPTMS), 2.0 M ammonia in ethanol were all purchased from Sigma-Aldrich. Methoxy-PEG(5-9)-silane (500g/mol) was purchased from Gelest. Cy5-maleimide, Cy5.5-maleimide, Cy3-maleimide were purchased from GE. TMR-maleimide (tetramethylrhodamine) purchased from Life Technologies. Alexa Fluor 647-COOH was purchased from Thermo Fisher. DI water generated using Millipore Milli-Q system (Milli-Q, 18.2 MΩ·cm). Atto647N-maleimide, Atto680-maleimide, and MB2-maleimide were purchased from Atto-Tec Gmbh. Xbridge Protein BEH C4 Column (300 Å, 3.5 µm, 4.6 mm X 150 mm, 10K-500K) and BioSuite. High Resolution SEC Column (250 Å, 5 µm, 7.8 mm X 300 mm, 10K – 500K) were purchased from Waters Technologies Corporation. Streptavidin and N-γ-maleimidobutyryl-oxysuccinimide ester (GMBS) were purchased from Life Technologies. All chemicals were used as received without further purification.

Particle synthesis

Cy5, TMR, Cy3, and Atto680 C' dots were synthesized as previously described *(15)*. Briefly, a mono functional maleimido derivatized dye was dissolved in DMSO overnight in a glovebox. A 25-fold excess of mercaptopropyltrimethoxysilane was added to the dissolved dye and allowed to react overnight in the glove box. The next day a flask containing deionized water adjusted to pH 8 using 2.0 M ammonia in ethanol solution was prepared and stirred vigorously. Tetramethylorthosilicate (TMOS) and the prepared dye-silane conjugate were added to the flask and allowed to react overnight. The following day, 100uL of mPEG(5-9)-silane was added to the flask and allowed to react overnight. The following day the stirring of the solution was stopped and the flask was heated to 80 C for 24 hours. Following this the particles are extensively dialyzed using 10k MWCO cellulose dialysis tubing, followed by syringe filtration with a 200 nm membrane, spin filtering with a 30k MWCO PES membrane spin filter and finally GPC purification through Superdex 200 resin on a Bio-Rad FPLC. The particles are then characterized using fluorescence correlation spectroscopy on a home-built setup and UV/Vis spectroscopy on a Cary 5000 spectrometer. Atto647N and MB2 C' dots have a slight adjustment to the protocol, for a 10 mL reaction 2 mL of 0.02 M NH_4OH solution and 8 mL of DI water are added to the reaction flask instead of the previously reported 1 mL the resultant increase in pH was used to decrease the final size of the nanoparticles, as dyes with positive charges tend to form larger nanoparticles under standard conditions.

High-performance liquid chromatography

All high-performance liquid chromatography (HPLC) runs were carried out on a Waters Alliance 2965 separations module equipped with a column heater, a Waters 2424 evaporative light scattering detector, and a Waters 2996 photodiode array detector. The sample loop was 50 μL, the standard size for an analytical system. The hardware was controlled by a computer running Empower 3 Feature Release 2 and all chromatograms were analyzed using the ApexTrack peak integration algorithm. Deionized water was generated from a Millipore Milli-Q water system (18.2 MΩ resistivity) and acetonitrile was obtained from BDH (UHPLC grade). The columns used were 150 mm Waters Xbridge BEH C4 Protein separation columns with 300 Å pore size and 3.5 μm particle size. All injections were 8 μL of 15 μM C' dots. Concentrations for injected samples were determined by FCS. The separation method used is as follows: The sample was first injected onto the column in a flow of 90:10 water:acetonitrile at a flow rate of 1 mL/min. These conditions were maintained for 20 minutes to allow equilibration of the analyte with the stationary phase. After 20 minutes the flow rate was slowed to 0.5 mL/min and the baseline was allowed to equilibrate. Then the mobile phase composition was changed to 45:55 water:acetonitrile in a step-like fashion and the baseline was allowed to equilibrate again. Finally a composition gradient of 45:55 to 5:95 water:acetonitrile was carried out for 20 minutes, during this time the analyte elutes from the column. The analytical run above was followed by a short washing step and column equilibration period to ensure that all material from the previous run had eluted from the column and that the column conditions for the next sample analysis were identical to those for the previous sample analysis. In addition to the above method, the same separation method can be used with a constant flow rate of 0.75 mL/minute for

the entirety of the experiment for identical results. The use of either method is based entirely on preference, as flow rate changes between 0.5 mL/min and 1 mL/min do not have any drastic effect on the particle separation. The data was collected and analyzed in Empower 3. The ApexTrack integration algorithm native to the Empower 3 software was used to identify peaks and determine the area percentage associated with each eluting peak. For plotting purposes, data was exported after analysis and baseline subtracted with a blank taken before the chromatographic run using OriginLab. For a comparison between baseline subtracted and raw data, see Figure S3.4.

Analytical gel permeation chromatography

Analytical scale gel permeation chromatography (GPC) was performed on as made solutions prior to preparative scale GPC purification. Injection volumes were 30 μL of native synthesis solution diluted with 70 μL of deionized water for a final injection volume of 100 μL. The solution used was the same as the preparative scale GPC solution, prepared the same way directly prior to injection. The column used was a 300 mm Water BioSuite High Resolution Size Exclusion Chromatography column. The separations were performed under isocratic conditions with a flow rate of 1mL/min. Particle samples including free dye and unreacted PEG-silane eluted within 30 minutes, but the column was run for an additional 20 minutes to ensure that all material had eluted during the chromatographic run.

Dye incorporation efficiency was calculated by using the ApexTrack integration algorithm native to the Empower3 software used to control the instrument and collect

data. The peak area percentage attributed to dye at the absorption maximum of the dye is taken to be the percentage of dye successfully incorporated in the nanoparticle.

Gel permeation chromatography

Preparative scale gel permeation chromatography (GPC) was carried out on a Bio-Rad FPLC equipped with a UV detector set to 275 nm and a conductivity detector. Particles were purified in isocratic mode using 0.9 wt.% NaCl in deionized water. The solution was prepared at the time of purification by diluting 0.2 μm membrane filtered 5 M NaCl in water (Santa Cruz Biotechnology) with deionized water. The column used was hand-packed with Superdex 200 resin with dimensions 20 mm x 300 mm and run at a flow rate of 2.0 mL/min. All samples were concentrated in GE Life Sciences 30 kDa MWCO VivaSpin filters prior to injection the total injection volume was less than 1 mL per run. Particles eluted around the 15 minute mark and the total run lasted 30 minutes.

Steady-state absorption spectroscopy

Absorbance spectra of particle samples and dye were measured in DI water on a Varian Cary 5000 spectrophotometer in a 3 mL quartz cuvette with a 10 mm light path (HellmaAnalytics) from 200 nm to 800 nm in 1 nm increments. All spectra were baseline corrected using a cuvette with DI water as reference cell. Peak intensities were kept between 0.01 and 0.06.

Fluorescence correlation spectroscopy

All fluorescence correlation spectroscopy (FCS) measurements were carried out on a homebuilt confocal FCS setup. In short, a continuous wave laser beam (635 nm solid state laser for particle containing Cy5, ATTO647N, or ATTO680, and a 543 nm HeNe laser for particles containing TMR, or Cy3) is focused onto the image plane of a water immersion microscope objective (Zeiss Plan-Neofluar 63x NA 1.2). The stokes-shifted emitted fluorescence is collected by the same objective, passed through a dichroic mirror, spatially filtered by a 50 μm pinhole, split into two paths with a beam splitter, spectrally filtered by long pass filters (ET665lp, Chroma, for 635 nm excitation, and ET560lp, Chroma, for 543 nm excitation), and detected by two avalanche photodiode detectors (SPCM-AQR-14, PerkinElmer). To filter detector afterpulsing effects from sample fluorescence fluctuations, the detector signals were cross-correlated by a digital correlator (Flex03LQ, Correlator.com)*(30)*, allowing lag time resolution of 15 ns. Respective correlation curves were fitted accounting for translational diffusion, photo-induced cis-trans isomerization, and rotational diffusion by using equation (1):

$$G(\tau) = 1 + \frac{1}{N_m}\left(\frac{1}{1+\tau/\tau_D}\right)\left(\frac{1}{1+\tau/(\tau_D\kappa^2)}\right)^{1/2} \frac{1}{(1-P)}(1-P+P\exp(\tau/\tau_P)) \left(1+\alpha_{Rot}\, exp\,(\tau/\tau_{Rot})\right) \quad (1)$$

where N_m is the number of dye molecules or particles in the ellipsoidal observation volume, defined by a structure factor $\kappa = \omega_z/\omega_{xy}$ with axial (ω_z) and radial (ω_{xy}) radii.

τ_D is the average diffusion time of a dye or particle through the observation volume. P is the fraction of Cy5 dye molecules being in the non-fluorescent cis-conformation, which the characteristic relaxation time τ_P. For particles a third relaxation time is noticeable at very short lag times (τ = 100 ns) that can be attributed to particle rotation, where α_{Rot} is the pre-exponential amplitude of particle rotation, and τ_{Rot} the characteristic rotational diffusion time of a particle. Particle rotation was not further characterized and only used for improved fits. All correlation curves were normalized according to equation (2):

$$G(\tau) = (G(\tau) - 1)\, N_m \tag{2}$$

The FCS observation volume V_{eff} was calibrated before each measurement by diluting a dye stock solution with DI water to nanomolar concentrations and determining the structure factor with a standard dye (Alexa Fluor for 635 nm laser and TMR for 532 nm laser). To avoid singlet-triplet transitions in Cy5 dye, all measurements were carried out at 5 kW cm^{-2}*(20)*. All FCS samples were measured five times in five individual 30 s runs in a 35 mm glass bottom dish (P35G-1.5-10-C, Mattek Corporation) at nanomolar concentration in DI water at 20 °C. The particle diameters, d, were determined from the fits using equation (3) and (4):

$$D = \frac{{\omega_{xy}}^2}{4\tau_D} \tag{3}$$

$$d = 2\frac{k_B T}{6\pi\eta D} \tag{4}$$

where D is the diffusion constant, k_B is the Boltzmann's constant, and T is the absolute temperature. Since cis-trans isomerization of co-diffusion Cy5 molecules is independent

from each other, the amplitude of isomerization, α, appears smaller, for particles carrying more than one Cy5 molecule. Therefore, P needs to be adjusted for the average number of dyes per particle, n_m, using equations (5) and (6):

$$P = \alpha/(1+\alpha) \tag{5}$$

$$\alpha = \alpha_P/n_m \tag{6}$$

To determine n_m the measured optical density of each sample was compared to the mean particle concentration as obtained by FCS using equation (7):

$$n_m = \frac{C_{Abs}}{\langle C \rangle_{FCS}} \tag{7}$$

Total Internal Reflection Fluorescence Microscopy (TIRFM)

Samples for photobleaching experiments were prepared by immobilizing biotinylated particles on streptavidin coated glass slides. Streptavidin coated slides were prepared by binding streptavidin via GMBS and MPTMS to a plasma cleaned glass bottom slide (P35G-1.5-14-C, Mattek Corporation) as previously described *(31)*. Free particles were removed by rinsing the slides with PBS twice before covering the sample with 1 mL of PBS and a glucose oxidase/catalase oxygen scavenger system. Single particle imaging was performed on an inverted Zeiss Elyra microscope operated at TIRF angles of 62–65° as indicated in the Zen 2012 (Zeiss) software, using a 1.46 NA 100X oil immersion objective, and 642 nm laser (laser power 0.165 mW, measured at the objective) with typical integration times of 100 ms per frame. Fluorescence emission was spectrally filtered with a 655 nm long pass filter. Each movie was recorded at 10 Hz until 99% of the initial fluorescence signal decayed. The excitation laser was turned

on right after the photobleaching movie recording was started. The "Definite focus" focal-drift compensation was activated during data acquisition. To avoid overlapping point spread functions only samples that were sparsely labeled with particles were included in the analysis.

Single particle photobleaching analysis

To analyze the recorded movies *.zvi files were loaded into ImageJ and converted to 8-bit *.tiff files. Individual particle fluorescence time traces (arbitrary units, A.U.) were extracted using the custom software (ImageC.exe), developed and kindly provided by Dr. Warren Zipfel (Cornell University, NY, USA). Due to sparse labeling it was assumed that each point spread functions (PSF) in the image represents one particle. Particles were automatically located from the summed projection of the image stack by applying a Gaussian mask algorithm. Particle fluorescence time trace were the summed pixel intensities of 5x5 region of interest (ROI) centered around the brightest pixel and plotted against measurement time. The brightest pixel was maintained as the center of each ROI for each frame. Due to shot noise variations and possible minor drift, the ROI was allowed to move at most 1 pixel per frame. Fluorescence bleaching steps were counted by hand. Traces with undiscernable bleaching steps were rejected from the analysis. A total number of 644 particles were analyzed.

Simulations

All-atom molecular dynamics (MD) simulations were performed using the AMBER 16 molecular dynamics package (*32*). Initial coordinates as well as force field

parameters for the amorphous silica surfaces were those published by Heinz et al. (*33*). All dye molecules were constructed in Discovery Studio Visualizer (*34*) and assigned force field parameters from the general AMBER force field (GAFF) version 1.8 (*35*). Dyes with attached silane units also included force field parameters from the CHARMM silicate force field published by Lopes et al. (*36*) applied to silicon and silicon-adjacent atoms. Partial charges were assigned to the dye molecules via the restrained electrostatic potential (R.E.S.P.) method using R.E.S.P. ESP charge Derive (R.E.D.) Server Development (*37*). During R.E.S.P. calculations, the net molecule charge and the local charge on atoms shown with a formal charge were restrained. All dye molecules were individually energy minimized in vacuum prior to their addition to surface-solvent systems. The TIP3P water model (*38*) and monovalent ion parameters were employed as reported in (*39*).

Systems containing silica surfaces, dye, and water were constructed by first copying and translating the coordinates for an amorphous silica surface in (*33*) to create a bonded silica surface approximately 80 x 80 x 20 Å in the *x*, *y*, and *z* directions, respectively. Hydrogens were randomly removed to reach the desired deprotonation percentage, followed by changing the dangling oxygen atom types and partial charges as necessary. The target dye molecule was then added to the system with a center-of-mass 4-9 Å above the surface in the positive *z*-direction, with the distance chosen to ensure that the dye does not overlap with the silica surface after addition. The dye molecule was then randomly rotated by first choosing a random unit vector through the molecule center-of-mass as the axis of rotation and then a random angle between 0 and 2π by which to rotate the dye molecule. For each surface-dye combination, five

independent systems differing only by this random dye molecule rotation were created and simulated. Reported linear interaction energies are the average of these five simulations. The dye molecule and silica surface were then solvated with TIP3P water using a buffer distance of 40 Å in the positive and negative *z*-directions. Random water molecules were then removed and replaced by positively-charged ammonium ions to reach a net neutral charge for the entire system. Thus, the starting simulation coordinates were approximately 80 x 80 x 130 Å with 85,000-95,000 atoms total. A visualization of a representative starting system conformation with Cy5 maleimide is shown in Figure 3.4A and Figure S3.4.

All simulations utilized periodic boundary conditions, the Langevin thermostat with a collision frequency of 2 ps^{-1}, the Berendsen barostat (if NPT ensemble) with a relaxation time of 1 ps, and a van der Waals cutoff value of 8 Å with long-range electrostatics calculated via the Particle Mesh Ewald method. Prior to production simulations, each system was independently equilibrated with the silica surface and dye molecule harmonically restrained with a force constant of 5.0 kcal/mol by the following five-step procedure: (1) structural energy minimization, (2) a constant-volume (NVT ensemble) heating step from 0 to 300 K at a rate of 3 K/ps, (3) an NVT equilibration step at 300 K for 0.3 ns, (4) a constant-pressure (NPT ensemble) equilibration step at 1 atm and 300 K for 0.5 ns, and (5) an NPT equilibration step at 1 atm and 300 K with a timestep of 2 fs and the SHAKE algorithm (*40*) applied to covalent bonds involving a hydrogen for 1 ns (steps 1 to 4 used a 1 fs timestep). Production simulations, from which all reported data was calculated, were performed in the NPT ensemble at 1 atm and 300

K with a timestep of 2 fs for 100 ns. Linear interaction energies were calculated using AMBER's cpptraj post-processing software (*41*).

Results and Discussion

We studied ultrasmall poly(ethylene glycol) coated (PEGylated) fluorescent core-shell silica NPs known as Cornell prime dots or simply C' dots (*13, 14*). We focused on fluorescent Cy5 dye encapsulating particles synthesized in water referred to PEG-Cy5-C' dots and cyclic targeting peptide, c(RGDyC), functionalized c(RGDyC)-PEG-Cy5-C' dots (*15, 16*). While a first human clinical trial with such NPs suggested their safety (*3*), future high-dose therapeutic NP applications would tremendously benefit from improved characterization. After synthesis, C' dot batches were subjected to GPC purification removing impurities including particle aggregates, free dye, and free PEG/c(RGDyC)-PEG resulting in single-peak chromatograms as shown for PEG-Cy5-C' dots in Figure 3.1A (*17*). Purified C' dots were subsequently characterized using an HPLC method tuned to separate NPs based on small differences in surface chemical properties (see Appendix B). A representative HPLC chromatogram for PEG-Cy5-C' dots as detected at the 647 nm Cy5 absorbance wavelength (Figure 3.1B, blue line) revealed four distinct features, three dominant peaks <34 min and a small peak ~35 min. Using a 275 nm detector sensitive to PEG, the chromatogram reproduced the three dominant peaks, albeit with different intensities (Figure 3.1B, red line). The corresponding HPLC chromatogram for the c(RGDyC)-PEG-Cy5-C' dots (Figure 3.1C) was less well resolved due to peak broadening, but the main features of the PEG-Cy5-C' dot chromatogram were still present. This suggested that the main source of heterogeneity was not the targeting peptides, but associated with the PEG-Cy5-C' dot synthesis (*3, 18*).

Cross experiments identified the origin of these heterogeneities. First, we synthesized same size PEG-C' dots without Cy5 dye. Our HPLC method with 275 nm detection revealed a single peak at the position of the first peak observed for PEG-Cy5-C' dots (Figure 3.1B, black line), suggesting its assignment to a particle fraction with the same surface characteristics as the PEG-C' dots, i.e. a purely PEGylated silica surface (*8*). These particles may or may not contain a dye. If they do, it must be fully encapsulated within the silica core (see illustration in Figure 3.1B inset). Results revealed Cy5 dye encapsulation chemistry as the source of the heterogeneities.

We next immobilized biotin-functionalized PEG-Cy5-C' dots on glass slides previously functionalized with streptavidin (Figure 3.1D) for exposure to the evanescence field of a fluorescence microscope in total internal reflection geometry at low laser power and in the presence of an oxygen scavenger system (see Appendix B). Continuous exposure caused Cy5 dye photobleaching. Image stacks were recorded until 99% of the original fluorescence signal was muted (Figure 3.1E). Representative fluorescence time traces were extracted from the images (Figure 3.1F). When a dye bleaches, a sharp step in the intensity trace is observed (orange arrows). The traces show NPs with one, two, three, and four steps, respectively, before the intensity reaches the background, suggesting one to four dyes per particle. About 650 immobilized NPs of a single synthesis batch were analyzed. The resulting statistics (Figure 3.1G) indicated that ~55% of the dots had one dye, with increasingly smaller numbers of NPs carrying two, three, or four dye molecules per particle, respectively. Together with the HPLC results this led us to the hypothesis that the four HPLC peaks are associated with zero, one, two, or three Cy5 dyes, respectively, at the silica core surface.

Cyanine dyes like Cy5 undergo photo-induced cis-trans isomerization around the polymethine bridge between a fluorescent trans-state and a non-fluorescent cis-state (*26*). The associated rates are sensitive to the steric environment, have been used to probe membrane micro-viscosity of cells (*19, 20*), and can be observed in FCS at short lag times (<10-5 s) by a change of the amplitude in the correlation curve, as well as a change of associated characteristic relaxation time (*19*). We compared FCS measurements on HPLC fractions associated with each of the three dominant peaks 1-3 (Figure 3.1H(i)) with unfractioned particles and free Cy5 dye. Particle curves are shifted to longer times relative to free dye due to larger size. Isolated contributions of cis-trans photo-isomerization to the respective FCS curves are shown in (ii). From FCS, all NPs had the same size (inset of Figure 3.1H and Figure 3.1I) confirming that HPLC is separating peaks predominantly as a function of particle surface chemistry. Fractions showed increasing numbers of dyes per particle as elution time increased (Figure 3.1K), corroborating that additional dye on the particle surface is the source of the heterogeneity. From Figure 3.1J, brightness per dye decreases with increasing peak elution time (*21*), consistent with energy transfer between dyes or near surface dye locations. With a Cy5 hydrodynamic diameter of roughly 1.3 nm (Figure 3.1I), two or more dyes may not fully reside inside a silica NP core of only 2.5 nm hydrodynamic radius. Dyes on the NP surface are less confined than dyes fully encapsulated within the rigid silica matrix and may be prone to additional forms of non-radiative energy dissipation (*21*). One of those for Cy5 is photo-isomerization, which we analyzed for each HPLC fraction as compared to unfractionated PEG-Cy5-C' dots. As peak elution time increases, the percentage of dye undergoing photo-isomerization increases (Figure

3.1L), suggesting that particles with larger dye numbers are likely to have more Cy5 molecules on the particle surface, consistent with our hypothesis. The sensitivity of the HPLC method is so high, that the difference of one dye on the silica core surface will have significant effects on elution time. We estimated the percentage of particles with zero, one, two, or three dyes on the surface from HPLC peak area integrations (Appendix B Table S3.5). Differences to results from the dye photobleaching statistics (Figure 3.1G) can be rationalized by the fact that HPLC does not separate based on the absolute number of dyes per particle, which includes particles that have dyes on the surface and fully encapsulated in the core.

To elucidate variations in surface chemical properties as a function of particle size within a particle synthesis batch expected to have substantial impact, e.g. on biological properties of NPs (*22,23*), we performed coupled GPC-HPLC separations. A sample of pre-purified PEG-Cy5-C' dots was split into 15 fractions using GPC, which were then linearly up-concentrated to retain their GPC concentration relationship (inset Figure 3.2A) and sequentially injected into the HPLC. Results are plotted in two-dimensional (2D waterfall) plots with HPLC and GPC resolution along the x and y axes, respectively, and absorbance along the z axis (Figure 3.2). Concentration differences between tailing and central GPC fractions caused loss of full peak resolution for the tailing fractions (Figure 3.2A). This could be circumvented by moving to a subset of eight GPC fractions, each adjusted to the same final concentration and run through the HPLC (Figure 3.2B and inset), exhibiting no substantial dependence of the surface chemical properties on particle size. Detailed comparison of fractions 13, 16, and 20 representing large, medium, and small NPs of the distribution, respectively, reveal a

small increase in surface bound dyes with NP size as expected from their increased surface area (Figure 3.2D). For these PEG-Cy5-C' dot batches fear of the "worst-case scenario", with surface chemical properties strongly correlated with size, and thus maximum complexity in particle heterogeneity, is unsubstantiated.

To control particle heterogeneity, HPLC results were evaluated as a function of dye chemistry/charge. In addition to working with negatively charged Cy5, we synthesized PEG-C' dots from zwitterionic TMR and positively charged ATTO647N dyes (Figure 3.3). We used GPC on native synthesis solutions to monitor dye incorporation efficiency and HPLC on GPC purified samples to characterize surface chemical properties. Dye incorporation efficiency and homogeneity of surface chemical properties substantially increased in the sequence Cy5 < TMR < ATTO647N (Figure 3.3A-F), with ATTO647N resulting in single peak chromatograms for both GPC and HPLC (Figure 3.3C and F). Incorporation efficiencies were near 100% for ATTO647N, 82% for TMR, and only 62% for Cy5 (Figures S3.3-S3.5, Tables S3.2-S3.4). Net dye charge plays a crucial role in both efficient dye encapsulation in silica and heterogeneity of surface chemical properties. Results can be rationalized by considering Coulomb interactions between dye and silica NPs during growth: At our basic synthesis conditions silica NPs are far above their isoelectric point (pH~2-3) and are stabilized by negative surface charges before surface PEGylation (*16*). Interactions therefore switch from repulsive to attractive when moving from Cy5 across TMR to ATTO647N, consistent with increasing dye incorporation efficiency as revealed by GPC, numbers of dyes per particle for the latter two as determined by FCS (Table S3.1 and Figure S3.1-

S3.2), and improved homogeneity of surface chemical properties as documented by HPLC.

Trends were primarily dependent on dye charge and not on specific dye chemical characteristics as revealed by substituting Cy5, TMR, and ATTO647N with same net charge series Cy3, ATTO680, and weakly fluorescent dye MB2, respectively. Despite slight differences, e.g. in HPLC retention time between PEG-ATTO647N-C' dots and PEG-MB2-C' dots (compare Figure 3.3F and I) or in peak width between PEG-TMR-C' dots and PEG-ATTO680-C' dots (compare Figure 3.3E and H), this series (Figure 3.3G to I) matches the overall peak structure of the earlier series remarkably well with negatively charged Cy3 dye (like Cy5 dye) producing 4 peaks and positively charged MB2 dye (like ATTO647N dye) resulting in essentially a single relatively sharp peak.

The origin of the observed differences in dye incorporation efficiency and dye location either on the surface or in the NP core was elucidated by all-atom MD simulations (*24, 25*). Atomistic MD has been extensively employed to study silica surfaces and their interactions with silanes and other organics (*26–29*). We constructed systems (see Appendix B) of amorphous silica with a given surface charge (ratio of SiO-/SiOH units available on the surface referred to as the deprotonation percentage), a single dye molecule, water, and the number of ammonium ions necessary to reach a net-neutral system charge (Figure 3.4A, for dimensions see Figure S3.7). The resulting total non-bonded interaction energies between the silica surfaces and the dye silanes over the last 20 ns of the production simulations are shown in Figure 3.4B where large negative values indicate strong attraction, whereas positive values indicate repulsion (Figure S3.8). All three dyes have a similarly strong affinity to the passivated surface of a fully-

formed nanoparticle (with Cy5 potentially being slightly more attracted) as represented by the 1% deprotonated surface. A more-negatively-charged 15% deprotonated surface, representative of intermediate silica cluster surfaces during synthesis, shows unchanged affinity for TMR and ATTO647N. In contrast, Cy5 shows little to slightly repulsive interaction, suggesting that Cy5 is less attracted to these clusters and therefore less likely to be incorporated into the core of the particle. Moreover, analyzing the interaction energies between specific atomic groups within the dye molecules and the silica surface (Figure S3.9) provides evidence that these interactions are indeed driven by electrostatics, consistent with experiments. For example, the electrostatic repulsion between Cy5 and the 15% deprotonated surface is the strongest interaction measured in this study.

Conclusion

The highest degree of particle homogeneity in surface chemical properties was obtained for PEG-MB2-C' dots (see Figure 3.3). For a synthesis batch of these particles we conducted coupled GPC-HPLC experiments. PEG-MB2-C' dots fractionated with GPC, normalized in concentration, and subjected to HPLC, revealed no substantial dependence of the surface chemical properties on particle size (Figure 3.2C). Detailed comparison of different fractions revealed a small increase in surface bound dyes with particle size (Figure 3.2E), similar to PEG-Cy5-C' dots. Results corroborated earlier conclusions for PEG-Cy5-C' dots that for this synthesis approach to fluorescent core-shell silica NPs, heterogeneities in particle size and surface chemical properties are essentially uncorrelated. Comparison of waterfall plots in Figure 3.2A and C for PEG-Cy5-C' dots and PEG-MB2-C' dots demonstrate remarkable control in particle batch surface chemical homogeneity achieved by the appropriate choice of dye chemistry.

Figures

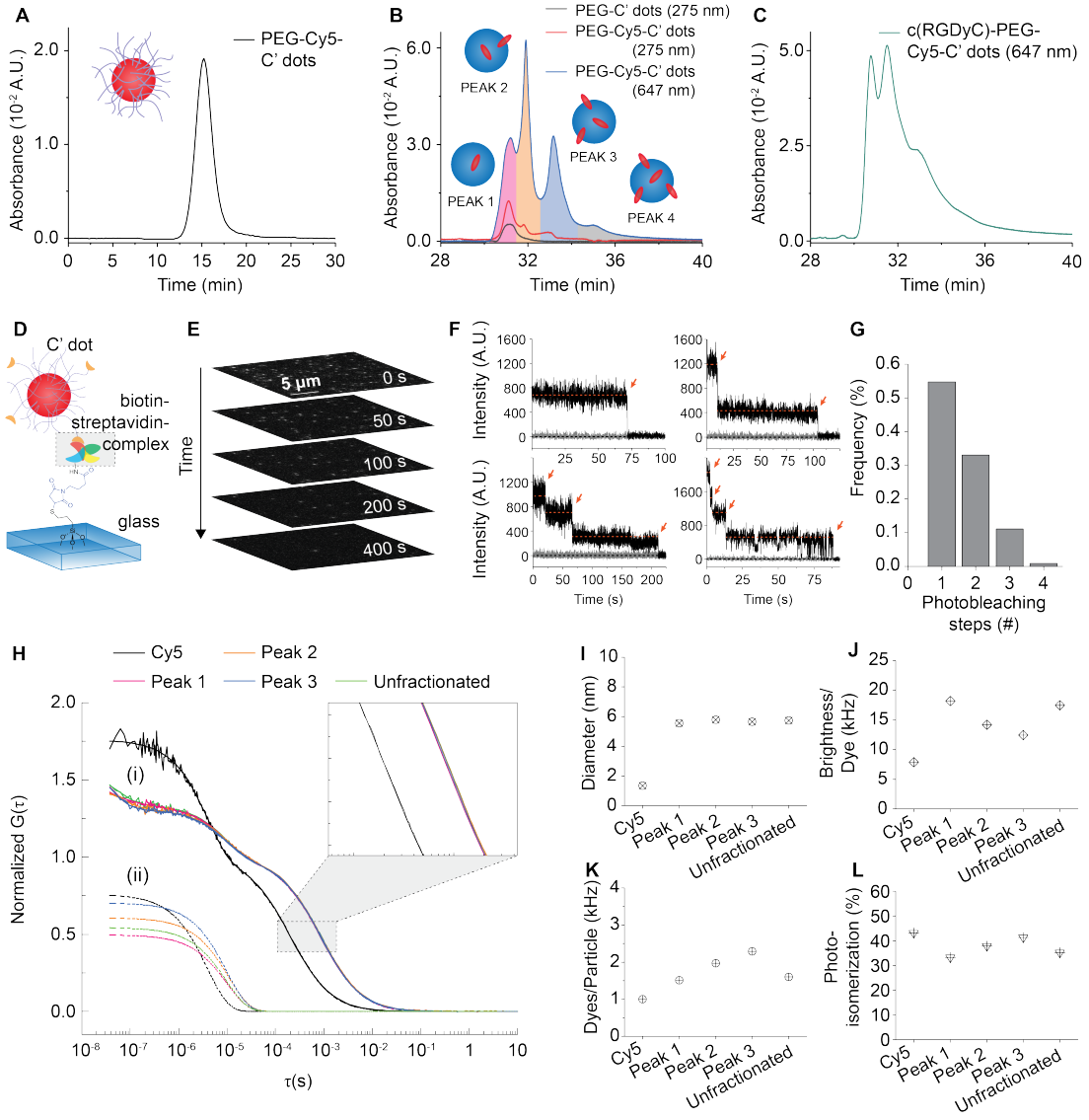

Figure 3.1. ***Nanoparticle heterogeneity and its analysis.*** (**A**) GPC chromatogram of purified PEG-Cy5-C' dots recorded at 275 nm with particle illustration (inset). (**B**) HPLC chromatograms of PEG-Cy5-C' dots recorded at 647nm (main) as well as of PEG-C' dots (black) and PEG-Cy5-C' dots (red) recorded at 275 nm. Next to the main peaks are schematics of suggested particle structure (blue circles) and dye locations (red ellipses). (**C**) HPLC chromatogram of c(RGDyC)-PEG-Cy5-C' dots recorded at 647 nm. (**D**) Schematic of a biotin functionalized PEG-Cy5-C' dot immobilized on a streptavidin coated glass slide for TIRFM, and (**E**) image stack of representative photobleaching time series. (**F**) Representative particle fluorescence intensity time traces from photobleaching. Red arrows indicate bleaching events. (**G**) Dye distribution in PEG-

Cy5-C' dot batch derived from photobleaching. (**H**) (i) FCS correlation curves for free Cy5 dye and PEG-Cy5-C' dots under peaks 1-3 in (B) collected from successive HPLC runs. (ii) Individual contributions of cis-trans photoisomerization to respective FCS curves in (i). (**I**) Hydrodynamic diameter, (**J**) brightness per dye, (**K**) dyes per particle, and (**L**) photoisomerization percentage for free Cy5 dye as compared to PEG-Cy5-C' dots from HPLC fractionated peaks 1-3 in (**B**).

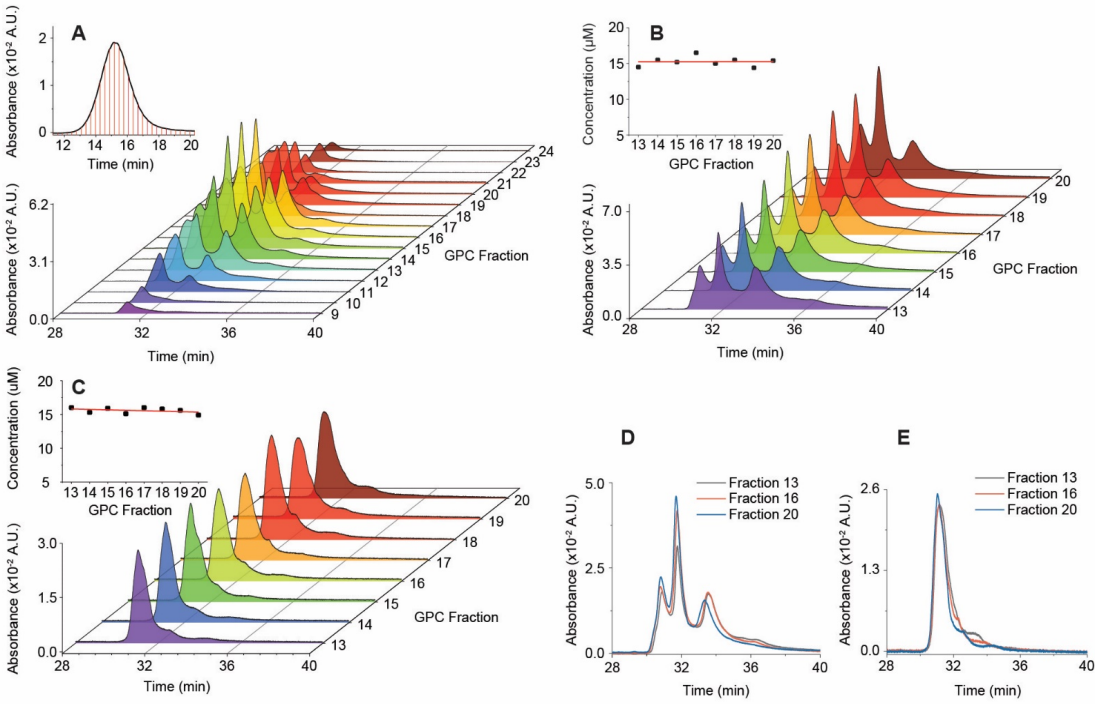

Figure 3.2. ***Coupled GPC-HPLC nanoparticle characterization.*** **(A)** Waterfall plot of coupled GPC-HPLC runs for PEG-Cy5-C' dots. Inset shows GPC trace of PEG-Cy5-C' dots; red lines are the fraction collection starting points. (**B**) Waterfall plot of coupled GPC-HPLC runs for PEG-Cy5-C' dots from subset of GPC fractions collected in (A) and concentrated to a uniform concentration (inset) as determined by a combination of UV/Vis absorbance and FCS. (**C**) Same as in (B) for MB2 C' dots (PEG-MB2-C' dots), but with less uniform particle concentration, in part because methylene blue is a non-fluorescent dye, and FCS could not be performed. (**D,E**) Overlay of three representative chromatograms from concentration normalized coupled GPC-HPLC runs in (B) and (C). Large (black), mid-sized (red), and small (blue) particles show only minor differences in surface chemistry heterogeneity.

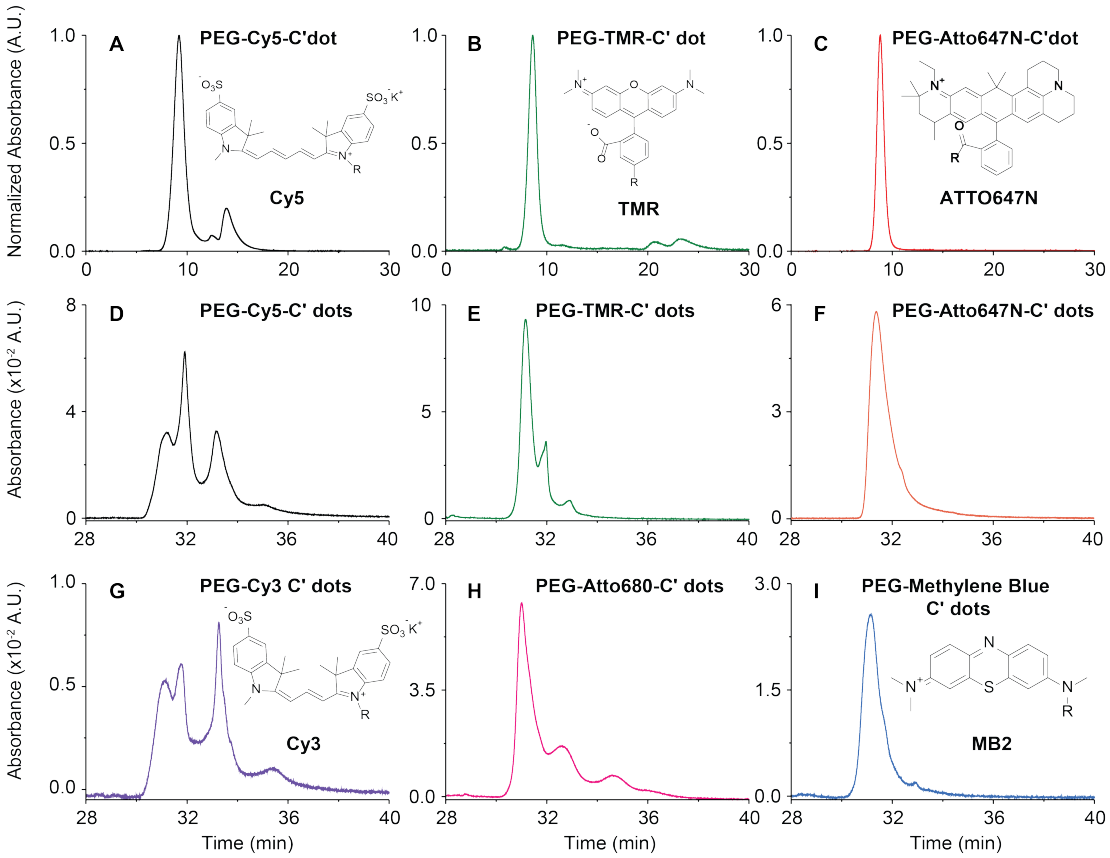

Figure 3.3. ***Dye incorporation efficiency and nanoparticle heterogeneity as a function of dye charge.*** **(A-C**) Analytical GPC chromatograms of native synthesis solutions prior to preparative scale purification: PEG-Cy5-C' dot solution (A) as detected at 647 nm with peaks corresponding to particles, PEG-Cy5 conjugates, and free Cy5, in order of elution (for incorporation efficiency, see Appendix B Table S3.3); PEG-TMR-C' dot solution (B) as detected at 553 nm with largest peak corresponding to PEG-TMR-C' dots (for incorporation efficiency see Appendix B Table S3.2); PEG-ATTO647N-C' dot solution (C) detected at 647 nm, (incorporation efficiency ~100%). (**D-I**) HPLC chromatograms of: PEG-Cy5-C' dots (D), PEG-TMR-C' dots (E), PEG-ATTO647N-C' dots (F), PEG-Cy3-C' dots (G), PEG-ATTO680-C' dots (H), and PEG-MB2-C' dots (I). Dye structures are shown in insets (the structure of ATTO680 is not available, but according to ATTO-Tec GmBH, the dye is zwitterionic).

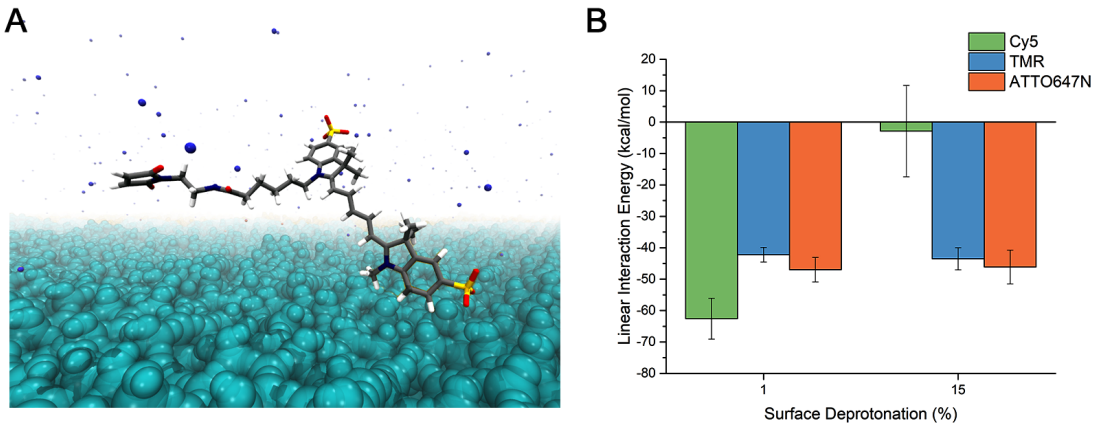

Figure 3.4. ***Molecular dynamics (MD) simulations and analysis.*** **(A)** Representative system setup of silica surface - dye MD simulations as-constructed, composed of water (not shown for clarity), amorphous SiO_2 (cyan), Cy5 maleimide (carbon=gray, hydrogen=white, nitrogen=blue, oxygen=red, silicon=yellow), and ammonium ions (blue spheres). In other systems Cy5 maleimide is replaced with the dye of interest. **(B)** Total linear interaction energies calculated between silica surfaces and dye silane molecules. Reported values are the average of the last 20 ns of five 100 ns simulations with randomly-oriented initial dye coordinates (see Materials & Methods for more details).

Acknowledgments

The authors thank Dr. Warren Zipfel and Dr. Teresa Kao for helpful discussions. **Funding:** Research reported in this publication was funded by the National Cancer Institute of the National Institutes of Health under Award Number U54CA199081. HPLC and GPC data were acquired through MC2TCN Center for Cancer Nanotechnology Excellence, which is supported by the National Cancer Institute of the National Institutes of Health under Award Number U54CA199081. Imaging data was acquired through the Cornell University Biotechnology Resource Center, with National Science Foundation (NSF) funding (MRI-1428922). Simulation work was supported by the NSF DGE-1633587). M.Turker gratefully acknowledges fellowship support by the Ministry of National Education of the Republic of Turkey. **Author contributions:** T. Gardienier, F. F. E. Kohle, K. Ma, and U. B. Wiesner designed experiments. T. Gardinier carried out HPLC and GPC experiments. F. F. E. Kohle carried out photobleaching experiments. F. F. E. Kohle carried out FCS measuremnts and data analysis. T. Gardinier, F. F. E. Kohle, K. Ma, and M. Turker synthesized particles. J. Peerless, T. Gardinier, K. Ma, Y. G. Yingling, and U. B. Wiesner discussed relevant simulation parameters. MD simulations were designed and executed by J. Peerless and Y. G. Yingling.

REFERENCES

(*1*) Jadzinsky, P. D., Calero, G., Ackerson, C. J., Bushnell, D. A., Kornber, R. D., Structure of a Thiol Monolayer-Protected Gold Nanoparticle at 1.1 A Resolution. *Science*, **318,** 430–433 (2007).

(*2*) Turner, M., Golovko, V. B., Vaughan, O. P. H., Abdulkin, P., Berenguer-Murcia, A., Tikhov, M. S., Johnson, B. F. G., Lambert, R. M. Selective oxidation with dioxygen by gold nanoparticle catalysts derived from 55-atom clusters. *Nature*, **454,** 981–983 (2008).

(*3*) Phillips, E., Penate-Medina, O., Zanzonico, P. B., Carvajal, R. D., Mohan, P., Ye, Y., Humm, J., Gonen, M., Kalaigian, H., Schoder, H., Strauss, H. W., Larson, S. M., Wiesner, U., Bradbury, M. S. Clinical translation of an ultrasmall inorganic optical-PET imaging nanoparticle probe. *Sci Transl Med.*, **6,** 260ra149-260ra149 (2014).

(*4*) Fenn, J. B., Mann, M., Meng, C. K. A. I., Wong, S. F., Whitehouse, C. M. Electrospray Ionization for Mass Spectrometry of Large Biomolecules. *Science*, **246,** 64–71 (1989).

(*5*) Lee, S.-W., Berger, S. J., Martinović, S., Pasa-Tolić, L., Anderson, G. A., Shen, Y., Zhao, R., Smith, R. D. Direct mass spectrometric analysis of intact proteins of the yeast large ribosomal subunit using capillary LC/FTICR. *Proc. Natl. Acad. Sci. U. S. A*, **99,** 5942–7 (2002).

(*6*) Aebersold, R., Mann, M. Mass spectrometry-based proteomics. *Nature*, **422,** 198–207 (2003).

(*7*) Korevaar, P. A., George, S. J., Markvoort, A. J., Smulders, M. M. J., Hilbers, P. A. J., Schenning, A. P. H. J., De Greef, T. F. A., Meijer, E. W. Pathway complexity in supramolecular polymerization. *Nature*, **481,** 492–496 (2012).

(*8*) Mullen, D. G., Fang, M., Desai, A., Baker, J. R., Orr, B. G., Banaszak-Holl, M. M. A quantitative assessment of nanoparticle-ligand distributions: Implications

for targeted drug and imaging delivery in dendrimer conjugates. *ACS Nano*, **4,** 657–670 (2010).

(*9*) Howes, P. D., Chandrawati, R., Stevens, M. M. Colloidal nanoparticles as advanced biological sensors. *Science*, **346,** 1247390-1-1247390–10 (2014).

(*10*) Peer, D., Karp, J. M., Hong, S., Farokhzad, O. C., Margalit, R., Langer, R. Nanocarriers as an emerging platform for cancer therapy. *Nat. Nanotechnol*, **2,** 751–760 (2007).

(*11*) Nel, A. E., Mädler, L., Velegol, D., Xia, T., Hoek, E. M. V., Somasundaran, P., Klaessig, F., Castranova, V., Thompson, M. Understanding biophysicochemical interactions at the nano-bio interface. *Nat. Mater,* **8,** 543–557 (2009).

(*12*) Volpi, N., Linhardt, R. J. High-performance liquid chromatography-mass spectrometry for mapping and sequencing glycosaminoglycan-derived oligosaccharides. *Nat. Protoc*, **5,** 993–1004 (2010).

(*13*) Ow, H., Larson, D. R., Srivastava, M., Baird, B. A., Webb, W. W., Wiesner, U. Bright and stable core-shell fluorescent silica nanoparticles. *Nano Lett,* **5,** 113–117 (2005).

(*14*) Herz, E., Ow, H., Bonner, D., Burns, A., Wiesner, U. Dye structure–optical property correlations in near-infrared fluorescent core-shell silica nanoparticles. *J. Mater. Chem*, **19,** 6341 (2009).

(*15*) Ma, K., Werner-Zwanziger, U., Zwanziger, J., Wiesner, U. Controlling growth of ultrasmall sub-10 nm fluorescent mesoporous silica nanoparticles. *Chem. Mater*, **25,** 677–691 (2013).

(*16*) Ma, K., Zhang, D., Cong, Y., Wiesner, U. Elucidating the Mechanism of Silica Nanoparticle PEGylation Processes Using Fluorescence Correlation Spectroscopies. *Chem. Mater*, **28,** 1537–1545 (2016).

(*17*) Ma, K., Mendoza, C., Hanson, M., Werner-Zwanziger, U., Zwanziger, J., Wiesner, U. Control of Ultrasmall Sub-10 nm Ligand-Functionalized Fluorescent Core-Shell Silica Nanoparticle Growth in Water. *Chem. Mater*, **27,** 4119–4133 (2015).

(*18*) Yoo, B., Ma, K., Wiesner, U., Bradbury, M. Expanding analytical tools for characterizing ultrasmall silica-based nanoparticles. *RSC Adv*, **7,** 16861–16865 (2017).

(*19*) Widengren, J., Schwille, P. Characterization of Photoinduced Isomerization and Back-Isomerization of the Cyanine Dye Cy5 by Fluorescence Correlation Spectroscopy. *J. Phys. Chem. A*, **104,** 6416–6428 (2000).

(*20*) Chmyrov, V., Spielmann, T., Hevekerl, H., Widengren, J. Trans-Cis isomerization of lipophilic dyes probing membrane microviscosity in biological membranes and in live cells. *Anal. Chem*, **87,** 5690–5697 (2015).

(*21*) Burns, , J. Vider, Ow, H., Herz, E., Penate-medina, O., Baumgart, M., Larson, S. M., Wiesner, U., Bradbury, M. Fluorescent Silica Nanoparticles with Efficient Urinary Excretion for Nanomedicine. *Nano Lett*, **9,** 442–448 (2009).

(*22*) Jain, R. K., Stylianopoulos, T. Delivering nanomedicine to solid tumors. *Nat. Rev. Clin. Oncol*, **7,** 653–664 (2010).

(*23*) Jiang, W., Kim, B. Y. S., Rutka, J. T., Chan, W. C. W. Nanoparticle-mediated cellular response is size-dependent. *Nat. Nanotechnol*, **3,** 145–150 (2008).

(*24*) Kim, , B. L. Farmer, , Y. G. Yingling, H. S. Effect of Graphene Oxidation Rate on Adsorption of Poly-Thymine Single Stranded DNA. *Adv. Mater. Interfaces*, **4,** 1601168 (2017).

(*25*) Peerless, J. S., Bowers, G. H., Kwansa, A. L., Yingling, Y. G. Effect of C60 adducts on the dynamic structure of aromatic solvation shells. *Chem. Phys. Lett*, **678,** 79–84 (2017).

(*26*) Zhao, Y., Qi, X., Ma, J., Song, L., Yang, Y., Yang, Q. Interface of polyimide–silica grafted with different silane coupling agents: Molecular dynamic simulation. *J. Appl. Polym. Sci*., **135,** 45725 (2018).

(*27*) Manning, J. R. H., Yip, T. W. S., Centi, A., Jorge, M., Patwardhan, S. V. An Eco-Friendly, Tunable and Scalable Method for Producing Porous Functional Nanomaterials Designed Using Molecular Interactions. *ChemSusChem*, **10,** 1683–1691 (2017).

(*28*) Roscioni, O. M., Muccioli, L., Mityashin, A., Cornil, J., Zannoni, C. Structural characterization of alkylsilane and fluoroalkylsilane self-assembled monolayers on SiO2 by molecular dynamics simulations. *J. Phys. Chem. C*, **120,** 14652–14662 (2016).

(*29*) Cruz-Chu, E. R., Aksimentiev, A., Schulten, K. Water-silica force field for simulating nanodevices. *J. Phys. Chem. B*, **110,** 21497–21508 (2006).

(*30*) Widengren, J., Rigler, R., Mets, Ü. Triplet-state monitoring by fluorescence correlation spectroscopy. *J. Fluoresc*, **4,** 255–258 (1994).

(*31*) Kao, T., Kohle, F., Ma, K., Aubert, T., Andrievsky, A., & Wiesner, U. Fluorescent silica nanoparticles with well-separated intensity distributions from batch reactions. *Nano Lett.*, **18,** 1305–1310 (2018).

(*32*) Case, D. A., Wang, J., Wolf, R. M., Caldwell, J. W., Kollman, P. A., Case, D. A. AMBER (2017).

(*33*) Emami, F. S., Puddu, V., Berry, R. J., Varshney, V., Patwardhan, S. V., Perry, C. C., Heinz, H. Force Field and a Surface Model Database for Silica to Simulate Interfacial Properties in Atomic Resolution. *Chem. Mater.*, **26,** 2647–2658 (2014).

(*34*) Accelrys Software Inc., Discovery Studio Visualizer 4.0 (2013).

(*35*) Wang, J., Wolf, R. M., Caldwell, J. W., Kollman, P. A., Case, D. A., Development and Testing of a General AMBER Force Field. *J. Comput. Chem.* **25,** 1157–1174 (2004).

(*36*) Lopes, P. E. M., Murashov, V., Tazi, M., Demchuk, E., & MacKerell, A. D. Development of an empirical force field for silica. Application to the quartz-water interface. *J. Phys. Chem. B*, **110,** 2782–2792 (2006).

(*37*) Vanquelef, E., Simon, S., Marquant, G., Garcia, E., Klimerak, G., Delepine, J. C., Cieplak, P., Dupradeau, Y. F. R.E.D. Server: a web service for deriving RESP and ESP charges and building force field libraries for new molecules and molecular fragments. *Nucl. Acids Res*, **39,** W511–W517 (2011).

(*38*) Jorgensen, W. L., Chandrasekhar, J., Madura, J. D., Impey, R. W., Klein, M. L. Comparison of Simple Potential Functions for Simulating Liquid Water. *J. Chem. Phys*. **79,** 926–935 (1983).

(*39*) Li, P., Song, L. F., Merz, K. M. Systematic Parameterization of Monovalent Ions Employing the Nonbonded Model. *J. Chem. Theory Comput*, **11,** 1645–1657 (2015).

(*40*) Ryckaert, J.-P., Ciccotti, G., Berendsen, H. J. Numerical integration of the cartesian equations of motion of a system with constraints: molecular dynamics of n-alkanes. *J. Comput. Phys*, **23,** 327–341 (1977).

(*41*) Roe, D. R. , Cheatham, T. E. III, PTRAJ and CPPTRAJ: Software for Processing and Analysis of Molecular Dynamics Trajectory Data". *J. Chem. Theory Comput*, **9,** 3084–3095 (2013).

APPENDIX B

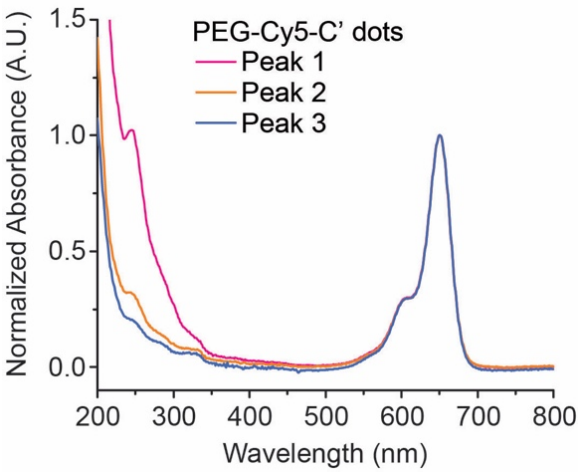

Figure S3.1: UV/Vis spectra of peak 1 (pink), peak 2 (orange), and peak 3 (blue), collected from HPLC fractionation.

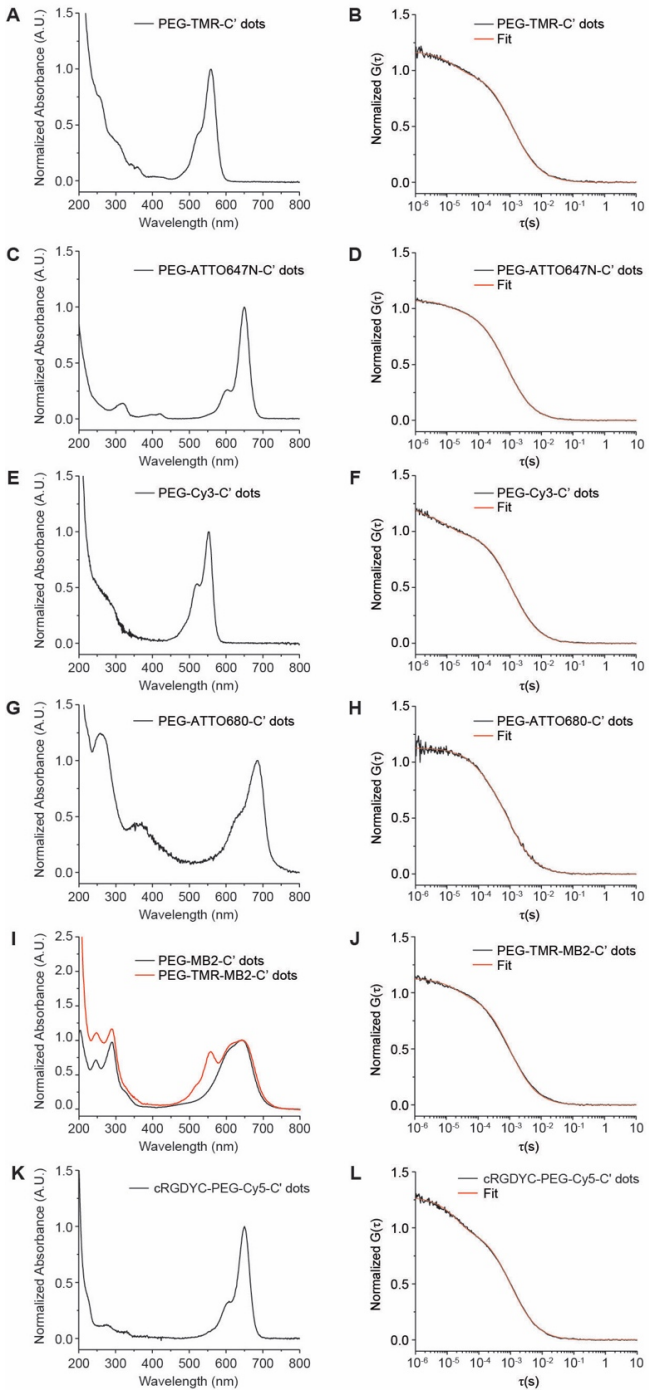

Figure S3.2: (A) & **(B)** UV/Vis spectrum and FCS correlation curve of PEG-TMR -C' dots. **(C)** & **(D)** UV/Vis spectrum and FCS correlation curve of PEG- ATTO647N -C' dots. **(E)** & **(F)** UV/Vis spectrum and FCS correlation curve of PEG-Cy3-C' dots. **(G)** & **(H)** UV/Vis spectrum and FCS correlation curve of PEG-ATTO680-C' dots. **(I)** & **(J)** UV/Vis spectrum and FCS correlation curve of PEG-TMR-MB2-C' dots. **(K)** & **(L)** UV/Vis spectrum and FCS correlation curve of cRGDyC-PEG-Cy5-C' dots.

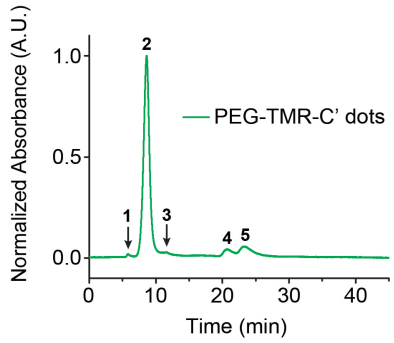

Figure S3.3: GPC chromatogram of native synthesis solution of PEG-TMR-C' dots collected at 550nm to measure dye incorporation. Peak labels correspond to Table S3.2.

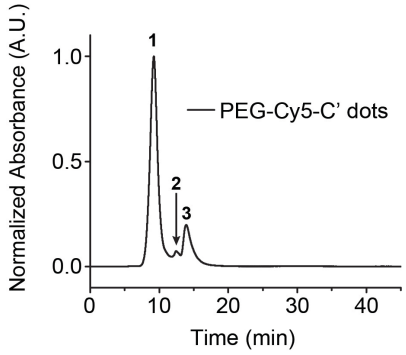

Figure S3.4: GPC chromatogram of native synthesis solution of PEG-Cy5-C' dots collected at 647nm to measure dye incorporation. Peak labels correspond to Table S3.3.

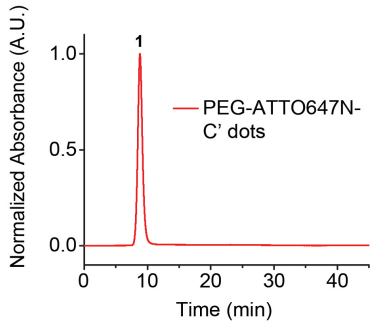

Figure S3.5: GPC chromatogram of native synthesis solution of PEG-ATTO647N-C' dots collected at 647nm to measure dye incorporation.

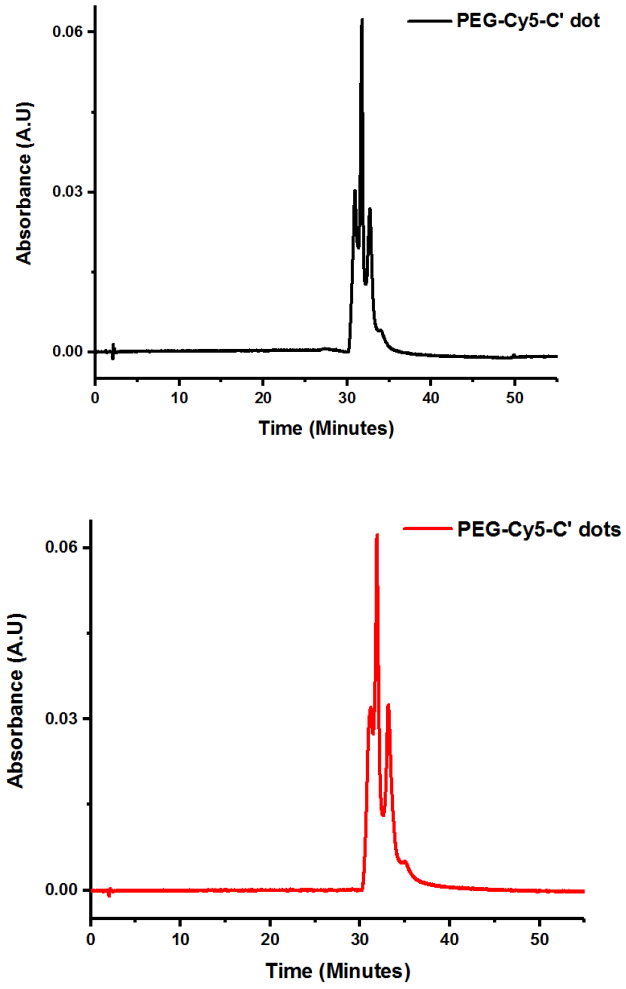

Figure S3.6: (A) representative chromatogram of PEG-Cy5-C' dots with no post processing done i.e, baseline subtraction, **(B)** the same chromatogram with baseline subtraction applied.

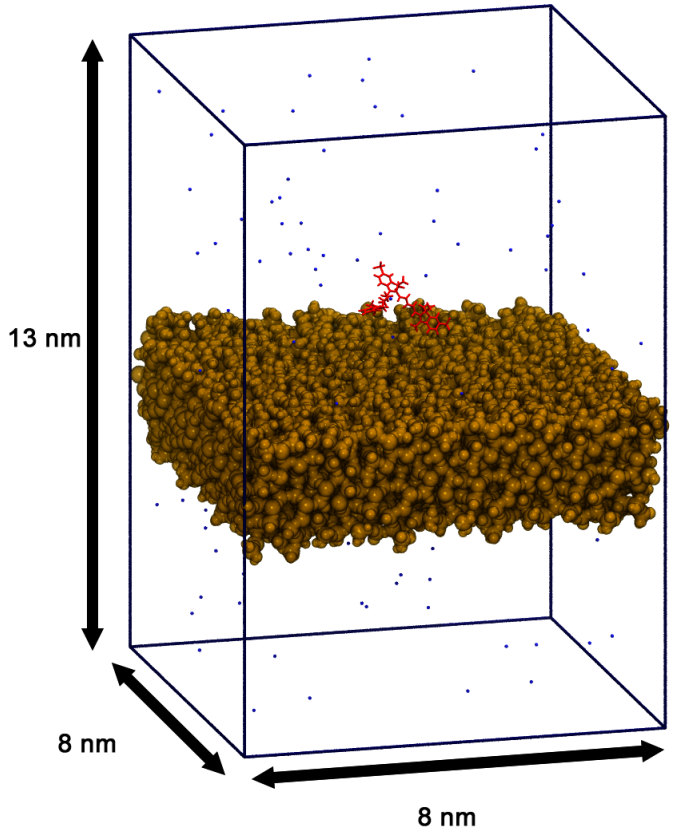

Figure S3.7: Representative system of silica surface-dye MD simulations as-constructed, composed of water (not shown for clarity), amorphous SiO_2 (brown), Cy5 maleimide (red), and ammonium ions (blue). In other systems, Cy5 maleimide is replaced with the dye of interest, with or without attached silane unit.

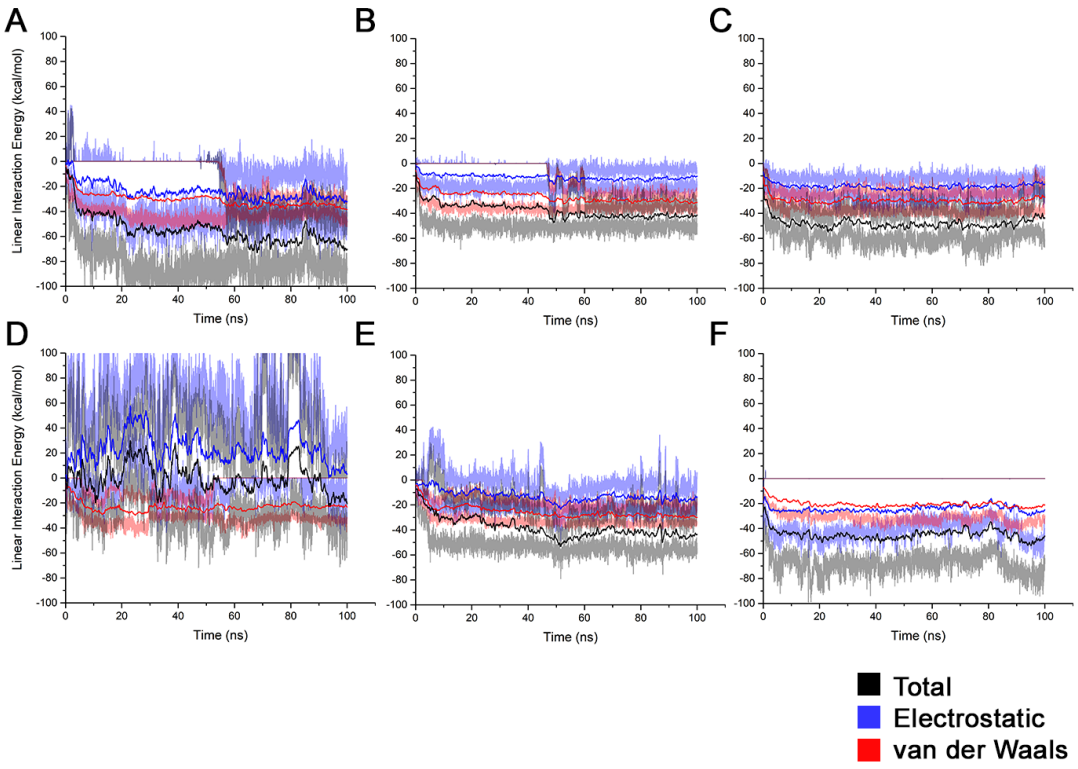

Figure S3.8 (A-F): Linear interaction energy between silica surface and dye silanes over the entirety of the production simulations. Solid lines denote average of five simulations with random starting dye orientation, transparent lines indicate maximum and minimum of five simulations with random starting dye orientation. (A-C) 1% deprotonated silica surface, (D-F) 15% deprotonated silica surface. (A,D) Cy5, (B,E) TMR, and (C,F) ATTO647N.

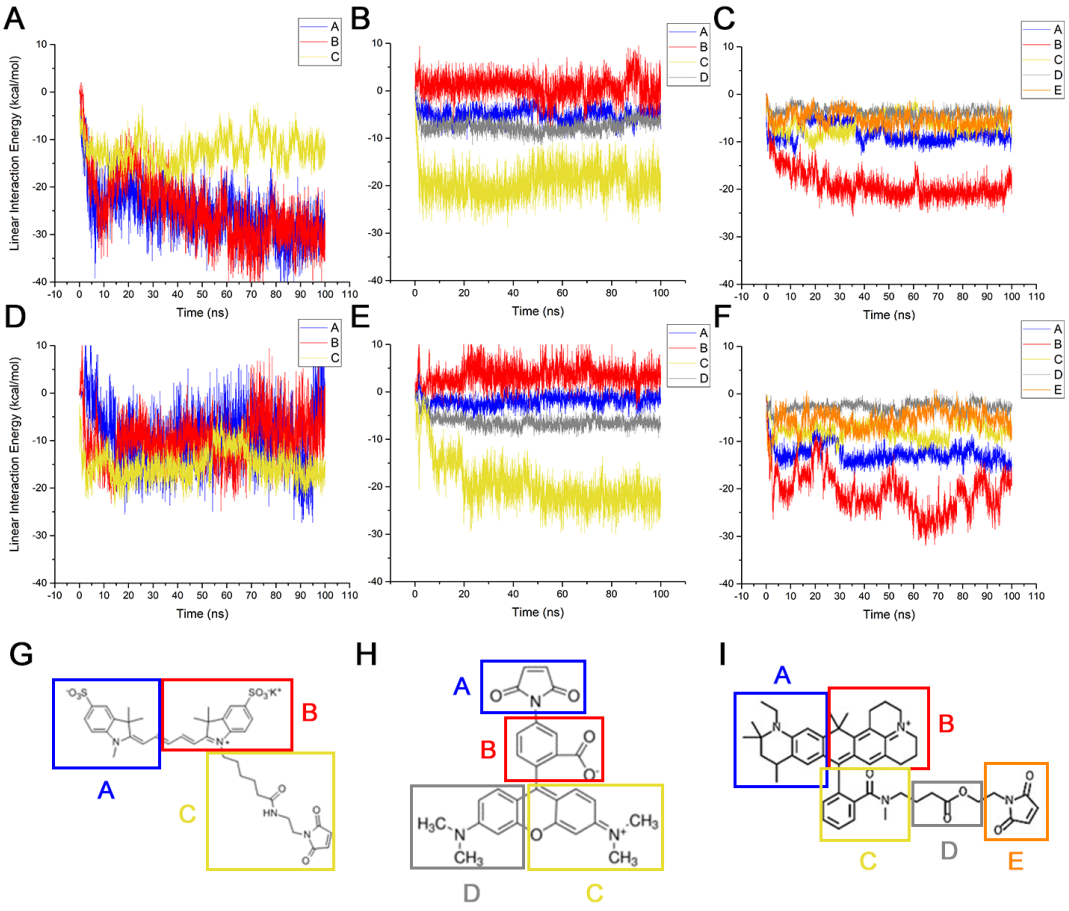

Figure S3.9: (A-F) Linear interaction energies between silica surface and specific groups of maleimide dye atoms. (A-C) 1% deprotonated silica surface, (D-F) 15% deprotonated silica surface. (A,D) Cy5, (B,E) TMR, and (C,F) ATTO647N. **(G-I)** Illustrations of atom groupings for Cy5 (G), TMR (H), and ATTO647N (I), respectively. Group interactions highlight how the charged sections of the dye molecule dominate interactions with the silica surface.

Sample	Diameter (nm)	Dyes/Particle (#)	Photoisomerization *P* (%)	Brightness/Dye (kHz)
Cy5 (free dye)	1.3	1.0	43.2	7881
PEG-Cy5-C' dots	5.8	1.6	35.2	17443
PEG-Cy5-C' dots Peak 1	5.6	1.5	33.2	18203
PEG-Cy5-C' dots Peak 2	5.8	2.0	37.8	14203
PEG-Cy5-C' dots Peak 3	5.7	2.3	41.3	12424
PEG-TMR-C' dots	6.4	3.6	-	-
PEG-ATTO647N-C' dots	6.2	2.0	-	-
PEG-ATTO680-C' dots	7.0	1.4	-	-
PEG-MB2-C' dots	4.3	2.6	-	-
cRGDyC-PEG-Cy5-C' dots	6.1	2.1	-	-

Table S3.1: Particle size and dyes per particle of the various C' dots used in the study. For samples subjected to fluorescence correlation spectroscopy (FCS), photoisomerization and brightness per dye is also tabulated.

Peak Number	Retention Time (min)	Area (%)
1	5.784	0.59
2	8.622	82.08
3	10.477	5.68
4	20.704	4.22
5	23.231	7.42

Table S3.2: Peak integration areas and retention times for native synthesis solution of PEG-TMR-C' dots shown in Figure S3.3 as determined by Empower3 software using the ApexTrack peak detection algorithm. Corresponding peaks are labeled in Figure S3.3.

Peak Number	Retention Time (min)	Area (%)
1	9.037	62.11
2	11.946	7.45
3	13.412	30.44

Table S3.3: Peak integration areas and retention times for native synthesis solution of PEG-Cy5-C' dots shown in Figure S3.4 as determined by Empower3 software using the ApexTrack peak detection algorithm. Corresponding peaks are labeled in Figure S3.4.

Peak Number	Retention Time (min)	Area (%)
1	8.87	100

Table S3.4: Peak integration area and retention time for native synthesis solution of PEG-ATTO647N-C' dots shown in Figure S3.5 as determined by Empower3 software using the ApexTrack peak detection algorithm.

Peak Number	Retention Time (min)	Area (%)
1	30.940	27.68
2	31.779	37.70
3	32.725	28.65
4	33.785	5.96

Table S3.5: Peak integration areas as determined with ApexTrack integration in Empower 3 for the HPLC chromatogram of PEG-Cy5-C' dots as shown in Figure 3.1B.

CHAPTER 4

DESIGNING PEGYATED AND FUNCTIONALIZED SUB-10 NM SILICA METHYLENE BLUE NANOPHOTOSENSITIZERS[*]

Abstract

Photodynamic therapy (PDT) presents an alternative non-invasive therapeutic modality for the treatment of cancer and other diseases. PDT relies on cytotoxic singlet oxygen that is locally generated through energy transfer between a photosensitizer and molecularly dissolved triplet oxygen. To minimize side-effects, *i.e.* damage of healthy tissue, targeted delivery to places of disease, high local photosensitizer concentrations, high singlet oxygen quantum yield, and rapid post-treatment clearance of photosensitizers are desired. Ultrasmall (sub-10 nm) organic-inorganic hybrid silica nanoparticles loaded with photosensitizer molecules, referred to as silica nanophotosensitizers (SNPSs), present a way to meet these requirements. Here, we investigate two different particle designs of ultrasmall poly(ethylene glycol) coated (PEGylated) SNPSs covalently binding the methylene blue derivate MB2. In the first approach (design one), MB2 is encapsulated into the silica matrix, while in the second approach (design two), MB2 is grafted on the particle surface in between chains of the stabilizing PEG corona. We compare both cases with regard to their singlet oxygen quantum yields, Φ_{Δ}, with the effective Φ_{Δ}^{eff} per particle reaching 111% and 161% for

[*] Ferdinand F. E. Kohle, Songying Li, Ulrich B. Wiesner. Designing PEGyated and Functionalized Sub-10 nm Silica Methylene Blue Nanophotosensitizers. Manuscript in preparation.

design one and two, respectively. Finally, we show that both particle designs allow functionalization with a targeting peptide, c(RGDyC), rendering SNPSs a promising platform for medical applications.

Introduction

Photodynamic therapy (PDT) emerged as a minimally invasive and minimally toxic therapeutic modality for the treatment of cancer and other diseases (*1*). The principle of PDT can generally be described in four steps: A photosensitizer (PS) is localized around diseased tissue (step 1), and activated by a light source (step 2). The absorbed photon energy leads to the generation of highly reactive singlet oxygen, $^1O_2$ (step 3), causing oxidative stress and cellular damage, eventually initiating cell death mechanisms such as necrosis and/or apoptosis in the local environment of the PS (step 4) (*2*). These steps impose chemical, photophysical, and structural requirements onto PDT probes.

Photophysical requirements: A PS has unique photophysical characteristics. Generation of $^1O_2$ is catalyzed by photoexcitation of the PS. Figure 4.1A depicts a simplified Jablonski scheme illustrating the photophysical processes leading to $^1O_2$ generation. From an electronically excited singlet state the PS undergoes a forbidden electron spin-flip (intersystem crossing, ISC) into an energetically lower lying excited triplet state, ^{3}PS*. From here, ^{3}PS* relaxes into the singlet ground state, ^{1}PS, via energy transfer (ET) with dissolved molecular triplet oxygen, $^3O_2$, yielding cytotoxic reactive singlet oxygen, $^1O_2$. High intersystem crossing rates (k_{ISC}) and long triplet state lifetimes ($\tau_T > 1$ μs) of the PS promote $^1O_2$ generation, which is reflected in high singlet oxygen quantum yields, Φ_Δ (*3*). An ideal PS should have a molar extinction coefficient of $\varepsilon \geq 50\ 000\ M^{-1}\ cm^{-1}$ (*3, 4*) in the therapeutic window of ~600–1200 nm (*5*) and a singlet oxygen quantum yield of $\Phi_\Delta \geq 0.5$ (*4*). In addition, high photostability, as well as low phototoxicity in the dark are desired.

Chemical requirements: Besides the general requirement of a PDT probe to be non-toxic itself, a key challenge is its localization at a specific site of interest. Singlet oxygen is highly reactive, and locally produced by the PS. Typical diffusion lengths of singlet oxygen in tissue before it reacts are on the order of tens of nanometers (*6*). Therefore, to minimize damage of healthy tissue, selective targeting is crucial. Since most PS molecules are hydrophobic and prone to aggregation in physiological environments, low selectivity towards diseased tissue and adverse pharmacokinetics have hindered their clinical translation (*7, 8, 4*). Nanoparticles (NPs) as PS delivery vehicles can promote solubility, overcome aggregation issues to improve pharmacokinetics, and protect PSs from enzymatic degradation (*9, 10*). Furthermore, NP surface functionalization with targeting moieties reduces systemic side effects, increases the therapeutic concentration of PSs at the target site, and gives room for multi-modality platforms simultaneously enabling diagnosis, imaging, and treatment (*10*). However, while NP-based PS systems help overcome shortages associates with the PS molecules, they themselves impose additional requirements.

Structural requirements: First, since PSs are bound to NPs and don't have to be released, it is essential that oxygen species can easily diffuse to and away from the PS molecule. Second, after NPs have targeted the site of interest and PDT has been performed (or if the NPs have failed to target the site of disease in the first place) it is essential that they are rapidly cleared from the body to reduce potential side effects (principle of *target-or-clear* (*11*)). Both of these requirements favor small hydrodynamic diameters leading to rapid renal clearance via the kidneys with a cutoff for spherical NPs below 10 nm hydrodynamic diameter (*12*).

Different NP-based systems, organic, inorganic, and organic-inorganic hybrid, have been described in the literature, including PEGylated liposomes, polymeric NPs, iron oxide NPs, or gold NPs (*13-16*). While numerous NPs systems are able to load large amounts of PS molecules, few NP platforms combine the necessary ease of chemical functionalization with precise particle size control on the sub-10 nm length scale, to meet stringent requirements for successful clinical translation and synthesis scale-up (*17-19*). While metal-organic framework NPs in principle offer these capabilities, targeted delivery and systematic *in vitro* and *in vivo* studies on NP activity and fate demonstrating favorable characteristics are still lacking (*20*).

Ultrasmall organic-inorganic hybrid silica nanoparticles (SNPs) meet these requirements today. It has been demonstrated in first published human clinical trials that fluorescent sub-10 nm PEGylated and functionalized SNPs efficiently target and clear from the human body (*21, 22*). In addition, the chemical inertness, optical transparency of silica, and cost-effective water-based synthesis paired with exceptional size and structural control on the sub-nanometer length scale, insusceptibility to swelling due to pH changes, and high silica matrix porosity render such particles ideal candidates for PDT (*17, 23-26*).

Here, we introduce ultrasmall sub-10 nm organic-inorganic hybrid SNPs covalently binding the PS dye MB2, a derivate of methylene blue (MB) (Figure 4.1B and Figure S4.1). In the following we will refer to these particles as silica nanophotosensitizers (SNPSs). MB is a PS molecule that is FDA-approved and has been used in photodynamic therapy (*27, 28*), due to its high singlet oxygen quantum yield and extinction coefficient in the near infrared ($\Phi_\Delta \approx 0.5$, $\varepsilon = 10^5$ M^{-1} cm^{-1} at 664 nm).

Despite earlier attempts to synthesize MB containing SNPs, to the best of our knowledge sub-10 nm functionalized SNPs covalently binding MB have not been reported to date (*9, 29, 30*).

We demonstrate two different SNPS designs (Figure 4.1C). In design one, MB2 is encapsulated within the silica network of an ultrasmall poly(ethylene glycol) coated (PEGylated) SNP; in design two, MB2 is grafted onto the SNP surface, inserted between the PEG corona chains. In both cases the PS molecules are covalently bound to the SNPSs via a thiol-Michael addition click reaction between maleimide functionalized MB2 and (3-mercaptopropyl)trimethoxysilane (MPTMS). We show that both particle types can be further functionalized with the $\alpha_v\beta_3$ integrin-targeting cyclic(arginine-glycine-aspartic acid-D-tyrosine-cysteine) peptide (cRGDyC, Figure 4.1D). Photosensitizing action is successfully demonstrated using the singlet oxygen sensor 1,3-diphenylisobenzofuran (DPBF, inset Figure 4.3A). We demonstrate effective per particle singlet oxygen quantum yields of 111% (design one) and 161% (design two), respectively.

Materials and Methods

Materials

Aluminum-tri-sec-butoxide (ASB), (3-aminopropyl)triethoxysilane (APTES), ammonium hydroxide (28 wt% in H_2O), ammonia solution (2.0 M in ethanol), dimethyl sulfoxide (DMSO), 1,3-diphenylisobenzofuran (DPBF, 97%), hydrochloric acid (HCl, 0.5018 N in H_2O), (3-iodopropyl)trimethoxysilane (IPTMS), methylene blue (MB), (3-mercaptopropyl) trimethoxysilane (MPTMS), 2-propanol (anhydrous 99.5%), and tetramethyl orthosilicate (TMOS) were purchased from Sigma Aldrich. (3-aminopropyl)trimethoxysilane (APTMS) and methoxy-terminated poly(ethylene glycol) (PEG-silane, molar mass of ~0.5 kg/mol) were purchased from Gelest. Heterobifunctional PEG (NHS-PEG-mal, molar mass of ~960 g/mol) was purchased from Quanta BioDesign. ATTO MB2-maleimide was purchased from ATTO-Tec. Tetramethylrhodamine-5-maleimide (TMR) was purchased from AnaSpec. Ethanol (absolute anhydrous 99.5%) was purchased from Pharmco-Aaper. c(RGDyC) was purchased from Peptide International. Deionized (DI) water (18.2 MΩ·cm) was generated using a Millipore Milli-Q system. All chemicals were used as received.

Synthesis of nanophotosensitizers (design one)

First, 3.67×10^{-7} moles MB2 with a maleimide group are reacted with MPTMS in DMSO at a molar ratio of 1:25 (fluorophore:MPTMS) to generate a MB2-silane conjugate. To synthesize sub-10 nm PEGylated SNPs with MB2 inside the silica core, 2 mL of 0.02 M ammonia aqueous solution is first added into 8 mL of DI water yielding

a pH of ~9. The solution is then stirred at room temperature for 5 min. As the silica precursor, 0.43 mmol of TMOS are added under vigorous stirring, followed by the addition of all MB2-silane. The molar ratio of MB2-silane to TMOS is about 1:1000. The solution is left stirring at room temperature overnight. Then, 0.21 mmol of PEG-silane are added and the solution is kept stirring at room temperature overnight. Finally, to promote covalent bond formation between PEG-silane and particles, stirring is stopped and the particle dispersion is heated to 80 °C for 8 hours. To remove any unreacted precursors, aggregates, or dust from the particle dispersion, particles are transferred into a dialysis membrane tube (molecular weight cutoff, MWCO = 10,000), and dialyzed in 2 L of DI water with three water exchanges every 8 hours. After dialysis, the dispersion is subject to syringe filtration (0.2 μm, Fisherbrand) and finally up-concentrated for gel permeation chromatography (GPC) using a membrane spin filter (GE Healthcare, molecular weight cutoff = 30,000) and a centrifuge at 2300 rpm.

Synthesis of nanophotosensitizers (design two)

Particles binding MB2 to the particle surface are synthesized according to the synthesis of design one (excluding the addition of MB2-silane, or replacing MB2 with TMR-maleimide, see main text). MB2 is added to the final silica particles by using the method of post-PEGylation surface modifications by insertion (PPSMI) (*24*). To that end, MPTMS is added to the PEGylated particle dispersion under vigorous stirring at a concentration of 2.3 mM. The particle/MPTMS mixture is stirred at room temperature overnight, followed by the addition of 3.67×10^{-7} moles MB2-maleimide at a concentration of 37 μM. The solution is vigorously stirred at room temperature for 24

hours for the dye to react with the thiol group on the silica core surface of the particles. Afterwards, the particle dispersion is subjected to the same cleaning process as described before (dialysis, syringe filtration, GPC). Particles containing TMR on the surface were synthesized in the same way by replacing MB2-maleimide with TMR-maleimide.

Targeting peptide c(RGDyC) functionalization

Particles were peptide-functionalized with c(RGDyC)-PEG-silane (Supplementary Figure S4.3 in Appendix C). c(RGDyC)-PEG-silane was prepared by exploiting the mercapto group of cysteine of c(RGDyC) (Figure 4.1D) to click to the maleimide group of a heterobifunctional mal-PEG-NHS first, and then clicking the NHS to the amine group of (3-aminopropyl)trimethoxysilane (APTES). The concentration of NHS ester-PEG-maleimide in DMSO was 0.23 M. The mixed solution was left at room temperature in the glovebox for 3 hours to form silane-PEG-maleimide. After that, c(RGDyC) was added and the solution left at room temperature in the glovebox overnight to produce c(RGDyC)-PEG-silane. The molar ratio c(RGDyC):NHS-PEG-mal:APTES was 1.0:1.0:0.9. In order to functionalize particles with c(RGDyC) peptide ligands, previously prepared c(RGDyC)-PEG-silane was added to the particle dispersion immediately before the addition of PEG-silane. The remainder of the synthesis and purification protocol is as described before.

Gel permeation chromatography

To remove unreacted precursors from the native particle dispersion, samples were purified using gel permeation chromatography (GPC). A BioLogic LP system with 275 nm UV detector and cross-linked copolymer of allyl dextran and N,N'-methylene bisacrylamide (Sephacryl S-300 HR, GE Healthcare) as solid phase was used. Before GPC purification each sample was up-concentrated with centrifuge spin-filters (Vivaspin with MWCO 30k, GE Healthcare) to an approximate sample volume of 600 µL, run through the column with a 0.9 wt% NaCl solution, and fraction-collected by a BioFrac fraction collector. Sample fractions were transferred to DI water by washing samples five times with centrifuge spin-filters. The resulting particles could be subjected to long-term storage in nitrogen bubbled DI water in the dark at 4 °C.

Steady-state absorption spectroscopy

Absorbance spectra were measured on a Varian Cary 5000 spectrophotometer. Spectra were measured in DI water using a quartz cuvette (HellmaAnalytics) with a 10 mm light path, and baseline corrected using a second cuvette with pure DI water as a reference cell. All spectra were measured in 1 nm increments and peak intensities were kept between 0.01 and 0.06.

Fluorescence correlation spectroscopy

A homebuilt confocal fluorescence correlation spectroscopy (FCS) setup was used to determine particle hydrodynamic diameter, solution concentration, and number of dye molecules per particle. Particles containing TMR dye were excited with a 543 nm HeNe laser, that was focused by a water immersion microscope objective (Zeiss

Plan-Neofluar 63x NA 1.2). The fluorescence signal passed through a 50 μm pinhole and a long pass filter (ET560lp, Chroma) before being detected by an avalanche photo diode (APD) detector (SPCM-AQR-14, PerkinElmer) and auto-correlated with a digital correlator (Flex03LQ, Correlator.com). Data was fitted using a non-linear least-squares Levenberg-Marquardt algorithm and a triplet corrected correlation function, G(τ), shown in equation (1):

$$G(\tau) = 1 + \frac{1}{N_m}\left(\frac{1}{1+\tau/\tau_D}\right)\left(\frac{1}{1+\tau/(\tau_D\kappa^2)}\right)^{1/2}\frac{1}{(1-T)}(1-T + T\exp(\tau/\tau_T)) \quad (1)$$

Where τ is the lag time, N_m the time- and spaced-averaged number of TMR labeled particles in the FCS observation volume, that is defined by a structure factor $\kappa = \omega_z/\omega_{xy}$ with radial (ω_{xy}) and axial (ω_z) radii. τ_D is the time that a particle takes to diffuse through the observation volume. T is the fraction of TMR molecules being in the triplet state, with a triplet relaxation time, τ_T. FCS correlation curves were normalized using equation (2):

$$G(\tau) = (G(\tau) - 1)\, N_m \quad (2)$$

All samples were measured in 35 mm glass bottom dishes (P35G-1.5-10-C, Mattek Corporation) at nanomolar concentration in DI water at 20 °C, 5 kW cm^{-2} laser power, and in triplets with five 30 s long collection intervals. The observation volume was calibrated before each FCS measurement. Particle diameters, d, were calculated using

the Stokes-Einstein equation (3) with the diffusion constant, D, obtained from equation (4):

$$d = 2\frac{k_B T}{6\pi\eta D} \tag{3}$$

$$D = \frac{\omega_{xy}{}^2}{4\tau_D} \tag{4}$$

The number of TMR or MB2 molecules per particle, n_m, was determined by comparing the dye concentration from steady state absorption spectroscopy, C_{Abs}, and the particle concentration measured in FCS, $\langle C \rangle_{FCS}$, using equation (5):

$$n_m = \frac{C_{Abs}}{\langle C \rangle_{FCS}} \tag{5}$$

where it was assumed that the molar extinction coefficients do not change upon dye encapsulation.

Determination of singlet oxygen quantum yields

Singlet oxygen quantum yield, Φ_Δ, measurements were carried out in ethanol with 1,3-diphenylisobenzofuran (DPBF) as a detector molecule for trapping singlet oxygen. The generation of singlet oxygen could be observed by a reduction of the DPBF absorption band at 410 nm (Figure 4.3A). Measurements were carried out at sample optical densities of 0.15 – 0.50 in a 100 µL quartz cuvette (Starna). Samples were evenly exposed to a 635 nm, expanded, and collimated laser beam of a solid-state laser (Power Technology Inc.) at 3 mW/cm^2 with a spot size of about 1 cm in the same cell. To acquire a 0.5 - 0.6 absorption, DPBF was added at a concentration of approximately 18.75 µM. All absorption spectra were measured in 1 nm steps and baseline-corrected

against a second cuvette with ethanol as a reference cell. The sample absorption was recorded at defined time intervals and corrected for the sample absorption spectrum in the absence of DPBF. Φ_Δ was calculated by comparing all samples to the standard methylene blue (MB) dye with known singlet oxygen quantum yield of $\Phi_\Delta = 0.52$ (in ethanol) (31) by plotting the natural logarithm of the reduction of the 410 nm DBPF band against the exposure time and using equation (6), where m represents the slope of a linear fit through the data points (Figure 4.3B):

$$\Phi_\Delta(sample) = \Phi_\Delta(MB)\frac{m(sample)}{m(MB)} \quad (6)$$

To determine the effective singlet oxygen quantum yield, Φ_Δ^{eff}, the particle concentration as determined by FCS and the MB concentration were matched.

Results and Discussion

Silica nanophotosensizers (SNPSs) covalently encapsulating the methylene blue derivate MB2 inside the particle (design one, Figure 4.1C) were synthesized by combining tetramethylorthosilcate (TMOS) and MB2-silane (Figure 4.1B) in basic aqueous solution. After particle formation, further particle growth was quenched by the addition of PEG-silane (Figure 4.1B) to the reaction mixture. Particles containing MB2 on the particle surface (design two, Figure 4.1C) were synthesized in the same way, however, MB2 was attached using a grafting method referred to as post-PEGylation surface modification by insertion (PPSMI) (*24*). This method employs amine-reactive or sulfhydryl-reactive click chemistry, by adding amine-silanes or thiol-silanes, respectively, below the nucleation threshold into an aqueous dispersion of PEGylated SNPs. The small molar mass silane precursors diffuse through the PEG corona chains and react with the silica particle surface. The pending amine or thiol groups can further be reacted with N-hydroxysuccinimide or maleimide functional groups, respectively (*24*). For design two, we used (3-mercaptopropyl)trimethoxysilane (MPTMS) to functionalize the particle surface with thiol groups to click MB2-maleimide to the particle (for details see Materials and Methods). Finally, all particles were cleaned from unreacted precursors via gel permeation chromatography (GPC) prior to further characterization.

Due to the weakly-emissive nature of MB2 (Supplementary Figure S4.2 in Appendix C), fluorescen-based size determination of MB2 functionalized particles by fluorescence correlation spectroscopy (FCS) was not possible. To make particle samples accessible for the determination of hydrodynamic diameters and particle concentrations

by FCS, particles were further functionalized with the fluorescent dye tatramethylrhodamine-silane (TMR-silane) (Figure 4.1B). For design one we grafted TMR onto the particle surface using PPSMI and for design two we synthesized SNPs encapsulating TMR dye before MB2 was grafted on the particle surface. A combination of FCS and steady state absorption spectroscopy was used to determine the number of MB2 and TMR molecules per particle. Particle diameter and concentration were determined by measuring the fluorescence fluctuations of particles diffusing through a well-defined observation volume of a laser beam and subsequently auto-correlating the fluorescence time signal. The resulting FCS correlation curves were fitted with a correlation function (see equation (1), Materials and Methods) from which the time averaged number of particles and the diffusion constant were extracted. To determine the number of dyes per particle, the dye concentration as determined by steady-state absorption spectroscopy was compared to the concentration of the particles as determined by FCS (equation (5), Materials and Methods), yielding the average number of dyes per particle. For accurately determining the number of MB2 dyes per particle, it is necessary that every MB2 containing particle carries at least one TMR dye, a requirement that is not necessarily met. We accounted for that to the best possible degree by working with high concentrations of TMR. Dye molecules that were not covalently bound during synthesis were washed away by dialysis and separated from the particles by GPC. Supplementary Figure S4.4A and S4.4B in Appendix C show the GPC elugrams before and after TMR and MB2 surface functionalization of particles, respectively. Both elugram-pairs show a single peak and were congruent to each other,

indicating that TMR dye molecules (design one), or MB2 dye molecules (design two) were grafted onto the respective SNPs.

Figure 4.2A and 4.2B show the FCS correlation curves of the fluorescent particles containing the photosensitizer MB2. The curves were fitted using a triplet corrected translational diffusion correlation function (equation (1), Materials and Methods). Particle hydrodynamic diameters of 5.9 nm for MB2 encapsulating C' dots with TMR surface functionalization (TMR-PEG-MB2-C' dots), 5.2 nm for TMR encapsulating C' dots (PEG-TMR-C' dots), and 5.2 nm for TMR encapsulating C' dots with MB2 surface functionalization (MB2-PEG-TMR-C' dots) were obtained (a comprehensive nomenclature to describe C' dots is described in the supporting information of reference (*24*)). Figure 4.2C and 4.2D show the UV-vis absorption spectra of PEG-MB2-C' dots, TMR-PEG-MB2-C' dots, PEG-TMR-C' dots, and MB2-PEG-TMR-C' dots in water, respectively. For comparison, the absorption spectra of TMR-maleimide and MB2-maleimide are superimposed onto the particle spectra. For TMR-PEG-MB2-C' dots and MB2-PEG-TMR-C' dots, a TMR absorption peak can be observed indicating successful functionalization of particles with TMR and MB2, respectively.

Comparing the absorption profiles of MB2 for the two different designs, a relative hypsochromic shift (blue-shift) from 668 nm to 644 nm of the main peak for design one relative to free MB2 is observed that is absent in design two. This hypsochromic shift likely originates from dimethylation of the auxochrome groups of MB2, from $-N(CH_3)_2$ to $-NH(CH_3)$ and/or $-NH_2$, which is promoted in basic media (*32, 33*). In addition, both designs display a heightened left shoulder in the absorption peak

as compared to free MB2 dye that is more pronounced in design one than it is in design two. The heightened shoulders around 620 nm and 605 nm for design two and one, respectively, are a result of dimerization of MB2 at high concentrations (1×10^{-6} to 4×10^{-4} M) in aqueous media (MB2 concentrations during synthesis is $3.67\text{x}10^{-5}$ M) (*34*). MB monomers and dimers are known to have distinct absorption peaks located at 664 nm and 590 nm, respectively, with an equilibrium constant of $3.8\text{x}10^{3}$ M^{-1} in water (*35*). However, the formation of dimers is not only dependent on concentration but is additionally promoted by the presence of oppositely charged surfaces (*36*). For design one, the cationic MB2 sensitizer was added to the synthesis during the silica particles formation and hence was exposed to negatively charged silica nucleation seeds (at pH 9). For design two, MB2 was grafted onto the PEGylated silica particle surface at neutral conditions (pH 7), consequently showing no peak shift and relatively fewer MB2 dimers, despite the same MB2 concentration during the synthesis as for design one.

To determine the number of MB2 molecules per particle we compared the particle concentrations estimated by FCS and the MB2 concentrations from steady-state absorption measurements. For practical reasons, we assumed that the extinction coefficient remained unaffected in the particle synthesis. This is not necessarily true due to the metachromatic nature of methylene blue and demethylation. Based on this assumption we estimated the average number of dyes per particle (equation (5), Materials and Methods) to be 2.4/3.3 for MB2/TMR for design one and 3.4/2.3 for MB2/TMR for design two.

Next, we measured the singlet oxygen quantum yield, Φ_{Δ}, for both particle designs using the singlet oxygen sensor 1,3-diphenylisobenzofuran (DPBF). For these

measurements, we matched the particle concentrations as determined by FCS to yield an effective singlet oxygen quantum yield per SNPS (Φ_{Δ}^{eff} (SNPS)). Figure 4.3A demonstrates the principle of oxygen sensing using DPBF and the particle TMR-PEG-MB2-C' dots (design one) in ethanol. The mixture is evenly exposed to an expanded and collimated 635 nm laser beam for defined time intervals. The singlet oxygen that is generated by the SNPSs reacts with DPBF molecules, yielding 1,2-dibenzoylbenzene (*37*). The formation of 1,2-dibenzoylbenzene was monitored via a reduction of the absorption band at 410 nm. By comparing samples to a methylene blue standard (Φ_{Δ}(MB) = 0.52), Φ_{Δ}^{eff}(SNPS) was determined (see equation (6), Materials and Methods), resulting in values of 111% for design one (TMR-PEG-MB2-C' dots) and 161% for design two (MB2-PEG-TMR-C' dots). This translates to an estimated per dye singlet oxygen quantum yield of 46% and 47%, respectively, based on the estimated number of MB2 dyes per particle. The relatively lower values for Φ_{Δ} of the dyes associated with the particles versus free methylene blue dye can be rationalized by the steric shielding effects of encapsulation or grafting within the PEGylation corona. The silica network and/or the PEG molecules shield diffusing oxygen, first, from MB2, and then, from DPBF resulting in a reduced singlet oxygen quantum yield. Although for both designs the per dye Φ_{Δ} values are similar, surface grafted MB2 molecules are likely less shielded than dyes fully encapsulated in the silica network. In addition, it is known that methylene blue dimers and monomers engage in different photochemical processes. While monomers undergo energy transfer reaction with triplet oxygen, dimers engage in electron transfer reactions with other methylene blue molecules (*36*). These different energy dissipation pathways of dimers correlate negatively with the singlet oxygen

quantum yield contributing to the reduced singlet oxygen quantum yield per dye molecule of design one and design two (*38*). However, the multiplicity effect stemming from multiple MB2 molecules colocalized on one particle compensates for a reduced per dye singlet oxygen quantum yield by steric shielding and/or dimerization.

To exclude the possibility of $^1O_2$ formation in the absence of irradiation with light (dark toxicity) for the different particle designs, we repeated singlet oxygen quantum yield measurements, but did not expose the samples to the laser beam. Supplementary Figure S4.5 in Appendix C shows results of the same experiment as shown in Figure 4.3A for design one (PEG-MB2-C' dots). This time, the DPBF peak at 410 nm remains unchanged, however, indicating no formation of 1,2-dibenzoylbenzene and hence no generation of singlet oxygen. This is the case for both designs.

Specific targeting of photosensitizers to diseased tissue increases the efficacy of PDT and minimizes collateral damage to healthy tissue. We therefore functionalized SNPSs with the targeting moiety cyclo(arginine-glycine-aspartic acid-D-tyrosine-cysteine) (c(RGDyC)) (Figure 4.1C), which targets $\alpha_v\beta_3$ integrins overexpressed, e.g. on various cancer cells including melanoma (*22*). It has been shown that the endocytosis-mediated cellular uptake of c(RGDyC) functionalized particles correlates with the $\alpha_v\beta_3$-expression levels of cells (39, 40), and increases the intracellular particle concentration, rendering c(RGDyC) a specific targeting moiety with high affinity for the treatment of the melanoma cancer (*11, 41*).

Particles were functionalized by adding c(RGDyC)-PEG-silane (Supplemenatry Figure S4.3A in Appendix C) during the PEGylation step (for details see Materials and Methods) (23). To allow more steric freedom for ligand binding to integrins, the

c(RGDyC)-PEG-silane was chosen to be three ethylene oxide (EO) units longer than the PEG-silane (twelve versus six-nine units). Due to the weakly-fluorescent nature of MB2, a FCS analysis could not be conducted. Instead we compared the GPC elugrams before and after peptide functionalization for particle design one (PEG-MB2-C' dots and c(RGDyC)-PEG-MB2-C' dots), and two (MB2-PEG-C' dots and MB2-c(RGDyC)-PEG-C' dots) (Supplementary Figures S4.6A and S4.6B in Appendix C). In both cases, we observed single peaks that were congruent to each other. All particles were then characterized using steady-state absorption spectroscopy. Figure 4.4A and 4.4D show the absorption spectra of design one and design two, respectively, with and without c(RGDyC)-functionalization in water. In both cases, increased absorption between 200 and 300 nm was noticeable. Due to strong absorption features in that region it is difficult to clearly identify the peptide absorption by qualitative comparison. For that reason, we subtract the two spectra from each other and display the difference spectra in Figures 4.4B and 4.4E. In both cases a band at ~260 to 270 nm can clearly be identified, which coincides with the absorption band of the c(RGDyC) spectrum (Supplementary Figure S4.6C in Appendix C). Using the relative absorption peaks of tyrosine in c(RGDyC) and of MB2, we estimated 17 and 14 c(RGDyC) units per MB2 molecule for design one and design two, respectively, which is close to the desired number based on earlier studies (*41*).

Finally, we tested the effect of c(RGDyC)-functionalization on the relative singlet oxygen quantum yield performance. We compared particles with and without c(RGDyC) for absorption matched samples of the same design. For both designs we measured a reduction of singlet oxygen quantum yield by a relative 25% for design one

and by a relative 12% for design two (Figure 4.4C and 4.4F). This finding is surprising. Given the spatial proximity of surface MB2 and c(RGDyC), one would expect a stronger effect of c(RGDyC) in design two. Results suggest, however, that c(RGDyC) increases the steric shielding more significantly for the encapsulated MB2 than for the surface grafted MB2.

Conclusion

In this study, we have presented the synthesis of two different designs for ultrasmall organic-inorganic hybrid silica nanophotosenistizers, that covalently bind the methylene blue derivate MB2. We found that the properties of MB2 strongly depend on the particle design. Both particle designs yielded sub-10 nm size particles that could be functionalized with c(RGDyC) as a targeting moiety. Despite reduced singlet oxygen quantum yields of MB2 upon particle association, the effective particle singlet oxygen quantum yields far exceed the quantum yield of a single MB2 dye. The advantages of ultrasmall organic-inorganic hybrid functionalized silica nanoparticles as a delivery and protective system for photosensitizers make such probes interesting candidates for applications in PDT.

Although this study focuses on the photosensitizer MB2, described design principles and synthesis methods are in principle applicable to other photosensitizers. This might be of special interest for hydrophobic NIR and IR photosensitizers with large singlet oxygen quantum yields, *i.e.* porphyrins, chlorins, phthalocyanines, naphthalocyanines, bacteriochlorins, and BODIPY dyes. PEGylated silica can provide a water-soluble carrier for these cargos, to allow specific targeting and achieve high local concentrations at targeted sites, while avoiding aggregation in aqueous media. However, more work is necessary to fine tune such synthesis protocols to fully harvest the potential of ultrasmall organic-inorganic hybrid silica nanophotosensitizers.

Figures

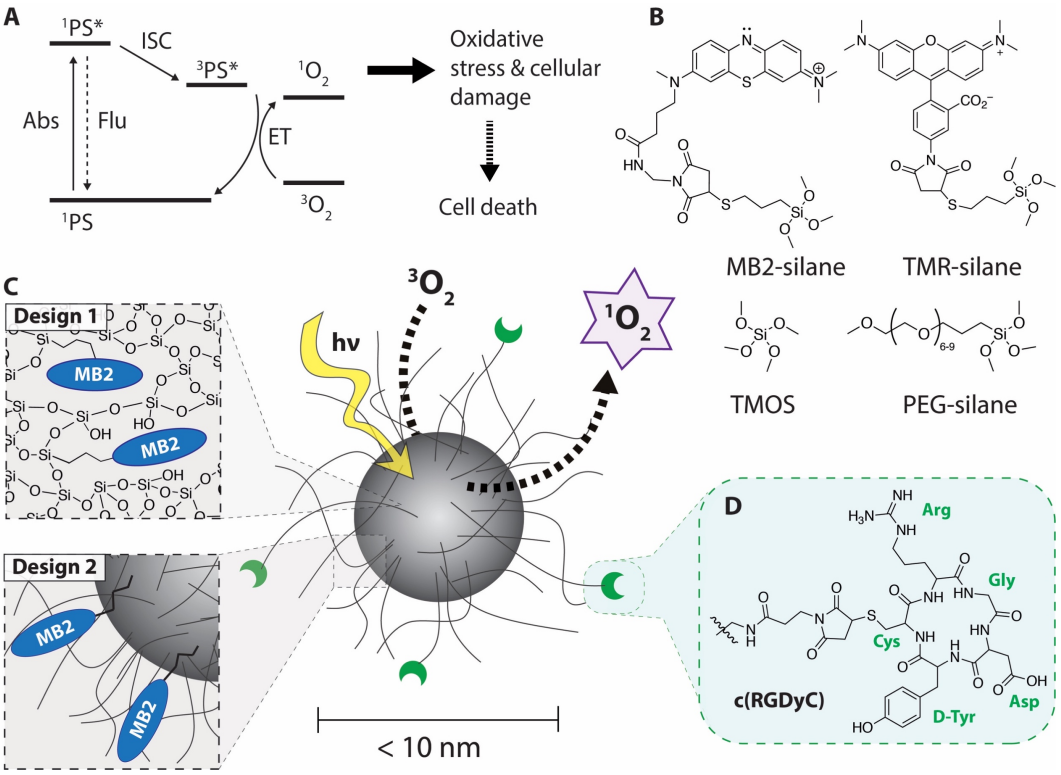

Figure 4.1. (A) Simplified Jablonski Scheme illustrating the creation of reactive singlet oxygen, $^1O_2$. ^{1}PS denotes the singlet ground state, ^{1}PS* the electronically excited singlet state, and ^{3}PS* the electronically excited triplet state of a photosensitizer. $^3O_2$ denotes the triplet ground state of molecularly dissolved oxygen. (B) Precursor molecules for the synthesis of sub-10 nm silica nanoparticles, showing the methylene blue derivate MB2-silane, the rhodamine dye TMR-silane, tetramethyl orthosilicate (TMOS), and polyethylene glycol-silane (PEG-silane). (C) Schematic representation of two different designs of functionalized photosensitizing sub-10 nm silica nanoparticles (center). Design 1: Covalent encapsulation of one or more MB2 molecules in the silica matrix (PEG-MB2-C' dots). Design 2: Particle surface functionalization with one or more MB2 molecules (MB2-PEG-C'dot). (D) Targeting moiety cyclo(Arg-Gly-Asp-D-Tyr-Cys) (cRGDyC).

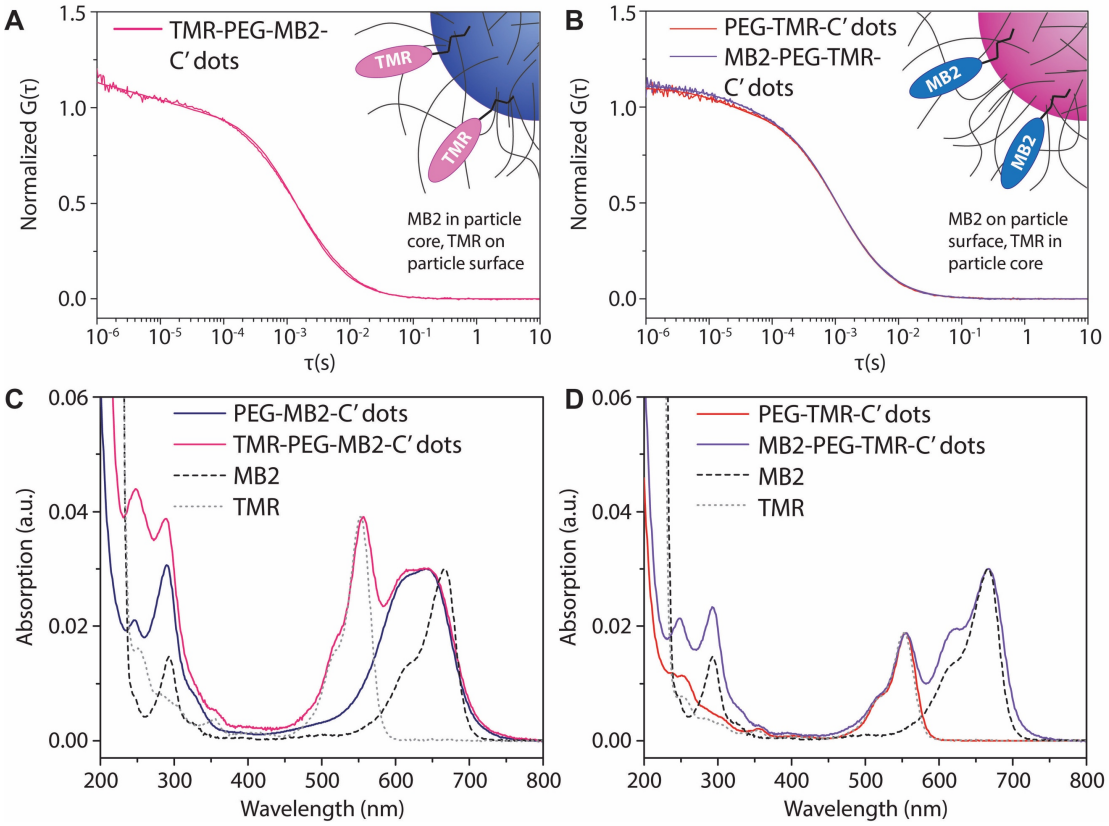

Figure 4.2. (A) and (C) FCS autocorrelation curve of MB2-PEG-TMR-C'dot (design one) and absorption spectra before and after TMR surface functionalization as compared to free TMR dye and MB2 photosensitizer. (B) and (D) FCS autocorrelation curves of PEG-TMR-C' dots and TMR-PEG-MB2-C' dots (design two) and absorption spectra before and after MB2 surface functionalization as compared to free TMR dye and MB2 photosensitizer.

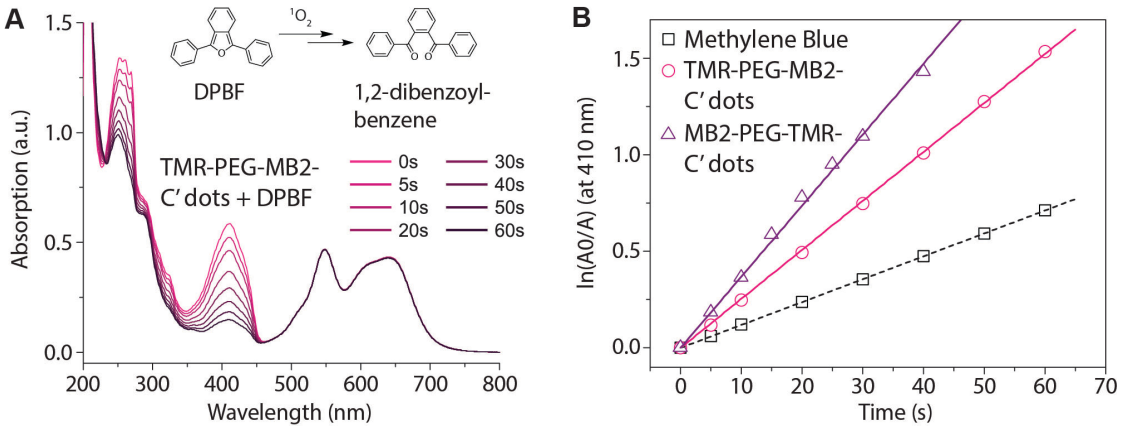

Figure 4.3. (A) Schematic representation of a photosensitizing measurement using 1,3-diphenylisobenzofuran (DPBF) as a singlet oxygen, $^1O_2$, sensor. Absorption of a solution containing TMR-PEG-MB2-C' dots and DPBF irradiated at 635 nm for 60 s in intervals of 5 and 10 s (see legend). (B) Comparative $^1O_2$ generation of methylene blue, TMR-PEG-MB2-C' dots, and MB2-PEG-TMR-C' dots.

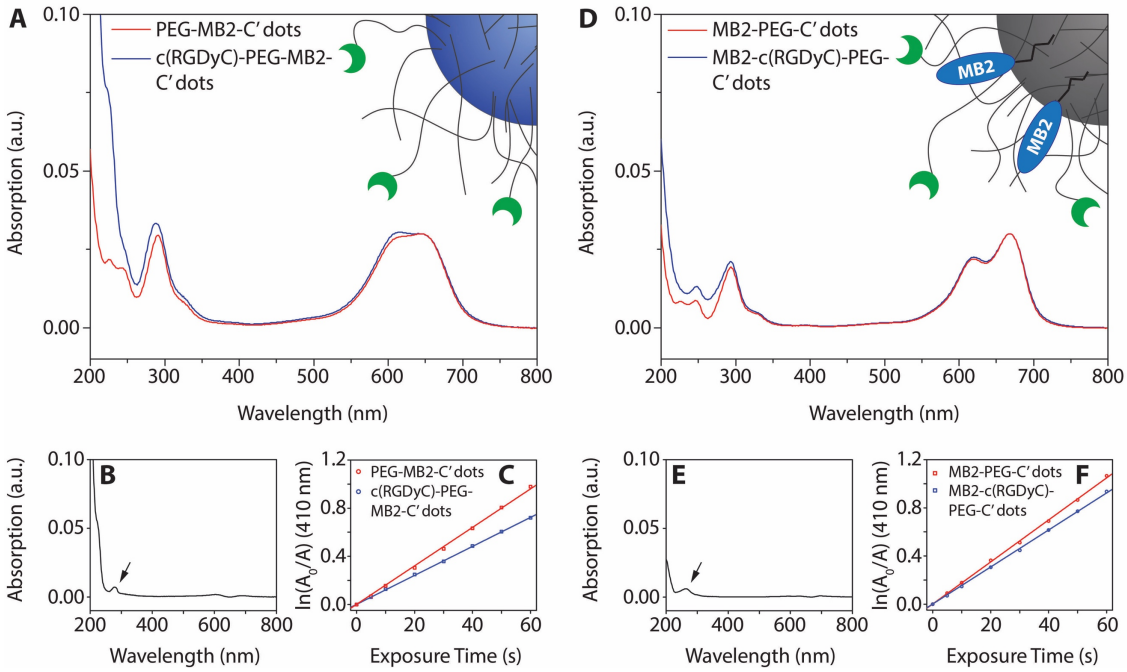

Figure 4.4. (A) Intensity matched absorption spectra of PEG-MB2-C' dots and c(RGDyC)-PEG-MB2-C' dots. (B) Difference spectrum of the spectra in (A). (C) Photosensitizing measurement of intensity matched PEG-MB2-C' dots and c(RGDyC)-PEG-MB2-C' dots. (D) Intensity matched absorption spectra of MB2-PEG-C' dots and MB2-c(RGDyC)-PEG-C' dots. (E) Difference spectrum of the spectra in (D). (F) Photosensitizing measurement of intensity matched MB2-PEG-C' dots and MB2-c(RGDyC)-PEG-C' dots.

Acknowledgements

F.F.E.K. gratefully acknowledges the financial support from the Department of Energy (DOE) under Award No. DE-SC0010560 and the National Institutes of Health (NIH) under Award No. U54CA199081. This work made use of the Cornell Center for Materials Research (CCMR) shared facilities which are supported through the NSF MRSEC program (DMR-1719875) at Cornell. The authors gratefully acknowledge L. Estroff (Cornell University) for helpful discussions.

F. F. E. Kohle and U. B. Wiesner developed the experimental design. F. F. E. Kohle and S. Li synthesized nanoparticles. F. F. E. Kohle conducted and analyzed steady-state absorption and emission spectroscopy, and FCS measurements. F. F. E. Kohle and S. Li carried out singlet oxygen quantum yield measurements.

REFERENCES

(*1*) Felsher, D. W. Photodynamic Therapy for Cancer. *Nat. Rev. Cancer*, ***3*,** 375–380 (2003).

(*2*) Ochsner, M. Photophysical and Photobiological Processes in the Photodynamic Therapy of Tumours. *J. Photochem. Photobiol. B Biol.*, ***39*,** 1–18 (1997).

(*3*) DeRosa, M. C.; Crutchley, R. J. Photosensitized Singlet Oxygen and Its Applications. *Coord. Chem. Rev*., ***233–234***, 351–371 (2002).

(*4*) Ormond, A. B.; Freeman, H. S. Dye Sensitizers for Photodynamic Therapy. *Materials*., ***6*,** 817–840 (2013).

(*5*) Agostinis, P.; Berg, K.; Cengel, K. a; Foster, T. H.; Girotti, A. W.; Gollnick, S. O.; Hahn, S. M.; Hamblin, M. R.; Juzeniene, A.; Kessel, D.; Korbelik, M.; Moan, J.; Mroz, P.; Nowiz, D.; Piette, J.; Willson, B. C.; Golab, J. Photodynamic Therapy of Cancer : An Update. *Am. Cancer Soc.*, ***61*,** 250–281 (2011).

(*6*) Mehraban, N.; Freeman, H. S. Developments in PDT Sensitizers for Increased Selectivity and Singlet Oxygen Production. *Materials*., ***8*,** 4421-4456 (2015).

(*7*) Kamkaew, A.; Lim, S. H.; Lee, H. B.; Kiew, L. V.; Chung, L. Y.; Burgess, K. BODIPY Dyes in Photodynamic Therapy. *Chem. Soc. Rev. Chem. Soc. Rev.*, ***42*,** 77–88 (2013).

(*8*) Zhang, Y.; Lovell, J. F. Porphyrins as Theranostic Agents from Prehistoric to Modern Times. *Theranostics.*, ***2*,** 905–915 (2012).

(*9*) Tang, W.; Xu, H.; Park, E. J.; Philbert, M. A.; Kopelman, R. Encapsulation of Methylene Blue in Polyacrylamide Nanoparticle Platforms Protects Its Photodynamic Effectiveness. *Biochem. Biophys. Res. Commun.*, ***369*,** 579–583 (2008).

(*10*) Singh, R.; Lillard, J. W. Nanoparticle-Based Targeted Drug Delivery. *Exp. Mol. Pathol.*, ***86*,** 215–223 (2009).

(*11*) Chen, F.; Ma, K.; Zhang, L.; Madajewski, B.; Zanzonico, P.; Sequeira, S.; Gonen, M.; Wiesner, U.; Bradbury, M. S. Target-or-Clear Zirconium-89 Labeled Silica Nanoparticles for Enhanced Cancer-Directed Uptake in Melanoma: A Comparison of Radiolabeling Strategies. *Chem. Mater.*, ***29*****,** 8269–8281 (2017).

(*12*) Soo Choi, H.; Liu, W.; Misra, P.; Tanaka, E.; Zimmer, J. P.; Itty Ipe, B.; Bawendi, M. G.; Frangioni, J. V. Renal Clearance of Quantum Dots. *Nat. Biotechnol.*, ***25*****,** 1165–1170 (2007).

(*13*) Abrahamse, H.; Kruger, C. A.; Kadanyo, S.; Mishra, A. Nanoparticles for Advanced Photodynamic Therapy of Cancer. *Photomed. Laser Surg.*, ***35*****,** 581-588 (2017).

(*14*) Debele, T. A.; Peng, S.; Tsai, H. C. Drug Carrier for Photodynamic Cancer Therapy. *Int. J. Mol. Sci*., ***16*****,** 22094-22136 (2015).

(*15*) Lucky, S. S.; Soo, K. C.; Zhang, Y. Nanoparticles in Photodynamic Therapy. *Chem. Rev., **115*****,** 1990–2042 (2015).

(*16*) Gupta, A.; Avci, P.; Sadasivam, M.; Chandran, R.; Parizotto, N.; Vecchio, D.; de Melo, W. C. M. A.; Dai, T.; Chiang, L. Y.; Hamblin, M. R. Shining Light on Nanotechnology to Help Repair and Regeneration. *Biotechnol. Adv.*, ***31*****,** 607–631 (2013).

(*17*) Chouikrat, R.; Seve, A.; Vanderesse, R.; Benachour, H.; Barberi-Heyob, M.; Richeter, S.; Raehm, L.; Durand, J.-O.; Verelst, M.; Frochot, C. Non Polymeric Nanoparticles for Photodynamic Therapy Applications: Recent Developments. *Curr. Med. Chem.*, ***19*****,** 781–792 (2012).

(*18*) Ragelle, H.; Danhier, F.; Préat, V.; Langer, R.; Anderson, D. G. Nanoparticle-Based Drug Delivery Systems: A Commercial and Regulatory Outlook as the Field Matures. *Expert Opin. Drug Deliv.*, ***14*****,** 851–864 (2017).

(*19*) Bobo, D.; Robinson, K. J.; Islam, J.; Thurecht, K. J.; Corrie, S. R. Nanoparticle-Based Medicines: A Review of FDA-Approved Materials and Clinical Trials to Date. *Pharm. Res.*, ***33*****,** 2373–2387 (2016).

(*20*) Lismont, M.; Dreesen, L.; Wuttke, S. Metal-Organic Framework Nanoparticles in Photodynamic Therapy: Current Status and Perspectives. *Adv. Funct. Mater.*,

27**,** 1–16 (2017).

(*21*) Burns, A. a; Vider, J.; Ow, H.; Herz, E.; Penate-medina, O.; Baumgart, M.; Larson, S. M.; Wiesner, U.; Bradbury, M. Fluorescent Silica Nanoparticles with Efficient Urinary Excretion for Nanomedicine. *Nano Lett.*, ***9*****,** 442–448 (2009).

(*22*) Phillips, E.; Penate-Medina, O.; Zanzonico, P. B.; Carvajal, R. D.; Mohan, P.; Ye, Y.; Humm, J.; Gonen, M.; Kalaigian, H.; Schoder, H.; Strauss, H. W.; Larson, S. M.; Wiesner, U.; Bradbury, M. S. Clinical Translation of an Ultrasmall Inorganic Optical-PET Imaging Nanoparticle Probe. *Sci. Transl. Med.*, ***6*****,** 260ra149 (2014).

(*23*) Ma, K.; Mendoza, C.; Hanson, M.; Werner-Zwanziger, U.; Zwanziger, J.; Wiesner, U. Control of Ultrasmall Sub-10 nm Ligand-Functionalized Fluorescent Core-Shell Silica Nanoparticle Growth in Water. *Chem. Mater.*, ***27*****,** 4119–4133 (2015).

(24) Ma, K.; Wiesner, U. Modular and Orthogonal Post-PEGylation Surface Modifications by Insertion Enabling Penta-Functional Ultrasmall Organic-Silica Hybrid Nanoparticles. *Chem. Mater.*, ***29*****,** 6840–6855 (2017).

(*25*) Ma, K.; Werner-Zwanziger, U.; Zwanziger, J.; Wiesner, U. Controlling Growth of Ultrasmall Sub-10 Nm Fluorescent Mesoporous Silica Nanoparticles. *Chem. Mater.*, ***25*****,** 677–691 (2013).

(*26*) Kim, S. E.; Zhang, L.; Ma, K.; Riegman, M.; Chen, F.; Ingold, I.; Conrad, M.; Turker, M. Z.; Gao, M.; Jiang, X.; Monette, S.; Pauliah, M.; Gonen, M.; Zanzonico, P.; Quinn, T.; Wiesner, U.; Bradbury, M. S.; Overholtzer, M. Ultrasmall Nanoparticles Induce Ferroptosis in Nutrient-Deprived Cancer Cells and Suppress Tumour Growth. *Nat. Nanotechnol.*, ***11*****,** 977–985 (2016).

(*27*) *PROVAYBLUETM (methylene blue) injection, for intravenous use*; U.S. Food and Drug Administration, **2016**.

(*28*) Tardivo, J. P.; Giglio, A. Del; Santos De Oliveira, C.; Santesso Gabrielli, D.; Couto Junqueira, H.; Tada, D. B.; Severino, D.; De Fátima Turchiello, R.; Baptista Phd, M. S. Methylene Blue in Photodynamic Therapy: From Basic Mechanisms to Clinical Applications. *Photodiagnosis Photodyn. Ther.*, ***2*****,** 175–191 (2005).

(*29*) Tang, W.; Xu, H.; Kopelman, R.; A. Philbert, M. Photodynamic Characterization and In Vitro Application of Methylene Blue-Containing Nanoparticle Platforms. *Photochem. Photobiol.*, ***81*,** 242 (2005).

(*30*) Qin, M.; Hah, H. J.; Kim, G.; Nie, G.; Lee, Y.-E. K.; Kopelman, R. Methylene Blue Covalently Loaded Polyacrylamide Nanoparticles for Enhanced Tumor-Targeted Photodynamic Therapy. *Photochem. Photobiol. Sci.*, ***10*,** 832–841 (2011).

(*31*) Redmond, R. W.; Gamlin, J. N. A Compilation of Singlet Oxygen Yields from Biologically Relevant Molecules. *Photochem. Photobiol.*, ***70*,** 391–475 (1999).

(*32*) Yogi, C.; Kojima, K.; Wada, N.; Tokumoto, H.; Takai, T.; Mizoguchi, T.; Tamiaki, H. Photocatalytic Degradation of Methylene Blue by TiO_2 Film and Au Particles-TiO_2 Composite Film. *Thin Solid Films.*, ***516*,** 5881–5884 (2008).

(*33*) Marbán, G.; Vu, T. T.; Valdés-Solís, T. A Simple Visible Spectrum Deconvolution Technique to Prevent the Artefact Induced by the Hypsochromic Shift from Masking the Concentration of Methylene Blue in Photodegradation Experiments. *Appl. Catal. A Gen.*, ***402*,** 218–223 (2011).

(*34*) Patil, K.; Pawar, R.; Talap, P. Self-Aggregation of Methylene Blue in Aqueous Medium and Aqueous Solutions of Bu_4NBr and Urea. *Phys. Chem. Chem. Phys.*, ***2*,** 4313–4317 (2000).

(*35*) Junqueira, H. C.; Severino, D.; Dias, L. G.; Gugliotti, M. S.; Baptista, M. S. Modulation of Methylene Blue Photochemical Properties Based on Adsorption at Aqueous Micelle Interfaces. *Phys. Chem. Chem. Phys.*, ***4*,** 2320–2328 (2002).

(*36*) Severino, D.; Junqueira, H. C.; Gugliotti, M.; Gabrielli, D. S.; Baptista, M. S. Influence of Negatively Charged Interfaces on the Ground and Excited State Properties of Methylene Blue. *Photochem. Photobiol.*, ***77*,** 459–468 (2003).

(*37*) Greci, L. On the Use of 1, 3-Diphenylisobenzofuran Reactions With Carbon and Oxygen Centered Radicals in Model and Natural Systems., ***19*,** 395–405 (1993).

(*38*) Nuñez, S. C.; Yoshimura, T. M.; Ribeiro, M. S.; Junqueira, H. C.; Maciel, C.; Coutinho-Neto, M. D.; Baptista, M. S. Urea Enhances the Photodynamic Efficiency of Methylene Blue. *J. Photochem. Photobiol. B Biol.*, ***150*,** 31–37 (2015).

(*39*) Mundra, V.; Li, W.; Mahato, R. I. Nanoparticle-Mediated Drug Delivery for Treating Melanoma. *Nanomedicine.*, ***10*****,** 2613–2633 (2015).

(*40*) Kang, W.; Svirskis, D.; Sarojini, V.; McGregor, A. L.; Bevitt, J.; Wu, Z. Cyclic-RGDyC Functionalized Liposomes for Dual-Targeting of Tumor Vasculature and Cancer Cells in Glioblastoma: An in Vitro Boron Neutron Capture Therapy Study. *Oncotarget.*, ***8*****,** 36614–36627 (2017).

(*41*) Chen, F.; Ma, K.; Benezra, M.; Zhang, L.; Cheal, S. M.; Phillips, E.; Yoo, B.; Pauliah, M.; Overholtzer, M.; Zanzonico, P.; Sequeira, S.; Gonen, M.; Quinn, T.; Wiesner, U.; Bradbury, M. S. Cancer-Targeting Ultrasmall Silica Nanoparticles for Clinical Translation: Physicochemical Structure and Biological Property Correlations. *Chem. Mater.*, ***29*****,** 8766–8779 (2017).

APPENDIX C

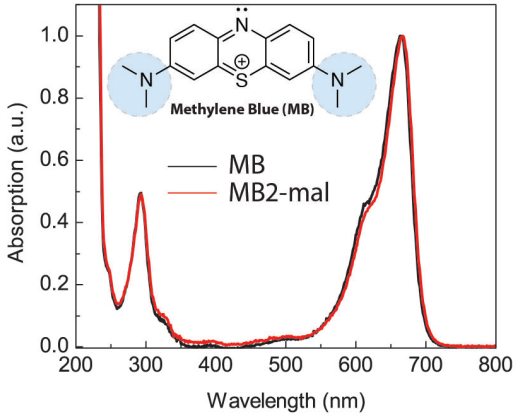

Figure S4.1. Methylene blue (MB) and MB2 absorption spectra. A minor bathochromic shift (red-shift) from 665 to 667 nm is noticeable. The inset shows the chemical structure of MB with auxochrome groups circled in blue.

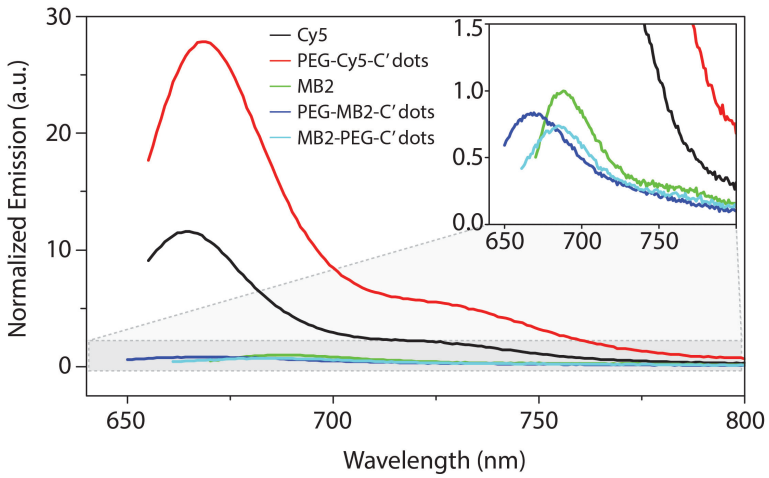

Figure S4.2. Fluorescence emission spectra of Cy5 dye, PEG-Cy5-C' dots, MB2, PEG-MB2-C' dots, and MB2-PEG-C' dots. The concentration of Cy5 and MB2 was matched. The emission spectra were normalized for the emission of MB2. The inset shows the enlarged emission of MB2, PEG-MB2-C' dots, and MB2-PEG-C' dots, showing a more than one order of magnitude brightness difference between the Cy5 and PEG-Cy5-C' dots and MB2, PEG-MB2-C' dots, and MB2-PEG-C' dots. Cy5 particles show the typical emission enhancement that is observed upon dye encapsulation in a silica matrix as compared to the free dye in solution (*S1, S2*). The emission of PEG-MB2-C' dots as compared to MB2-PEG-C' dots is slightly larger, however both particles demonstrate a reduction of emission as compared to free MB2. This can likely be associated with the increased shoulder of MB2 in the particles.

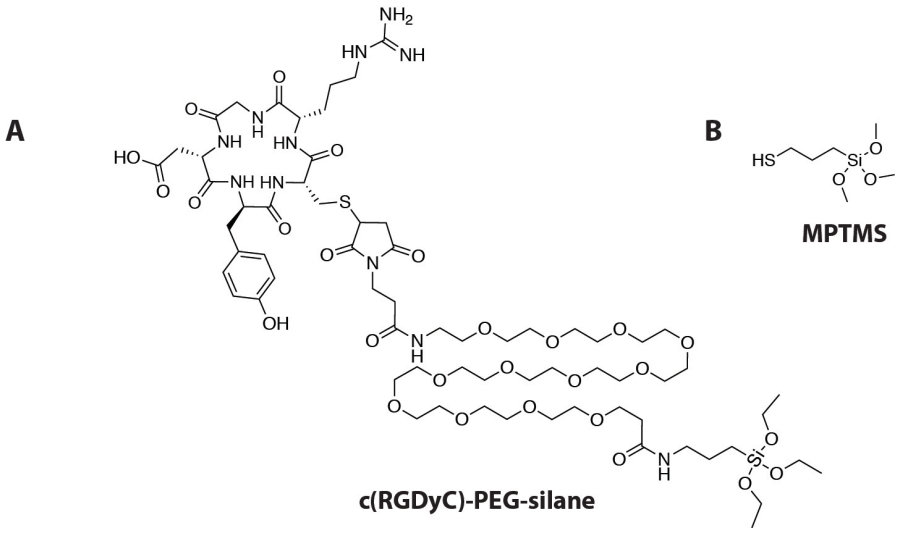

Figure S4.3. (A) Chemical structure of the targeting moiety precursor (cRGDyC)-PEG(12)-silane. (B) Chemical structure of (3-mercaptopropyl)trimethoxysilane (MPTMS).

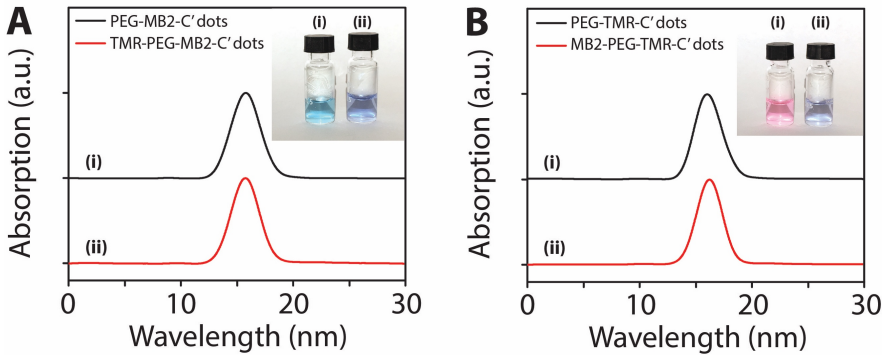

Figure S4.4. (A) GPC elugrams of PEG-MB2-C' dots (i) and TMR-PEG-MB2-C' dots (ii). Inset shows photographs of the respective samples. (B) GPC elugrams of PEG-TMR-C' dots (i) and MB2-PEG-TMR-C' dots (ii). Inset shows photographs of the respective samples. Each sample pair was measured on the same day. Different sample pairs were measured on different days leading to differences in absolute peak elution times.

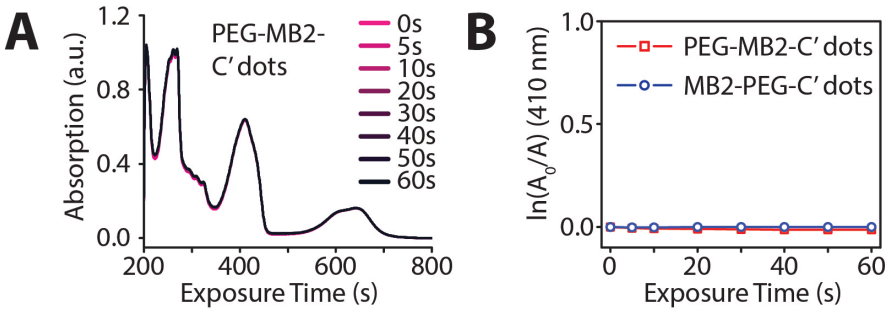

Figure S4.5. (A) Schematic representation of a photosensitizing measurement using 1,3-diphenylisobenzofuran (DPBF) as a singlet oxygen, $^1O_2$, sensor. Absorption of a solution containing PEG-MB2-C' dots and DPBF, measured at different time points, in the absence of 635 nm irradiation (dark toxicity). (B) Comparison of singlet oxygen, $^1O_2$, generation from PEG-MB2-C' dots and MB2-PEG-C' dots in the dark.

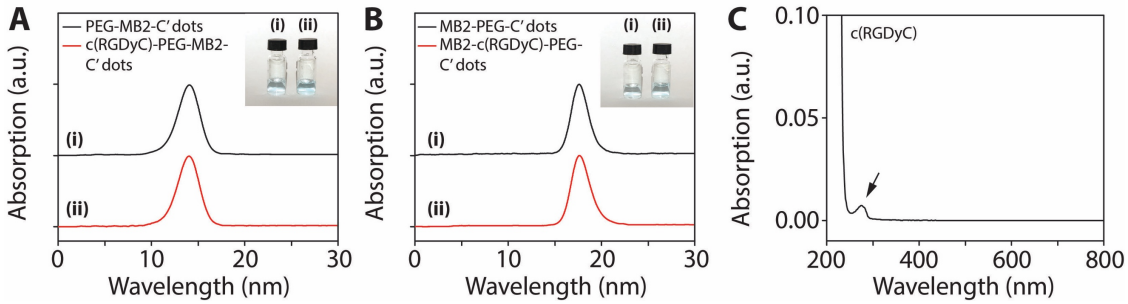

Figure S4.6. (A) GPC elugrams of PEG-MB2-C' dots (i) and c(RGDyC)-PEG-MB2-C' dots (ii). Inset shows photographs of the respective samples. (B) GPC elugrams of MB2-PEG-C' dots (i) and MB2-c(RGDyC)-PEG-C' dots (ii). Inset shows photographs of the respective samples. Each sample pair was measured on the same day. Different sample pairs were measured on different days leading to differences in absolute peak elution times. (C) Absorption spectrum of c(RGDyC) in water, showing an isolated tyrosin peak ($\varepsilon \approx 1400\ M^{-1}\ cm^{-1}$) (*S3*).

REFERENCES (Appendix C)

(*S1*) Ow, H.; Larson, D. R.; Srivastava, M.; Baird, B. A.; Webb, W. W.; Wiesner, U. Bright and Stable Core−Shell Fluorescent Silica Nanoparticles. *Nano Lett.*, **5**, 113–117 (2015).

(*S2*) Larson, D. R.; Ow, H.; Vishwasrao, H. D.; Heikal, A. A.; Wiesner, U.; Webb, W. W. Silica Nanoparticle Architecture Determines Radiative Properties of Encapsulated Fluorophores. *Chem. Mater.*, ***20***, 2677–2684 (2008).

(*S3*) Ma, K.; Mendoza, C.; Hanson, M.; Werner-Zwanziger, U.; Zwanziger, J.; Wiesner, U. Control of Ultrasmall Sub-10 nm Ligand-Functionalized Fluorescent Core-Shell Silica Nanoparticle Growth in Water. *Chem. Mater.*, ***27***, 4119–4133 (2015).

CHAPTER 5

ULTRASMALL SILICA NANOPARTICLES FOR SUPER-RESOLUTION OPTICAL MICROSCOPY AND PHOTODYNAMIC THERAPY[*]

Abstract

Super-resolution (SR) fluorescence microscopy has revolutionized optical imaging in the life sciences. Resolution rests on the ability of fluorescent markers to enter transient dark states. For organic fluorophores this often requires imaging buffers interfering with biological function. Here, we instead design ultrasmall fluorescent silica nanoparticles, tailoring the precise chemical environment around covalently bound dyes to optimize their properties for SR microscopy. We engineer bright photoswitchable nanoprobes embedding cyanine dyes, functionalizing the silica network with mercaptopropyl groups, and demonstrating stochastic optical reconstruction microscopy without the use of toxic β-mercaptoethanol. We alternatively employ iodopropyl groups for quantum mechanical spin-orbit coupling to control triplet state populations of encapsulated carborhodamine dye ATTO647N and methylene blue derivate MB2, important for ground state depletion microscopy and photodynamic therapy, respectively. This particle molecular photoengineering concept should be applicable to other dyes, chemistries, and nanoprobes, with the resulting ultraefficient

[*] Ferdinand F. E. Kohle, Joshua A. Hinckley, Songying Li, Nikhil Dhawan, William P. Katt, Jacob A. Erstling, Ulrike Werner-Zwanziger, Josef Zwanziger, Richard A. Cerione, Ulrich B. Wiesner. Ultrasmall Silica Nanoparticles for Super-Resolution Optical Microscopy and Photodynamic Therapy. Manuscript in preparation.

optical labels facilitating minimally invasive super-resolution live cell imaging and therapeutic effects.

Introduction

Abbe's diffraction limit describes the maximum optical resolution as λ/2, *e.g.* around 250 nm for green-laser illumination, smaller than a mammalian cell, but far larger than the average virus or protein. Efforts to overcome this have led to multiple new microscopy concepts (*1, 2*) and renewed interest in the photochemistry and photophysics of fluorescent markers (*3, 4*). Super-resolution (SR) microscopy involves the activation of a single point-like emitting source within a diffraction-limited area at any time, while other emitters are in a dark state. The origin of the emitting source can then be precisely localized (Figure 5.1a and 5.1b). Different microscopy concepts impose different requirements onto fluorescent markers. Stimulated emission depletion (STED) microscopy demands photostable fluorophores to withstand high laser intensities (*5*). In ground state depletion (GSD) microscopy, photoswitching is achieved by shelving fluorophores in triplet states accessed at low irradiances, reducing phototoxicity but requiring high triplet yields (*6*). Stochastic SR methods, *e.g.* stochastic optical reconstruction microscopy (STORM), rely on bright and photoswitchable fluorescent probes to localize single molecules (*7-9*).

A fluorophore's behavior is dependent upon both its structure and its local environment. Consider the cyanine dye, Cy5 (*10*): Following exposure to primary thiols, such as β-mercaptoethanol (βME), Cy5 undergoes photo-conversion between bright and long-lived dark states by forming a Cy5-thiol adduct (Figure 5.1c) (*11-13*), promoting the use of 'imaging cocktails' (*14-16*). However, while additives such as βME support favorable emissive behavior, they typically compromise cell integrity or are otherwise incompatible with experimental conditions (*4, 17, 18*).

Fluorescent proteins (FPs) and photoswitchable nanoparticles (NPs), such as quantum dots (QDs) or photochromic dye–containing NPs, present alternatives for cocktail-free SR microscopy (*19-21*). FPs can be genetically encoded, but often lack brightness and photostability (*21*). QDs have broad absorption bands, high photon yields and are photostable, while SR exploits intrinsic QD-blinking (*19, 22*). However, emissive properties are size dependent (*23*), and use in biological samples requires passivation layers, complicating syntheses and limiting size tenability (*24*). Photochromic dyes encapsulated into polymeric NPs or silica nanoparticles (SNPs) provide alternatives to QDs (*20, 25*). Host NPs overcome drawbacks of free dyes, such as low solubility in aqueous media, pH dependent emission, or cytotoxicity. However, encapsulation may retard dye photo-isomerization kinetics (*26*), leading to longer acquisition times (*20*). Furthermore, for dyad systems (photochrome-fluorophore), three excitation wavelengths are needed (*i.e.* switch-on, switch-off, and probe) (*25*), resulting in excitation/erasing problems caused by triggering the switching-mechanism while probing the sample (*27, 28*). A problem of most photoswitchable NPs systems, in particular those used for stochastic SR microscopy, is their large size (>10 nm), which may interfere with biological function, bias labeling sites, or broaden localization accuracy (*20, 28*). Furthermore, in order to enable translation of SR microscopy techniques into clinical settings, SNP hydrodynamic diameters below 7 nm have recently been demonstrated to lead to rapid renal clearance in first human clinical trials in oncology, making such ultrasmall sizes highly desirable (*29*).

Here, we tailor the photo-properties of ultrasmall (<10 nm) core-shell SNPs by covalently enclosing key ‘imaging-cocktail’ ingredients and organic fluorophores

within a sub-10 nm and polyethylene glycol (PEG) surface functionalized and stabilized SNP, with particular emphasis on enabling stochastic SR microscopy (Figure 5.1c). This approach enjoys the benefits of silica, *i.e.* size-independent bright dye emissive properties, biocompatibility, optical transparency, and multifunctionality, while avoiding disadvantages of imaging cocktails, *e.g.* interference with biological function and odor of mercapto compounds. In the following, we refer to this concept as particle molecular photo-engineering (PMPE).

Materials and Methods

Materials

Aluminum-tri-sec-butoxide (ASB), (3-aminopropyl)triethoxysilane (APTES), ammonium hydroxide (28 wt% in H_2O), ammonia solution (2.0 M in ethanol), dimethyl sulfoxide (DMSO), 1,3-diphenylisobenzofuran (DPBF), (3-iodopropyl)trimethoxysilane (IPTMS), (3-mercaptopropyl) trimethoxysilane (MPTMS), 2-propanol (anhydrous 99.5%), tetramethyl orthosilicate (TMOS), isopropanol, methylene blue (MB), β-mercaptoethanol (βME), glucose, guanosine 5′-triphosphate sodium salt hydrate (GTP), Paclitaxel, and glucose oxidase were purchased from Sigma Aldrich. Catalase was purchased from Roche Applied Science. Methoxy-terminated poly(ethylene glycol) (PEG-silane, molar mass of ~0.5 kg/mol) was purchased from Gelest Inc.. 50% glutaraldehyde in PBS was purchased from Electron Microscopy Sciences. Heterobifunctional PEGs with biotin and maleimide groups (biotin-PEG-mal, molar mass of ~922 g/mol), with biotin and NHS ester groups (biotin-PEG-NHS, molar mass of ~589 g/mol), and maleimide and NHS ester groups (Mal-PEG_6-NHS, molar mass of ~602 g/mol) were purchased from Quanta BioDesign. Cy3-NHS, Cy3-maleimide, Cy5-NHS, and Cy5-maleimide florescent dyes were purchased from GE Healthcare. ATTO647N-NHS, and ATTO647N-maleimide, MB2-NHS, and MB2-maleimide dyes were purchased from ATTO-Tec. DY-782-NHS dye was purchased from Dyomics. Cy5-biotin and Cy3-maleimide (for synthesis of Cy3-biotin) dyes were purchased from Click Chemistry Tools. Ethanol (absolute anhydrous 99.5%) was purchased from Pharmco-Aaper. N-γ-maleimidobutyryl-oxysuccinimide ester (GMBS)

and streptavidin were purchased from Life Technologies. RPMI-1640, fetal bovine serum (FBS), phosphate buffered saline (PBS), 50X penicillin/streptomycin (pen/strep), and presto blue were purchased from Invitrogen. BxPC3 cells were obtained from ATCC. 97% pure porcine brain tubulin protein, PEM general tubulin buffer, and 60% tubulin glycerol buffer were purchased from Cytoskeleton Inc. Methanol was obtained from Macron Chemicals. All chemicals were used as received. Deionized (DI) water (18.2 MΩ·cm) was generated using a Millipore Milli-Q system.

Synthesis of fluorescent srC' dots

All reactions were conducted at room temperature, unless otherwise noted. For a 10 mL reaction of srC' dots, 145.4 μL (2 mg/1 mL in DMSO) of Cy5-NHS and 0.86 μL APTES (molar ratio 1:10) were combined in inert nitrogen atmosphere in the dark to form Cy5-silane. The mixture was allowed to react for 12 hours. Under vigorous stirring, 51 μL MPTMS and 27.2 μL TMOS (molar ratio 6:4 or 60% MPTMS) were added into 10 mL 0.2 M HCl (pH ~ 1.5) in a 25 mL round bottom flask, immediately followed by the entire prepared Cy5-silane dye solution and then 20 μL ASB. ASB was used in small molar amounts, but was necessary in the particle formation process by contributing to charge stabilization of particles in acidic solution (*30*). The mixture was allowed to react for 25 min, before the particle growth was quenched by rapidly adding 150 μL PEG-silane (~0.5 kg/mol). 5 minutes after PEG-silane addition the pH was adjusted by rapidly adding 100 μL of a 14% aqueous solution of ammonia. This brought the pH to about ~8. The particles were stirred for another 12 hours, before the stirring was stopped, and the samples heated to 80 °C over night. Finally, samples were

transferred into a dialysis membrane (Pierce, molecular weight cutoff, MWCO = 10,000) and placed in 2,000 mL of DI water to wash away any unreacted reagents and neutralize the particle dispersions. Water was changed twice at 6 and 12 hour time points after which the characteristic mercapto odor of MPTMS disappeared. The particles were then filtered through a 0.22 μm syringe filter (Fisher brand) to remove any large aggregates or dust that may have accumulated in the solution. All final solutions appeared faint blue and clear. Particles were also prepared with varied molar ratios of MPTMS to TMOS; particles synthesized from 0%, 30%, 60%, and 80% MPTMS are denoted as 0%, 30%, 60%, and 80% srC' dots, respectively.

Biotinylated srC' dots were synthesized by following the same protocol but adding biotin-PEG-silane to the particle dispersion immediately prior to the PEG-silane addition. Biotin-PEG-silane precursor was prepared by reacting MPTMS with biotin-PEG-mal in a molar ratio of 1.1:1. For a 10 mL batch, 0.5 μL of MPTMS were combined with 45 μL of biotin-PEG-mal (50 mg/mL in DMSO) for 12 hours under an inert nitrogen atmosphere.

Synthesis of iC' dots

The synthetic pathway for iC' dots closely followed that for srC' dots, except that ATTO647N-NHS replaced Cy5-NHS, and IPTMS replaced MPTMS. The mixture was allowed to react for 15 min, before the particle growth was quenched by rapidly adding 150 μL PEG-silane (~0.5 kg/mol). The reaction was then treated identically to those of srC' dots above. Particles were synthesized with 0%, 1%, 2.5%, 5%, 7.5%,

10%, and 20% IPTMS, and are denoted as 0%, 1%, 2.5%, 5%, 7.5%, 10%, and 20% iC' dots respectively.

MB2 0%, 7.5%, and 15% iC' dots were synthesized according to the protocol above, replacing ATTO647N-NHS with MB2-NHS. Due to the non-emissive nature of MB2, MB2 iC' dots were surface functionalized with TMR dye according to a previously reported protocol (*46*). This enabled FCS measurements for the determination of hydrodynamic radii. Since it could not be guaranteed that all iC' dots in one batch were functionalized with TMR, the number of MB2 molecules per particle were not determined, except for the case of a regular MB2 based C' dot, i.e. without addition of IPTMS in the synthesis *(vide infra)*.

Synthesis of fluorescent C' dots

In contrast to srC' dots or iC' dots, C' dots are solely composed of silica and are synthesized under basic conditions. C' dots were synthesized according to Ma *et al*. (*30*) The dye concentrations for Cy3 and Cy5 were kept the same as for srC' dots, while MB2 was reduced to 66% of the molar amount used for iC' dots, due to the positive charge of MB2 in basic solution during the synthesis. Here, all dyes had maleimide functional groups, instead of NHS functional groups. The conjugation ratio of dye to MPTMS was 1:25. MB2 C' dots were surface-functionalized with TMR (*46*). Compared to iC' dots, the number of TMR-functionalized particles was much larger, allowing an estimation of concentration by FCS. The purification of C' dots was analogous to iC' dots and srC' dots.

Particle filtration

To increase SNP purity, we performed gel permeation chromatography (GPC) using a BioLogic LP system alongside a 275 nm UV detector with cross-linked copolymer of allyl dextran and N,N'-methylene bisacrylamide (Sephacryl S-300 HR) from GE Healthcare. Particle solutions were up-concentrated by centrifuge spin-filters (GE Healthcare Vivaspin with MWCO 30K), sent through the column with a 0.9 wt% NaCl solution, and collected by a BioFrac fraction collector. The corresponding GPC fractions were transferred back into DI water by washing the particles at least 5 times in a spin-filter. The cleaning steps via dialysis and GPC are of crucial importance to remove unreacted MPTMS, whose thiol groups could alter the photophysical properties in post synthesis particle characterization. Purified samples were subjected to storage in DI water in the dark at 4 °C for further characterization.

^{29}Si, ^{27}Al and ^{13}C solid-state NMR characterization

Solid-State NMR (ssNMR) samples were synthesized according to the protocol described above. For one ssNMR sample five 10 mL batches per particle type were synthesized and combined into one sample. Samples were freeze-dried and then kept in a vacuum oven for three days at 30 °C.

^{29}Si and ^{13}C solid state NMR (ssNMR) experiments were conducted on a Bruker Avance DSX NMR spectrometer with a 9.4 T magnet (400.24 MHz proton Larmor frequency, 100.64 MHz ^{13}C Larmor frequency, 79.52 MHz ^{29}Si Larmor frequency) using probe heads for rotors of 7 mm (^{29}Si NMR) and 4 mm diameters (^{13}C NMR). The ^{27}Al NMR experiments were performed on a Bruker Avance NMR spectrometer with a

16.45 T magnet (182.47 MHz ^{27}Al Larmor frequency) using a probe head for rotors of 2.5 mm diameter.

^{29}Si cross-polarization/magic angle spinning (CP/MAS) NMR experiments were conducted in rotors of 7 mm diameter spinning at 5.0 kHz. The CP parameters were optimized with 4,4-dimethyl-4-silapentane-1-sulfonic acid (DSS), which also served as secondary chemical shift standard at 1.50 ppm. The ^{29}Si CP/MAS NMR spectra were acquired with a 5 second repetition time, 5 ms CP contact time, acquiring 1200 scans (0% srC' dots), 800 scans (30% srC' dots), and 1440 scans (60% srC' dots).

^{27}Al spectra were acquired by single pulse excitation. The ^{27}Al NMR chemical shift scale was referenced externally against potassium alum at -0.033 ppm as a secondary reference. The 90 degree pulse time was also determined on this sample. The final 1-d MAS spectra were acquired with a nominally 10 degree pulse (on a nearly cubic sample) at 95 kHz rf field strength at 25.00 kHz sample spinning with 100 ms repetition times accumulating 7200 scans. The ^{27}Al background of probe and rotor were characterized by acquiring the spectrum of an empty rotor under identical conditions. The signal of the empty rotor was subtracted from the sample spectra.

For ^{13}C CP/MAS NMR experiments samples were spun at 7.0 kHz at the magic angle. The experimental parameters for the ^{13}C CP/MAS experiments with TPPM proton decoupling were optimized on glycine, whose carbonyl resonance also served as external, secondary chemical shift standard at 176.06 ppm. For the final ^{13}C CP/MAS NMR spectrum 1600 scans (0% srC' dots and 30% srC' dots) and 2400 scans (60% srC' dots) were accumulated using 200 μs CP contact times and 3.0 s repetition times due to the probe duty cycle.

Fluorescence correlation spectroscopy

Fluorescence correlation spectroscopy (FCS) experiments were performed on a home-built instrument based on a confocal microscope setup. A 635 nm solid state diode laser was used as excitation source (excitation intensity 5 kW/cm^2). The fluorescence signal was split into two paths by a 50/50 beam splitter (Chroma) and spectrally filtered from scattered light by two 650 nm long pass filters (Chroma). Photons were collected by two different avalanche photodiode detectors (SPCM 14, Perkin-Elmer) to eliminate effects of afterpulsing and dead-time, as well as uncorrelated noise in the correlation curves (*41*). The photocurrents from the two detectors were digitally cross-correlated with a correlator card (Correlator.com). Before each set of measurements, the observation volume was calibrated with Alexa Fluor 647 as a standard dye. For TMR-functionalized particles a 543 nm HeNe laser was employed and TMR was used as standard dye.

Data were collected in sets of three consisting of five 30 s runs each. Correlation curves were fit to a correlation function, $G(\tau)$, accounting for translational and rotational diffusion, as well as for fast photophysical processes (photoinduced cis-trans isomerization or singlet-triplet transitions), as shown in equation (1):

$$G(\tau) = 1 + \frac{1}{N} \cdot \left(1 + \frac{\tau}{\tau_D}\right)^{-1} \cdot \left(1 + \frac{\tau}{\kappa^2 \tau_D}\right)^{-1/2} \cdot \frac{1}{1-T} \cdot \left(1 - T + T \cdot e^{-\tau/\tau_T}\right) \cdot \left(1 + a_R e^{-\tau/\tau_R}\right) \quad (1)$$

Here, N is the mean number of particles within the detection volume, and κ is the structure factor calculated from a known diffusion coefficient and given by $\kappa = \omega_z/\omega_{xy}$, where ω_{xy} and ω_z are the radial and axial radii, respectively, of the observation volume. τ_D is the characteristic diffusion time of a particle through the observation volume. τ_D is defined as $\tau_D = \omega_{xy}/4D$, where D is the respective particle diffusion coefficient. T is the time- and space-averaged fraction of fluorophores in the cis photoisimer form or triplet state (triplet state population), respectively, and τ_T is the characteristic relaxation time that is related to either the photoisomerization process or singlet-triplet state transitions. τ_R is the typical particle rotation time and a_R the pre-exponential amplitude of rotational relaxation. The Stokes-Einstein relation was applied to determine particle diameters, equation (2):

$$d = 2\frac{k_B T}{6\pi\eta D} \tag{2}$$

with k_B being the Boltzmann's constant, T being the absolute temperature, and η being the dynamic viscosity. The average number of dyes per particle, n, was calculated according to equation (3):

$$\mathrm{n} = \frac{\mathrm{C_{dye}}}{\mathrm{C_{particle}}} \tag{3}$$

Here C_{dye} is the measured dye concentration derived from the dye extinction coefficient using the relative absorbance, and $C_{particle}$ is the particle concentration determined by FCS.

The triplet state population, T, as obtained from FCS measurements for different ATTO647N iC' dots was fitted (see Figure 5.5e) using the logistic function of equation (4):

$$\mathrm{T(x)} = \frac{\mathrm{T}_{max}}{1 + e^{-m(x-x_0)}} \tag{4}$$

where T_{max} is the maximum value of $T(x)$, x is the percentage amount of IPTMS used in the synthesis, x_0 is the IPTMS amount at $\mathrm{T}_{max}/2$, and m is the steepness of the curve.

Cell toxicity studies

BxPC3 pancreatic cancer cells were maintained in RPMI 1640 supplemented with 10% FBS at 37 °C with 5% CO_2. To measure effects of srC' 60% dots or βME on cells, cells at ~70% confluence were washed with PBS, exposed to trypsin, resuspended, and dispensed into 96-well tissue culture plates (20,000 cells per well). Cells were allowed to settle overnight, forming a monolayer ~70-80% confluent. The medium was removed from each well, and replaced with medium supplemented with varying amounts of either 60% srC' dots or βME, or with DMSO (carrier agent for βME) alone as a control, as well as 1X Pen-Strep antibiotic. Cells were then incubated for 6 days (srC' dots) or 16 hours (βME). Following incubation, medium was removed, cells washed with fresh medium and then incubated for one hour with fresh medium and Presto Blue per the manufacturer's recommendations. The absorbance of the Presto Blue was determined at 570 nm (background 600 nm) using a Tecan Safire microplate reader. Absorption was compared to that of a blank (medium plus Presto) to determine %

viability of remaining cells, with the DMSO control lane defined as 100% viability, and the empty wells defined as 0% viability. All experiments were performed in triplicate.

Ensemble photoswitching experiments

Photoswitching behavior was studied in nitrogen bubbled deionized water at pH 7.4, using a 100 μL quartz cuvette (Starna) covered with parafilm for the duration of the experiment. All samples were exposed to a defocused 100 mW/cm^2 633 nm laser for 60 min and subsequently illuminated with a 300 nm UV LED source of 10 mW/cm^2 for 5 min. For every exposure, it was guaranteed that the entire sample window was evenly illuminated. The absorption was measured before and after red light, and after UV light exposure.

Total internal reflection fluorescence microscopy measurements

Single particle and single molecule measurements were performed using an inverted Zeiss Elyra microscope operated in TIRF geometry. Samples were placed on an oil-immersion 1.46 NA 100X objective and simultaneously excited by a 640 nm laser (13 mW) and a 405 nm laser (98 μW). Fluorescence signal was spectrally filtered using a 640 nm band pass filter and recorded with an Andor iXon EMCCD camera. For each sample, multiple movies with a series of 10,000 frames and a resolution of 50 ms/frame were acquired. To avoid focal drift, the 'definite focus' focal-drift compensation was activated during image acquisition. For dual color images, particles we first imaged with 640 nm laser line to avoid excitation of Cy3 and Cy5. After collection, band pass filters

were changed and immediately imaged with the 561 nm laser line (54 mW) and the same 405 nm laser.

Glass bottom dishes (MatTek P35G-0.170-14-C) were coated with streptavidin using a protocol that was previously established[47]. Immediately before the measurement, biotinylated srC' dots, Cy3-biotin, or Cy5-biotin were immobilized on the streptavidin-coated glass bottom dishes by incubation of nanomolar stock concentrations of sample for several minutes before washing away excess dye or particles with PBS. Cy3-biotin was synthesized by first combining biotin-PEG-NHS with cysteamine for 24 hours in the glovebox, followed by the addition of Cy3-maleimide and reaction for another 24 hours (molar ratios 4:2:1). All imaging experiments were performed on sparsely labeled surfaces in 1 mL PBS at pH 7.4 containing an enzymatic oxygen-scavenging system of 50 μL glucose oxidase (10 mg/mL in PBS), 20 μL catalase (2 mg/mL in PBS), and 5% (w/v) glucose. For experiments in the presence of βME, 100 μL βME was added to 10 mL PBS of 5% (w/v) glucose and the pH adjusted to pH 7.4. The enzymatic oxygen-scavenging system was freshly prepared before each measurement by adding respective amounts of glucose oxidase and catalase to the imaging buffer prior to each measurement. Cy5 srC' dot-labeled microtubules were imaged in PEGylated glass bottom dishes under the same imaging conditions as described above. For microtubule labeling and fixation protocols please see the Appendix D.

Particle photon statistical analysis

Photo-switching behavior of hundreds of different nanoparticles were studied using a custom built Matlab script (Figure S5.4). Fluorescence signal locations were

identified by taking a maximum intensity projection of the stack and then placing a 7x7 pixel region around it. Fluorescence time traces for every molecule/particle were extracted by integrating a 7x7 pixel region located around the maximum fluorescence intensity signal in the 7x7 pixel region for each frame of the movie and subsequently converting intensity counts to photons based on the electron multiplication gain settings used during fluorescence signal acquisition. Switching events were identified in time traces as signals greater than five times the standard deviation of the background fluctuations. The number of photons per switching event were determined by integrating the switching event above the threshold and then subtracting the calculated average background of the movie. Optical probe on-off duty cycles were calculated by taking the total on-time within a 100 second window, and then averaging over all nanoparticles not yet photobleached. Only switching events with on-times less than one second (20 frames) were considered for analysis.

Particle image reconstruction

Reconstructed super-resolution STORM images where generated using ImageJ plugin ThunderSTORM (*37*). Approximate locations of the particles were identified as the maximum peak in a region above an intensity threshold five times the standard deviation of the background. Each localization per frame was fit using maximum likelihood fitting (*48*) with a two-dimensional Gaussian point spread function (PSF). The final drift-corrected reconstructed image was 1280x1280 pixels with 20 nm per pixel and viewed using normalized Gaussian rendering. For dual color images, both

channels were reconstructed independently into two different .tiff files then combined to form the dual colored image.

Energy-dispersive X-ray spectroscopy

For sample preparation particle dispersions were up-concentrated using centrifuge spin-filters (GE Healthcare Vivaspin with MWCO 30K) and then drop-casted onto silicon wafers. Samples were kept in a vacuum oven for 7 days at 30 °C. The final dry particle layers were about 500 μm thick. Energy-dispersive X-ray spectroscopy (EDS) measurements were carried out on a TESCAN MIRA3 LM field-emission scanning electron microscope with a Quantax System attached, equipped with a Bruker XFlash6160 silicon drift detector. Data were collected at 10 kV. Spectra were normalized for the Si peak and relative peak heights were used to estimate the relative atomic ratios present in the particles.

Determination of singlet oxygen quantum yields

Singlet oxygen quantum yields, Φ_Δ, measurements were carried out in ethanol with DPBF as a singlet oxygen detector molecule. The DPBF band at 410 nm and λ_{max} of each dye were absorption matched across a particle series. For measurements of effective Φ_Δ samples were concentration matched. The spectra were exposed and measured in a 100 μL quartz cuvette (Starna). Samples were evenly exposed to a 635 nm solid-state laser at 3 mW/cm^2 and 1 cm spot size. Measurements were started immediately after DPBF addition. The decrease of the 410 nm DPBF band was measured at various exposure times and corrected against a baseline. Φ_Δ for each sample

was calculated by comparing to MB (Φ_{Δ} = 0.520 in ethanol) as a standard (see example calculation in Appendix D).

Results and Discussion

To vary the chemical composition of photoswitchable sub-10 nm SNPs, we utilized a silica growth quenching mechanism covalently encapsulating Cy5 dye in aqueous solution (see Methods) (*30, 31*). Four different super-resolution Cornell prime dots (srC' dots) were synthesized from varying molar ratios of (3-mercaptopropyl) trimethoxysilane (MPTMS) and tetramethylorthosilicate (TMOS) (Figure 5.1d): 0:10 (0% srC' dots), 3:7 (30% srC' dots), 6:4 (60% srC' dots) and 8:2 (80% srC' dots).

Particle hydrodynamic diameters, d_{sample}, were determined by fluorescence correlation spectroscopy (FCS, Figure 5.2a and 5.2b) employing a fit model that accounts for translational diffusion, photoinduced cis-trans isomerization, and rotational diffusion (see Methods, equations (1) and (2)) (*32, 33*). These measurements yielded hydrodynamic diameters of less than 8 nm for all Cy5 srC' dot species, and showed that srC' dots contained on average 1.1 dye molecules per particle (Figure 5.2a, Methods equation (3), Table S5.1). In order to access hydrodymamic diameters of less than 7 nm enabling rapid renal clearance (*29*), we further investigated size tunability of 60% srC' dots by quenching particle growth via PEG-silane addition at different reaction times (*30*). Careful control of reaction time enabled us to prepare PEGylated particles as small as 5.2 nm (Figure S5.3, Table S5.1), approaching the size of FPs.

To investigate changes of Cy5 dye upon particle encapsulation we measured intensity-matched UV-vis spectra and respective fluorescence emission spectra of srC' dots and free Cy5 dye, in deionized water at pH 7 (Figure 5.2c). In contrast to free dye and 0% srC' dots, other srC' dots exhibited an additional absorption peak emerging around 245 nm and a shoulder around 300 nm. While the peak at 245 nm is likely a

combination of the absorption of mercaptopropyl groups and PEG (Figure S5.2), the shoulder around 310 nm suggests a Cy5-thiol adduct. This adduct has been described in detail (*11-13*), and is a result of thiol binding to the polymethine bridge of Cy5. All particles showed a minor bathochromic shift of Cy5 absorption and emission peaks, and a per dye fluorescence brightness enhancement expected from encapsulation into a rigid silica matrix. Enhancements have been shown to originate from an increase in radiative rate, a decrease in non-radiative rate, or both (*30, 33*). The largest per dye brightness enhancement of 1.9 was observed for the control particle (0% srC' dots), and decreased slightly to 1.7 with increasing MPTMS/TMOS molar ratio (Figure 5.2c).

Our synthetic approach of preparing srC' particles leads to a silica network with a number of different atomic connectivities. To investigate the detailed aluminosilicate network structure, we performed ^{29}Si, ^{27}Al, and ^{13}C solid state NMR (ssNMR) experiments on 0%, 30%, and 60% srC' dots (see Appendix D for details). ^{29}Si ssNMR results (Figure 5.2d) were consistent with increased incorporation of MPTMS lowering the silica network density (as demonstrated by increasing signals for oxygen tri-coordination of silicon (T-groups) versus quarternary coordination (Q-groups)), corroborated by energy-dispersive X-ray spectroscopy (EDS, Figure S5.3). ^{27}Al ssNMR spectra (Figure 5.2e) primarily exhibited four-fold (tetrahedrally) coordinated aluminum, with aluminum atoms likely replacing silicon in the silica network, contributing to particle stabilization below the isoelectric point of SNPs during particle formation (*30*). Finally, solid-state CP/MAS ^{13}C NMR measurements (Figure 5.2f) confirmed successful PEGylation of the srC' dots and revealed that the majority of

sulfur containing moieties are mercaptopropyl groups, but also suggested oxidative formation of disulfide bonds during synthesis (*34*).

We next compared ensemble photoswitching behavior of srC' dots to free Cy5 dye. The Cy5-thiol adduct is formed by exposure to red light (633 nm), leading to a quenching of the primary Cy5-absorption band, and enhancement of a band at 310 nm. The adduct dissociates upon UV light (300 nm) irradiation (Figure 5.1c), leading to reduction of the 310 nm band and recovery of the primary band. Figure 5.3a shows the normalized absorption spectra for a SR imaging cocktail comprised of Cy5 dye and 140 mM βME (Cy5-βME), as well as for 0%, 30%, 60%, and 80% srC' dots without βME. Upon 633 nm illumination of Cy5-βME, the main 647 nm absorption peak decreases while a shoulder at 310 nm emerges. Subsequent exposure to 300 nm light partially restores the 647 nm peak, indicating partial photo-bleaching of some Cy5 molecules, and in agreement with previous observations (*13*). For 0% srC' dots, exposure to 633 nm light causes the 647 nm peak to substantially decrease, but without forming a significant peak at 310 nm. Subsequent exposure to 300 nm light cannot recover the primary peak, but instead further decreases it, indicating photo-bleaching. Thiol containing srC' dots also show the decrease of the 647 nm peak and unchanged shoulder at ~310 nm. However, under 300 nm UV exposure the shoulder absorption decreases and the main peak at 647 nm partially recovers, similar to the Cy5-βME. The extent of recovery of srC' dots increases with increasing thiol content, suggesting that the mercapto-enriched silica matrix can give rise to Cy5-thiol adducts either during the synthesis or upon 633 nm illumination or both.

To better understand the fluorescence characteristics of the particles, we analyzed them using total internal reflection fluorescence microscopy (TIRFM). We prepared Cy5-biotin and biotinylated 0% and 60% srC' dots (Figure 5.1d and Figure S5.4h), immobilized each on streptavidin-coated glass surfaces, and compared srC' dots to immobilized Cy5-biotin with and without βME cocktail via TIRFM. Figures 5.3b and 3c show three fluorescence time traces for each sample in PBS buffer (see Appendix D and Figure S5.5). While Cy5 and 0% srC' dots bleach in a matter of seconds, Cy5-βME and 60% srC' dots, show fluorescence blinking behavior over the entire acquisition time. This suggests that the local thiol group concentration within these srC' dots enables encapsulated Cy5 to enter long-lived dark states. Similar results were obtained by replacing Cy5 with Cy3 (Figures 5.3d, 5.3e, and Figure S5.4g), but with blinking intensities of 60% Cy3 srC' dots substantially enhanced over Cy3-biotin dye. This is further reflected via photon histograms (Figure 5.3f to 5.3i). While Cy5 srC' dots show a factor of about 1.1 more photons per switching event than Cy5-biotin, this factor increases to 2.7 for Cy3. These factors are consistent with brightness enhancements as estimated by steady-state emission spectra of absorption matched samples of Cy3- and Cy5-biotin as compared to respective srC' dots (Figure S5.4 and Table S5.2). Since for specific dyes enhancements via silica encapsulation can easily reach an order of magnitude (see results for DY782 dye in Figure S5.4c and Table S5.2), results suggest a path to ultrabright SR imaging probes.

Another important parameter to evaluate fluorescent probes for STORM is the on-off duty cycle[3]. It should be low to minimize the probability that another probe fluoresces within the diffraction limited area to optimize image resolution according to

the Nyquist criterion (*35*). Analysis yielded averages of 0.0003 for Cy5-biotin, Cy5 60% srC' dots, and Cy3-biotin, and 0.0007 for Cy3 60% srC' dots. These results place 60% srC' dots in the category of viable super-resolution fluorescent probes[3].

To illustrate the biological benefits of srC' dots, we compared the effects of 60% srC' dots and βME when applied to BxPC3 pancreatic cancer cells in complete media. Figure 5.4a shows relative cell viability for BxPC3 cells following 6 days of treatment with 60% srC' dots, versus only a 16-hour treatment with βME. For meaningful comparison, the compound concentrations on the X-axis were scaled as 'fraction of imaging concentration'. This is the concentration typically reported for dye labeling (1 μM for srC' dots used here) (*36*), or for βME in a typical STORM imaging cocktail (140 mM) (*3, 13*). At only 10% (*i.e.* 14 mM) of the typical imaging concentration for βME, substantial cell death is observed after only 16 hours, while srC' dots were well tolerated for 6 days at nearly ten-fold a typical imaging concentration (*i.e.* 7.5 μM).

We next examined the ability of biotinylated srC' dots to generate enhanced resolution by utilizing STORM data processing of TIRFM images. We analyzed image stacks of 60% srC' dots with the ImageJ plugin ThunderSTORM (*37*). Figure 5.4b shows an excerpt from a diffraction-limited TIRFM image with multiple localized srC' dots. The particles seem well resolved by TIRFM alone, but Figure 5.4c shows that several particles only resolved via STORM analysis. This is demonstrated in Figure 5.4d, which zooms in on two particles unresolved by TIRFM, and the accompanying STORM reconstruction of these particles in Figure 5.4e. The inset of Figure 5.4e shows the corresponding cross-sectional line profiles of the diffraction limited TIRFM image (dashed line) and reconstructed STORM image (solid line) revealing a center-to-center

particle distance of 175 nm. Corresponding analysis (Figure 5.4f) of localized particles for their full width half maximum (FWHM), shows a decrease from 215 ± 35 nm to 36 ± 6 nm. To demonstrate dual color STORM, we combined Cy5 (red) and Cy3 (green) srC' dots for imaging (Figures 5.4g and 5.4h). To expand biological relevancy, we used srC' dots coated with amino-group-reactive N-hydroxysuccinimide (NHS) esters to label microtubules (see methods and Appendix D). Figures 5.4i to 5.4k compare TIRFM and STORM images of Cy5 srC' dot labeled microtubules demonstrating resolution enhancement. Figure 5.4j shows a single microtubule while Figure 5.4k reveals multiple parallel microtubules only resolved via STORM.

We were also interested in engineering particles for use in GSD microscopy, which depends upon control over triplet state populations in fluorophores (*6*). In analogy to STORM, additives that enhance photoinduced triplet state formation are added to 'imaging cocktails' (*32, 38*), but often interfere with live cell imaging. We utilized the external heavy atom effect of iodine to finely tune the triplet state population of carbo-rhodamine dye ATTO647N (Figure 5.5a) employing PMPE. Intersystem crossing (ISC, *i.e.* singlet-triplet transition) is a spin forbidden transition usually suppressed, but is enhanced by quantum mechanical spin-orbit coupling. The presence of heavy atoms leads to increased ISC rates for a fluorophore (*39, 40*). By eliminating the effects of detector afterpulsing (Figure 5.2a) (*41*), singlet-to-triplet transitions can be studied by FCS, where increased triplet populations are manifested by increases in amplitudes of fast processes at lag times between 100 ns and 10 μs (*32, 38*).

We prepared iodine containing C' dots (iC' dots) covalently encapsulating ATTO647N dye from assorted ratios of (3-iodopropyl)trimethoxysilane (IPTMS) to

TMOS: 0%, 1%, 2.5%, 5%, 7.5%, 10%, and 20% iC' dots (Figure 5.5a and 5.5b, bottom inset), using a protocol similar to that for srC' dots (see Methods). Figure 5.5b shows the ATTO647N intensity-matched UV-vis spectra of this particle series in deionized water. Spectra exhibited the 647 nm absorption of ATTO647N, as well as a 255 nm UV absorption band which increased with increasing IPTMS incorporation, matching a band from pure IPTMS recorded in 100% anhydrous ethanol to avoid precursor condensation. Iodine was independently evidenced by EDS measurements on 0%, 5%, and 20% iC' dots (Figure S5.6). Particle hydrodynamic diameters determined by FCS (Figure 5.5c) were all below 9 nm (Table S5.3), and increased roughly linearly with increasing IPTMS ratio (Figure 5.5d). The number of dyes per particle stayed close to n=1 over the entire series (Table S5.3).

FCS results in Figure 5.5c reveal a substantial increase in amplitude for singlet-triplet transitions with increasing IPTMS precursor amounts, making iC' dots attractive candidates for GSD microscopy. As shown in Figure 5.5e, the %-triplet population for iC' dots strongly increases between 0% and 10% IPTMS and then saturates, amounting to an increase of about 610% relative to 0% iC' dots. The triplet population follows the iodopropyl-group density in a particle (Figure S5.7). As expected, the fluorescence brightness per dye, as revealed by FCS determined particle brightness, simultaneously decreases to about a fourth of its initial value (Figure 5.5f).

An increase in triplet state dye population is often associated with an increase in singlet oxygen ($^1O_2$) quantum yield, Φ_Δ. $^1O_2$ is produced by energy transfer between the triplet state dye and dissolved triplet oxygen, $^3O_2$ (Figure 5.6a and 5.6b). By introducing a photosensitizer (PS) dye, ultrasmall SNPs transition from diagnostic (passive) to

therapeutic (active) probes, *e.g.* applicable for photodynamic therapy (PDT), where a targeted probe with high Φ_Δ would specifically bind to biological sites of interest, be excited with light to produce $^1O_2$, and induce cell death (*42*). The enhancement of Φ_Δ by heavy atoms in sub-10 nm PEGylated SNPs, a critical size range for renal clearance, to our knowledge has not been reported (*43, 44*).

We measured Φ_Δ for ATTO647N encapsulated in iC' dots by using the singlet oxygen sensor 1,3-diphenylisobenzofuran (DPBF), which forms 1,2-dibenzoylbenzene with $^1O_2$ (Figure 5.6c) as indicated by reduction of a 410 nm absorption band (Figures 5.6d and S5.8). Upon dye encapsulation in 0% iC' dots, Φ_Δ slightly decreased as compared to free dye, likely due to steric shielding. However, values of Φ_Δ increased with increasing IPTMS concentration (Figure 5.6e, see Figure S5.8 for a sample calculation). While the maximum Φ_Δ value of 8.0% is much greater than that for ATTO647N alone (1.2%), it is far below the desired Φ_Δ of 50% for PDT applications (*45*). We therefore synthesized 0%, 7.5%, and 15% iC' dots replacing ATTO647N with methylene blue derivate MB2 (Figure 5.6f inset and Figure S5.9), with resulting MB2 Φ_Δ values up to 71% (Figure 5.6f, Table S5.4), and no signs of dark toxicity ($^1O_2$ generation in the absence of light, Figure S5.10). This places MB2 dye encapsulated in iC' dots in the range of top-performing PSs (*45*), while simultaneously enabling surface functionalization with, *e.g.* targeting moieties and radiolabels providing multifunctional nanoprobes (*46*). Finally, we investigated the ability to co-localize multiple MB2 dyes in one particle (n>1), and measured the apparent singlet oxygen quantum yield of a particle, Φ_Δ^{app} (dye multiplicity effect). For that purpose, we synthesized PEGylated and TMR dye-functionalized sub-10 nm pure silica core NPs (C' dots, *i.e.* without iodide),

enabling estimation of particle concentration, size, and number of dyes per particle by FCS (Figure S5.11) (*46*). Measurements yielded an Φ_{Δ}^{app} of 114% (Figure 5.6f). With an estimated number of 2.9 MB2 dyes per particle, this comprises an estimated Φ_{Δ} contribution of each MB2 dye of about 39% to Φ_{Δ}^{app}. In principle both approaches, *i.e.* PMPE and multiplicity effect, can be combined to maximize Φ_{Δ}^{app} to create potent PDT probes.

Conclusion

In conclusion, we have engineered ultrasmall silica nanoparticles, srC' dots, which incorporate sulfur atoms to quench Cy5 or Cy3 dyes in a reversible manner, enabling SR STORM imaging. The srC' dots exhibit very low cell toxicity compared to commonly employed βME. We have further prepared iC' dots, which use quantum spin-orbit coupling to enhance the formation of triplet-states in ATTO647N or MB2 dyes. These iC' dots may be of use for GSD microscopy, and may have potential therapeutic value, with MB2 containing iC' dots producing high yields of singlet oxygen. Since a number of characteristics of the SNPs studied, including size and surface PEGylation, are similar to clinically translated probes (*29*), we expect these materials to provide increased relevance of SR fluorescence imaging methods and PDT to e.g. oncological studies and clinical applications. While we demonstrated the concept of particle molecular photo-engineering of dye-containing SNPs for only a few dye and additive chemistries, we expect it to be applicable to a variety of fluorophores and nanoparticle compositions. We therefore hope, that this work will stimulate research and development activities in a variety of communities.

Figures

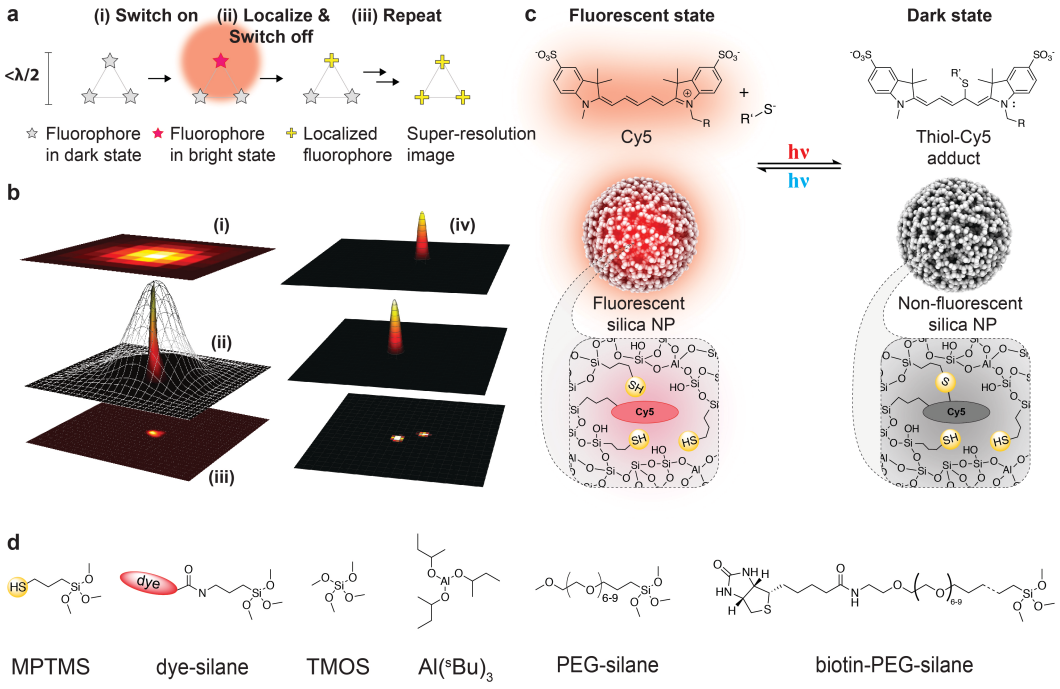

Figure 5.1. ***Introduction to particle synthesis and the principle of STORM.*** **a**, Principle of stochastical optical reconstruction microscopy (STORM) imaging of a hypothetical triangular and switchable red fluorophore arrangement with side lengths below the diffraction limit (<λ/2). Fluorophores are stochastically switched on (i), localized, and switched off (ii). Repeated photoswitching and localization (iii) resolves spatial features below the diffraction limit. **b**, Visualization of localization algorithm used in STORM. Pixelated point-spread function of a single fluorophore, imaged by total internal reflection fluorescence microscopy (TIRFM) (i) is modeled by a three-dimensional Gaussian point-spread function (PSF) (ii). Fitting multiple fluorescent states from the same fluorophore leads to a super-resolution image with a localization distribution (iii). When the point-spread functions of two different fluorophores overlap in TIRFM, each fluorophore can be individually localized using STORM (iv). **c**, Cy5 reversible photoswitching mechanism in the presence of thiol components from fluorescent state (left) to dark state (right) with corresponding particle rendering and local molecular structure models. R and R' represent functional groups attached by a carbon atom. **d**, Chemical structures of the precursor molecules used for the synthesis of biotin-functionalized srC' dots. From left to right: (3-

mercaptopropyl)trimethoxysilane (MPTMS), dye-silane, tetramethylorthosilicate (TMOS), aluminum-tri-sec-butoxide ($Al(^{s}Bu)_3$), polyethylene glycol-silane (PEG-silane), and biotin-polyethylene glycol-silane (biotin-PEG-silane) (dotted line represents a thioether linker).

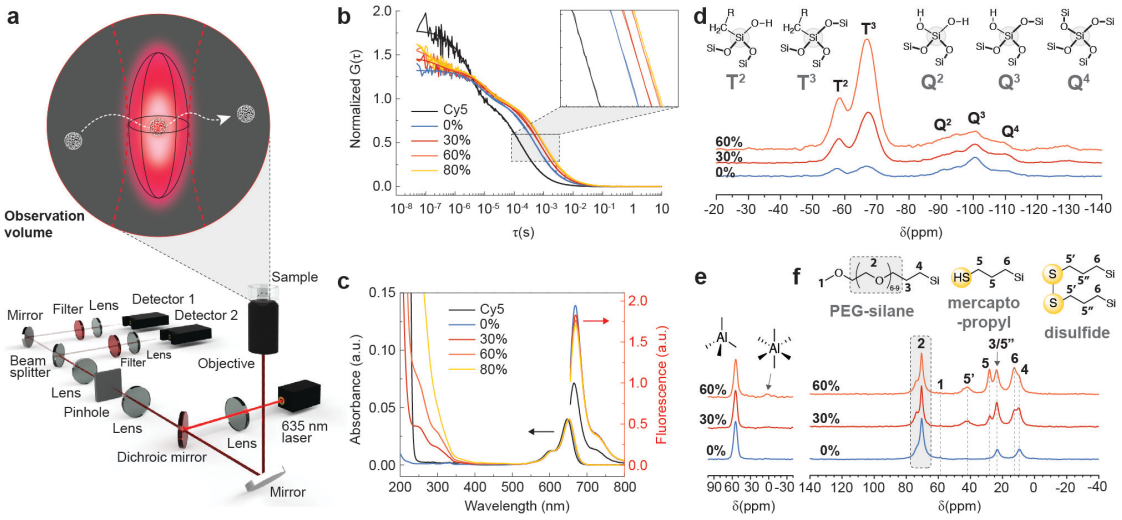

Figure 5.2. ***Materials characterization.*** **a**, Fluorescence correlation spectroscopy (FCS) setup. A laser is focused into an aqueous solution above an objective, forming an observation volume. The fluorescence signal from particles diffusing trough the observation volume is split detected by two avalanche photo diode (APD) detectors to suppress afterpulsing effects. **b**, Normalized FCS autocorrelation curves of free Cy5 dye and various 25 min srC' dots with increasing thiol content (0, 30, 60, and 80%). Corresponding fits used a correlation function with translational diffusion, cis-trans isomerization, and rotational diffusion components. **c**, Corresponding intensity-matched absorption (left black arrow) and emission spectra (right red arrow) from 645 nm excitation. **d**, Solid-state ^{29}Si CP/MAS NMR spectra of srC' dots (0, 30, and 60%) showing T- and Q-group assignments with structural illustrations. **e**, Solid-state ^{27}Al MAS NMR spectra of srC' dots (0, 30, and 60%) with assignments to four- and six-fold coordinated aluminum. **f**, Solid-state ^{13}C CP/MAS NMR spectra of srC' dots (0, 30, and 60%) with peak assignments to carbons from PEG-silane, mercaptopropyl, and disulfide groups. The peak of carbon position 5" at 22 ppm is only partially visible as a high-field shoulder of the carbon peak of position 3.

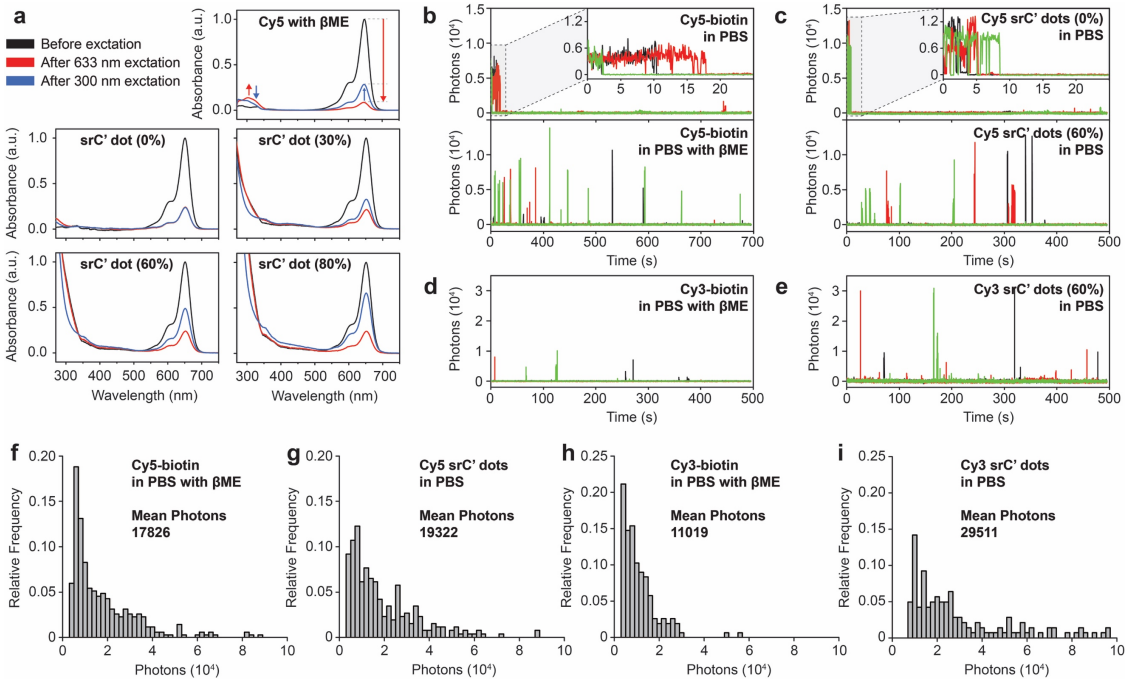

Figure 5.3. ***Photo-physical behavior of srC' dots.*** **a**, Photoswitching absorption spectra, before excitation (black), after 30 min 633 nm light (red, arrows), and 5 min 300 nm light (blue, arrows) exposure, of Cy5 in DI water in the presence of βME and different srC' dots (0, 30, 60, and 80%) in the absence of βME. **b** to **e,** Single molecule and single particle fluorescence traces recorded for different imaging buffer conditions with insets highlighting short time behavior in **b** and **c**. Black, red, and green lines refer to three different fluorophores or particles. **f** to **i,** Photon histograms of different dyes and particles for different imaging buffer conditions (as indicated).

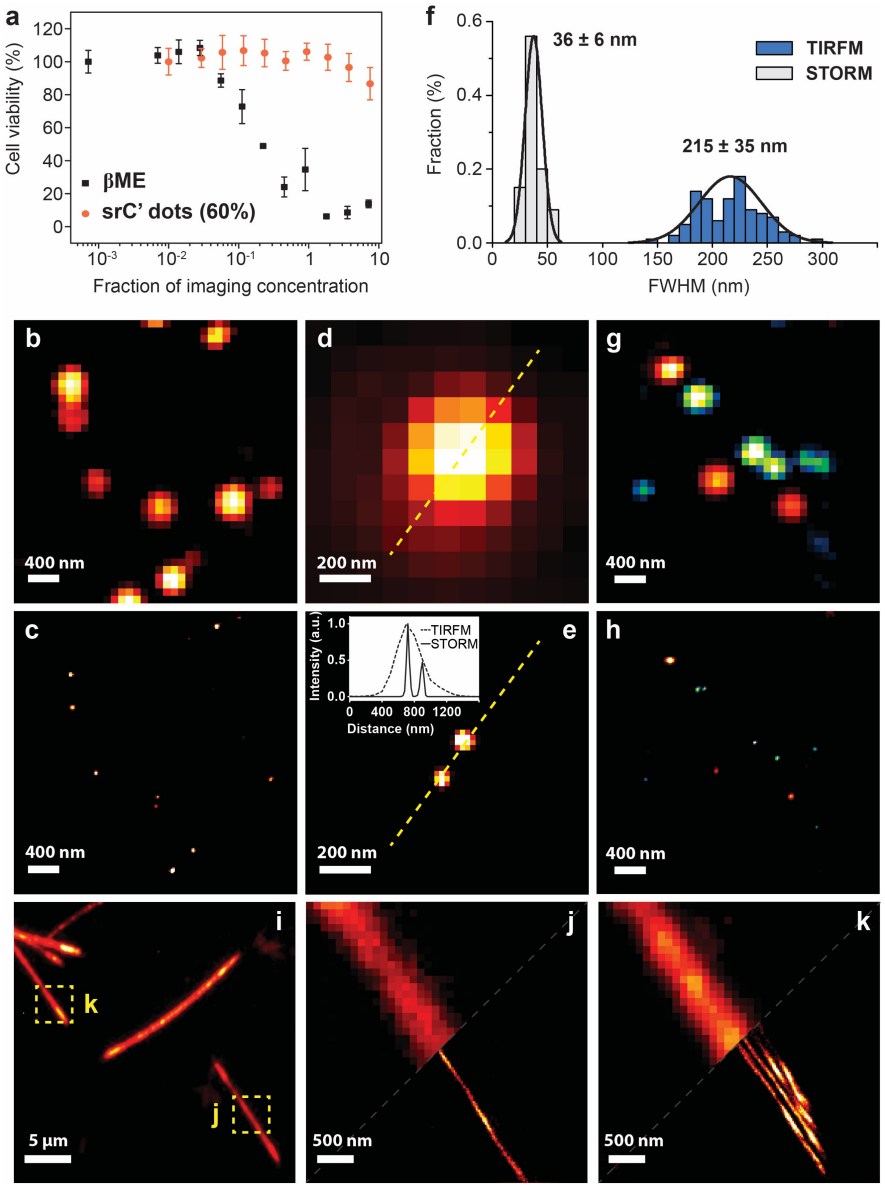

Figure 5.4. ***Cell viability and STORM microscopy.*** **a,** Cell viability tests with BxPC3 cell line in complete media under the influence of βME or Cy5 srC' dots (60%) at different concentrations, normalized to typical values used in STORM microscopy for comparative purposes as detailed in the text. Error bars represent the standard deviation from the mean of three independent experiments. **b** and **d,** Total internal reflection fluorescence microscopy (TIRFM) images of Cy5 srC' dots (60%) in PBS in the absence of βME. **c** and **e,** Corresponding reconstructed super-resolution images. For yellow lines in **d** and **e** line intensity profiles are plotted in the inset of **e** revealing resolution enhancement for the reconstructed STORM image (solid line) over the diffraction limited TIRFM image (dashed line). **f,** FWHM image analysis of TIRFM

images and reconstructed super-resolution images from STORM. **g,** Dual color TIRFM images of Cy5 srC' dots and Cy3 srC' dots in PBS in the absence of βME, and **h,** corresponding reconstructed super-resolution image. **i,** TIRFM image of Cy5 srC' dots labeled microtubules. **j** and **k,** SR images of a single microtuble and multiple parallel microtubules partially overlaid with conventional TIRFM images of selected areas from **i** (yellow boxes).

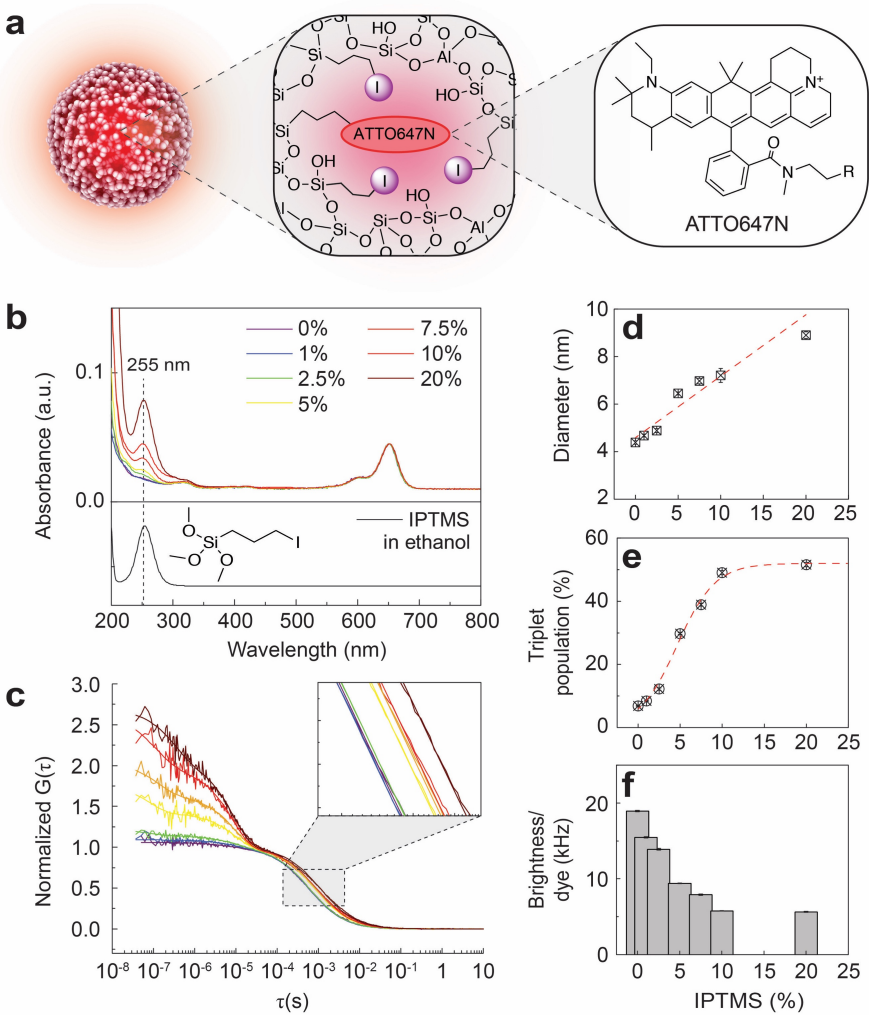

Figure 5.5. ***Particle molecular triplet state photo-engineering.*** **a,** ATTO647N particle rendering with local molecular structure model and chemical structure of encapsulated ATTO647N. R represents a functional group attached by a carbon atom. **b,** Comparison of absorption spectra of ATTO647N iC' dots in water (top), synthesized from different relative molar amounts of (3-iodopropyl) trimethoxysilane (IPTMS) precursor (0, 1, 2.5, 5, 7.5, 10, and 20%), and of IPTMS in ethanol (bottom). The inset shows the chemical structures of IPTMS. **c,** Normalized afterpulse-corrected FCS autocorrelation curves of ATTO647N iC' dots from **b**. Fits used a correlation function with translational diffusion, singlet-triplet transition, and rotational diffusion components. Inset shows enlarged correlation curves with fits. **d,** Diameter from FCS fits plotted against ITPMS precursor amount. **e,** Triplet population plotted against IPTMS precursor amount. Red dotted lines in **d** and **e** serve as visual guides. **f,** FCS derived brightness per dye plotted against IPTMS precursor amount.

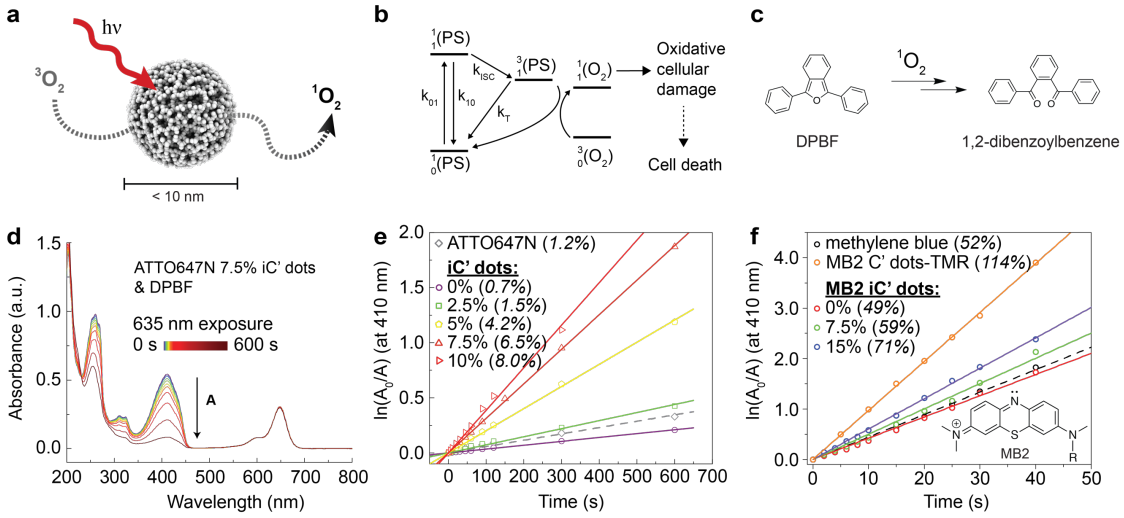

Figure 5.6. ***Singlet oxygen quantum yield determination.*** **a,** Particle rendering with schematic of singlet oxygen, $^1O_2$, diffusing through the microporous silica network and being transformed into triplet oxygen, $^3O_2$, by encapsulated dyes under red light illumination. **b,** Simplified Jablonski diagram illustrating the creation of singlet oxygen. $_0{}^1$(PS) denotes the singlet ground state, while $_1{}^1$(PS) and $_1{}^3$(PS) denote electronically excited singlet and triplet states of a dye photosensitizer (PS), respectively. $_0{}^3(O_2)$ and $_1{}^1(O_2)$ denote triplet ground state and excited singlet state of molecularly dissolved oxygen, respectively. **c,** Singlet oxygen sensor 1,3-diphenylisobenzofuran (DPBF) and its reaction to 1,2-dibenzoyl-benzene in the presence of $^1O_2$. **d,** Absorption spectra of a solution of ATTO647N encapsulating 7.5% iC'dots and DPBF, irradiated at 635 nm (ATTO647N absorption band) for 0 s to 600 s (black arrow). Singlet-oxygen generation for, **e,** ATTO647N dye (dashed line) as compared to ATTO647N encapsulating 0, 2.5, 5, 7.5 and 10 % iC'dots (solid lines). Values for Φ_Δ are in parentheses. **f,** methylene blue dye (dashed line) as compared to MB2 encapsulating 0, 7.5, 15% iC'dots, and MB2 encapsulating C' dots with TMR surface functionalization (solid lines). Values for Φ_Δ are in parentheses. The inset of **f** shows the chemical structure of encapsulated methylene blue derivate MB2. R represents a functional group attached by a carbon atom.

Acknowledgements

This work was funded by the Department of Energy, Office of Science, Basic Energy Sciences, under Award No. DE-SC0010560. J.A.H. thanks the National Institutes of Health (NIH) for financial support under Award No. U54CA199081. J.A.E. would like to thank the Alfred P. Sloan Foundation's Minority Ph.D. Program for financial support. This work made use of the Cornell Center for Materials Research (CCMR) shared facilities which are supported through the NSF MRSEC program (DMR-1719875) at Cornell. Imaging data was acquired through the Cornell University Biotechnology Resource Center, with NSF funding (DBI-1428922) for the shared Zeiss Elyra Microscope. R.A.C. and W.P.K. acknowledge funding from the National Institutes of Health (GM122575, CA201402, CA210184). The authors gratefully acknowledge B. Baird, W. Zipfel and R. Williams (Cornell University) for helpful discussion and kind experimental assistance.

F. F. E. Kohle and U. B. Wiesner developed the experimental design. F. F. E. Kohle developed and synthesized nanoparticles, conducted and analyzed steady-state absorption and emission spectroscopy, FCS, EDS and ensemble photoswitching experiments. N. Dhawan and S. Li helped with optimization and synthesis of nanoparticles. U. Werner-Zwanziger and J. Zwanziger acquired and analyzed ssNMR data. S. Li performed singlet oxygen quantum yield measurements. J. A. Hinckley, F. F. E. Kohle, and J. A. Erstling carried out microscopy measurements and photon statistical analysis. Cell studies were carried out by W. P. Katt. All authors were involved in data interpretation and discussion.

REFERENCES

(*1*) Hell, S. W. Far-Field Optical Nanoscopy. *Science*, **316,** 1153–1158 (2007).

(*2*) Sahl, S. J., Hell, S. W., & Jakobs, S. Fluorescence nanoscopy in cell biology. *Nat. Rev. Mol. Cell Biol.*, **18,** 685–701 (2017).

(*3*) Dempsey, G. T., Vaughan, J. C., Chen, K. H., Bates, M., & Zhuang, X. Evaluation of fluorophores for optimal performance in localization-based super-resolution imaging. *Nat. Methods*, **8,** 1027–1036 (2011).

(*4*) Fernández-Suárez, M., & Ting, A. Y. Fluorescent probes for super-resolution imaging in living cells. *Nat. Rev. Mol. Cell Biol.*, **9,** 929–943 (2008).

(*5*) Klar, T. A., & Hell, S. W. Subdiffraction resolution in far-field fluorescence microscopy. *Opt. Lett*, **24,** 954 (1999).

(*6*) Bretschneider, S., Eggeling, C., & Hell, S. W. Breaking the Diffraction Barrier in Fluorescence Microscopy by Optical Shelving. *Phys. Rev. Lett*, **98,** (2007).

(*7*) Rust, M. J., Bates, M., & Zhuang, X. Sub-diffraction-limit imaging by stochastic optical reconstruction microscopy (STORM). *Nat. Methods*, **3**, 793–796 (2006).

(*8*) Hess, S. T., Girirajan, T. P. K., & Mason, M. D. Ultra-High Resolution Imaging by Fluorescence Photoactivation Localization Microscopy. *Biophys. J*, **91,** 4258–4272 (2006).

(*9*) Betzig, E. *et al*. Imaging Intracellular Fluorescent Proteins at Nanometer Resolution. *Science*, **313,** 1642–1645 (2006).

(*10*) Levitus, M., & Ranjit, S. Cyanine dyes in biophysical research: the photophysics of polymethine fluorescent dyes in biomolecular environments. *Q Rev Biophys*, **44,** 123–151 (2010).

(*11*) Heilemann, M., Margeat, E., Kasper, R., Sauer, M., & Tinnefeld, P. Carbocyanine Dyes as Efficient Reversible Single-Molecule Optical Switch. *J.*

Am. Chem. Soc., **127,** 3801–3806 (2005).

(*12*) Heilemann, M., van de Linde, S., Mukherjee, A., & Sauer, M. Super-Resolution Imaging with Small Organic Fluorophores. *Angew. Chem. Int. Ed.*, **48,** 6903–6908 (2009).

(*13*) Dempsey, G. T. *et al*. Photoswitching Mechanism of Cyanine Dyes. *J. Am. Chem. Soc.*, **131,** 18192–18193 (2009).

(*14*) Steinhauer, C., Forthmann, C., Vogelsang, J., & Tinnefeld, P. Superresolution Microscopy on the Basis of Engineered Dark States. *J. Am. Chem. Soc.*, **130,** 16840–16841 (2008).

(*15*) Vaughan, J. C., Jia, S., & Zhuang, X. Ultrabright photoactivatable fluorophores created by reductive caging. *Nat. Methods*, **9,** 1181–1184 (2012).

(*16*) Vaughan, J. C., Dempsey, G. T., Sun, E., & Zhuang, X. Phosphine Quenching of Cyanine Dyes as a Versatile Tool for Fluorescence Microscopy. *J. Am. Chem. Soc*, **135,** 1197–1200 (2013).

(*17*) White, K., Bruckner, J. V., & Guess, W. L. Toxicological Studies of 2-Mercaptoethanol. *J. Pharm. Sci*, **62,** 237–241 (1973).

(*18*) Huang, B., Wang, W., Bates, M., & Zhuang, X. Three-Dimensional Super-Resolution Imaging by Stochastic Optical Reconstruction Microscopy. *Science*, **319,** 810–813 (2008).

(*19*) Lidke, K. A., Rieger, B., Jovin, T. M., & Heintzmann, R. Superresolution by localization of quantum dots using blinking statistics. *Opt. Express*, **13,** 7052 (2005).

(*20*) Hu, D., Tian, Z., Wu, W., Wan, W., & Li, A. D. Q. Photoswitchable Nanoparticles Enable High-Resolution Cell Imaging: PULSAR Microscopy. *J. Am. Chem. Soc*, **130,** 15279–15281 (2008).

(*21*) Gayda, S., Hedde, P. N., Nienhaus, K., & Nienhaus, G. U. Probes for Nanoscopy: Fluorescent Proteins. *In Springer Series on Fluorescence Far-Field Optical Nanoscopy* 111–158 (2011).

(*22*) Wang, Y., Fruhwirth, G., Cai, E., Ng, T., & Selvin, P. R. 3D Super-Resolution

Imaging with Blinking Quantum Dots. *Nano Lett.*, **13,** 5233–5241 (2013).

(*23*) Efros, A. L., & Nesbitt, D. J. Origin and control of blinking in quantum dots. *Nat. Nanotechnol.*, **11,** 661–671 (2016).

(*24*) Bruchez Jr., M., Moronne, M., Gin, P., Weiss, S., & Alivisatos, A. P. Semiconductor Nanocrystals as Fluorescent Biological Labels. *Science*, **281,** 2013–2016 (1998).

(*25*) Fölling, J. et al. Synthesis and Characterization of Photoswitchable Fluorescent Silica Nanoparticles. *Small*, **4,** 134–142 (2008).

(*26*) Zhu, M.-Q. et al. Spiropyran-Based Photochromic Polymer Nanoparticles with Optically Switchable Luminescence. *J. Am. Chem. Soc*, **128,** 4303–4309 (2006).

(*27*) Fukaminato, T., Sasaki, T., Kawai, T., Tamai, N., & Irie, M. Digital Photoswitching of Fluorescence Based on the Photochromism of Diarylethene Derivatives at a Single-Molecule Level. *J. Am. Chem. Soc*, **126,** 14843–14849 (2004).

(*28*) Aramendía, P. F., & Bossi, M. L. Probes for Nanoscopy: Photoswitchable Fluorophores. In Springer Series on *Fluorescence Far-Field Opitcal Nanoscopy* 189–213 (2012).

(*29*) Phillips, E. *et al*. Clinical translation of an ultrasmall inorganic optical-PET imaging nanoparticle probe. *Sci. Transl. Med*, **6,** 260ra149-260ra149 (2014).

(*30*) Ma, K. *et al*. Control of Ultrasmall Sub-10 nm Ligand-Functionalized Fluorescent Core–Shell Silica Nanoparticle Growth in Water. *Chem. Mater*, **27,** 4119–4133 (2015).

(*31*) Ma, K., Zhang, D., Cong, Y., & Wiesner, U. Elucidating the Mechanism of Silica Nanoparticle PEGylation Processes Using Fluorescence Correlation Spectroscopies. *Chem. Mater*, **28,** 1537–1545 (2016).

(*32*) Widengren, J., & Schwille, P. Characterization of Photoinduced Isomerization and Back-Isomerization of the Cyanine Dye Cy5 by Fluorescence Correlation Spectroscopy. *J. Phys. Chem. A*, **104,** 6416–6428 (2000).

(*33*) Larson, D. R. et al. Silica Nanoparticle Architecture Determines Radiative

Properties of Encapsulated Fluorophores. *Chem. Mater*, **20,** 2677–2684 (2008).

(*34*) Kao, H.-M. et al. Oxidative transformation of thiol groups to disulfide bonds in mesoporous silicas: a diagnostic reaction for probing distribution of organic functional groups. *New J. Chem*, **33,** 2199 (2009).

(*35*) Shannon, C. E. Communication in the Presence of Noise. *Proceedings of the IRE*, **37,** 10–21 (1949).

(*36*) van de Linde, S. *et al*. Direct stochastic optical reconstruction microscopy with standard fluorescent probes. *Nat. Protoc.*, **6,** 991–1009 (2011).

(*37*) Ovesný, M., Křížek, P., Borkovec, J., Švindrych, Z., & Hagen, G. M. ThunderSTORM: a comprehensive ImageJ plug-in for PALM and STORM data analysis and super-resolution imaging. *Bioinformatics*, **30,** 2389–2390 (2014).

(*38*) Chmyrov, A., Sandén, T., & Widengren, J. Iodide as a Fluorescence Quencher and Promoter—Mechanisms and Possible Implications. *J. Phys. Chem. B*, **114,** 11282–11291 (2010).

(*39*) Koziar, J. C., & Cowan, D. O. Photochemical heavy-atom effects. *Acc. Chem. Res*, **11,** 334–341 (1978).

(*40*) Kasha, M. Collisional Perturbation of Spin-Orbital Coupling and the Mechanism of Fluorescence Quenching. A Visual Demonstration of the Perturbation. *J. Chem. Phys*, **20,** 71–74 (1952).

(*41*) Widengren, J., Mets, U., & Rigler, R. Fluorescence correlation spectroscopy of triplet states in solution: a theoretical and experimental study. *J. Phys. Chem.*, **99,** 13368–13379 (1995).

(*42*) Lucky, S. S., Soo, K. C., & Zhang, Y. Nanoparticles in Photodynamic Therapy. *Chem. Rev.*, **115,** 1990–2042 (2015).

(*43*) Kim, S. *et al*. Organically Modified Silica Nanoparticles with Intraparticle Heavy-Atom Effect on the Encapsulated Photosensitizer for Enhanced Efficacy of Photodynamic Therapy. *J. Phys. Chem. C*, **113,** 12641–12644 (2009).

(*44*) Zhou, L., Wei, S., Ge, X., Zhou, J., Yu, B., & Shen, J. External Heavy-Atomic Construction of Photosensitizer Nanoparticles for Enhanced in Vitro Photodynamic Therapy of Cancer. *J. Phys. Chem. B*, **116,** 12744–12749 (2012).

(*45*) Ormond, A., & Freeman, H. Dye Sensitizers for Photodynamic Therapy. *Materials*, **6,** 817–840 (2013).

(*46*) Ma, K., & Wiesner, U. Modular and Orthogonal Post-PEGylation Surface Modifications by Insertion Enabling Penta-functional Ultrasmall Organic-Silica Hybrid Nanoparticles, *Chem. Mater*, **29,** 6840–6855 (2017).

(*47*) Kao T. et al. Fluorescent Silica Nanoparticles with Well-Separated Intensity Distributions from Batch Reactions, *Nano Lett.*, in press (2018).

(*48*) Mortensen, K. I., Churchman, L. S., Spudich, J. A., & Flyvbjerg, H. Optimized localization analysis for single-molecule tracking and super-resolution microscopy. *Nat. Methods*, **7,** 377–381 (2010).

APPENDIX D

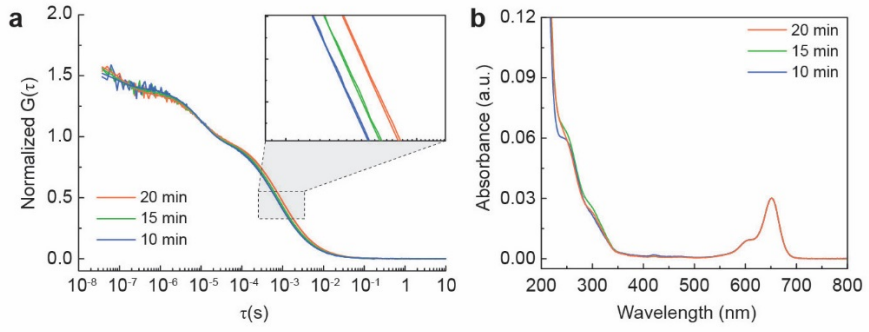

Figure S5.1. ***Particle size tuning.*** **a**, Normalized FCS autocorrelation curves of srC' dots synthesized at constant MPTMS to TMOS precursor ratio (60%) with particle growth quenched at 10 min (blue), 15 min (green), and 20 min (orange). Corresponding fits used a correlation function with translational diffusion, cis-trans isomerization, and rotational diffusion components. Shifts to larger lag times for the translational diffusion relaxation indicates larger particles for longer reaction times. **b**, Corresponding srC' dot absorption spectra normalized to Cy5 absorption. Variations in absorption spectra of these srC' dots were minimal and the characteristic shoulder at 310 nm was maintained.

Sample	**molar ratio *of* *MPTMS***	***Reaction time*** **[min]**	***d*** **[nm]**	***n*** **[#]**
Cy5-NHS	-	-	1.3	1.0
Cy5 srC' dots	0%	25	4.1	1.2
Cy5 srC' dots	30%	25	5.8	1.1
Cy5 srC' dots	60%	25	7.2	1.1
Cy5 srC' dots	80%	25	7.7	1.2
Cy5 srC' dots	60%	10	5.2	1.1
Cy5 srC' dots	60%	15	5.7	1.3
Cy5 srC' dots	60%	20	6.7	1.3

Table S5.1. Molar ratio of MPTMS relative to TMOS, reaction time, hydrodynamic diameter, *d*, and number of dyes per particle, *n*.

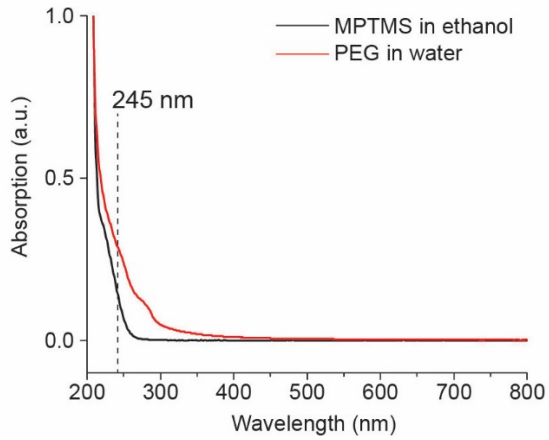

Figure S5.2. UV-vis spectra of the precursor (3-mercaptopropyl)trimethoxysilane (MPTMS) in ethanol and polyethylene glycol (PEG) in water.

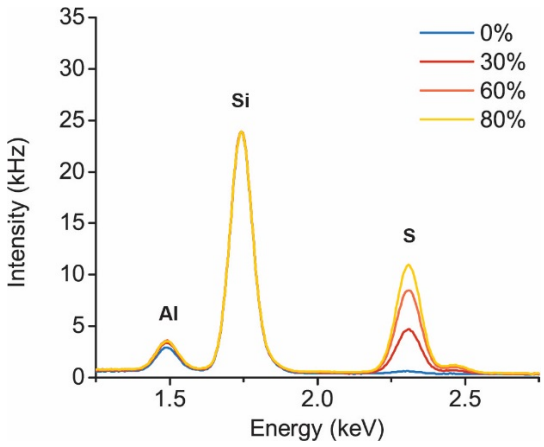

Figure S5.3. ***EDS spectra of srC' dots.*** EDS spectra of the 0%, 30%, 60%, and 80% srC' dots with peak assignments for aluminum (Al), silicon (Si), and sulfur (S).

Detailed compositional analysis of srC' dots via solid-state NMR spectroscopy and energy-dispersive X-ray spectroscopy (EDS)

We performed ^{29}Si, ^{27}Al, and ^{13}C solid state NMR (ssNMR) experiments on three particles: A 0% srC' dot negative control, and two (30% and 60%) srC' dot samples. Figure 5.2d in the main text shows the corresponding ^{29}Si ssNMR spectra. Each spectrum exhibits well separated chemical shifts for T- and Q-groups, respectively. The peaks located around -58 ppm and -67 ppm correspond to T^2 ($R\text{-}Si(OSi)_2(OH)$) and T^3 ($R\text{-}Si(OSi)_3$) groups, while peaks located around -95 ppm, -100 ppm, and -110 ppm reflect Q^2 ($Si(OSi)_2(OH)_2$), Q^3 ($Si(OSi)_3(OH)$), and Q^4 ($Si(OSi)_4$) groups, respectively (see corresponding local Si structures in insets of Figure 5.2d). Probably some amount of silica substitution by aluminum, for example of the Q^3 groups ($Si(OSi)_2(OAl)(OH)$), leads to the broadening of the Q species especially between -90 and -100 ppm. In case of 0% srC' dots, Q-group peaks dominate the spectrum expected from lower molar amounts of PEG-silane as compared to TMOS, and consistent with earlier studies on such sub-10 nm aluminosilicate particles (*S1*). For ultrasmall silica nanoparticles (C' dots), the presence of T-groups can only be explained by silicon atoms which have capped via termination of particle growth. For unmodified C' dots, this should occur only at the surface of the particle, where PEG-silane is bound to the silica surface. However, for srC' dots, the surface to volume ratio decreases with increasing particle size, moving from 0% (4.1 nm diameter, ~53 nm^2 surface area, ~36 nm^3 volume, ratio = 1.47), to 30% (5.8 nm diameter, ~106 nm^2 surface area, ~102 nm^3 volume, ratio = 1.03), to 60% srC' dots (7.2 nm diameter, ~163 nm^2 surface area, ~195 nm^3 volume, ratio = 0.84). The increase in T-group peak intensity relative to that of Q-group peaks,

and concomitant decrease in silica network density despite comparatively less material being located at the surface of the sphere, can only be due to incorporation of increasing amounts of MPTMS into the internal silica matrix. Furthermore, since the local surface PEG-silane chemistry itself is not expected to change substantially as a function of particle size, the increasing T^3 to T^2 ratio moving from 0% to 60% srC' dots is also indicative of increasing amounts of thiol-silane (MPTMS) incorporated into the aluminosilicate network. Increased presence of sulfur in the particle network was independently corroborated using energy-dispersive X-ray spectroscopy (EDS). Figure S5.2 shows EDS spectra for 0%, 30%, 60%, and 80% srC' dots. For comparison, the spectra were normalized to the silicon peak intensity at 1.75 keV, exhibiting a clear increase of the relative sulfur peak intensity at 2.31 keV. The intensity ratios between the three peaks for 30%, 60%, and 80% srC' dots were 1.0:1.8:2.3, close to the sulfur ratios expected from molar MPTMS precursor amounts, 1.0:2.0:2.7, used in the three syntheses.

The ^{27}Al NMR spectra of 0%, 30%, and 60% srC' dots (Figure 5.2e) displayed a narrow peak at approximately 54 ppm, consistent with four-fold (tetrahedrally) coordinated aluminum most likely replacing silicon in the silica network, as also indicated in the Q-species signals in the ^{29}Si NMR spectra. In addition, the 60% srC' dot spectrum exhibited a minor component around 5 ppm of six-fold (octahedrally) coordinated aluminum likely due to a small amount of out-of-network aluminum (*S2*). A reduction of Al content was noticeable with increasing MPTMS amount as compared to the control particle: 100% ± 5% (0% srC' dots), 80% ± 5% (30% srC' dots), and 69% ± 5% (60% srC' dots). This is not unexpected, as the sterically demanding 3-

mercaptopropyl ligand, with increasing amounts of MPTMS, may make it more difficult to coordinate aluminum into four-fold coordinated sites with silicon.

We performed solid-state CP/MAS ^{13}C NMR measurements on these hybrid SNPs to characterize the local structure of the organic moieties (Figure 5.2f). For the 0% srC' dots peaks appeared at 10 ppm, 23 ppm, and 70 ppm, assigned to carbons of the PEG-silane on the particle surface (see inset in Figure 5.2f), and consistent with previously reported observations for PEGylated mesopourous SNPs (*S3*). The same peaks were visible in both mercaptopropyl containing samples, indicating successful PEGylation of the srC' dots. srC' dots showed additional three peaks at around 13 ppm, 28 ppm, and 42 ppm, not seen for 0% srC' dots. The relative intensities of these three peaks increased with increasing MPTMS in the particle synthesis. These peaks correspond to carbons in mercaptopropyl and dipropyl disulfide groups in the particles (Figure 5.2f inset). The broad peak appearing at around 42 ppm is characteristic for the oxidative formation of disulfide bonds during the synthesis (*S4*). The peak at 13 ppm is due to the CH_2 group in mercaptopropyl and dipropyl disulfide groups directly bound to the silicon atom. The majority of sulfur containing moieties are mercaptopropyl groups, suggested by the dominant peak at 28 ppm, originating from α and β carbon atoms of these groups.

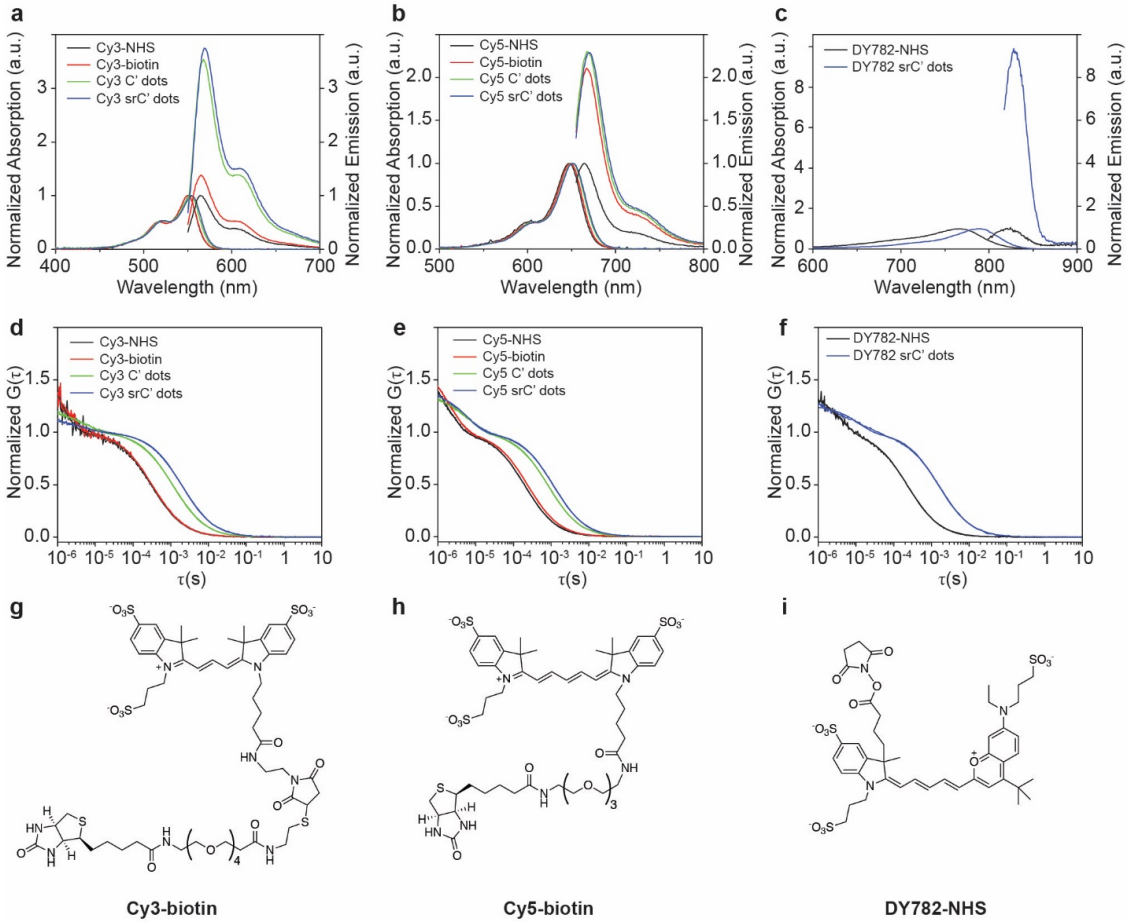

Figure S5.4. ***Comparison of different dyes and srC' dots.*** Normalized steady-state absorption and emission spectra and normalized FCS autocorrelation curves for, **a & d,** Cy3, Cy3-biotin, Cy3-C' dots, and Cy3-srC' dots, **b & e,** Cy5, Cy5-biotin, Cy5-C' dots, and Cy5-srC' dots, and **c & f,** DY782, and DY782-srC' dots. All samples were excited 10 nm below the absorption maximum. Chemical structures of, **g,** Cy3-biotin, **h,** Cy5-biotin, and, **i,** DY782-NHS. While in the case of Cy3 there is a significant brightness enhancement from Cy3-biotin to encapsulated Cy3 (factor of 2.7), the enhancement from Cy5-biotin to encapsulated Cy5 is small (factor of 1.1). Other cyanine dyes, *e.g.* Dy782, show very strong brigtness enhancements upon encapsulation of free dye (factor of 9.3), making them possible candidates for NIR/IR super-resolution dyes when encapsulated in srC' dots.

Sample	BE [%]	d [nm]	n [#]
Cy3-NHS	1.0	1.4	1.0
Cy3-biotin	1.4	1.5	1.0
Cy3 C' dots	3.5	5.1	1.5
Cy3 srC' dots	3.7	7.6	1.1
Cy5-NHS	1.0	1.3	1.1
Cy5-biotin	2.1	1.6	1.0
Cy5 C' dots	2.3	5.4	1.6
Cy5 srC' dots	2.3	7.4	1.1
DY782-NHS	1.0	1.6	1.0
DY782 srC' dots	9.3	10.6	1.1

Table S5.2. Brightness enhancement as compared to free dye of absorption matched samples, *BE*, hydrodynamic diameter, *d*, and number of dyes per particle, *n*.

STORM photon statistical analysis

To analyze the photon statistical behavior of the nanoparticles, we used a custom designed Matlab protocol based on the STORM methodology described by Rust *et al.* (*S5*). Since the microscopy was performed on immobilized particles on a substrate, typical drift correction could not be performed. The following protocol was used assuming the microscope had little to no bilateral stage drift and is illustrated in Figure S5.5:

1) A maximum intensity projection of the acquired microscopy tiff movie was performed to locate the initial x and y pixel coordinates of the localizations. Any area above the threshold ten times the standard deviation of the background fluctuations was considered a localization. In these areas, we used a maximum-likelihood estimation

(MLE) to find the center of the localization since MLE provides the highest precision estimation of position versus other methods (*S6, S7*).

2) A 7x7 pixel region was then formed around the center of the positions found in the previous step. Since there was no formal drift correction, it was assumed that if the stage had slightly drifted the particle maximum intensity peak would most likely still be within this 7x7 pixel region.

3) Again, using MLE, the maximum of the region was found in the frame. Within this region, the pixel intensity fluctuations were fit to a 2-dimensional 3-parameter Gaussian function defined as:

$$I(x,y) = A + I_0 e^{\left[-\left(\frac{x-x_0}{a}\right)^2 - \left(\frac{y-y_0}{b}\right)^2\right]}$$

A is the background level of the event, I_0 is the amplitude of the peak, a and b define the width of the Gaussian distribution along the x and y directions, respectively, and x_0 and y_0 are the center coordinates found by MLE. The Gaussian was fit to a 7x7 pixel region to provide more data points thus improving the quality of the fit to the region.

4) To obtain the final intensity values for each localization, the above equation was integrated to determine the localization intensity:

$$I_{int}(x,y) = A + I_0 \frac{ab\pi}{4}\left[\mathrm{erf}\left(\frac{x+\delta-x_0}{a}\right) - \mathrm{erf}\left(\frac{x-\delta-x_0}{a}\right)\right]\left[\mathrm{erf}\left(\frac{y+\delta-y_0}{b}\right) - \mathrm{erf}\left(\frac{y-\delta-y_0}{b}\right)\right]$$

where δ is the obtained fixed half-width of a pixel in the object plane. The final integrated values were then converted to photoelectrons, yielding the photons detected,

using the camera's calibrated curve for the electron multiplication gain settings used during image acquisition.

Photons for each switching event were calculated by integrating between the beginning and the end of each switching event. The integrated values were stored to be plotted as a histogram for probe comparison. Duty cycles were calculated according to the following equation:

$$Duty\ cycle = \left\langle \frac{\sum \tau_{on,i}}{100s} \right\rangle$$

A one hundred second sliding window was used to analyze the dye and the particles to compare their blinking statistics. Large duty cycles are obtained by a high frequency of blinks inside of the one hundred second window.

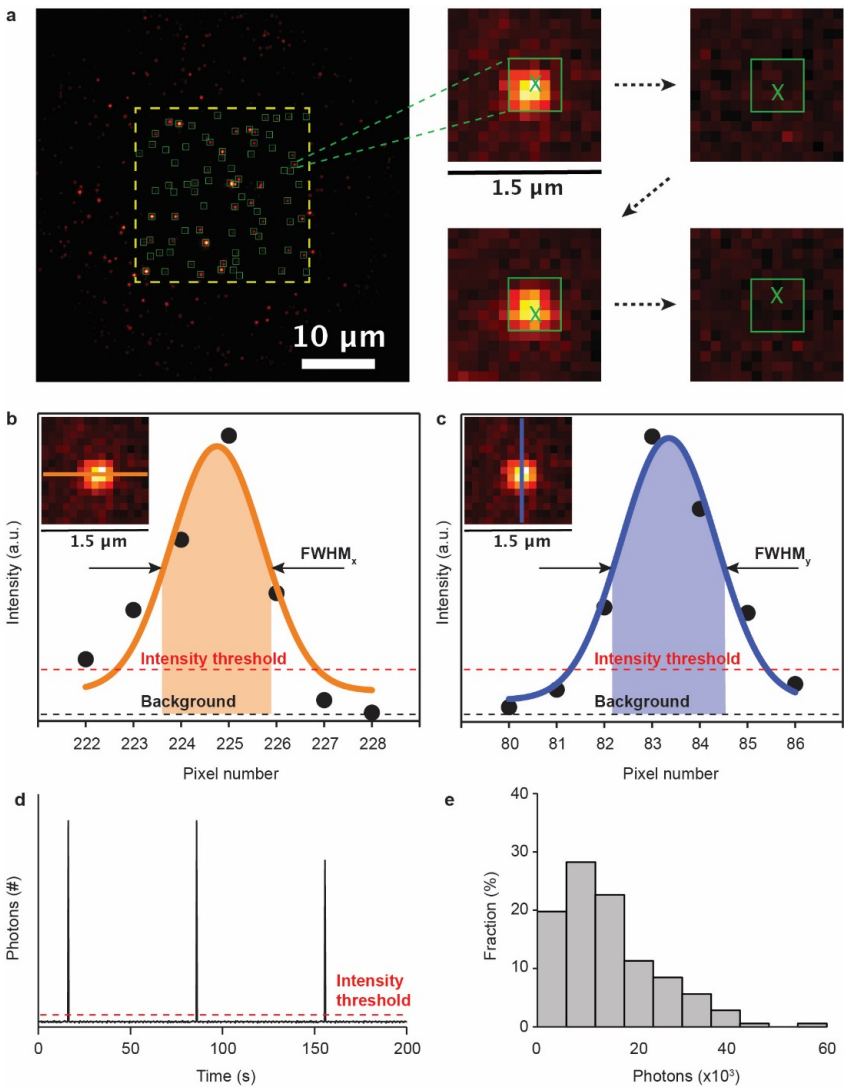

Figure S5.5. ***STORM photon statistical analysis illustration.*** **a**, Maximum intensity projection of image stack of a 512x512 pixels TIRF microscope movie. To guarantee even illumination, the image stack was cropped to 256x256 pixels (yellow dotted line) and was then processed using the photon statistics algorithm described in this section. Green boxes indicate the 5x5 pixel regions centered on the locations (green X) derived from the MLE calculation. The dashed arrows between the enlarged sample region indicate the frame progression of the same region throughout the image stack. **b** and **c**, Gaussian fitted x (orange) and y (blue) pixel intensity values of the sample region. The indicated intensity threshold was only used to determine if the region qualifies as a localization based on the criteria described above. Once the positions are determined, the x and y regions were fit to a Gaussian and integrated between the full-width half-

maximum (FWHM) values of the pixel intensity values and above the background. The final integrated values are then converted to photons as described above. **d**, A representative photon time trace derived from the collective integrated values of one localization through all frames of the image stack. **e**, An example photon histogram of one sample derived from the integrated photon number that is above the photon intensity threshold (switching event).

Microtubule Labeling and Fixation

Microtubule polymerization, fixation, and labeling were adapted from Dempsey *et al* (*S8*). 0.2 mg tubulin was suspended to 5 mg/mL in a chilled solution of PEM, 10% glycerol, and 1 mM GTP. Tubulin was polymerized into microtubules by incubating the suspension at 37°C in a water bath for 20 min. Paclitaxel was added to a concentration of 1 mM to stabilize microtubules followed by incubating at 37°C for 5 min in water bath. This microtubule solution was incubated 1 hr at 25°C with 1.68 nmol NHS-PEG-Cy5-srC'dots. NHS-PEG-Cy5-srC'dots were formed by post-PEGylation surface modification of 300 μL of 38.6 μM PEG-Cy5-srC'dots with 45 μL of 20 mg/mL Mal-PEG_6-NHS. The maleimide of the Mal-PEG_6-NHS clicks to surface mercapto groups on the PEG functionalized particle surface. The microtubule-particle solution was centrifuged for 5 min (3000xg, 25°C), the supernatant was discarded, and the pellet was resuspended in 120 μL PEM. Glass bottom dishes (MatTek P35G-1.5-10-C) were wetted by 15 min incubation at 25°C with 50:1 (mol/mol) methanol:HCl, followed by the DI water washes. Glass bottom dish PEGylation was accomplished by incubation at 50°C in a water bath overnight using 37:1:5 (mol/mol/mol) methanol:PEG-silane:ammonium hydroxide, followed by three DI water washes. 15 μL (0.025 mg) microtubule solution was fixed to wells by 10 min incubation at 37°C with 1%

glutaraldehyde in PBS. Dishes were washed three times with PBS and replaced with imaging buffer.

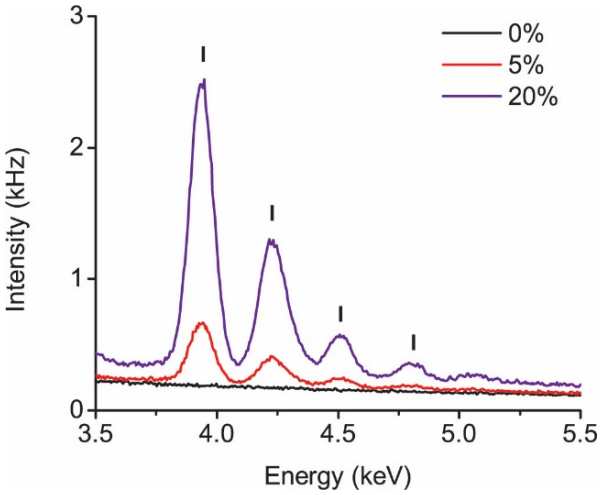

Figure S5.6. ***EDS spectra of iC' dots.*** EDS spectra of the 0%, 5% and 20% iC' dots and peak assignments for iodine (I). The characteristic L-edge line series of iodine is only observed for the latter two dots with peaks at 3.9 keV, 4.2 keV, 4.5 keV, and 4.7 keV.

Sample	*Molar ratio of IPTMS*	***d*** **[nm]**	***n*** **[#]**
ATTO647N iC' dots	0%	4.4	1.0
ATTO647N iC' dots	1%	4.7	1.3
ATTO647N iC' dots	2.5%	4.9	1.3
ATTO647N iC' dots	5%	6.5	1.3
ATTO647N iC' dots	7.5%	7.0	1.2
ATTO647N iC' dots	10%	7.2	1.0
ATTO647N iC' dots	20%	8.9	1.0

Table S5.3. Molar ratio of IPTMS relative to MPTMS, hydrodynamic diameter, *d*, and number of dyes per particle, *n*.

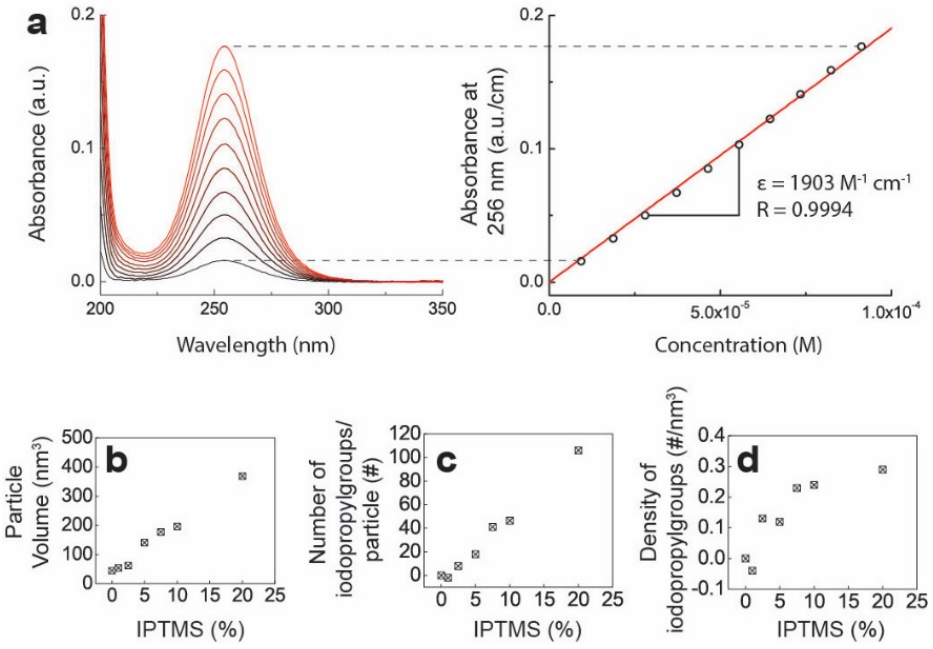

Figure S5.7. ***Characterization of iodopropyl groups in iC' dots.*** **a**, Determination of molar extinction coefficient of IPTMS in ethanol. Absorption spectra at different IPTMS concentrations (left), and plot of corresponding peak maxima at 256 nm against IPTMS concentration (right). **b**, Particle volume as calculated from particle diameter. **c**, Number of iodopropyl groups as determined from a combination of FCS and absorption measurements. **d**, Estimated iodopropyl group density as obtained from data in **b** and **c**.

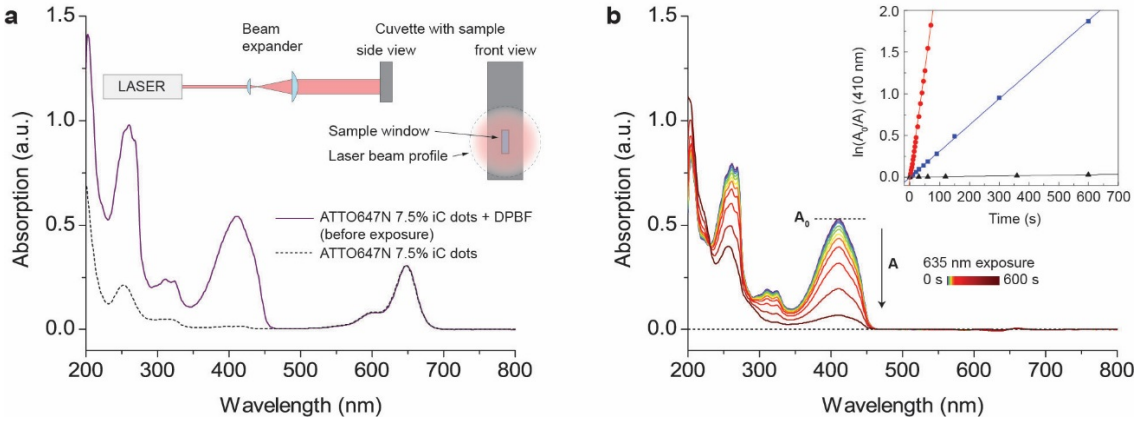

Figure S5.8. ***Determination of singlet oxygen quantum yields,*** Φ_Δ. **a**, Absorption spectra of ATTO647N 7.5% iC' dots with and without DPBF in ethanol. The particle-only spectrum is used as a baseline and subtracted from the DPBF containing spectrum leading to the spectrum in **b** (purple line). The inset in **a** shows the optical setup for the exposure of a sample in a microcuvette to a 635 nm solid state laser beam (3 mW/cm^2). A beam expander is used to evenly illuminate the sample window. **b**, Baseline-corrected absorption spectra of DPBF at different exposure times. The inset in **b** shows the natural logarithm of the relative DPBF absorption at 410 nm at different exposure times plotted against exposure time, and respective linear fits for the standard methylene blue (MB) (red), the ATTO647N 7.5% iC' dots (blue), and a negative control of DPBF only (black).

Example calculation to determine singlet oxygen quantum yield, Φ_Δ

Φ_Δ(sample) is determined relative to a standard with known Φ_Δ(standard) using

$$\Phi_\Delta(\text{sample}) = \Phi_\Delta(\text{standard})\frac{\text{m(sample)}}{\text{m(standard)}}$$

Here, we used methylene blue (MB) as a standard with known Φ_Δ(MB) = 0.520. With the slopes, m, from the linear fits through the values of the 410 nm DPBF absorption band at different exposure times, Φ_Δ(sample) can be calculated. With the values from

Figure S5.8b inset m(ATTO647N 7.5% iC' dots) = 0.00314 s^{-1} and m(MB) = 0.02506 s^{-1}, $\Phi_{\Delta}(\text{ATTO647N 7.5\% iC' dots}) = 0.520(0.02506 s^{-1}/0.00314\, s^{-1}) = 0.065$ (6.5%).

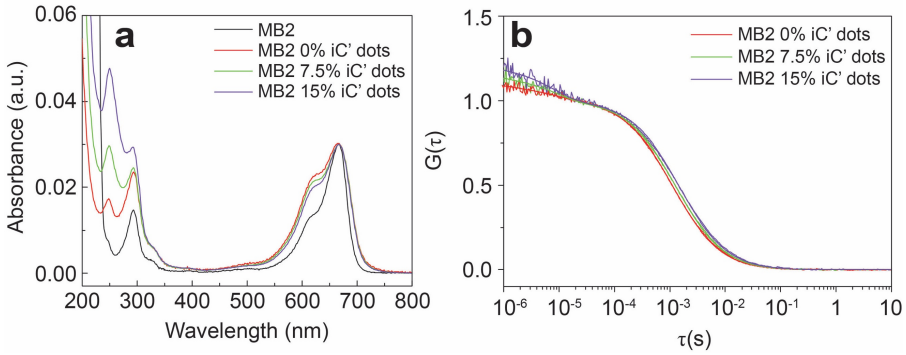

Figure S5.9. ***Characterization of iC' dots encapsulating MB2.*** **a**, Absorption spectra of MB2, and MB2 encapsulating 0, 7.5, and 15% iC' dots. **b**, FCS curves of TMR surface functionalized MB2 0, 7.5, and 15% iC' dots for particle size determination.

Sample	***Molar ratio of IPTMS***	***d*** **[nm]**
MB2 iC' dots	0%	4.8
MB2 iC' dots	7.5%	5.4
MB2 iC' dots	15%	6.2

Table S5.4. Molar ratio of IPTMS relative to MPTMS, and hydrodynamic diameter, *d*.

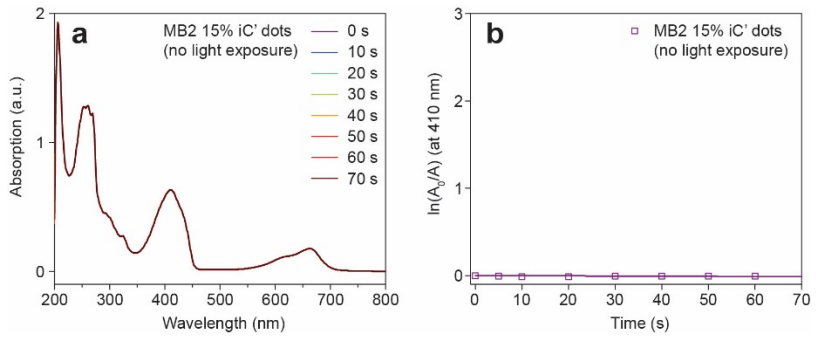

Figure S5.10. ***Dark toxicity measurement.*** **a**, Absorption spectra of MB2 15% iC' dots containing DPBF at different times after DPBF addition. **b,** Natural logarithm of the relative DPBF absorption at 410 nm at different times after DPBF addition.

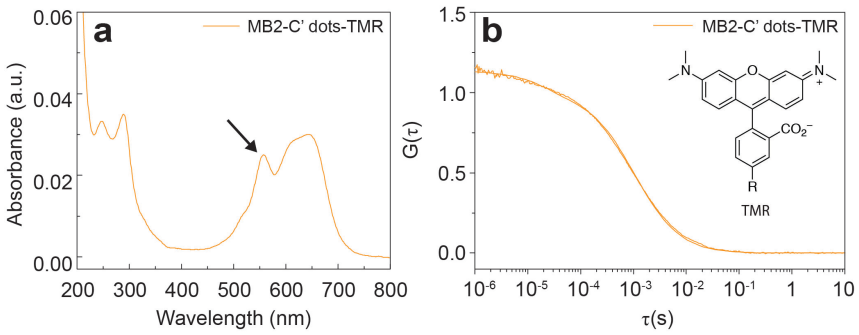

Figure S5.11. ***Characterization of C' dots encapsulating MB2.*** **a**, Absorption spectra of MB2 encapsulating C' dots with tetramethylrhodamine (TMR) grafted on particle surface*. The TMR absorption peak is visible at 550 nm (black arrow). **b**, FCS autocorrelation curve of particles in **a** for particle size and concentration determination. The particle hydrodynamic diameter was 4.6 nm with an average number of about 1.8 TMR dyes and about 2.9 MB2 dyes per particle. The inset shows the chemical structure of TMR. R represents a functional group attached by a carbon atom.

*Due to MB2 being weakly emissive, we used TMR dye as a fluorescent surface functionalization to determine particle size and concentration (*S9*).

REFERENCES (Appendix D)

(*S1*) Ma, K. *et al*. Control of Ultrasmall Sub-10 nm Ligand-Functionalized Fluorescent Core–Shell Silica Nanoparticle Growth in Water. *Chem. Mater*, **27,** 4119–4133 (2015).

(*S2*) Templin, M., Wiesner, U., & Spiesss, H. W. Multinuclear solid-state-NMR studies of hybrid organic-inorganic materials. *Adv. Mater*, **9,** 814–817 (1997).

(*S3*) Ma, K., Werner-Zwanziger, U., Zwanziger, J., & Wiesner, U. Controlling Growth of Ultrasmall Sub-10 nm Fluorescent Mesoporous Silica Nanoparticles. *Chem. Mater*, **25,** 677–691 (2013).

(*S4*) Kao, H.-M. et al. Oxidative transformation of thiol groups to disulfide bonds in mesoporous silicas: a diagnostic reaction for probing distribution of organic functional groups. *New J. Chem*, **33,** 2199 (2009).

(*S5*) Rust, M. J., Bates, M. & Zhuang, X. Sub-diffraction-limit imaging by stochastic optical reconstruction microscopy (STORM). *Nat. Methods* **3,** 793–796 (2006).

(*S6*) Nieuwenhuizen, R. P. J. *et al.* Measuring image resolution in optical nanoscopy. *Nat. Methods* (2013).

(*S7*) Mortensen, K. I., Churchman, L. S., Spudich, J. A. & Flyvbjerg, H. Optimized localization analysis for single-molecule tracking and super-resolution microscopy. *Nat. Methods* **7,** 377–381 (2010).

(*S8*) Dempsey, G. T., Vaughan, J. C., Chen, K. H., Bates, M., & Zhuang, X. Evaluation of fluorophores for optimal performance in localization-based super-resolution imaging. *Nat. Methods*, **8,** 1027–1036 (2011).

(*S9*) Ma, K., & Wiesner, U. Modular and Orthogonal Post-PEGylation Surface Modifications by Insertion Enabling Penta-functional Ultrasmall Organic-Silica Hybrid Nanoparticles, *Chem. Mater*, **29,** 6840–6855 (2017).

CHAPTER 6

FROM MOLECULAR DESIGN TO ARCHITECTURAL SCALE: AN IRIDESCENT FAÇADE COATING[*]

Abstract

The inspiration of art by scientific practice and scientific ideas is manifold and goes back to the very beginning of science itself. Here, we describe the development of a custom made iridescent block copolymer coating of transparent panels by means of biomimicry for the application as a façade for the ~14-meter-tall art installation, *A Needle Woman: Galaxy Was a Memory, Earth is a Souvenir* by Kimsooja. The installation was part of the 2014 Cornell Council for the Arts (CCA) biennial on the occasion of the sesquicentennial of Cornell University in 2015. This project provides an example of a formal collaboration between artistic practice and materials science research.

[*] Ferdinand F. E. Kohle, Hiroaki Sai, Peter Beaucage, Ethan M. Susca, Ulrich B. Wiesner. From Molecular Design to Architectural Scale: An Iridescent Façade Coating, Manuscript in preparation.

Introduction

The color of a material is a complex result of its material properties. Color can be described as an intensity spectrum graphed against a wavelength, λ. Life has developed three main forms of color: bioluminescence, pigments, and structural coloration. Bioluminescence is a result of chemical reactions whose byproduct is the emission of light (*1*). It is most commonly observed in deep sea where sunlight does not reach, and where weak luminescence can function as a signal. Pigments are compounds that selectively absorb or scatter all or some part of the optical spectrum. Colors from pigments are constant over all viewing angles because of this mechanism. Pigments are commonly found throughout natural organisms, such as melanins in human hair, hemoglobin in blood, carotenes in carrots, and so on. Pigments are also the dominant means of producing colors in inks, paints, stained glasses and other artificial objects due to the ease of synthesis and processing and wide availability. Both organic and inorganic materials that function as pigments have been extensively studied and engineered (*2*).

Structural coloration is the result of selective light reflection with subsequent interference of wavelengths caused by periodic structures on the order of the wave length of visible light (λ between 400-800 nm). The orientation of these structures can give rise to angle-dependent color presentation, namely iridescence. Use of structural colors in the visual arts has been rare in history due to lack of understanding of the color-producing structural requirements and limited iridescent material availability, *e.g.* iridescent minerals in jewelry or jewel beetles (chrysochroa fulgidissima) for the decoration of shrines (*3*). With advances in photolithography and development of structural color-forming artificial materials such as liquid crystals (*4*), colloidal

suspensions and crystals (*5-7*) and block copolymers (*8, 9*), modern artistic works have explored the use of structural coloration (*10-12*).

Natural organisms have encoded ways in their genes to present structural coloration as found in feathers of peacocks, wings of butterflies, or scales of Koi fish. As an example, morpho butterflies show vibrant structural coloration in their wing scales, formed during their development by the deposition of chitin into the gap between cellular plasma membrane and intracellular endoplasmic reticulum (*13-15*). Spontaneous self-organization and regulation is an inspiration for scientific advances in the field of self-assembly, where nanostructures can form from information-encoded designer (macro-)molecules (*16, 17*). Combining self-assembly processes with traditional painting or coating practices in such a way that inks can be applied to a surface resulting in structural coloration remains challenging, however, as artificial self-assembling materials usually lack pathway selectivity, or chaperoning. Current approaches typically involve slow solvent evaporation or thermal annealing steps, allowing materials to reach thermodynamic equilibrium structures, that are not readily applicable to industrial processes.

In this paper, we describe a biomimetic iridescent coating of transparent panels based on a block copolymer (BCP) poly(styrene-*block*-tert-butyl methacrylate) (StB), that was specifically designed for the art installation, *A Needle Woman: Galaxy Was a Memory, Earth is a Souvenir*, by artist Kimsooja (Figure 6.1 and Figure S6.1) (*18*). In the following, we lay out the steps that were taken from the molecular design of the material to the final panel application in three stages. Stage one focuses on polymer solution properties, nanostructure formation via bottom-up self-organization, the

interrelationship of molar mass and domain spacing, and resulting optical properties. Stage two describes the challenge of scaling the process from the lab bench, *i.e.* working with milligrams, milliliters, and square centimeters, to achieving architectural scale outcomes, *i.e.* working with grams, liters, and square meters, in particular addressing polymer synthesis and BCP film formation challenges. Stage three introduces the final window panel design that was used for the installation.

Materials and Methods

Materials

For the sequential living anionic polymerization of AB diblock copolymer poly(styrene-*block*-tert-butyl methacrylate) (PS-*b*-PtBMA, or StB), *n*-butyllithium (1.6 M in hexanes, Acros Organics), sec-butyllithium (1.4 M in hexanes, Sigma-Aldrich), dibutylmagnesium (1.0 M in heptane, Sigma-Aldrich), diisobutylaluminum hydride (1.0 M in hexanes, Sigma-Aldrich), triethylaluminum (1.0 M in hexanes, Sigma-Aldrich), methanol (anhydrous, J. T. Baker) and toluene (HPLC grade, J. T. Baker) were used as received. 1,1-diphenylethylene (DPE, >99%, TCI America) was vacuum distilled and stored under inert atmosphere at -40 °C. Cyclohexane (99.5 %, Sigma-Aldrich) was dried using n-butyllithium with 1,1-diphenylethylene as an indicator, and was vacuum distilled into the reaction flask prior to use. Tetrahydrofuran (THF, HPLC grade without inhibitor, J. T. Baker) was used immediately after opening the bottle, dried using n-butyllithium with 1,1-diphenylethylene as an indicator, and was vacuum-distilled immediately prior to usage. Styrene (99 %, Sigma-Aldrich) was stirred for an hour in an inert environment with dibutylmagnesium powder, dried from its heptane solution, before being vacuum distilled into a frozen ampoule that was kept at liquid nitrogen temperature until usage. Tert-butyl methacrylate (tBMA) (>98 %, TCI America) was freeze-pump-thawed three times, titrated with a 1:1 (v/v) mixture of diisobutylaluminum hydride and triethylaluminum solutions under inert atmosphere at ~0 °C until a yellow color persisted, and stirred for an hour before being vacuum distilled into a frozen ampoule immediately prior to usage. For light scattering and film

casting, THF (anhydrous, Sigma-Aldrich) and toluene (anhydrous, Sigma-Aldrich) were used as received.

Synthesis of PS-*b*-PtBMA (StB)

A standard Schlenk line with argon as inert gas and a glovebox with nitrogen environment were used in the anionic polymerization of PS-*b*-PtBMA. Due to the high viscosity of the reaction mixture, a high-power magnetic stirrer and a samarium cobalt magnetic stir bar were used for mixing. For a targeted PS-*b*-PtBMA molar mass of 1500 kg/mol, approximately 1 L of THF was vacuum distilled into a 2 L one-neck reaction flask equipped with a Rotaflo valve. To this flask, ~40 mL of freshly prepared styrene and 0.475 mL of sec-butyllithium solution (0.07 M, diluted from 1.4 M with cyclohexane) were added sequentially, and the polymerization was carried out at -78 °C for 1h. Within a minute, the orange reaction mixture became viscous. After an hour, distilled DPE was diluted 10 times with distilled THF inside a glovebox, titrated with a 0.07 M sec-butyllithium solution until a slight pink color persisted, and 0.15 mL of this pink solution was transferred to the reactor with a needle and a syringe. The solution turned red in color upon addition of DPE. Then, 40 mL of tBMA was added to the reactor, and the polymerization proceeded at -40 °C for about 2h. The solution turned opaline after about 10 min. Finally, the polymer was terminated with methanol, and precipitated in a 2:1 methanol/DI water mixture and dried with a diaphragm pump for 12 to 24 h, then in a vacuum oven at 50 °C for 24 h, and finally at 80 °C for another 24 h.

Polymer Characterization

Molar fractions of PS and PtBMA blocks were determined via proton nuclear magnetic resonance (^{1}H NMR) using a Varian INova-400 spectrometer. The spectra were integrated in two regions: between 6.2-7.2 ppm (corresponding to the 5 aromatic protons of the poly(styrene) block) and between 0.8-2.4 ppm (corresponding to the remaining 3 poly(styrene) backbone protons and all 14 protons of the poly(t-butylmethacrylate) block). These integrals were used to calculate the block fractions given in Table 6.1.

Polymers were characterized by gel permeation chromatography (GPC) equipped with a Waters 410 refractive index detector, using THF as the eluent. However, due to the high molar mass of polymers, elugrams could not be quantitatively analyzed against a polystyrene standard curve. Instead, the molar mass of the different StB batches were determined by light scattering measurements in THF to create Zimm plots using a Brookhaven BI-200SM Static Light Scattering System, equipped with a 632.8 nm He:Ne laser and an avalanche photodiode detector. Molar mass was determined by double extrapolation to zero concentration and zero angle from a series of measurements at different polymer concentrations and at different scattering angles (*19*). Steady shear rheological measurements of StB toluene solutions (7.5 wt% and 10 wt%) were carried out at room temperature on an ARES–LS rheometer (Rheometric Scientific) equipped with a cone and plate fixture of diameter 10 mm and cone angle 1°. Measurements spanned shear rates, $\dot{\gamma}$, from 0.1 to 1000 s^{-1}. To reduce solvent evaporation, a dome of aluminum was placed around the sample during measurements.

Film Formation and Characterization

StB BCP films were manually blade-casted using glass coverslip substrates (Fisher Scientific) and Scotch tape (3M) as spacers as described in the main text (see Figure 6.3). Typical casting conditions included 3 to 5 layers of scotch tape (50 μm gate height per layer), casting speeds of 0.5 to 1 cm s^{-1}, and StB solution concentration of 10 wt%. Gate height and film thickness were measured using a micrometer screw gauge. At least 10 measurements were taken at different film locations and results averaged.

The domain spacing of casted films was determined by ultra-small-angle X-ray scattering (USAXS) measurements performed at beamline 9-ID-C of the Advanced Photon Source (*20, 21*) operating at 17.6 keV. Data were reduced using the Indra package and desmeared. Samples were prepared as stacks of up to 20 thin films prepared with the same orientation and secured with Scotch tape (3M) to increase signal intensity. The scattering background contribution from the two layers of tape measured separately was subtracted from all final patterns.

Transmission electron microscopy (TEM) images were acquired on a FEI Tecnai T12 microscope operated at accelerating voltage of 120 kV in bright–field mode equipped with a high-resolution, thermoelectrically cooled Gatan Orius dual-scan CCD camera. StB samples were casted on a PET substrate (thickness 120 ± 3 μm, PET UV-laminate, provided by Laumont Photography) and prepared for TEM analysis by cryo-sectioning using a Leica EM UC7 cryo-ultramicrotome with stage and blade set to -65 °C. Films were mounted on holder stubs using OCT compound (Tissue-Tek®) in orientations such that the cross-sections would be either parallel or perpendicular to the casting direction. A wet cryo 35° diamond knife (DiATOME®) was used to cut StB

films with target thickness of 65 nm into a 60:40 (v/v) dimethyl sulfoxide:water bath. Floating sections were then transferred to copper TEM grids using a Deluxe Perfect Loop (Electron Microscopy Sciences®). No further sample preparation was necessary as the relative atomic mass contrast between the two blocks was sufficient to distinguish them in TEM even without contrast enhancing film staining procedures.

Scanning electron microscopy (SEM) images were acquired using a TESCAN MIRA3 LM FE-SEM operated at an accelerating voltage of 5 kV. StB films cast on paper were prepared for SEM by sputter coating with Pd/Au for 20 seconds at 30–40 mA. Conductive copper tape was applied post-sputtering to ensure samples had electrical grounding to the sample stub.

Optical Measurements

Angular dependent transmission and reflection spectra of StB films were measured using a homebuilt tunable spectroscopy setup (Figure 6.5a). The setup consisted of a collimated and polarized tungsten light source for illumination (spot size of ~0.5 cm) and an fiber-optic Ocean Optics QE65000 spectrometer for detection. The sample was mounted on the rotational axis of a goniometer holding the detection fiber and a lens to focus the signal into the fiber. The angle of incidence (α) and the detector angle (β) could be set independently (Figure 6.5a). Samples were casted on a PMMA substrate (thickness 1 mm). All spectra were corrected for the spectral profile of the tungsten light source.

Window Panel Fabrication

Window panels were fabricated using a self-developed casting-lamination process. To achieve homogenous color throughout the tower, at least four different synthesis batches with different molar mass were mixed and dissolved in toluene to a 6.5 to 7.5 wt% casting solution. Films were manually casted on a PET lamination sheet (thickness with adhesive layer of 120 ± 3 μm, 16" x 16" PET UV-laminate, provided by Laumont Photography) with 5 to 6 layers of scotch tape (3M) as spacers, and at shear rates between 80 and 140 s^{-1}. The PET sheet was adhered to a flat steel plate by using a water-soap mixture (99:1 volume fraction). The films were left to dry in a fume hood. The dried films were laminated across the StB coated laminate film with a second layer of PET for protection by Laumont Mounting and Framing, Queens, NY. The sandwich was then cut to the respective size of the previously heat bent PMMA plates and manually laminated to the concave surface.

Results and Discussions

One example of synthetic materials that contain periodic structures and exhibit structural color are photonic crystals. These materials are typically used in optoelectronic devices and fabricated by expensive top-down approaches, such as electron-beam lithography and etching methods. Alternatively, photonic structures can be created from block copolymers (BCPs) that spontaneously self-assemble into periodically ordered structures, thereby mimicking the bottom-up fabrication process often found in nature. In an AB diblock copolymer two polymeric chains (blocks), each made from a different kind of polymer and denoted as block A and B (Figure 6.2a), are covalently linked together. Morphology and structural dimensions (domain spacing, *d*)

are determined by the relative volume fractions of the blocks, block chemistry, their tendency for microphase segregation (described by the Flory-Huggins interaction parameter, χ), and overall molar mass of the BCP (*22*). With increasing relative volume fraction of block A different morphologies are accessible, ranging from spherical (S), cylindrical (C), gyroidal (G), and lamellar (L) all the way to their respective inverse structures. For lamellar structures, the periodic spacing between the two blocks is described by the domain spacing, *d*, and depends on BCP molar mass. If BCP molar mass and resulting *d* are not sufficiently large, visible light cannot efficiently couple to the lamellar structure and no iridescent color is observed.

In this project we used the AB diblock copolymer polystyrene-*block*-poly(tert-butyl methacrylate (PS-*b*-PtBMA, or StB, Figure 6.2b). The choice of this particular BCP was based on a number of design requirements for the final installation, including the need to produce of order a kilogram of polymer with a relatively narrow molar mass distribution, solution processability in painting-compatible solvents, as well as chemical and structural stability under outdoor conditions including temperatures between -20 to 50 °C and exposure to rain and sunlight. PS and PtBMA blocks have a Flory-Huggins interaction parameter of 0.08~0.10 (*23*), making it straight forward to select a single solvent that can dissolve both blocks even at ultrahigh molar mass required for solution processing. Both PS and PtBMA blocks have glass transition temperatures above 100 °C, making them mechanically stable in the expected outdoor temperature range.

StB was synthesized via sequential anionic polymerization (see Methods and Figure S6.2). Four different batches of StB (StB-1 to StB-4) were synthesized with varying molar mass. We targeted a volume fraction of 50% PS: 50% PtBMA to achieve

a lamellar morphology and molar mass between 1500 and 2000 kg mol^{-1}. BCP composition (% PS : % PtBMA mole fraction) and molar mass were determined from a combination of proton nuclear magnetic resonance spectroscopy (^{1}H NMR) and Zimm plot analysis of light scattering experiments (Table 6.1 and Figures S6.3, S6.4, and S6.5). We determined molar masses ranging from about 1250 to 1600 kg mol^{-1} for StB-1 to StB-3. StB-4 displayed a molar mass of about 2600 kg mol^{-1}. All batches contained significant amounts of PS homopolymer as indicated by a second peak at longer elution times in the GPC measurements, indicating that despite our best efforts to exclude water and/or air from the living anionic polymerization process, some of the organolithium chain ends were prematurely terminated in the process of DPE endcapping and second monomer addition (Figure S6.4). The total amount of initiator used for a 50 g synthesis of 2000 kg mol^{-1} BCP is only 25 μmol, emphasizing the high degree of air and water exclusion necessary for successful block copolymer synthesis. The large molar mass of sample StB-4 can be attributed to a larger number of PS homopolymer chains terminated after polymerization of the first block (see GPC elugram in Figure S6.4), followed by polymerization of the second block from fewer remaining chains that continued until all tBMA monomer was depleted, leading to a large second block for the living chains and a PtBMA mole fraction of over 70% (see Table 6.1).

Photographs in Figures 6.1, 6.2b, and 6.2c (also see Figure 6.3e) summarize the different states of BCP StB throughout the project. Figure 6.2b shows a photograph of the diblock copolymer StB after synthesis and precipitation in a methanol/water mixture and subsequent drying. Under these conditions the resulting BCP appears as a white powder, with white light randomly scattered off the material in all directions. Figure

6.2c shows a photograph of StB in a toluene solution with white light illumination from the right. Here, different color domains are visible spanning the entire visible spectrum, *i.e.* from blue to red, suggesting different orientations of a lyotropic liquid crystal in solution. The final installation in Figure 6.1 exhibits BCP StB casted into a thin film on transparent panel substrates resulting in strong iridescent colors. Unlike the dry powder state depicted in Figure 6.2b, during the solvent evaporation phase of the thin BCP film formation, StB chains undergo spontaneous microphase separation into a nanoscale morphology, whose length scale, periodicity, and orientation give rise to iridescent colors.

Whether a uniformly colored and transparent StB film can be casted from a solution depends on a number of parameters, including the solvent used, the StB solution concentration, and the shear rate during casting. For example, tetrahydrofuran (THF) as a solvent dissolved BCP StB but prohibited appropriate structure formation, likely due to its propensity to preferentially dissolve PS and to its fast evaporation rate that leads to water droplet condensation. In contrast, toluene, chloroform, and xylenes lead to uniform shear-casted films. Toluene was selected as the processing solvent of choice due to its relatively slow evaporation time and low toxicity.

To gain insights into the properties of StB solutions in toluene we performed steady shear rheological measurements with a 10 wt% (weight percent) solution of the batch StB-2. Solution viscosity was measured performing a shear rate sweep. The double logarithmic plot in Figure 6.3a shows three distinct regimes (I, II, III). Regime I and III are characterized by shear thinning, whereas regime II shows a pseudo-Newtonian behavior where viscosity is independent of shear rate between $\dot{\gamma}_1 \approx 2\ \mathrm{s}^{-1}$

to $\dot{\gamma}_1 \approx 50\ s^{-1}$. This plateau is shifted towards larger shear rates for a more dilute solution of 7.5 wt% (about $\dot{\gamma}_1' \approx 3\ s^{-1}$ and $\dot{\gamma}_2' \approx 80\ s^{-1}$). Wiesner described similar melt rheological behavior of lamellae-forming diblock copolymers under large amplitude oscillatory shear (LAOS), in which three frequency regimes of orientation were elucidated via *ex-situ* X-ray scattering experiments of sheared samples (*24*). While in the low and high frequency regimes the lamellar morphology oriented parallel to the substrate, in the intermediate frequency regime lamellar sheets oriented along the shear direction perpendicular to the substrate. We postulated from our viscosity measurements that similar orientation effects would occur in our cast films. In particular, we were interested in the perpendicular orientation favoring iridescence as a function of observation angle.

To that end, we used the StB toluene solution to develop a manual surface coating process to achieve iridescent films. We applied a blade casting method to StB solutions as shown in Figure 6.3b to 6.3d. Our metric for successful film formation was strong film iridescence, color uniformity throughout the film, and minimal film haziness. In our method, the StB solution was casted across a flat substrate (*e.g.* poly(methyl methacrylate, PMMA). On both sides of the substrates we applied multiple layers of tape to provide a rail for the casting blade that keeps it at a constant gate height above the substrate surface during casting (Figure 6.3b). To cast a film, the StB solution was first deposited in a thick line on the edge of the substrate between the tapes (Figure 6.3c), and then dragged with a blade across the substrate (Figure 6.3d). After solvent evaporation, an iridescent film formed (Figure 6.3e). To find the optimal conditions, we casted films at different gate heights (150 to 300 μm), different StB solution

concentrations (5 to 11 wt%), and different casting speeds (0.5 to 3.0 cm s^{-1}), equivalent to shear rates of about 20 to 100 s^{-1}. According to our metric best results were achieved for solution concentrations between 6.5 to 10 wt% and shear rates of 40 to 100 s^{-1}. We found that better film homogeneity was achieved, especially for larger film areas, by using higher casting speeds, lower concentrations, and larger gate heights. Smaller gate heights could result in faint color, while larger gate heights resulted in hazy films. Film quality was similar for different StB batches, however, the color of films from StB batches of larger molar mass was red-shifted. The final dry StB films were about 11 μm thick.

To probe the lamellar domain spacing, *d*, we characterized these films by ultra-small angle x-ray scattering (USAXS) (Figure 6.4a and Table 6.1). Figure 6.4b shows the domain spacing as determined by USAXS graphed against the molar mass as determined from Zimm plots of light scattering data. The expected increase of *d*-spacing with molar mass was verified. Fitting the data points to a theoretical model with $d \propto M^{2/3}$ (*25*), with M being the weight average molar mass of the BCP, we find that the lower three molar mass samples (StB-1 to StB-3) follow the power law well with an exponent of 0.68 and a scale factor of 0.20 (Figure 6.4b). Deviation of sample StB-4 from expected behavior may be the result of the large amount of homopolymer in the sample and the associated asymmetry in composition (see Table 6.1 and Figure S6.4).

To further investigate the morphology of casted StB films we employed transmission electron microscopy (TEM). Figure 6.4d to 6.4f show cross-sectional TEM micrographs of a StB-2 film that was casted according to the conditions described above

(for sample geometry, see Figure 6.4c). Figure 6.4d and 6.4e show a cross-section at different magnifications taken perpendicular to the casting direction (x-section), while Figure 6.4f shows a cross-section taken parallel to the casting direction (y-section). While Figure 6.4d and 6.4e exhibit lamellae standing normal to the substrate, Figure 6.4d does not reveal any clear morphology. These results are consistent with the shear forces during the solution casting process introducing shear alignment into the film leading to lamellar sheets parallel to the casting direction and perpendicular to the substrate. This geometry agrees with distinctly different optical properties of films observed by eye in x- versus y-directions, i.e. perpendicular or parallel to the shear direction. Looking at StB films from different angles around the y-axis results in the observation of a color change ranging from dark blue to orange-red (less red for StB-1 and dark red for StB-4). In contrast, looking at films from different angles around the x-axis does not have a noticeable color changing effect.

To quantitatively measure the angle-dependent optical properties of the StB films we used a tunable spectrometer setup as illustrated in Figure 6.5a. This instrument allowed us to measure the spectrum of light emitted from a white light source (tungsten light) and transmitted through the StB film as a function of sample orientation (incident angle α) and detection angle (β). Figure 6.5b shows a representative transmission measurement of a StB-2 film for incident light at $\alpha = 55°$ and sample position 1 (sample rotation around y-axis/shearing direction). While keeping the light and sample steady the spectra at different detection angles, β, were measured in an arch around the sample center. A peak emerges around ~400 nm that shifts towards 500 nm for larger β (Figure 6.5c). Repeating this experiment with a 90° rotated sample (sample position 2; sample

rotation around x-axis/perpendicular to shearing direction), no signal is detected at respective angles, β (Figure 6.5d). This can be explained by the orientation of the lamellar sheets. While the rotation around the sample y-axis, i.e. around the lamellar long axis, causes a change in the relative lamellar spacing and is detected by light of the excitation source, giving rise to angle dependent diffraction, the rotation around the sample x-axis (i.e. perpendicular to the lamellar long axis) does not influence the relative lamellar spacing. Consequently, no diffraction is observed for the given source/sample/detector geometry of this experiment. In Figure 6.5c the diffraction peak maxima are plotted against different detection angles, β, for different sample orientations (α = 35°, 45°, 55°, 65°, and 75°). We found that the films behave according to a volume-phase grating with a grating periodicity of 282 nm. The grating periodicity was derived by fitting the data points to the transmission diffraction equation (1)

$$\lambda_{max} = \Lambda_g(\sin(\alpha) + \sin(\beta)) \quad (1)$$

where Λ_g is the grating periodicity (*26*). Remarkably, this result is the same as that from the USAXS measurement, which also measured 282 nm for the domain spacing. Table 6.1 summarizes results for all polymers StB-1 to StB-4 demonstrating that the optical measurements provided values well within 3% of the domain spacings, *d*, obtained from the USAXS measurements.

To complement the slender and smooth geometry of the needle tower, we aimed at homogenizing the color appearance of each window panel so as to smoothly blend

one panel into the next, guiding the viewer's gaze along the structure, without breaking the flow by having different window panel color appearances. While it is easy to keep the appearance of multiple films the same on a small scale in the lab, *i.e.* by using the material from one synthesis batch, this is non-trivial for films on an architectural scale. Here, material demands easily exceed the capabilities of the lab synthesis scale. For example, a typical synthesis yield of StB is about 35 to 40 g from a one liter reactor with a success rate of 50%, mainly due to air or water contamination in the reactor (*vide supra*). However, we estimated a need of about 500 g StB to fully cover the needle tower. We therefore scaled up the lab synthesis by a factor of two by using a custom made two-liter reactor, which yielded 70 to 80 g material per successful batch. Further scale-up remained challenging both due to the lack of effective mixing during the polymerization as well as sufficient temperature-control of the reaction mixture. As a consequence, the window panels for the final tower had to be coated with BCP material from multiple batches, implying the use of varying molar mass samples, and consequently color variations as a result of poor control over absolute polymer molar mass. To address this issue, we investigated two strategies. Strategy one was to blend different StB batches with different molar mass together in solution and casting from such mixed batches. Strategy two was to adjust the color of each batch by swelling the domain spacing via addition of pure PS and PtBMA homopolymers (each ~75 kg mol^{-1}) to the StB solutions (Figure 6.6a). USAXS experiments on blended films from StB-2 and StB-3 (weight ratio 1:1) yielded a domain spacing lying between those of the original batches. Optical measurements supported this finding (Table 6.2 and Figure 6.6). The optical quality (i.e. transparency) of resulting films was not compromised by the blending approach as

suggested by similar full width at half maximum (FWHM) values of the optical transmission spectra for blended and original StB-2 and StB-3 derived films (Figures S6.6, S6.7, and S6.8).

Strategy two also allowed us to tune film color by changing lamellar domain spacings of individual StB batches (Table 6.2 and Figure S6.9). However, the lamellar structure definition was substantially compromised with increasing amount of homopolymers added. This was apparent by eye in the form of film opacity as well as by a significant peak broadening both in USAXS as well as optical measurements (Figure S6.9), leading to an increased discrepancy between d and Λ_g (within 8% of d). Therefore, we proceeded by using strategy one for the final installation.

Finally, we scaled the laboratory casting method up into a manual window panel fabrication method to produce 288 films, each 40 cm x 40 cm, for the final tower installation. The final casting solutions were composed of at least three to four synthesis batches to yield average film color appearances. For higher reproducibility of uniform films at this size, we found that faster casting speeds, ~2.5 to 3.5 cm s^{-1}, coupled with decreased solution concentration of 6.5 to 7.5 wt% yielded best results. To counteract the increased shear speed, we increased the gate height to 250 to 300 μm.

The final goal was to achieve iridescent coatings for curved acrylic window panels. This complicated the process, since the manual film casting method described above was incompatible with curved / uneven substrates (any surface irregularity resulted in strongly visible smears in the StB films). To achieve coatings of curved surfaces using our casting method, we developed a casting-lamination technique. This technique consisted of two steps. In step one, the PET substrate was replaced by a thin,

flexible PET lamination sheet with a thickness of about 120 μm and a protected adhesive layer on its back-side. This sheet was first adhered to a flat steel plate before solution casting (Figure S6.10a). This was achieved by applying a thin layer of water-surfactant mixture (soap-water) between the PET sheet and the steel plate, leading to short range van-der-Waals interactions between the two and holding the PET sheet tightly to the surface of the steel plate. The resulting steel-PET substrate created a flat and stable substrate for solution casting. In step two, the PET sheet with the dry StB film coating (Figure S6.10b) was removed from the steel plate and sandwiched under a second PET layer protecting against scratching and UV irradiation (Figure 6.6a(iii)). This final PET-StB-PET sandwich was then cut into the desired size and laminated to the curved PMMA substrate to yield the final window panel (Figure 6.6b).

In an effort to investigate the potential of our casting method to produce iridescent coatings on alternative substrates we applied it to paper. Unlike the previous PMMA and PET substrates, paper is composed of pressed cellulose fibers producing a porous surface. Despite this difference, we were able to apply the same approach as described above. We found that best results were achieved using gate heights for film casting of 300 to 350 μm. To our surprise, an iridescent film formed that adhered well to the substrate surface and remained flexible without delaminating from the paper. Figures 6.8a to 6.8d illustrate the properties of this coated paper using the example of an iridescent origami crane. Scanning electron microscope (SEM) images in Figure 6.8e to 8g reveal that the StB film is able to wrap around the paper fibers. A cross-sectional TEM image (Figure 6.8h) reveals a lamellar morphology with lamellar sheets standing

normal to the substrate surface, similar to what we saw in Figures 6.4d and 6.4e for the dense, solid polymer substrates.

Conclusion

We successfully developed a material synthesis and processing workflow for biomimetic pathways to create iridescent paints that are tunable in color, largely compatible with traditional film and substrate coating processes, and can be placed in outdoor weather. To transition from lab scale BCP research to a uniformly iridescent BCP façade coating for an architecture installation required overcoming obstacles on three separate scales. First, the lamellar BCP domain spacing needed to be enlarged to obtain the desired optical film properties, i.e. iridescent colors spanning the entire visible spectrum while maintaining optical transparency of the window panels. This was achieved by scaling the BCP chains to unusually large molar mass, and casting thin films onto PMMA or PET substrates. Second, the batch synthesis needed to be scaled up to synthesize sufficient amounts of material to cover large areas with the BCP film. Despite increased synthesis amounts one batch was not sufficient to cover the entire structure. To guarantee a mostly homogenous color appearance, we learned that different StB batches could be blended together without loss of optical film quality. Lastly, an appropriate BCP coating process needed to be developed to cover large areas with a thin StB film, which additionally needed to be applicable to curved substrate surfaces. This was achieved by a manual casting-lamination process. Finally, we found that the same principles could be applied to produce iridescent paper, that can be used for origami.

Figures

Figure 6.1. *A Needle Woman: Galaxy Was a Memory, Earth is a Souvenir* (Kimsooja). Cornell Arts Quad, 2015. Steel installation (1.3 m diameter at base, ~14 m height), window panels coated with iridescent self-assembling lamellar block copolymer film whose lamellar sheets were oriented vertically along the tower long axis.

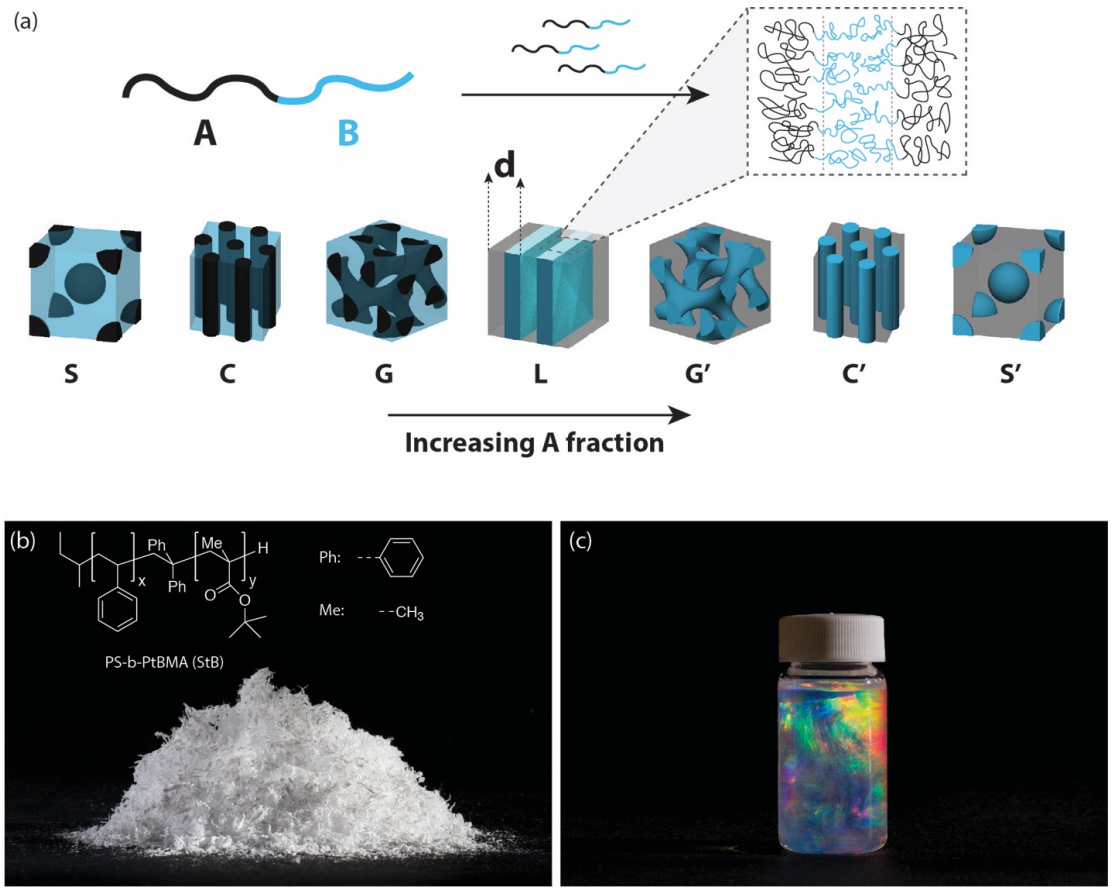

Figure 6.2. (a) Schematic molecular representation of an AB-diblock copolymer forming different morphologies. From left to right and with increasing fraction of block A: Spherical (S), cylindrical (C), gyroidal (G), and lamellar (L) morphology with domain spacing, *d*, and the respective inverse structures. (b) Photograph of ~10 g dry StB after synthesis. Inset: Chemical structure of StB. (c) StB in toluene solution in a 20 mL glass vial. Incident light from the right.

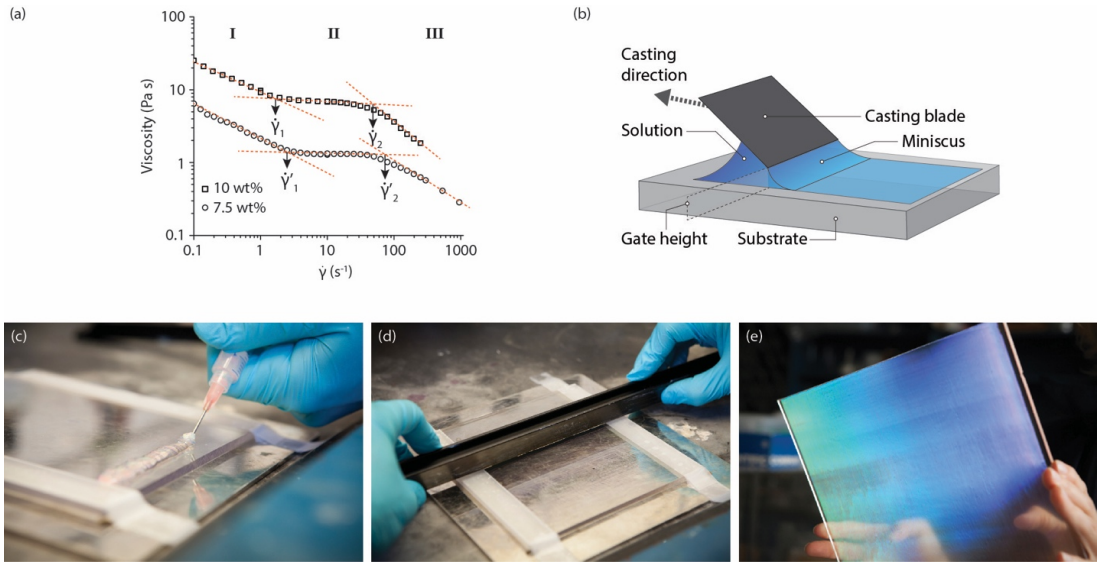

Figure 6.3. (a) Viscosity versus shear rate for two different StB solutions (10 vs. 7.5 wt%) indicating critical shear rates, $\dot{\gamma}$. (b) Schematic illustration of solution blade-casting process. (c) and (d) Photographs illustrating the solution blade-casting process. (e) Photograph of a casted prototype StB film on a flat PMMA substrate.

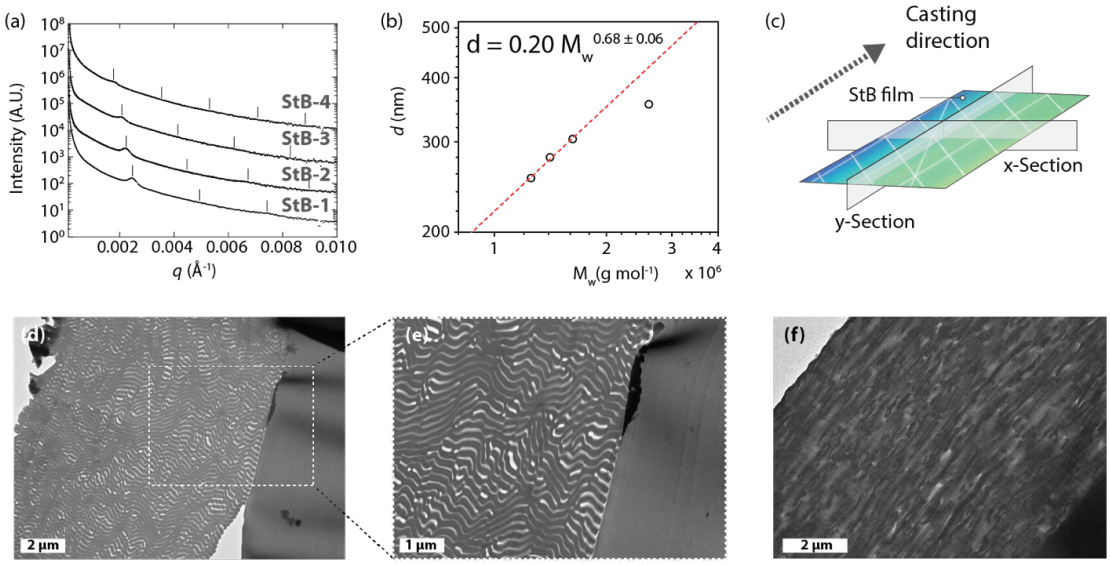

Figure 6.4. (a) Results of USAXS measurements on StB films from batches with different molar mass. (b) Double logarithmic plot of domain spacing, *d*, versus weight average molar mass, M_w. (c) Definition of sample geometry. (d) to (f) transmission electron micrographs perpendicular (d, e; x-section in c), and parallel (f; y-section in c) to casting direction.

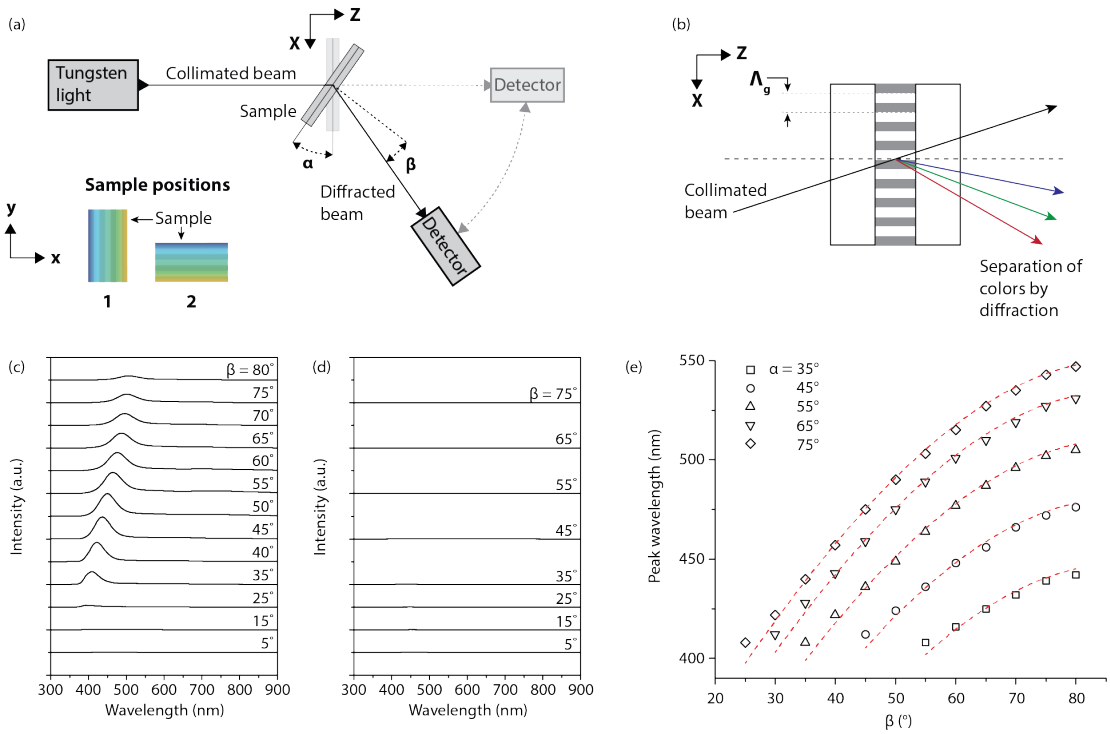

Figure 6.5. (a) Schematic of tunable spectrograph, showing different sample positions, and (b) schematic of a StB film sample in tunable spectrograph diffracting a white collimated beam of light into its spectral components. (c) Representative transmission diffraction measurements of StB-2 at α = 55° in sample position 1, and (d) in sample position 2. (e) Detection peak wavelengths against detector position, β, for different sample angles, α, for StB-2, fitted to the grating equation.

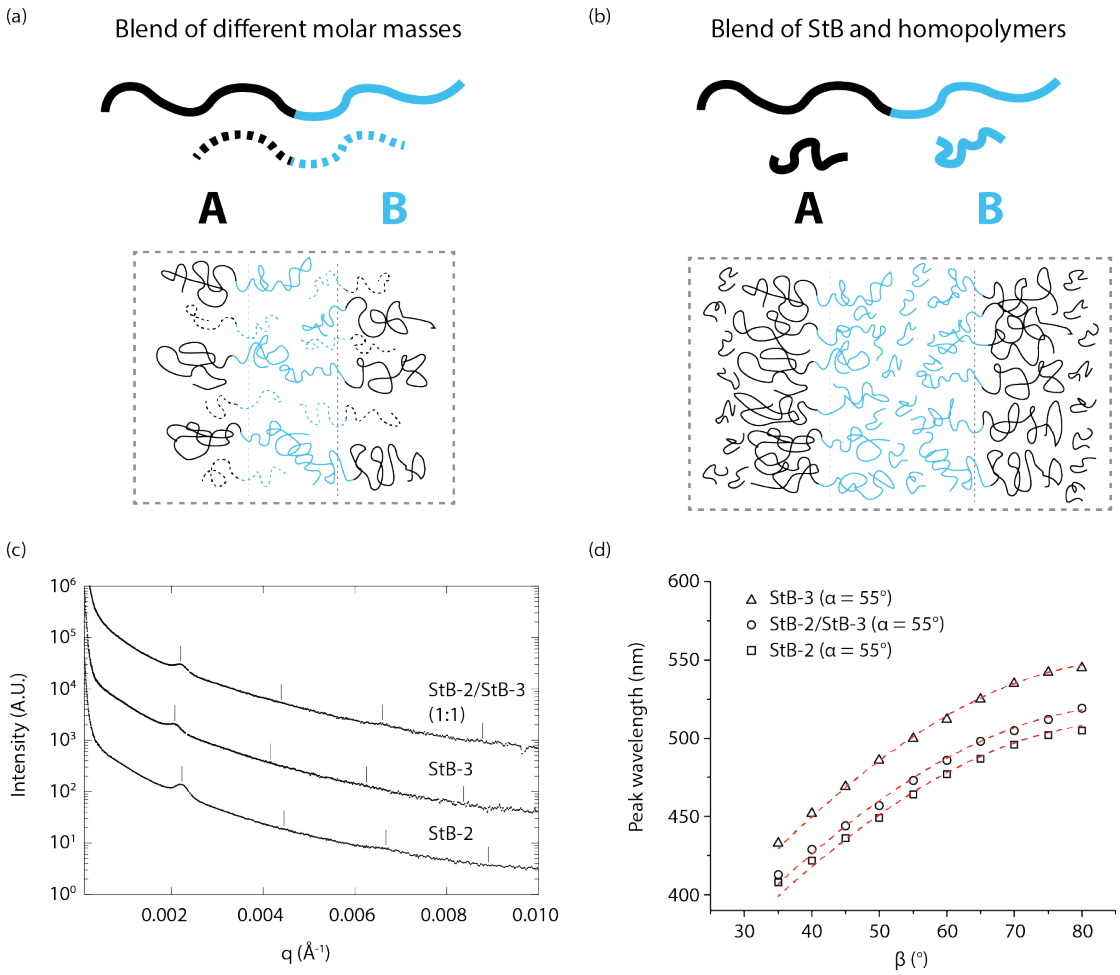

Figure 6.6. (a) Color tuning strategy one (BCP blends), and (b) color tuning strategy two (BCP/homopolymer blends). (c) USAXS measurements on StB films made from StB-2, StB-3 and a blend of the two (1:1 weight ratio). (d) Respective optical diffraction measurements (same samples as in c).

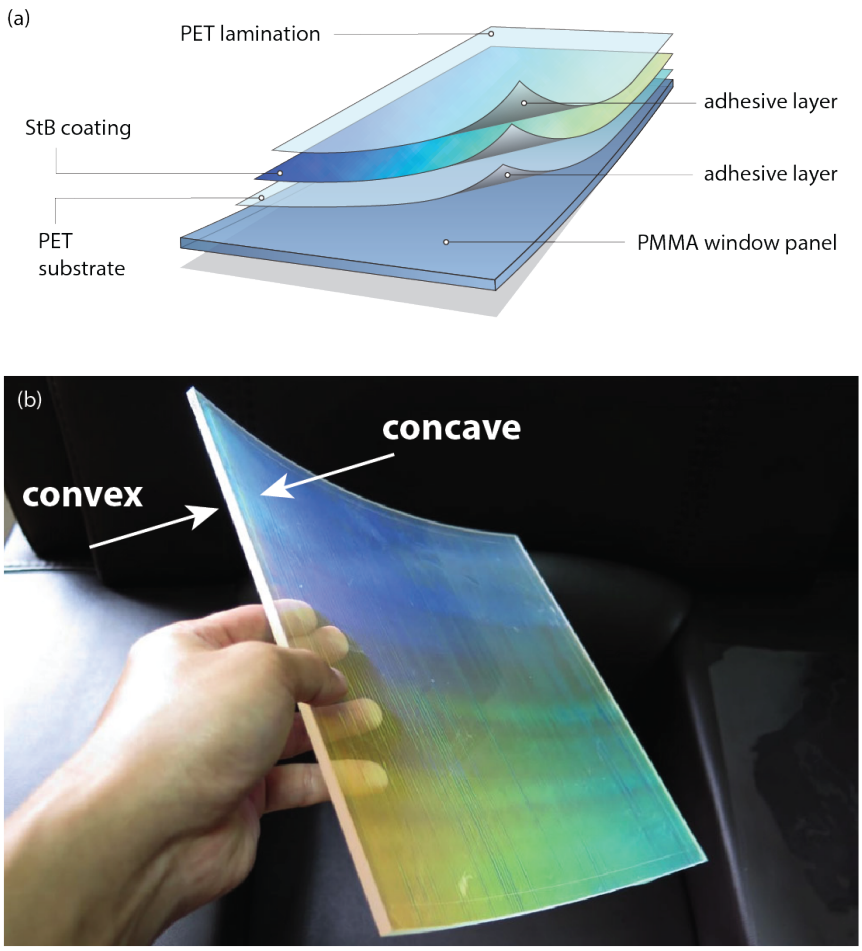

Figure 6.7. (a) Schematic illustration of the window panel design. (b) Final window panel of the installation. The PET-StB-PET sandwich shown in (a) is laminated to the concave side of the curved PMMA window panel. Photograph in (b) by Jaeho Chong.

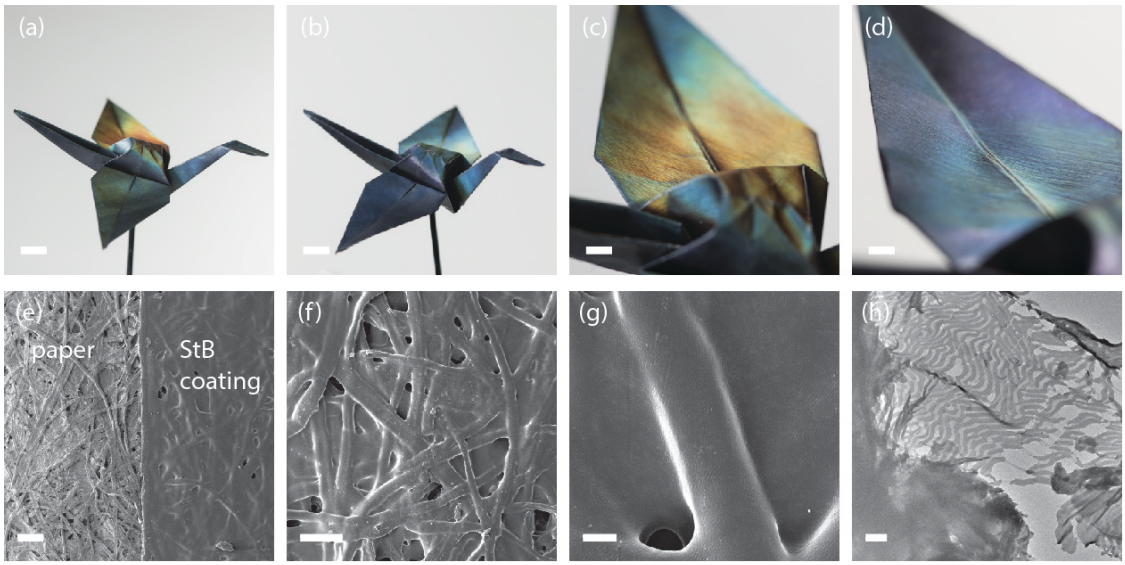

Figure 6.8. (a) & (b) Photographs of an origami paper crane. The paper was coated with StB applying a modified solution casting method (scale bar 1 cm); (c) & (d) Show a comparison of the left wing at different viewing angles (scale bar 500 μm). (e) to (g) Top-down scanning electron micrographs of StB coated paper (scale bars are 500 μm, 100 μm, and 50 μm, respectively). (h) Cross-sectional transmission electron micrograph of StB coated paper perpendicular to casting direction (scale bar 500 nm) showing the lamellar BCP morphology.

Tables

Sample	M_W [kg mol^{-1}]	R_g [nm]	A_2 [x10^{-4} cm^3 mol g^{-1}]	PS:PtBMA [%:%]	d (*USAXS*) [nm]	Λ_g (*Diff.*) [nm]
StB-1	1255 ± 18	64.2 ± 2.1	3.591 ± 0.092	36.8:63.2	255	258 ± 2
StB-2	1412 ± 51	66.5 ± 1.2	3.860 ± 0.063	39.2:60.8	282	282 ± 2
StB-3	1623 ± 28	69.8 ± 2.9	3.586 ± 0.052	38.5:61.5	304	303 ± 1
StB-4	2601 ± 19	91.1 ± 0.6	3.725 ± 0.081	29.9:70.1	355	343 ± 2

Table 6.1. Summary table of polymer characterization results from Zimm plots, ^{1}H NMR, USAXS, and optical transmission diffraction measurements for different batches of StB-1 to -4 diblock copolymer solutions and films derived from blade-casting. Columns display, from left to right, weight average molar mass, M_w, radius of gyration, R_g, second virial coefficient, A_2, mole fractions of PS and PtBMA, domain spacing, d, as determined by USAXS, and grating periodicity, Λ_g, from optical transmission diffraction measurements.

Sample	Mixing ratio StB-2:StB-3 or StB:PS:PtBMA [wt%]	d (*USAXS*) [nm]	Λ_g (*Diff.*) [nm]
StB-2	1:0 / 1:0:0	282	282 ± 2
StB-3	0:1	296	303 ± 1
StB-2/3	1:1	286	290 ± 10
StB-2a	8:1:1	N/A*	312 ± 1
StB-2b	4:1:1	353	333 ± 1
StB-2c	3:1:1	393	364 ± 1
StB-2d	1:1:1	N/A*	537 ± 5
StB (Tower blend)	All StB batches	N/A**	314 ± 1

Table 6.2. Summary table of results of USAXS and optical transmission diffraction measurements for different batches of StB diblock copolymer films made by blade-casting for color tuning strategy one (batch blending) and two (StB, PS, and PtBMA homopolymer blending), respectively. * failed measurement, ** not measured.

Acknowledgements

The authors gratefully acknowledge Kimsooja and Kimsooja Studio, Jaeho Chong, and Stephanie Owens for the opportunity to collaborate. F.F.E.K., H.S., and U.B.W. are gratefully acknowledging Troy Batugal, Camila S. Brey Gil, Zhe Chen, Andrew Moorman, and Max Vanatta for the help in the panel production. F.F.E.K. thanks Dr. Warren Zipfel for helpful discussions and experimental assistance as well as access to optical parts. F.F.E.K. thanks Dr. Frank Wise and Dr. Eduardo Mendes for inspiring and helpful discussions and Dr. Rahul Mangal for experimental assistance with rheological measurements.

H.S. synthesized the block copolymer, F.F.E.K. performed polymer characterization and optical characterizations on polymer films and developed the casting and casting-lamination protocols, P.B. and H.S. performed USAXS measurements, E.M.S. performed SEM measurements on paper samples.

This work made use of the Cornell Center for Materials Research shared facilities which are supported through the NSF MRSEC program (DMR-1120296) at Cornell. F.F.E.K. gratefully acknowledges the Department of Energy for financial support through Grant No. DE-SC0010560.

REFERENCES

(*1*) Haddock, S. H. D.; Moline, M. A.; Case, J. F. Bioluminescence in the Sea. *Annu. Rev. Mar. Sci.*, **2,** 443-493 (2010).

(*2*) Gürses A.; Açıkyıldız M.; Güneş K.; Gürses M. S. Dyes and Pigments: Their Structure and Properties. In Springer Briefs in Molecular Science (pp. 13–29). Springer International Publishing (2016).

(*3*) Schenk, F.; Wilts, B. D.; Stavenga, D. G. The Japanese jewel beetle: a painter's challenge. *Bioinspiration Biomim.*, **8,** 45002 (2013).

(*4*) Fergason, J. L. Cholesteric Structure-1 Optical Properties. *Molecular Crystals,* **1,** 293-307 (1966).

(5) Hiltner, P. A.; Krieger, I. M. Diffraction of light by ordered suspensions. *J. Phys. Chem.,* **73,** 2386-2389 (1969).

(*6*) Lotsch, B. V.; Ozin, G. A. Photonic Clays: A New Family of Functional 1D Photonic Crystals. *ACS Nano,* **2,** 2065-2074 (2008).

(*7*) Stein, A.; Wilson, B. E.; Rudisill, S. G. Design and functionality of colloidal-crystal-templated materials-chemical applications of inverse opals. *Chem. Soc. Rev.*, **42,** 2763-2803 (2013).

(*8*) Parnell, A. J.; Fairclough, J. P. A., Self-Assembling Polymer Photonics. In *Organic and Hybrid Photonic Crystals*, Comoretto, D., (pp 127-143), Springer International Publishing (2015).

(*9*) Allegra L., L.-M.; Chu, C. K.; Grubbs, R.,H. Application of Bottlebrush Block Copolymers as Photonic Crystals. *Macromol. Rapid Commun.*, **38,** 1700058 (2017).

(*10*) Makow, D. M. Color Properties of Liquid Crystals and Their Application to Visual Arts. *Color Res. Appl.*, **4,** 25-32 (1979).

(*11*) Makow, D. Liquid-Crystals in Painting and Sculpture. *Leonardo*, **15,** 257-261 (1982).

(*12*) Rubio, O. M. "Kimsooja: Less is More" - Kimsooja To Breathe - A Mirror Woman. Catalogue from the Exhibition at the Palacio de Cristal, Parquedel Retiro, Madrid, published in Madrid: Museo Nacional Centro de ArteReina Sofía (2006).

(*13*) Ghiradella, H. Structure and development of iridescent butterfly scales: Lattices and laminae. *J. Morphol.*, **202,** 69-88 (1989).

(*14*) Saranathan, V.; Osuji, C. O.; Mochrie, S. G. J.; Noh, H.; Narayanan, S.; Sandy, A.; Dufresne, E. R.; Prum, R. O. Structure, function, and self-assembly of single network gyroid (I4132) photonic crystals in butterfly wing scales. *Proc. Natl. Acad. Sci.* **107,** 11676-11681 (2010).

(*15*) Wilts, B. D.; Apeleo Zubiri, B.; Klatt, M. A.; Butz, B.; Fischer, M. G.; Kelly, S. T.; Spiecker, E.; Steiner, U.; Schröder-Turk, G. E. Butterfly gyroid nanostructures as a time-frozen glimpse of intracellular membrane development. *Sci. Adv.*, **3,** e1603119 (2017).

(*16*) Lehn, J. M. Perspectives in Supramolecular Chemistry - From Molecular Recognition towards Molecular Information Processing and Self-Organization. *Angew. Chem. Int. Ed. Engl.*, **29,** 1304-1319 (1990).

(*17*) Whitesides, G. M.; Grzybowski, B. Self-Assembly at All Scales. *Science*, **295,** 2418-2421 (2002).

(*18*) Chong, J. An Architecture of Gaze. *Space*, **566,** 116-118 (2015).

(*19*) Zimm, B. H. The Scattering of Light and the Radial Distribution Function of High Polymer Solutions. J. Chem. Phys., **16,** 1093-1099 (1948).

(*20*) Ilavsky, J.; Jemian, P. R.; Allen, A. J.; Zhang, F.; Levine, L. E.; Long, G. G. Ultra-small-angle X-ray scattering at the Advanced Photon Source. J. Appl. Crystallogr., **42,** 469-479 (2009).

(*21*) Ilavsky, J.; Zhang, F.; Allen, A. J.; Levine, L. E.; Jemian, P. R.; Long, G. G. Ultra-Small-Angle X-ray Scattering Instrument at the Advanced Photon Source:

History, Recent Development, and Current Status. Metall. Mater. Trans. A, **44,** 68-76 (2013).

(*22*) Hamley, I. W. The Physics of Block Copolymers. Oxford Univ. Press, Oxford (1998).

(*23*) du Sart, G. G.; Rachmawati, R.; Voet, V.; van Ekenstein, G. A.; Polushkin, E.; ten Brinke, G.; Loos, K. Poly(tert-butyl methacrylate-b-styrene-b-4-vinylpyridine) Triblock Copolymers: Synthesis, Interactions, and Self-Assembly. *Macromolecules*, **41,** 6393–6399 (2008).

(*24*) Wiesner, U., Lamellar diblock copolymers under large amplitude oscillatory shear flow: Order and dynamics. *Macromol. Chem. Phys.*, ***198*****,** 3319-3352 (1997).

(*25*) Matsushita, Y.; Mori, K.; Saguchi, R.; Nakao, Y.; Noda, I.; Nagasawa, M. Molecular weight dependence of lamellar domain spacing of diblock copolymers in bulk. *Macromolecules*, **23,** 4313–4316 (1990).

(*26*) Baldry, I. K.; Bland-Hawthorn, J.; Robertson, J. G. Volume Phase Holographic Gratings: Polarization Properties and Diffraction Efficiency. Publ. Astron. Soc. Pac., **116,** 403–414 (2004).

APPENDIX E

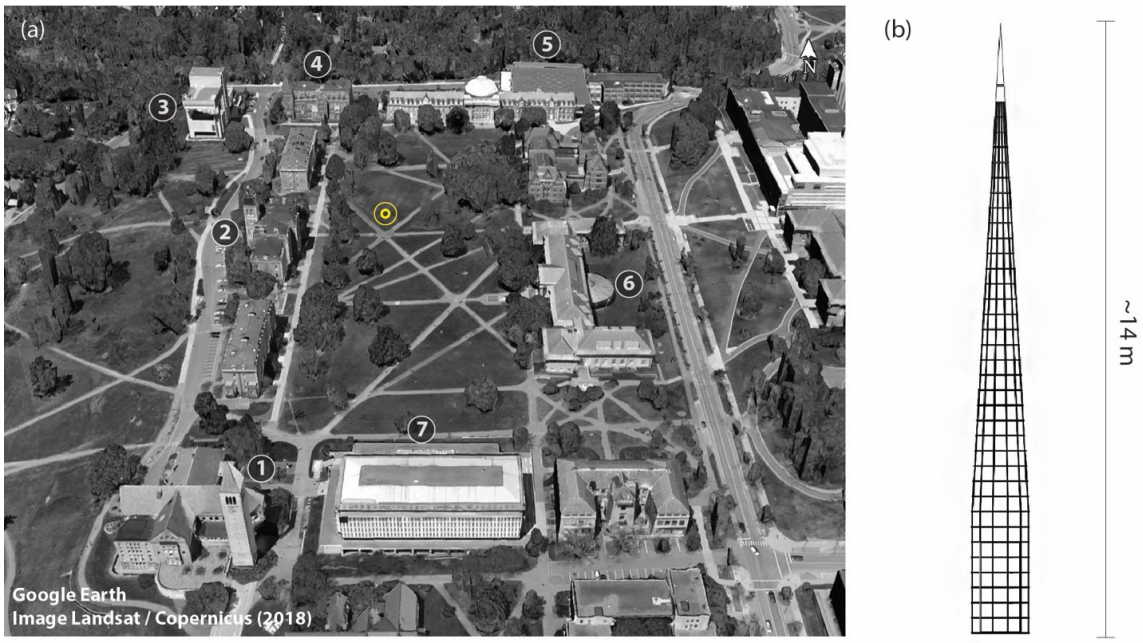

Figure S6.1. (a) Aerial photograph of the Cornell Arts quad (42°26'58.93"N 76°29'04.91"W). Yellow dot: location of the needle installation, 1: McGraw Tower, 2: McGraw Hall, 3: Johnson Museum, 4: Tjaeden Hall (Art Department), 5: Meilstein Hall (Architecture Department), 6: Goldwin Smith Hall, 7: Olin Library. (b) Architectural drawing of the needle tower. Drawing in (b) by Jaeho Chong.

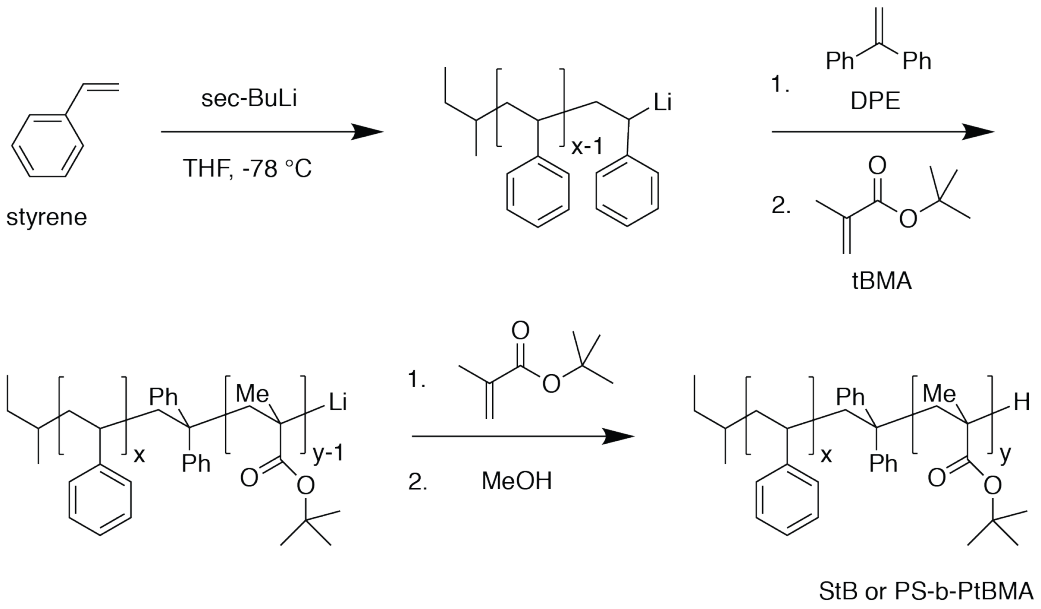

Figure S6.2. Schematic of the different steps of the anionic polymerization of StB using styrene, sec-butyllithium (sec-BuLi), 1,1-diphenylethylene (DPE), tert-butyl methacrylate (tBMA), and methanol (MeOH).

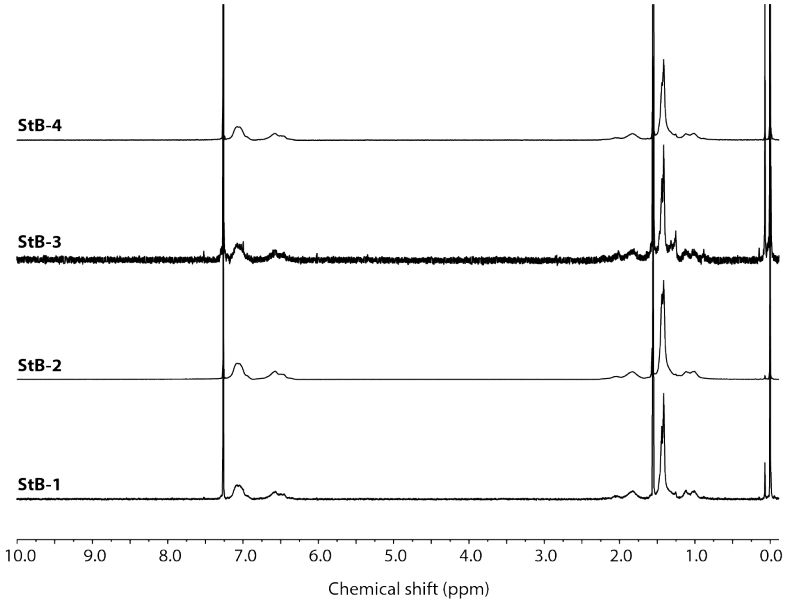

Figure S6.3. ^{1}H NMR of different StB batches with different molar mass.

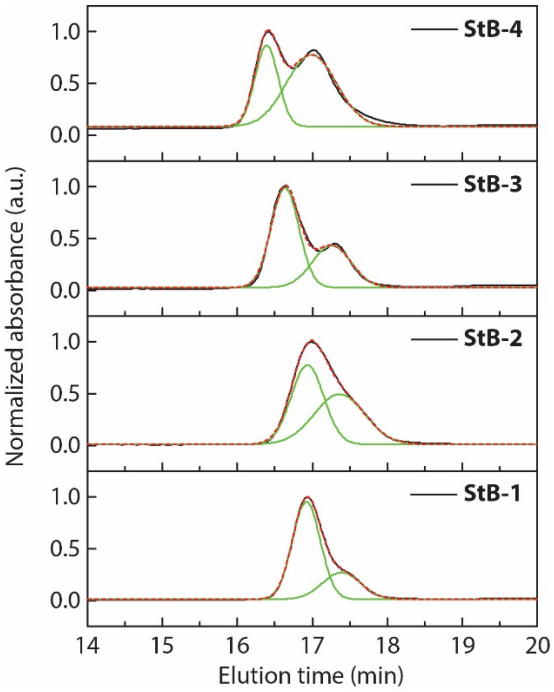

Figure S6.4. GPC elugrams of different batches of StB with different molar mass (black solid lines), with a bimodal Gaussian fit (red dashed lines). The relative contributions of the left and right Gaussians (green solid lines) are 72:28 for StB-1, 50:50 for StB-2, 63:37 for StB-3, and 34:66 for StB-4.

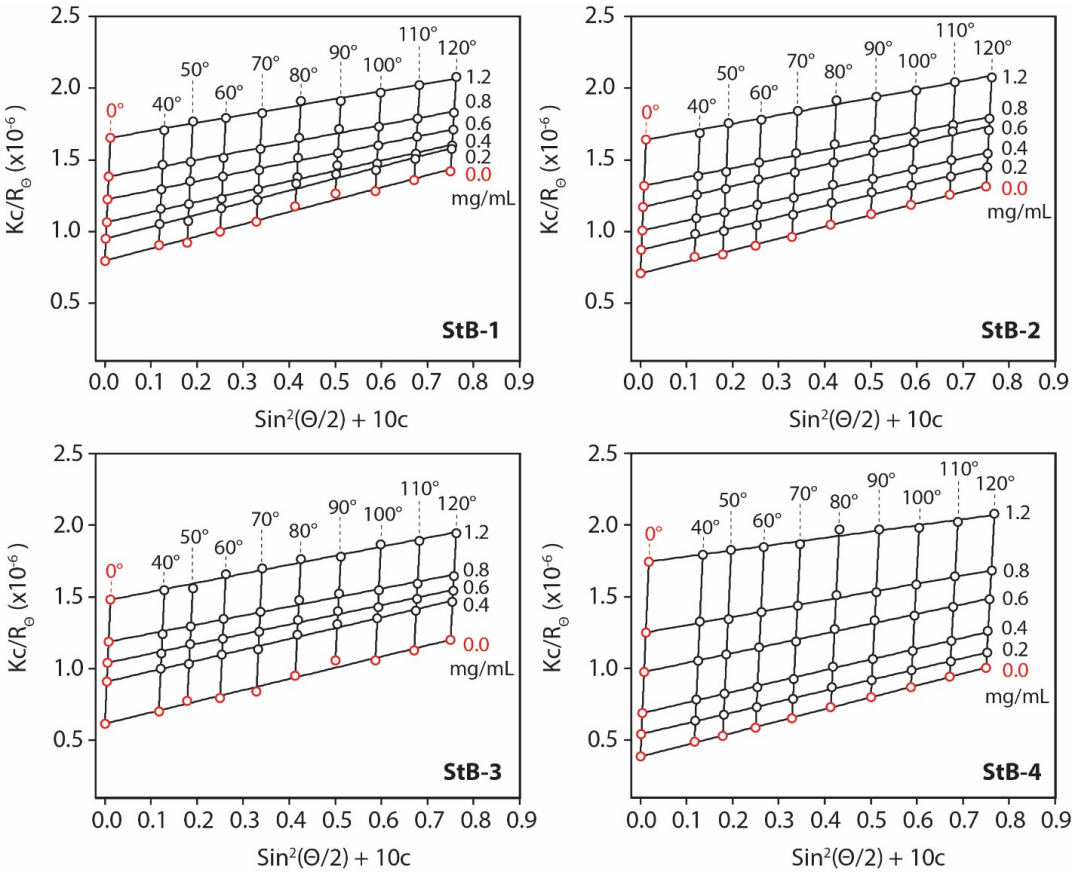

Figure S6.5. Zimm plots obtained for different StB batches with different molar mass. Black dots indicate measured values, red dots indicate values for zero concentration and zero angle extrapolation.

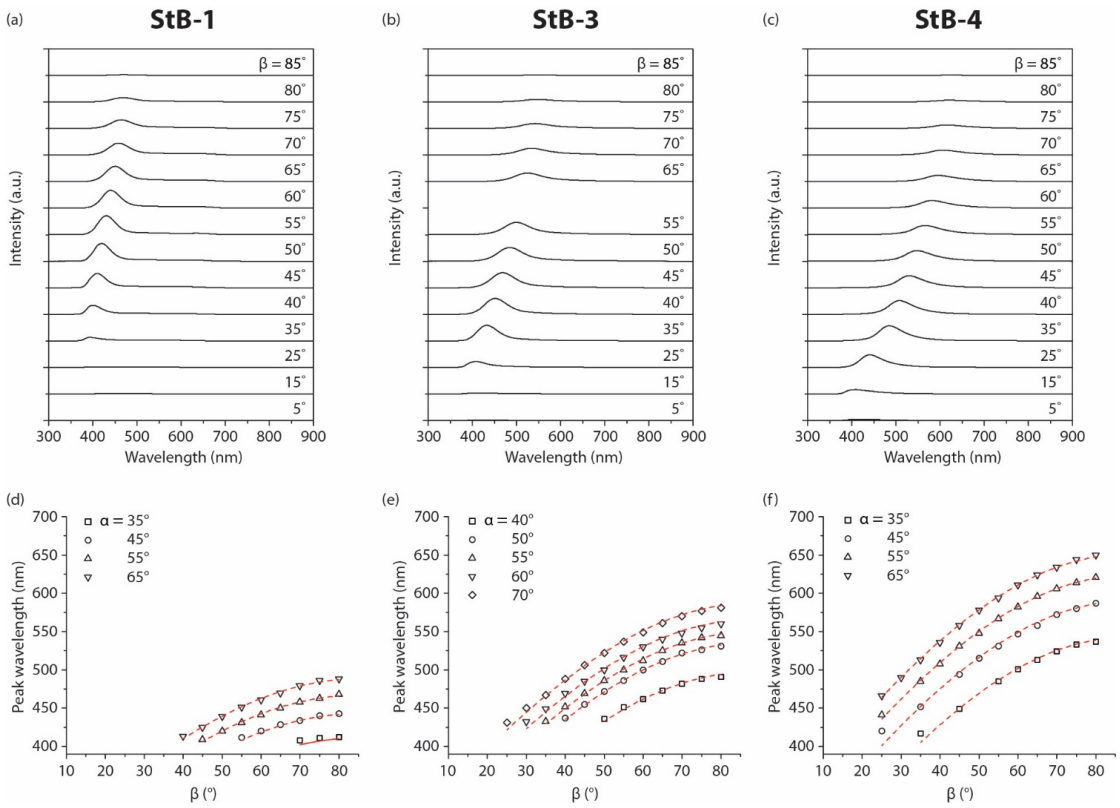

Figure S6.6. (a) to (c), Representative transmission diffraction measurements at $\alpha = 55°$ in sample position 1, and (d) to (f) detection peak wavelengths against detector position, β, for different sample angles, α, fitted to the grating equation. (a) and (d): StB-1. (b) and (e): StB-3. (c) and (f): StB-4.

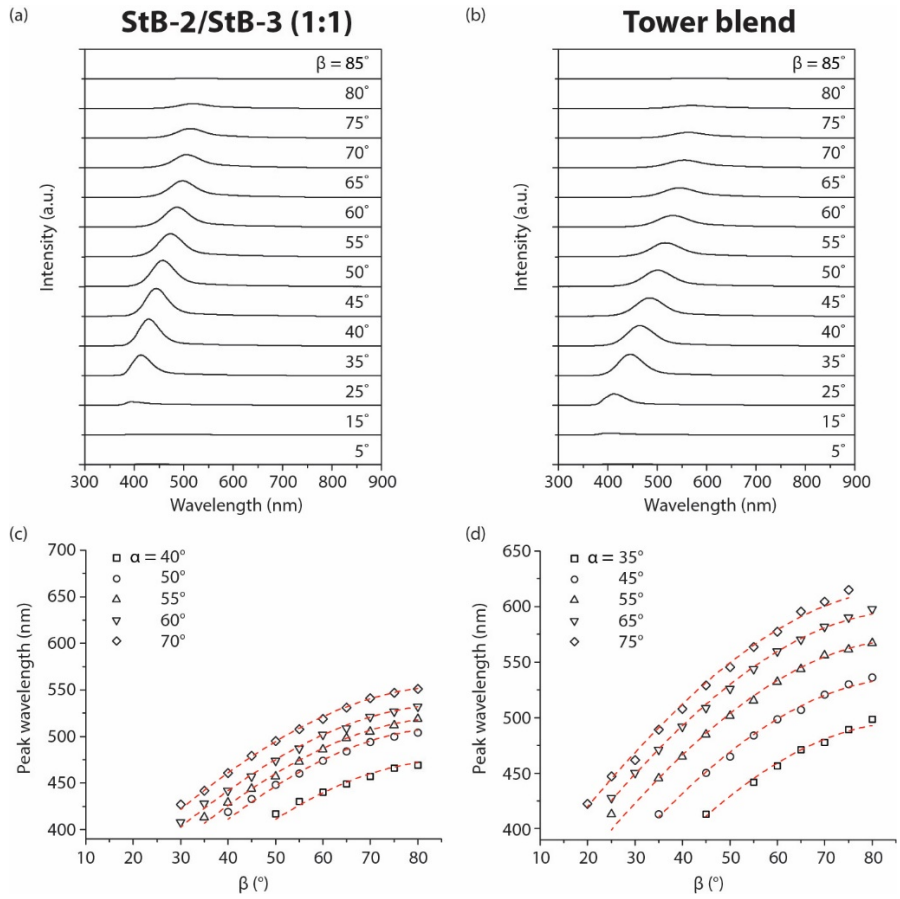

Figure S6.7. (a) and (b), Representative transmission diffraction measurements at α = 55° in sample position 1, and (c) and (d) detection peak wavelengths against detector position, β, for different sample angles, α, fitted to the grating equation. (a) and (c): Blend of batches StB-2 and StB-3 at a 1:1 weight ratio. (b) and (d): Blend of batches StB-1, StB-2, StB-3, and StB-4 at about a 1:1:1:1 weight ratio.

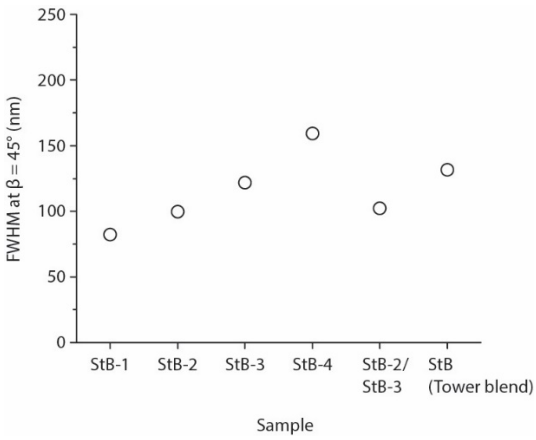

Figure S6.8. Full width at half maximum, FWHM, of transmission diffraction measurements at $\alpha = 55°$ and $\beta = 45°$ for different samples (as indicated) in sample position 2 (see schematic in Figure 6.5a).

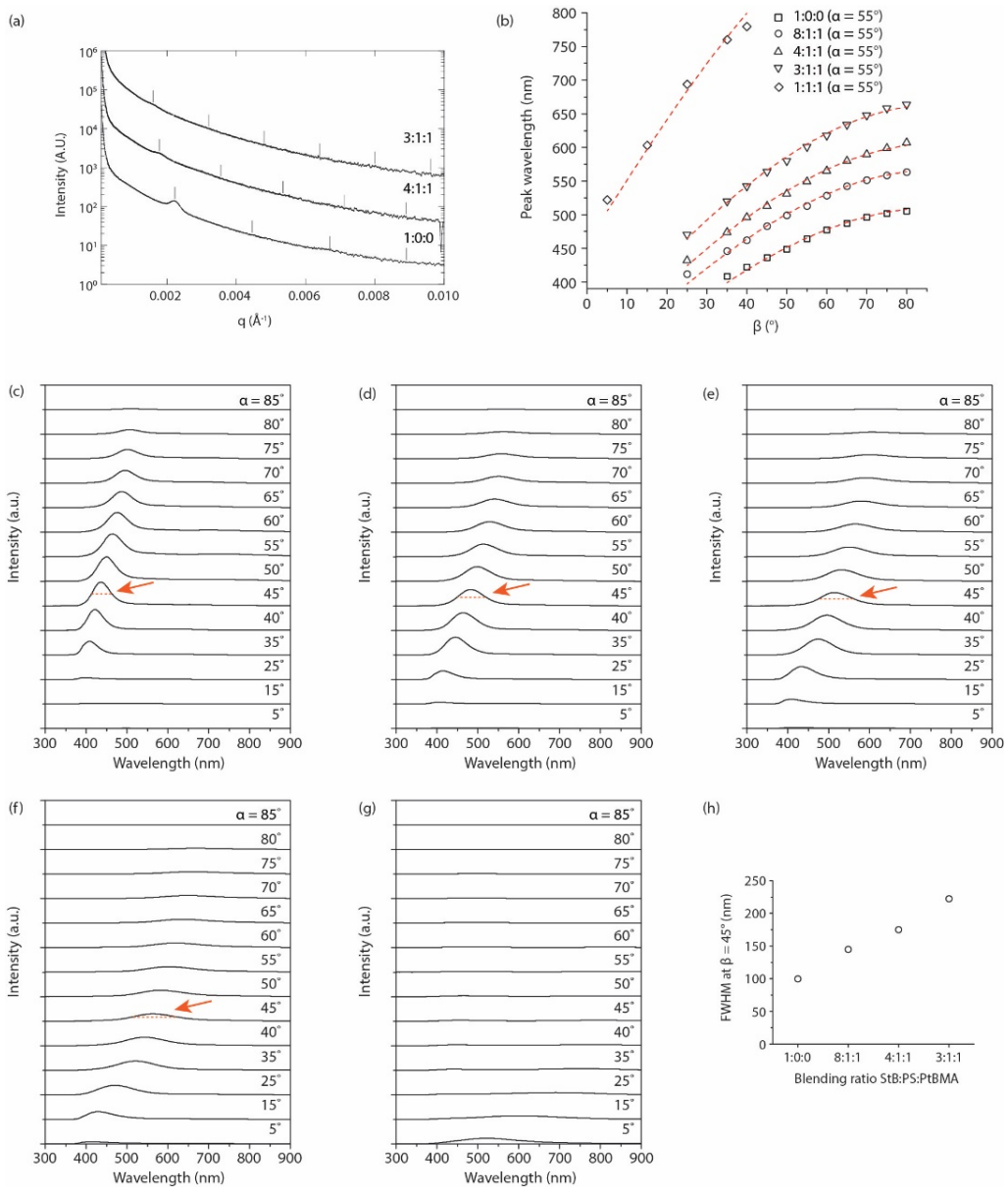

Figure S6.9. (a) USAXS measurements on StB films made from StB-2 and both homopolymers at different swelling ratios. (b) Transmission diffraction measurements at α = 55° in sample position 1 (see schematic in Figure 6.5a). Detection peak wavelengths against detector position, β, fitted to the grating equation for StB-2 and both homopolymers at different swelling ratios. (c) to (g), Representative transmission diffraction measurements at α = 55° in sample position 1 for StB-2 and both homopolymers at different swelling ratios. (h) Full width at half maximum, FWHM, of transmission diffraction measurements at α = 55° and β = 45° (indicated by red arrows in (c) to (g)).

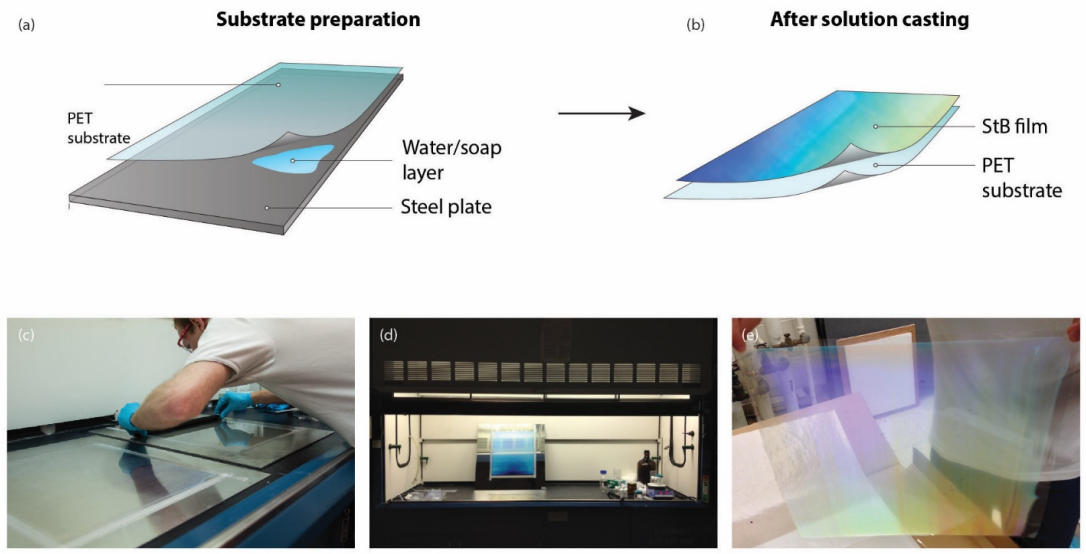

Figure S6.10. Schematic illustration of large area substrate preparation and solution casting. First the PET substrate is laminated with soap-water to a flat steel plate (a), then the BCP solution is casted onto the PET substrate (b,c), and the film is left to dry (d). Once the StB film is dry, the PET-StB layer is peeled off the steel plate (b,e).

CHAPTER 7

CONCLUSIONS

In the previous chapters, different types of optical nanomaterials and their properties were discussed and their respective potential for applications ranging from optical super-resolution microscopy, to nanomedicine in the form of, *e.g.* photodynamic therapy, as well as applications of optical materials in the arts and architecture were demonstrated.

In Chapter 2 the particle architecture of sub-10 nm core-shell C' dots was investigated by employing fluorescence correlation spectroscopy (FCS). It was found that fast fluorescence fluctuations, introduced *e.g.* by photo-induced cis-trans isomerization of Cy5 dye, are well suited to investigate aspects of the photophysics and local dye environment of fluorescent nanoparticles. The findings suggested that Cy5 dyes incorporated into C' dots are located near or on the surface. These findings were further supported in Chapter 3 by the application of high-performance liquid chromatography (HPLC). HPLC chromatograms revealed batch reaction induced surface chemical heterogeneities of Cy5 encapsulating C' dots. In combination with FCS and single particle bleaching experiments using total internal reflection fluorescence microcopy, the origin of these surface-chemical heterogeneities was identified. They were assigned to particles with different numbers of Cy5 dyes distributed over the C' dot surface, with that number ranging from zero to three (with one dye fully encapsulated into the core of the particle, this brought the overall dye

number per particle up to a maximum of four). It was further demonstrated that the net-charge of a dye molecule is the main driver for this surface chemical heterogeneity and is more important than details of the dye chemistry. For example, findings revealed that the positively charged dye ATTO647N resulted in single peak HPLC chromatograms suggesting that in contrast to negatively charged Cy5, these dyes get fully encapsulated into the silica core. These findings likely are important for optimal surface functionalization of ultrasmall dye-functionalized silica nanoparticles or the development of sensor-type particles where the sensor molecule location relative to the particle core is important. Further studies are also needed to elucidate how different surface chemical properties influence biodistribution and pharmacokinetics of these dots.

In Chapter 4 the first active (as opposed to passive) sub-10 nm silica nanoparticles in the form of nanophotosensitizers were introduced. These inorganic-organic hybrid silica nanoparticles covalently encapsulate the photosensitizer molecule and methylene blue derivate MB2. It was demonstrated that high effective per-particle singlet oxygen quantum yields of up to 161% relative to the individual MB2 molecule could be achieved by placing multiple dyes into the dots. Furthermore, particles could be functionalized with the targeting peptide c(RGDyC) leading to highly efficient and targeted photosensitizers. Next steps for the translation of these particles include in vitro and in vivo photodynamic therapy studies, pharmacokinetical studies, as well as testing of other photosensitizer molecules, *e.g.* the BODIPY dye or porphyrin dye families. Due to the water-based room temperature synthesis, therapeutic particles as described in this chapter may be produced cost-effectively and in large quantities, generating a pathway

for commercialization of such cancer treatments. In future studies it would be interesting, e.g. to test how scaling up of the synthesis volume of these reactions influences material quality and performance.

In Chapter 5 the research focus was shifted away from the encapsulation of functional molecules towards the chemical modification of the silica network. To that end, the concept of particle molecular photo-engineering (PMPE) was introduced. This entails modification of the chemical environment of the silica core around a fluorescent dye or other molecules, *e.g.* photosensitizer, to alter their photophysical properties. PMPE provides an alternative to time-consuming synthetic molecular modifications of dyes or to the use of imaging buffers, *e.g.* in sensitive live cell experiments. The modification of SNPs with mercaptopropyl groups to produce super-resolution dots (srC' dots) and iodopropyl groups (iC' dots) to introduce heavy atoms into the silica resulted in particles with new optical behavior, *i.e.* ultrabright probes applicable to stochastic optical super-resolution microscopy (srC' dots and iC' dots) and ultraefficient probes for photodynamic therapy (iC' dots). The concepts introduced are very general and should not be limited to the systems that were investigated. PMPE can be expected to play a role in further developments of SNPs, *e.g.* self-healing fluorescent particles, sensor particles, and others. Although super-resolution was demonstrated using stochastical optical reconstruction microscopy (STORM), further studies are needed to fully test out the potential of srC' dots, *i.e.* brightness, resolution, and their application to cell imaging in fixed and live cells. In addition, other super-resolution techniques may be applicable, *e.g.* utilizing triplet state dynamics introduced by iC' dots to engineer probes applicable for ground state depletion (GSD) microscopy.

In Chapter 7 block copolymer-based bottom-up self-assembled photonic material structures were investigated for applications in arts and architecture. The conditions for large scale self-assembly of a poly(styrene-block-tert-butyl methacrylate) with molar mass above 1M g/mol were studied and a method for the fabrication of an iridescent façade coating was described which was applied in the art installation *A needle woman: Galaxy Was a Memory, Earth is a Souvenir* by artist Kimsooja. This project provided a unique opportunity for a meaningful collaboration between the sciences and the arts, where both artist and scientists were challenged to go beyond the bounds of their own fields. The project included field-specific developments on both sides as well as finding common ground between the two fields in the pursuit of new discoveries and new perspectives.

While there has been significant progress of nanomedicine in the last 15 years with several nano-medical products on the market (*1*), the success rate for clinical translation with respect to the number of research projects investigating nanomaterials for medical applications is shockingly low (*2*). Until today, Cornell dots and Cornell prime dots have been the only inorganic particles that have received investigational new drug (IND) approval by the United States Food and Drug Administration (FDA) for stage I and stage II human clinical trials (*3*) for targeted molecular imaging. The versatility and biocompatibility of silica chemistry, the extraordinary size control in a batch synthesis and the ease of surface functionalization in aqueous solution as demonstrated by these particles has met all material requirements to date. This high-quality materials platform coupled with highly sensitive characterization methods such

as those introduced in this body of work, as well as fruitful collaborations between materials scientists and medical researchs provide an ideal situation for the translation of nanomaterials from the lab bench to the clinic. The progress described in this thesis on the design, synthesis, and characterization has brought ultrasmall fluorescent SNPs closer to the translation of the *Lab-on-a-Particle* concept than ever. New clinical applications can therefore be expected in the near future.

REFERENCES

(*1*) Bobo, D.; Robinson, K. J.; Islam, J.; Thurecht, K. J.; Corrie, S. R. Nanoparticle-Based Medicines: A Review of FDA-Approved Materials and Clinical Trials to Date. *Pharm. Res.*, **33,** 2373–2387 (2016).

(*2*) Peer, D.; Karp, J. M.; Hong, S.; Farokhzad, O. C.; Margalit, R.; Langer, R. Nanocarriers as an emerging platform for cancer therapy. *Nat Nanotechnol.*, **2,** 751–760 (2007).

(*3*) Phillips, E.; Penate-Medina, O.; Zanzonico, P. B.; Carvajal, R. D.; Mohan, P.; Ye, Y.; Humm J.; Gönen M.; Kalaigian H.; Schöder H.; Strauss H. W.; Larson S. M.; Wiesner U.; Bradbury, M. S. Clinical translation of an ultrasmall inorganic optical-PET imaging nanoparticle probe. *Sci. Transl. Med.*, **6,** 260ra149-260ra149 (2014).